

UNIVERSITÉ DU QUÉBEC À TROIS-RIVIÈRES

COMPOSÉS DE COORDINATION À BASE D'IONS DE MÉTAUX DE  
TRANSITION ET DE TERRES RARES POUR DES APPLICATIONS DE  
DÉTECTION D'IONS MÉTALLIQUES ET DE PHOTOLUMINESCENCE

TRANSITION AND RARE-EARTH METAL IONS-BASED COORDINATION  
COMPOUNDS FOR METAL ION SENSING AND PHOTOLUMINESCENCE  
APPLICATIONS

THÈSE PRÉSENTÉE  
COMME EXIGENCE PARTIELLE DU  
DOCTORAT EN SCIENCES DE L'ÉNERGIE ET DES MATÉRIAUX

PAR  
LOVE KARAN

AOÛT 2025

Université du Québec à Trois-Rivières Service de la bibliothèque

### Avertissement

L'auteur de ce mémoire ou de cette thèse a autorisé l'Université du Québec à Trois-Rivières à diffuser, à des fins non lucratives, une copie de son mémoire ou de sa thèse.

Cette diffusion n'entraîne pas une renonciation de la part de l'auteur à ses droits de propriété intellectuelle, incluant le droit d'auteur, sur ce mémoire ou cette thèse. Notamment, la reproduction ou la publication de la totalité ou d'une partie importante de ce mémoire ou de cette thèse requiert son autorisation.

## UNIVERSITÉ DU QUÉBEC À TROIS-RIVIÈRES

## DOCTORAT EN SCIENCES DE L'ÉNERGIE ET DES MATÉRIAUX (PH. D.)

**Direction de recherche :**

2023 – 2025 Mihaela Cibian

2019 – 2022 Adam Duong

---

Nom du directeur de recherche

Directeur de recherche

**Jury d'évaluation de la thèse :**

Mihaela Cibian

---

Nom du directeur de recherche

Directeur de recherche

Pierre Bénard

---

Nom du président de jury

Président de jury

Thomas Auvray

---

Nom de l'évaluateur interne

Évaluateur interne

Amlan Kumar Pal

---

Nom de l'évaluateur externe

Évaluateur externe

Thèse soutenue le 6 juin 2025.

## ACKNOWLEDGEMENT

My first and foremost thanks to Dr. Adam Duong for giving me the chance to pursue my research at the Université du Québec à Trois-Rivières (UQTR) under his supervision during 1019-2022. I convey my special thanks to Dr. Mihaela Cibian, Associate Professor, Department of Biochemistry, Chemistry, Physics and Forensic Science (DBCPFS), UQTR for her valuable suggestions in the compilation of this thesis. My sincere thanks to my parents for their rational and logical approach, humbleness, forgiveness, enormous love, support, and numerous sacrifices, which empowered me to cope with challenges in my life. I am heartily thankful to my younger brother Raj Karan Rana for his care and assistance during all ups and downs during my PhD. I am thankful to my lab mates for all their love and support. There are more names to be mentioned here, to whom I am highly thankful for lending their support to liberally use different instruments which were imperative for my research work. These names are Mr. Jocelyn Bouchard and Mr. Jean-Philippe Marineau, who provided me open access to the instruments at the times when I needed them most, without any restriction. I would like to thank Dr. Thierry Maris, Univesité de Montréal for the data collection of some of my compounds.

A sincere thanks to my friend and collaborator Mr. Alborz Bavandsavadkouhi for always being available whether it is to re-synthesize a compound or data acquisition on the instruments, he always helped me whenever I needed him.

I owe my thanks to my wife Prabhjyot Kaur who always stood by me with her support, replenishing me with power and endurance. A special thanks is reserved for my daughter Naisha Rana and my son Liaan Rana for their love, care, and encouragement that made the compilation of my research work possible.

I want to express my gratitude to the DBCPSF and the l'Institut de Recherche sur l'Hydrogène (IRH) for providing me pleasant and positive environment for conducting my research work. Finally, financial assistance from QES-II Diamond Jubilee, and Mitacs scholarships is deeply acknowledged.

**Love Karan**



## Abstract

The ideology that the property of a material is governed by its structure is a fundamental concept in chemistry and the related fields such as medicine, biochemistry, engineering, and materials sciences. Following this notion, we have focused our research on understanding and delineating the factors concerning structure-property relationship in transition metal and rare earth metal ions-based coordination compounds, which have been explored for metal ion sensing and photoluminescence studies. The Chapter 1 of the thesis is the introduction and review of literature where we have given an account of the history of coordination compounds, their design strategies and crystallization techniques. Besides, we have summarized some metal complexes of related secondary amide (-CONH-) ligands with different molecular designs and terphenyltetracarboxylic acid-based ligands and discussed their applications. In Chapter 2 of the thesis, a novel Co-MOF is explored as sensor for the detection of toxic metal ions using fluorescence titrations. In addition, Zn-MOF and Ni(II) based coordination polymer both having intriguing three-dimensional framework have also been synthesized and characterized. In Chapter 3 of the thesis, isostructural 1D coordination polymers of Cu(II), Co(II), and Zn(II) with a different naphthalene dicarboxamide ligand differing in the position of pyridine nitrogen with respect to amide group (-CONH-) are discussed. These compounds are characterized by various characterization techniques such as single crystal x-ray diffraction, nuclear magnetic resonance and infrared spectroscopy, thermogravimetric analysis, UV-Vis absorption and fluorescence spectroscopy. Moreover, chemical state identification of metal ions and chemical environments of different elements in these complexes are depicted by XPS spectroscopy. Chapter 4 is a review article on pyridine mono- and dicarboxamide ligands with tertiary amide or fully substituted nitrogen atom. Here, we have compiled diverse molecular designs of this class of ligands and grouped them into different categories based on the position of pyridine ring in the ligand molecules. Furthermore, the pertinent metal complexes of each category of the ligand are segregated systematically based on the dimensionality of their coordination frameworks. Besides, an account on the coordination chemistry of the metal complexes and their applications is also given. The Chapter 5 of the thesis involves the discussion on the photoluminescence studies of highly porous, isomorphous Metal-organic frameworks synthesized using terphenyl tetracarboxylic acid with Ln(III) ions. In this research, we have studied the room temperature photoluminescence of the compounds to investigate the antenna effect of the ligand. The results have shown that although ligand molecule prompts the emission from the Ln(III) ions to some extent, it cannot be used as an antenna molecule owing to the

incomplete transfer of electrons from its triplet state to the excited state of Ln(III) ions. This justification is further supported by theoretical calculations (TDDFT) performed on the ligand molecule. Conclusions and perspectives of the thesis are presented in Chapter 6. Overall, my research intends to portray the design strategies of the ligand and associated coordination compounds for desired application by meticulous selection of the organic functionalities and/or metal ions following the concept of “crystal engineering”.

**Keywords:** coordination polymers, Metal-Organic Frameworks (MOFs), fluorescence titrations, metal-ion sensing, photoluminescence studies, x-ray diffraction, computational studies.

## Résumé

L'idéologie selon laquelle la propriété d'un matériau est régie par sa structure est un concept fondamental en chimie et dans les domaines connexes tels que la médecine, la biochimie, l'ingénierie et les sciences des matériaux. Suivant cette notion, nous avons concentré nos recherches sur la compréhension et la délimitation des facteurs concernant la relation structure-propriété à l'aide de composés de coordination à base d'ions de métaux de transition et de terres rares, qui ont été explorés pour les applications de détection d'ions métalliques et de fluorescence. Le Chapitre 1 de la thèse est l'introduction et la revue de la littérature où nous avons rendu compte de l'histoire des composés de coordination, de leurs stratégies de conception et de leurs techniques de cristallisation. En outre, nous avons résumé certains complexes métalliques de ligands d'amide secondaire (-CONH-) apparentés avec différentes conceptions moléculaires et des ligands à base d'acide terphényltétracarboxylique, et discuté des applications dans le contexte de ces complexes. Dans le Chapitre 2 de la thèse, un nouveau Co-MOF est exploré comme matériau de détection pour d'ions métalliques toxiques à l'aide de titrages par fluorescence. De plus, des polymères de coordination à base de Zn-MOF et de Ni (II), tous deux dotés d'une structure tridimensionnelle intrigante, ont également été synthétisés et caractérisés. Dans le Chapitre 3 de la thèse, des polymères de coordination 1D isostructuraux de Cu(II), Co(II) et Zn(II) avec un ligand naphthalène dicarboxamide différent différant par la position de l'azote de la pyridine par rapport au groupe amide (-CONH-) sont discutés. Ces composés sont caractérisés par diverses techniques de caractérisation, par exemple : diffraction des rayons X sur monocristal, spectroscopie de résonance magnétique nucléaire, spectroscopie infrarouge, analyse thermogravimétrique, spectroscopies d'absorption UV-Vis et fluorescence. De plus, l'identification de l'état chimique des ions métalliques et des environnements chimiques de différents éléments de ces complexes est réalisée par spectroscopie XPS. Le Chapitre 4 est un article de synthèse sur les ligands pyridine mono- et dicarboxamide avec un amide tertiaire ou un atome d'azote entièrement substitué. Ici, nous avons compilé diverses conceptions moléculaires de cette classe de ligands et les avons regroupés en différentes catégories en fonction de la position du cycle pyridine dans les molécules du ligand. De plus, les complexes métalliques pertinents de chaque catégorie de ligand sont systématiquement séparés en fonction de la dimensionnalité de leurs cadres de coordination. En outre, un exposé sur la chimie de coordination des complexes métalliques et leurs applications est également présenté. Le Chapitre 5 de la thèse concerne la discussion sur les études de photoluminescence de structures métallo-organiques isomorphes synthétisées à l'aide d'acide

terphényltétracarboxylique avec des ions Ln(III). Dans cette recherche, nous avons étudié les propriétés de photoluminescence à température ambiante des composés afin d'étudier l'effet d'antenne du ligand. Les résultats ont montré que, bien que la molécule de ligand provoque dans une certaine mesure l'émission des ions Ln(III), elle ne peut pas être utilisée comme molécule d'antenne en raison du transfert incomplet des électrons du triplet à l'état excité des ions Ln(III). La justification de cela est donnée à l'aide des calculs théoriques (TDDFT) effectué sur la molécule de ligand. Les conclusions et les perspectives de la thèse sont présentées dans le Chapitre 6. Dans l'ensemble, mes recherches visent à décrire les stratégies de conception du ligand et des composés de coordination associés pour l'application souhaitée par une sélection méticuleuse des fonctionnalités organiques et/ou des ions métalliques en suivant le concept de "l'ingénierie cristalline".

**Mots clés :** polymères de coordination, cadres métallo-organiques, titrages par fluorescence, détection d'ions métalliques, études de photoluminescence, diffraction des rayons X, calculs théoriques.

## Table of contents

Acknowledgement.....	iii
Abstract.....	iv
Résumé.....	vi
Table of Contents.....	viii
List of Figures.....	xi
List of schemes.....	xxiii
List of Tables.....	xxiv
List of Charts.....	xxv
List of Equations.....	xxvi
List of Abbreviations.....	xxvi

## Chapter 1 – Introduction and Review of literature

1. Introduction.....	1
1.1. Classification of coordination complexes.....	1
• Zero-dimensional coordination complexes	
• Coordination Polymers	
• Coordination network solids	
• Metal-organic Frameworks	
1.2. History of Coordination Polymers (CPs) and MOFs.....	2
1.3. HSAB principles.....	3
1.4. Design strategies of CPs and MOFs.....	4
1.4.1. Building blocks	
1.5. Motifs and dimensionality.....	6
1.6. Synthetic routes for the synthesis of coordination polymers and MOFs.....	8
1.6.1. Saturation method	
1.6.2. Diffusion methods	
1.6.3. Hydrothermal/Solvothermal synthesis	

1.6.4. Other methods	
1.7. Structure property relationship and application.....	11
1.8. Pore tuning/modification in MOFs.....	11
1.9. Activation of MOFs and classification.....	13
1.10. Analytical techniques for the characterizing of organic and coordination compounds.....	14
1.10.1. Single crystal X-ray diffraction	
1.10.2. Powder X-ray diffraction	
1.10.3. Infrared spectroscopy	
1.10.4. CHN elemental analysis	
1.10.5. Nuclear Magnetic Resonance	
1.10.6. Thermo-gravimetric Analysis	
1.10.7. Scanning electron Microscopy/Energy dispersive X-ray spectroscopy	
1.11. Applications of CPs and MOFs.....	18
1.11.1. Magnetism	
1.11.2. Sensing/Detection	
1.11.3. Adsorption and Photo-degradation of dyes	
1.11.4. Photoluminescence	
1.11.5. Acetone Sensor	
1.11.6. Gas Separation	
1.12. Present Work.....	31
1.13. References.....	32

## **Chapter 2 – Research Article 1 - An Insight into Sensitive Detection of Metal ions Using a Novel Cobalt MOF: Single Crystal, Photoluminescence, and Theoretical Studies.**

2.1	Introduction.....	37
2.2	Objective.....	38
2.3	Authors contribution.....	38
2.4	Article.....	39

### **Chapter 3 – Research Article 2 - Isostructural coordination polymers of tethering naphthalene anchored bis(2-methylpyridinecarboxamide) ligand: single crystal, XPS, EDS and theoretical studies**

3.1	Introduction.....	55
3.2	Objective.....	56
3.3	Authors contribution.....	56
3.4	Article.....	57

### **Chapter 4 – Review Article - Fascinating Tertiary Carboxamide Ligands and Their Coordination Complexes: An account on Structural Chemistry and Practical Applications**

4.1	Introduction.....	70
4.2	Objective.....	70
4.3	Authors contribution.....	71
4.4	Article.....	71

### **Chapter 5 – Research Article 3- Isomorphous Ln-MOFs with terphenyl tetra-carboxylate struts: Single crystal, Photo-physical, and Theoretical studies.**

5.1	Introduction.....	181
5.2	Objective.....	182
5.3	Authors contributions.....	182
5.4	Article.....	182
5.5	Conclusion.....	198

### **Chapter 6 – Conclusion and Future work**

6.	Conclusion and future work.....	199
7.	List of Publications.....	202

### **Annex/Appendix: Supplementary Information**

Annex 1:	Supplementary Information of Article 1.....	204
Annex 2:	Supplementary Information of Article 2.....	221

Annex 3: Supplementary Information of Article 4.....	238
--	-----

## List of Figures

### Chapter- 1

Figure 1- Primary and secondary valency of a metal ion in the coordination compound.

Figure 2- Change of pore diameter with the variation in the length of organic linkers.

Figure 3- List of analogous ligands used in the synthesis of coordination compounds reported in the literature. Note- The protonated form of carboxylic acid ligands is shown above.

Figure 4- View of a) Chain motifs of  $\{\text{Cu}_2\text{O}_2\}$  dimeric units of complex 1, b) three-dimensional framework of complex 1, c) 2D layer of complex 2 comprising *anti-syn* axial-equatorial bridged  $[\text{Cu}(\text{OCO})]_n$  motifs, and d) 2D layers pillared by 3-pna molecules to form a three-dimensional network in complex 2.

Figure 5-View of a) hybrid three-dimensional network formed by non-interpenetrated three-dimensional net and a two dimensional 7-connected slab of complex 3, b) two-dimensional slab of complex 3, c) one-dimensional tape of complex 4 containing adpA and adpB ions, and d) three-dimensional network of complex 4.

Figure 6- View of a) 1D chain (inset) and two-dimensional grid of complex 5, b) three-dimensional framework of complex 6 with octahedral Cu(II) ions, and c) three-dimensional framework of complex 7 with pcu topology.

Figure 7- Pictorial depiction of a) 1D chain of octahedral Cd(II) ions of complex 8, b) two-dimensional grid of complex 8, and c) three- dimensional framework of complex 7 with pcu topology.

Figure 8- View of a) one-dimensional network formed by 5-mip and Cu(II) ions in complex 10, b) two-dimensional (4,4) grid framework of complex 10, c) one-dimensional meso-helical chain containing arched 3-bpah molecules in complex 11, and d) two-dimensional (4,4) grid framework of complex 11 with different orientations of 5-mip ions relative to complex 10.



Figure 9- View of a) two-dimensional of complex 12 comprising two different Cu(II) ions, b) three-dimensional framework of complex 12, c) two-dimensional of complex 13 comprising two different Cu(II) ions complex 13, and d) three-dimensional framework of complex 13.

Figure 10- View of a) two-dimensional of complex 14 comprising bridged 1,2-pda ions, b) three-dimensional framework of complex 14, c) dimeric units of Cu(II) ions formed by bridged 1,2-pda ions and 3-bpcb molecules, respectively in complex 15, and d) two-dimensional network of complex 15.

Figure 11- View of a) two-dimensional network of complex 16 comprising bimetallic Eu(III) units, and b) three-dimensional framework of complex 16.

Figure 12- View of a) trinuclear SBU containing two different Cd(II) ions in complex 17, and b) three-dimensional framework with tetragonal channels of complex 17.

Figure 13- View of a) tri-nuclear  $[\text{Na}_3(\mu_2\text{-MeOH})_3(\mu_3\text{-DMSO})]^{3+}$  cationic unit surrounded by three binuclear  $[\text{NiNa}(\text{COO})_4]^-$  anionic unit in complex 18, and b) three-dimensional framework of complex 18.

Figure 14- View of a) bi-nuclear  $[\text{Na}_3(\mu_2\text{-MeOH})_3(\mu_3\text{-DMSO})]^{3+}$  cationic unit surrounded by three binuclear  $[\text{NiNa}(\text{COO})_4]^-$  anionic unit in complex 18, and b) three-dimensional framework of complex 18.

## Chapter- 2

Figure 1- Pictorial presentation of (a) Ring synthons involving amide moieties, (b) *Catemer* synthons, (c) Ring synthons involving pyridine rings and (d) 3D hydrogen bonded framework. Colour codes- carbon: green, nitrogen: blue, oxygen: red

Figure 2- Pictorial depiction of (a) Asymmetric unit in structure of 1, (b) Trimeric unit surrounded by L1 and BDC molecules, c) Coordination environment around Co3 and Co4, respectively and (d) Pictorial depiction of 2D coordination sheet of trimeric units. Colour codes- in L1 carbon: green and in BDC carbon: magenta and, nitrogen: blue, oxygen: red, cobalt: yellow.

Figure 3- Perspective view of 3D framework (a) Parallel to *bc* plane, (b) *ac* Plane and (c) The topological view of the framework. Colour codes- L1: green, BDC: magenta, and cobalt in yellow/orange in topology picture (3c).

Figure 4- (a) Different coordination geometry around Zn(II) ions, (b) and (c) Interpenetrated chains and corresponding macrocycles generated along the framework. Colour codes- L1: green, BTB: magenta and zinc in yellow (octahedral), cyan (square pyramidal or trigonal bipyramidal) and orange (tetrahedral).

Figure 5- (a) 3- And 7-branch points and (b) Topological view of 3D net.

Figure 6- (a) Picture showing centrosymmetric unit of 3, (b) Pictorial presentation of the linkage of 1D chains, (c) Perspective view of 3D coordination framework parallel to *ab*- and (d) *ac*- Planes. Colour codes- L1: green, BDC: Magenta, nickel: blue.

Figure 7- Fluorescence emission of 1 in different solvents.

Figure 8- Emission spectra of L1 and 1.

Figure 9- Frontier molecular orbitals of L1 and Co(II) complex, respectively, and the associated bandgaps.

Figure 10- Quenching of fluorescence intensity of 1 by different metal ions. (Note- Blank refers to the emission from 1 before the addition of analytes).

Figure 11- Comparison of quenching efficiency of analytes after first five additions to 1 suspension.

Figure 12- Percent quenching efficiency of various analytes after some additions. Note that the sample was excited at 265 nm and the emission was observed at 378 nm.

Figure 13- Fluorescence intensity change upon addition of NaBF<sub>4</sub>, NaI and KNO<sub>3</sub> to suspension of 1. (Note- Blank corresponds to the emission from 1 before the addition of analytes).

Figure 14- Fluorescence intensity change upon addition of a) FeCl<sub>3</sub>, b) HgBr<sub>2</sub>, c) CuCl<sub>2</sub>, and d) CdI<sub>2</sub>, to L1 solution. (Note- Blank corresponds to the emission from 1 before the addition of analytes).

Figure 15- Tentative mechanism of the sensor-analyte interactions proposed for 1 with different metal ions.

### Chapter- 3

Figure 1- a) Shows asymmetric unit of ligand. Pictorial presentation of b) 1D chain, c) 2D sheet and d) 3D hydrogen bonded framework.

Figure 2- a) 1D coordination chain of 1. b) Overlay diagram showing the orientation of L1 in all compounds. Pictorial presentation of c) 2D sheet and d) 3D hydrogen bonding networks of 1.

Figure 3- a) and b) Plots of  $\delta a$  ( $^\circ$ ) vs  $\delta p$  ( $^\circ$ ) and  $X$  vs  $\delta d$  ( $^\circ$ ) for the comparison of the structures of 1 and 3, and 2 and 3.

Figure 4- Showing the characteristic binding energies (eV) for respective elements present in compound 1.

Figure 5- Showing results of SEM and EDS analysis of 1.

Figure 6- View of increase in energies of HOMO-LUMO states of 2 affected by interaction with solvent molecules relative to HOMO-LUMO states of L1. (Note – Figure 6 shows the speculative extent to which HOMO-LUMO states of 2 are affected by solvent effects relative to HOMO-LUMO states of L1. In compound 2, solvent effect of DMF has led to increase in energy of HOMO by 0.194 eV than LUMO (0.05 eV)).

### Chapter- 4

Figure 1- Mononuclear complexes of different fully substituted dicarboxamide ligands due to convergent coordination sites.

Figure 2- Divergent coordination sites of different fully substituted dicarboxamide ligands that lead to coordination complexes of higher dimensionality.

Figure 3 a) Unique crystallographic unit of the complex 1 showing coordination environment around Co(II) ion, b) 2D hydrogen bonded network of 1 supported by C-H $\cdots$ Cl and  $\pi\cdots\pi$  interactions, c) coordination environment around Ag(I) ion in complex 2, and d) hydrogen bonded 2D sheet of the complex 2.

Figure 4 a) Crystallographic independent units of the complex 5 and coordination environment around Cu(II) ions, b) 2D hydrogen bonded network of 5 supported by C-H $\cdots$ Cl and C-H  $\cdots\pi$  interactions, c) coordination environment around Zn(II) ion in the complex 7, and d) 2D hydrogen bonded sheet of the complex 7 involving coordinated water molecules and isothiocyanate ions.

Figure 5 a) Unique crystallographic unit of the complex 8, b) perspective view of 2D hydrogen bonded sheet containing mononuclear units connected by  $\text{O-H}\cdots\text{O}$ ,  $\text{C-H}\cdots\text{O}$ , and  $\pi\cdots\pi$  interactions in the complex 8, and c) view of coordination unit of the complex 9.

Figure 6 a) View of crystallographic unit of the complex 10 with Cu(II) ions in different chemical environments, b) pictorial view of hydrogen bonded trinuclear units of the complex 10, c) coordination environment around Cu(II) ion in the complex 11, and d) perspective view of 2D hydrogen bonded sheet comprising metallic units and perchlorate anions.

Figure 7 a) View of a) crystallographic independent units of the complex 12 containing Cu(II) ions in octahedral geometry, b) hydrogen bonded between adjacent units of the complex 12, c) crystallographic independent units of complex 13 with Co(II) ions in different chemical environments, and d) 2D hydrogen bonded sheet comprising trimeric units and water molecules (in red spheres). (Note- In the Figure 7b, the ligand molecules of crystallographic units are shown in blue and green colours for better visualization of 2D network).

Figure 8 Single crystal to single crystal transformation (SCSC) of the complex 12 to complex 14 on heating.

Figure 9 View of the unique crystallographic unit of a) complex 15 containing Zn(II) ions in tetrahedral geometry, b) complex 16 with Cu(II) ions in trigonal-bipyramidal geometry, c) complex 17 with Zn(II) ions in tetrahedral geometry and d) complex 18 with Zn(II) ions in square pyramidal geometry.

Figure 10 View of a) crystallographic unit of the complex 19, b) 3D hydrogen bonded framework of 19, c) octahedral Cu(II) ions connected to each other ( $\text{Cu}\cdots\text{Cu}^{\text{I}} = 2.6481(9) \text{ \AA}$ ) in a binuclear paddlewheel of complex 20, and d) interlinked binuclear paddle-wheel units in a 3D hydrogen bonded network of the complex 20.

Figure 11 View of the combination of metal ions and carboxylate ions used in dimeric paddle wheel complexes 18-24.

Figure 12 View of a) centrosymmetric dimeric unit of the complex 25, and b) 3D hydrogen bonded framework involving  $\text{C-H}\cdots\text{O}$  and  $\pi\cdots\pi$  (inset) interactions.

Figure 13 Pictorial presentation of centrosymmetric  $\text{CaZn}_2$  trinuclear unit of the complex 26.

Figure 14 View of a) octahedral environment of Fe(II) in the complex 27, b) 1D coordination chain reinforced by  $\text{C-H}\cdots\pi$  interactions in the complex 27, c) unique crystallographic unit of the complex 28, and d) 2D hydrogen bonded sheet of the complex 28 constructed by  $\text{O}_w\text{-H}\cdots\text{O}$  and supported by  $\pi\cdots\pi$  interactions.

Figure 15 View of a) octahedral environment of Mn(II) ion in the centrosymmetric unit of the complex 29, and b) 1D coordination chain of the complex 29.

Figure 16 Perspective view of a) crystallographic independent dimeric units of the complex 30, b) 1D coordination chain formed by bridged Pmb anions and water molecules in the complex 30, c) unique crystallographic unit of complex 31 along with the 1D chain (inset), and d) 2D hydrogen bonded sheet of the complex 31. (Note- side groups on amide nitrogen atom have been deleted for structural clarity).

Figure 17 Pictorial presentation of a) centrosymmetric unit and the 1D chain of complex 32, b) 2D hydrogen bonded sheets with ABAB.... pattern involving 1D coordination chain (A) and a hydrogen bonded chain formed by perchlorate, acetone and water molecules (B) of the complex 32, c) unique crystallographic unit of 33 comprising distorted pentagonal-bipyramidal geometry around Cd(II) ion, and d) 1D tape formed by hydrogen bonding between coordinated carboxylate groups and water molecules of adjacent coordination chains in the complex 33.

Figure 18 View of a) 1D coordination chain of tetrahedral Co(II) ions of the complex 34, b) hydrogen bonded 2D sheet involving C–H...Cl interactions between 1D coordination chains in the complex 34, c) 1D tape of the complex 35 supported by  $\pi \cdots \pi$  interactions, and d) 2D hydrogen bonded corrugated sheet of the complex 35. (Note- Nitrate ions have not been shown in the Figure 18c and atoms not participating in hydrogen bonding have been deleted for clarity in the figure 18d).

Figure 19 Pictorial view of a) 1D coordination chain of the complex 36 supported by  $\pi \cdots \pi$  interactions, b) corrugated hydrogen bonded 2D sheet of the complex 36, c) 1D chain of the complex 37 supported by  $\pi \cdots \pi$  interactions, and d) 2D hydrogen bonded network of the complex 37 with ABAB.... pattern of coordination chains (Note- Nitrate ions have deleted in the Figure 19a for the sake of clarity).

Figure 20 a) View of a) mixed Co( $T_d$ )–Co( $O_h$ )–Co( $T_d$ ) assembly in the 1D chain of complex 38, b) 2D sheet formed by C–H...Cl hydrogen bonding interactions between adjacent chains in the complex 38, and c) transformation of the complexes on varying counter anions or/and reaction conditions (Note- Some atoms have been deleted from Figure 20b for the sake of clarity).

Figure 21 Pictorial representation of a) centrosymmetric unit of the complex 40, and b) 2D coordination sheet of the complex 40 formed by  $\mu_{1,3}$ -azido bridges. (Note- Amide chains have been deleted for better visualization of the structure.)

Figure 22 View of a) unique crystallographic unit of the complex 41 with N,N and S,S pairs of thiocyanato ions in *cis*-position, and b) 3D coordination framework of the complex 41.

Figure 23 Pictorial presentation of a) tetra-nuclear cluster of trigonal bipyramidal Cu(II) ions of the complex 42 with two fold axis passing through oxo and one of the chloride ligands, and b) tetrahedrally distorted cubane core  $\text{Cu}_4\text{I}_4$  of tetrahedrally coordinated Cu(I) ions of the complex 43.

Figure 24 Pictorial view of the trigonally distorted rectangular bipyramidal environment of Cu(II) ions in a) complex 44, and b) complex 45.

Figure 25 Pictorial view of a) octahedral coordination of Co(II) ion in the complex 46, b) 2D hydrogen bonded sheet involving lattice water molecules and perchlorate ions of the complex 46, and c) unique coordination unit of the complex 48. (Note – Counter anions are not shown in the coordination units of complexes 46 and 48. Oxygen atoms of water molecules in the Figure 25b are shown in yellow, while hydrogen atoms are shown in blue.)

Figure 26 Pictorial presentation of a) coordination environment of Ni(II) ion in the complex 49, b) nitrate ions showing monodentate coordination and ionic mode in the complex 50, c) bidentate chelating mode of nitrate ions in the complex 51, and d) mono- and bidentate modes of nitrate ions in the complex 53. (Note – Uncoordinated nitrate ions have been deleted for clarity in the complex 49)

Figure 27 View of a) distorted square-pyramidal geometry of Cu(II) ion in the complex 54, b) 2D hydrogen bonded network of 54 constructed by  $\text{C-H}\cdots\text{O}$  and  $\text{C-H}\cdots\text{F}$  interactions involving triflate ions and methylene groups, c) octahedral coordination of Cu(II) ion in the complex 57, and d) 2D hydrogen bonded network of the complex 57 involving triflate ions, and lattice and coordinated water molecules. (Note – In all figures, chlorine atoms are shown in cyan and fluorine atoms are shown in dark green colour. Lattice water molecules are shown in maroon/violet colour in the Figure 27d.

Figure 28 View of a) octahedral environment of Cu(II) ion in the complex 58, b) 3D hydrogen bonded framework of 58 constructed by hydrogen bonding between the octahedral units and the lattice acetonitrile molecules (violet colour), c) octahedral coordination of Cu(II) ion in the complex 59, and d) 2D hydrogen bonded network of 59 involving coordinated thiocyanate ions and ethanol molecules.

Figure 29 View of a) distorted pentagonal bipyramidal geometry of  $\text{UO}_2(\text{IV})$  ion of the complex 60, b) distorted mono-capped square antiprism environment of Eu(III) ion of the complex 62, and c) centrosymmetric unit  $[\text{La}(\text{NO}_3)_3(\text{L}^{12})_2]$  containing 12-coordinated La(III) ion in the complex 64. (Note- Amide nitrogen atoms and substituted groups on it have been deleted in the Figure 29b).

Figure 30 Pictorial view of a) mononuclear unit of the complex 65 and b) 1D polymeric chain (inset) of the complex 66, c) coordination environment of  $\text{UO}_2(\text{IV})$  ion in the complex 67, and d) coordination environment of  $\text{UO}_2(\text{IV})$  ion in the complex 68. (Note- The counter-anions have not been shown in the Figure 30c and 30d.)

Figure 31 View of a) distorted square-pyramidal geometry of  $\text{Cu}(\text{II})$  ions in the centrosymmetric dimeric unit of the complex 69, b) tetrahedral geometry of  $\text{Hg}(\text{II})$  ions in the complex 71, c) semi-localized type  $\text{Lp} \cdots \pi$  interactions among adjacent dimeric units of the complex 71, and d) representative dimeric unit of the complexes 72-74 supported by semi-localized type  $\text{Lp} \cdots \pi$  interactions.

Figure 32 View of a) tetrahedrally coordinated  $\text{Hg}(\text{II})$  ion in the complex 75, b) ligand driven 1D coordination chain of the complex 75, c) square-pyramidal coordination environment of  $\text{Hg}(\text{II})$  ion in the complex 76, and d) 1D coordination chain involving bridged halide ions and  $\text{L}^{16}$  molecules of the complex 76.

Figure 33 View of a) 2D sheet involving  $[\text{HgCl}_2]_n$  and  $[\text{Hg}(\text{L}^{17})\text{Cl}_2]_n$  chains connected by  $\text{Cl}^-$  bridges in the complex 78, b) 2D network containing edge sharing  $[\text{Hg}(\text{L}^{17})\text{X}_2]_2$  units connected by  $\mu_2$ -bridged  $\text{L}^{17}$  molecules in the complexes 79 and 80, c) ligand driven 2D network of the complexes 81 and 82 containing  $\mu_3$ -bridged  $\text{L}^{18}$  molecules with no halide bridges, and d) 2D framework of the complex 78 endorsed by mercurophilic interactions.

Figure 34 View of a) metallacycle of the complex 83 containing tetrahedrally coordinated  $\text{Hg}(\text{II})$  ions, b) 2D sheet of stacked metallocyclic units in the complex 83, c) 3D hydrogen bonding framework of 84 involving hydrogen bonding between water molecules and  $\text{Cu}(\text{II})$  metallacycles, and d) hydrogen bonded tape motif with  $\text{T6}(6)4(4)4(3)4(3)$  type aggregation of lattice water molecules of the complex 84. (Note- The oxygen atoms of water molecules are shown in mustard colour in the Figure 34b, while it is yellow colour in the Figures 34c and 34d. Hydrogen atoms of water molecules are shown in orange colour).

Figure 35 View of a) centrosymmetric unit containing octahedral  $\text{Cd}(\text{II})$  ion in the complex 85, b) 1D coordination chain of the complex 85 containing GG-conformation of ligand molecules, c) coordination unit containing tetrahedral  $\text{Cd}(\text{II})$  ion in the complex 86, and d) 2D hydrogen bonding framework of 86 involving  $\text{C}-\text{H} \cdots \text{S}$  interactions.

Figure 36 View of a) octahedral coordination environment around  $\text{Co}(\text{II})$  ion in the complex 88, b) 1D coordination chains connected by short  $\text{S}_{\text{NCS}} \cdots \text{O}_{\text{methanol}}$  contacts in the complex 88,

c) octahedral geometry of Co(II) ion in the complex 89, and d) 2D hydrogen bonded network involving 1D coordination chains, nitrate ions and water molecules in 89.

Figure 37 View of a) 2D layered structured comprising zig-zag 1D chains of the complex 90, b) octahedrally coordinated Co(II) ions in the cationic and anionic units of the complex 92, c) hydrogen bonded 1D tape of anionic  $[\text{Co}(\text{hmp})_2(\text{L}^{22})]_n^{2n-}$  and cationic  $[\text{Co}(\text{H}_2\text{O})_4(\text{L}^{22})]_n^{2n+}$  of the complex 92, and d) 3D hydrogen bonded network of the complex 94 with a rare topology  $(6^3)(6^98)$ .

Figure 38 View of a) 2D grid containing 14- and 24-membered macrocycles of the complex 95, b) 3D hydrogen bonded network comprising sandwiched SUL anions between 2D coordination sheets in the complex 96, c) 2D coordination network with zig-zag arrangement of bridged ligand molecules in the complex 97 and d) pyridine rings oriented out of plane relative to mercaptoimidazoline moiety in the complex 97.

Figure 39 View of a) 2D framework of the complex 98 containing 60-membered  $\text{Zn}_4(\text{L}^{21})_4$  rings, b) 2D coordination network supported by argentophilic and  $\pi \cdots \pi$  interactions in the complex 100, c) 2D framework of the complex 101 and d) 2D framework of the complex 102.

Figure 40 View of a) 2D framework of the complex 103 containing 14- and 24- membered metallo-cyclic rings, and b) stacked 2D sheets showing AAAA type pattern.

Figure 41 View of a) centrosymmetric unit of the complex 106, b) 2D network comprising Cd(II) ions bridged by  $\mu$ -1,3-azide ions, c) 3D framework involving 2D sheets of Cd(II) ions connected by bridged *trans*- $\text{L}^{21}$  molecules, and d) tetragonal prism channels cut off by  $\text{Cd}_4(\text{N}_3)_4$  grids in the complex 106.

Figure 42 Pictorial presentation of a) bi-capped square antiprism coordination geometry around Gd(III) ion in the complex 109 b) compression of  $\text{M}-\text{L}^{24}$  bonds due to the substitution of phenyl rings at 3, 5-position in the complex 111, c) elongation of  $\text{M}-\text{L}^{25}$  bonds due to substitution of methyl groups at 2,5- position of phenyl rings of  $\text{L}^{25}$  in the complex 112. (Note- The mononuclear complex in Figure 42a is the representative unit of isostructural complexes of Pr(III) (107), Nd(III) (108), and Tb(III) (110)).

Figure 43 View of a) 12-coordination geometry of La(III) ion in the complex 113, b) 10-coordination geometry of Gd(III) ion in the complex 115, c) tetragonal pyramid geometry around Cu(II) ion in the complex 117, and d) 7-coordinated Cd(II) ion in the complex 118.



(Note- Tertiary nitrogen atoms of amide group and the respective substituents appended to it have been deleted for clarity in the complexes 113, 116, and 118. Both the solvent molecules, and the counter anions crystallized in the lattice have also been deleted.)

Figure 44 View of a) 8-coordination geometry of U(VI) ion in the complex 119, b) 12-coordination geometry of Th(IV) ion in the complex 120, c) coordination environment around La(II) ion and the elongation of M-L<sub>amide</sub> bonds in the complex 121, and d) coordination environment of Eu(III) ion and the compression of M-L<sub>amide</sub> bonds in the complex 122. (Note- The solvent molecules and counter anions crystallized in the lattice have been deleted for complexes 119 and 120.)

Figure 45 View of a) centrosymmetric unit of the complex 123, b) dihedral angles between amide planes, and between amide and pyridine planes in the complex 123, and c) representative mononuclear unit of the complexes 124-128.

Figure 46 View of a) cationic unit  $[\text{Cu}_2(\text{phtH})_2(\text{L}^{34})_2(\text{H}_2\text{O})_4]^{+2}$  containing  $\text{L}^{34}$  molecules oriented in U-conformation, and b) 2D network of tubular channels formed by hydrogen bonding between neighbouring cationic units in the complex 129.

Figure 47 View of a) repeating centrosymmetric unit of the complex 130, b) orientation of pyridine ring w.r.t amide plane, and c) 1D coordination polymer containing bridged  $\text{L}^{31}$  molecules between Cu(II) paddlewheel units.

## Chapter- 5

Figure 1- View of a) ORTEP representation of asymmetric unit of the compound 1, b) Ho(III) paddlewheel units connected by bridged  $\mu_8$ -L ions to form 4- and 8c nodes, 3) polyhedral presentation of three-dimensional framework down the c-axis, and d) 4,8-c bi-nodal net.

Figure 2- Showing characteristic emission bands of L1, and Ln(III) ions in all complexes.

Figure 3- Simplified scheme showing the photosensitization of Ln(III) ions in the compounds 1 and 4 by L1 molecule, with associated photophysical phenomenon. (IC – Internal conversion, ISC – Intersystem crossing, ET – Energy-transfer/Photosensitization, BT- Back transfer of energy)

Figure 4- Colour coordinates of compounds 1-4 in the CIE 1931 color space.

## Annex- 1: Supplementary Information of Chapter 2 (Article 1).

Figure S1- Comparison of PXRD pattern of asynthesized **1** and patterns recorded after exposing the MOF (**1**) to different metal ions solutions with the simulated pattern.

Figure S2- Comparison of PXRD pattern of asynthesized **2** and its simulated pattern.

Figure S3- Comparison of PXRD pattern of asynthesized **3** and its simulated pattern.

Figure S4- BFDH morphologies of **L1**, compound **1** and **2**.

Figure S5-  $^1\text{H}$ -NMR of **L1**.

Figure S6-  $^{13}\text{C}$ -NMR of **L1**.

Figure S7- IR spectra comparison of **L1**, **H2BDC**, **1** and **3**.

Figure S8- IR spectra comparison of **L1**, **L3**, and compound **2**.

Figure S9- a) ORTEP diagram of **L1** at 30% probability, b) showing dihedral angle between naphthalene and amide plane.

Figure S10- ORTEP diagram of compound **1** at 30% probability.

Figure S11- ORTEP diagram of compound **2** at 30% probability.

Figure S12- ORTEP diagram of compound **3** at 30% probability.

Figure S13- Thermal stability curve of compound **1**, **2** and **3**.

Figure S14- Electrostatic potentials mapped on electron iso-density surface at 0.01 au. MEP plot a) for **L1**, and b) compound **1**.

Figure S15- Quenching of fluorescence intensity of **1** by  $\text{Cu}^{+2}$ ,  $\text{Fe}^{+2}$ ,  $\text{Pb}^{+2}$ ,  $\text{Cd}^{+2}$ ,  $\text{Co}^{+2}$ , and  $\text{Cu}^{+}$  ions.

Figure 16- Emission spectra and the corresponding Stern-Volmer plots of **1** in different a)  $\text{Ru}^{+3}$ , b)  $\text{Fe}^{+3}$  and c)  $\text{Hg}^{+2}$  concentrations in DMF.

Figure S17- Quenching of fluorescence of **1** by  $\text{Ni}^{+2}$ ,  $\text{Be}^{+2}$ ,  $\text{Mn}^{+2}$ , and  $\text{Zn}^{+2}$  ions.

Figure S18- Showing the comparison of fluorescence quenching of **1** with a) different Fe(III) and b) Cu(II) salts.

Figure S19- Illustrates negligible change in fluorescence intensity upon the addition of  $\text{ClO}_4^-$ ,  $\text{SCN}^-$ , and  $\text{Br}^-$  ions.

## **Annex- 2: Supplementary Figures of Chapter 3 (Article 2).**

Figure S1- Comparison of PXRD pattern of asynthesized compound **1** with the simulated pattern.

Figure S2- Comparison of PXRD pattern of asynthesized compound **2** with the simulated pattern.

Figure S3- Comparison of PXRD pattern of asynthesized compound **3** with the simulated pattern.

Figure S4- BFDH morphologies of **L1**, compound **1**.

Figure S5- Diffraction data plots showing weak diffraction from the crystal at higher angles.

Figure S6-  $^1\text{H}$ -NMR of **L1**.

Figure S7-  $^{13}\text{C}$ -NMR of **L1**.

Figure S8- ORTEP diagram of **L1** at 40% probability.

Figure S9- Showing the dihedral angle between pyridine and naphthalene ring planes of **L1**.

Figure S10- ORTEP diagram of compound **1** at 40% ellipsoidal probability.

Figure S11- ORTEP diagram of compound **2** at 40% ellipsoidal probability.

Figure S12- ORTEP diagram of compound **3** at 40% ellipsoidal probability.

Figure S13- Supramolecular synthons generated in a 2D sheet and 3D hydrogen bonded framework of compound **1**.

Figure S14- XPS spectral peaks for compound **2**.

Figure S15- XPS spectral peaks for compound **3**.

Figure S16- EDS spectra of compound **2**.

Figure S17- EDS spectra of compound **3**.

Figure S18- Thermogravimetry curves for **L1** and **1-3**.

Figure S19- Energy gap between excited and ground states of compounds **1** and **3**.

## **Annex- 3: Supplementary Figures of Chapter 5 (Article 4).**

Figure S1- IR spectra of **L** and compounds **1-4** .

Figure S2- ORTEP representation of compound **2** at 30% ellipsoidal probability.

Figure S3- ORTEP representation of compound **3** at 30% ellipsoidal probability.

Figure S4- ORTEP representation of compound **4** at 30% ellipsoidal probability.

Figure S5- Absorption spectra of **L1** and compounds **1-4**.

Figure S6- Simplified scheme showing the photosensitization of Ln(III) ions in the compounds **2** and **3** by **L1** molecule, with associated photophysical phenomenon.

## List of Schemes

### Chapter- 1

Scheme I- Classification of coordination complexes.

Scheme II – Examples of the ligand molecules used to synthesize coordination networks.

Scheme III – Metal nodes and organic linkers used for the construction of coordination networks.

Scheme IV – View of different motifs constructed using linear linkers with different types of connectors.

### Chapter- 2

Scheme I- Molecular structures of ligands **L1**, and deprotonated forms of carboxylic ligands with corresponding codes.

Scheme II- Coordination modes shown by the ligands (1) ( $\mu_2\text{-}\kappa^2\text{-}\eta^1\text{:}\eta^1$ ) in all complexes, (2) ( $\mu_4\text{-}\kappa^4\text{-}\eta^1\text{:}\eta^1\text{:}\eta^1\text{:}\eta^1$ ) in complex 1, (3) ( $\mu_4\text{-}\kappa^4\text{-}\eta^1\text{:}\eta^1\text{:}\eta^2\text{:}\eta^2$ ) in complex 1, (4) ( $\mu_2\text{-}\kappa^2\text{-}\eta^1\text{:}\eta^1$ ) in complex 3, and ( $\mu_3\text{-}\kappa^6\text{-}\eta^1\text{:}\eta^1\text{:}\eta^1\text{:}\eta^1\text{:}\eta^1\text{:}\eta^1$ ) in complex 2.

### Chapter- 3

Scheme I- Typical hydrogen bonded motifs in primary amides.

## Chapter- 4

Scheme I- Class 1, 2, and 3 ligands.

Scheme II- Coordination modes of ligands.

## List of Tables

### Chapter- 1

Table 1- Classification of Hard-Soft acids and bases.

### Chapter- 2

Table 1- Summary of the metal-ligand combination used, coordination mode of the ligands, and the framework topologies associated.

### Chapter-3

Table 1- Crystallographic parameters for L1 and 1-3.

Table 2- Values of core level binding energies of different elements involved in 1, 2 and 3.

Table 3- Variation in the HOMO-LUMO energies of compounds 1-3 relative to L1.

Table 4- Energy decomposition analysis on L1 and 1-3.

### Chapter- 4

Table 1- Pertinent crystallographic parameters of the complexes.

Table 2- Summary of the applications of coordination complexes.

### Chapter- 5

Table 1- Coordination geometries and CShM's values.

Table 2- Excited singlet states and their oscillator strengths.

Table 3- Energy difference ( $\Delta$ , in  $\text{cm}^{-1}$ ) of the emissive states of Ln(III) ions with respect to triplet state of L1.

Table 4- Colour coordinated of compounds **1-4**.

## **Annex 1- Supplementary Tables of Chapter 2 (Article 1).**

Table S1- I.R table of the complexes.

Table S2- Pertinent atomic parameters for **1**, **2**, and **3**.

## **Annex 2- Supplementary Information of Chapter 3 (Article 2).**

Table S1- I.R table.

Table S2- Hydrogen bonds for **L1** [Å and deg.].

Table S3- Hydrogen bonds for compound **1** [Å and deg.].

Table S4- Hydrogen bonds for compound **2** [Å and deg.].

Table S5- Hydrogen bonds for compound **3** [Å and deg.].

## **Annex 3- Supplementary Tables of Chapter 5 (Article 4).**

Table S1- Crystal data and structure refinement for compound **1**.

Table S2- Crystal data and structure refinement for compound **2**.

Table S3- Crystal data and structure refinement for compound **3**.

Table S4- Crystal data and structure refinement for compound **4**.

Table S5- Characteristic IR frequencies for different functional groups in the compounds **1-4**.

Table S6- Sub-states of Singlets.

Table S7- Sub-states of Singlets.

Table S8- Energy gap between excited states.

## **List of Charts**

### **Chapter- 4**

Chart 1- Structure of Ligand  $L^1-L^{34}$

## List of Equations

### Chapter- 1

Braggs Law

### Chapter- 5

Colour purity (%)

## List of Abbreviations

BTC – benzene-1,3,5-tricarboxylic acid

BBC - benzene-1,3,5-triyl-tris(benzene-4,1-diyl))tribenzoate

BPDC – 4,4'-biphenyldicarboxylic acid

CSD- Crystal structure database

CPs – Coordination polymers

CN – Coordination number

DMF – Dimethylformamide

DMA - N,N-dimethylacetamide

DEF - N,N-diethylformamide

DMSO – Dimethyl sulfoxide

DNA – Deoxyribonucleic acid

EDS - Energy dispersive X-ray spectroscopy

HSAB – Hard-soft acid base

LFT – Ligand field theory

MOFs- Metal-organic polymers

MOT – Molecular orbital theory

MB - Methyl blue

NLO – Nonlinear optics

NMR- Nuclear magnetic resonance

NIST – National Institute of standards and technology

PDC – 2,6-pyrazinedicarboxylic acid

PXRD - Powder X-ray diffraction

RhB- Rhodamine B

SBU- Secondary building unit

SCXRD – Single crystal x-ray diffraction

SEM - Scanning electron Microscopy

TGA - Thermo-gravimetric analysis

TDC – 2,5-thiophenedicarboxylic acid

TPDC- [p-Terphenyl]-4,4''-dicarboxylic acid

TDDFT – Time dependent density functional theory

t-1,4cdc - 1,4-cyclohexanedicarboxylate

3-pina - 3-pyridylisonicotinamide

3-pna - 3-pyridylnicotinamide

adp – Adipate

ip – Isophthalate

hip – 5-hydroxyisophthalic acid

hdin- *N,N'*-(hexane-1,6-diyl)diisonicotinamide

tdc - 2,5-thiophenedicarboxylate,



hdn-*N,N'*-(hexane-1,6-diyl)dinicotinamide

5-mip - 5-methylisophthalate

4-bpah - *N,N'*-bis(4-pyridinecarboxamide)-1,2-cyclohexane

3-bpah - *N,N'*-bis(3-pyridinecarboxamide)-1,2-cyclohexane

3,4-pdc- 3,4pyridinedicarboxalate

bbin - bis(butane-1,4-diyl)isonicotinamide

bbn - bis(butane-1,4-diyl)nicotinamide

4-bpfp = *N,N'* -bis(4-pyridylformyl)piperazine

3-bpcb = *N,N'*-bis(3-pyridinecarboxamide)-1,4-benzene

1,2-pda = 1,2phenylenediacetic acid

tptc=terphenyl-3,3'',5,5''-tetracarboxylate

# **Chapter- 1**

## **Introduction and Review of Literature**

## 1. Introduction

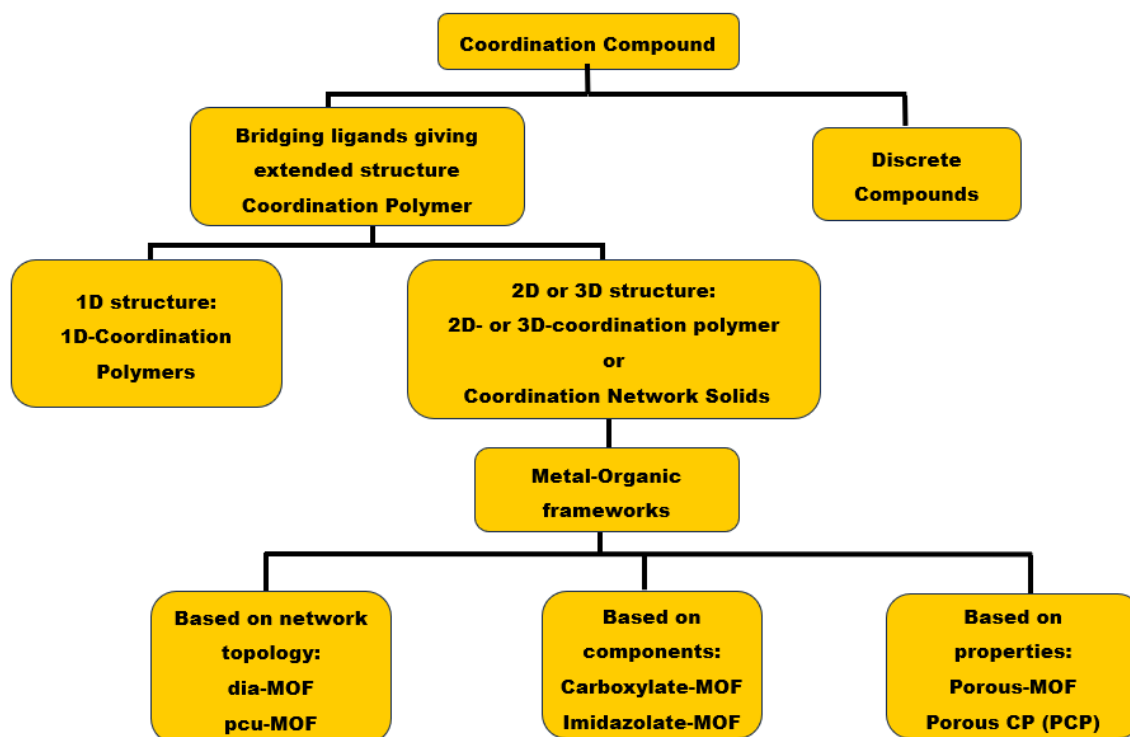
By the International Union of Pure and Applied Chemistry (IUPAC) definition [1] a coordination complex/compound is best described as a *coordination entity*: ‘an assembly consisting of a central atom (usually metallic) to which is attached a surrounding array of other groups of atoms (ligands)’. In inorganic/ coordination chemistry, the central atom is a metal ion and the ligand is: ‘the atoms or groups joined to the central atom’ [1a].

The field of coordination chemistry has flourished after the seminal work of Alfred Werner in 1893 [1b], who described the octahedral coordination sphere of Co(II) ion in the complex  $[\text{Co}(\text{NH}_3)_6]\text{Cl}_3$  and thus established the basis for the illustration of coordination environments using polyhedral shapes.

### 1.1 Classification of coordination complexes

Coordination complexes can be classified into three categories based upon the dimensionality (Scheme I) [2]

- Zero-dimensional coordination complexes- This category includes the mononuclear or dimeric complexes, in which extension to higher dimension is brought about by hydrogen bonds and other non-covalent interactions such as metallophilic,  $\pi \cdots \pi$ , C-H $\cdots\pi$ , halogen bonding etc.
- Coordination polymers- These are crystalline materials comprised of infinite one-dimensional chain constructed from metal ion nodes coordinated to bridged organic struts. Extensions to higher dimensions can be achieved by various non-covalent interactions.
- Coordination network solids- These are crystalline materials in which bridging of ligands (bridging) between metal centres leads to two- and three-dimensional coordination compounds.
- Metal organic frameworks (MOFs)- MOFs are the subclass of coordination network solids that own a special status of being porous 2D or/and 3D networks in which carbon containing ligands bridged among mono-nuclear, polynuclear or 1D coordination entities.



**Scheme I-** Classification of coordination complexes [2]

## 1.2 History of coordination polymers and MOFs

The term “Coordination polymer” was coined by J. C. Bailar in 1967 after he drew a comparison between organic polymers and a class of inorganic coordination complexes, which he called “coordination polymer” [3]. In this exceptional piece of work, he has described and established a set of rules to synthesize coordination chain compounds. Since then, coordination polymers have lured the interest of researchers owing to their fascinating framework structures and applications in the fields of luminescence, catalysis, nonlinear optics (NLO), magnetism etc. [4-6], and the fundamental chemistry and physics behind them. Various properties such as electrical, optical and magnetism of coordination polymer have a direct relation to their chemical composition i.e the type of metal ion and organic ligand, electronic environment, and framework structure [7]. In contrast to coordination polymers (CPs), the interest in porous coordination complexes also known as MOFs started around 1990 following the seminal work done by Hoskins and Robson [8].

In their research work, they have discussed the formation of a range of stable and crystalline microporous solids synthesized using structure-directing agents. They also have given an account of gas sorption, catalytic properties etc., which further allowed

post-synthetic modifications in the existing MOFs. The field of MOF got actual attention in the year 1995 by Yaghi et al. [9], where sorption properties of a layered Co(II) MOF was shown. Following this, syntheses of MOF-5 [10] have revolutionized the field. The feature that makes MOFs special over CPs is their highly porous nature together with large internal surface area [11-12] and the presence of pores/open spaces that grants them widespread properties. These features make them suitable materials for catalysis, gas storage, drug delivery, gas vapor separation, lithium-ion batteries, water treatment, and carbon dioxide capture applications [13].

### 1.3 HSAB principles

The compatibility between metal ion and the donor atom of ligand is an important parameter that decides whether an extended coordination framework could be formed or not. For instance,  $\text{Ln}^{+3}$  and  $\text{Zr}^{+4}$  prefers to bond linear ligands that contain oxygen as a donor atom. In contrast, transition metal ions such as  $\text{Ni}^{+2}$ ,  $\text{Co}^{+2}$ ,  $\text{Cu}^{+2}$ ,  $\text{Zn}^{+2}$  etc. are capable to coordinate to ligands whether linear or/and chelating containing oxygen, nitrogen, and sulfur atom. Why these ions have versatile coordination potential than trivalent lanthanide ions? Why zirconium and lanthanide ions prefer oxygen atom? These questions could be explained considering the acidic and basic behavior of both metal ion and the ligand donor atoms, respectively. In 1963, R. G. Pearson qualitatively gave generalized correlation between Lewis-acid (metal ions) and Lewis bases (N, O, S etc.) and classified them as hard and soft based on the Hard and soft Acids and Bases principles [14]. According to HSAB, Class ‘a’ acids prefer to bind to Class ‘a’ bases, while class ‘b’ acids prefer to bind to ‘class b’ bases. Class ‘a’ acids also known as Hard Acids are small, less polarizable metal ions in higher oxidation states that forms stable complexes with ligands whose donor atoms are Hard Bases i.e elements that are small, highly electronegative and not polarizable. Conversely, Class ‘b’ acids also called Soft Acids are metal ions having large ionic radius, low oxidation state and easily polarizable in nature prefers to bind Soft Bases i.e the elements (donor atom) that have large ionic radius, less electronegativity and are highly polarizable. Between these two extremes, there are some metal ions and non-metals that have intermediate properties for example lower charge and larger size than hard acids and higher charge and smaller size than soft acids. Table 1 shows some examples of of metal ions and anions/ligand species (in terms donor element) classified based on Hard and Soft criteria.

**Table 1** – Classification of Hard-Soft acids and bases [14].

Hard Acids and Bases (Class ‘a’)	Borderline Acids and Bases	Soft Acids and Bases (Class ‘b’)
Acids - $\text{Na}^+$ , $\text{Fe}^{+3}$ , $\text{Co}^{+3}$ , $\text{Ln}^{+3}$ (Lanthanide ions), $\text{Zr}^{+4}$ , $\text{Al}^{+3}$ , $\text{Ti}^{+4}$ , $\text{Cr}^{+3}$	Acids - $\text{Fe}^{+2}$ , $\text{Co}^{+2}$ , $\text{Ni}^{+2}$ , $\text{Cu}^{+2}$ , $\text{Zn}^{+2}$ , $\text{Ru}^{+3}$ , $\text{Ir}^{+3}$	Acids - $\text{Cu}^+$ , $\text{Pb}^{+2}$ , $\text{Cd}^{+2}$ , $\text{Hg}^{+2}$ , $\text{Pt}^{+2}$ , $\text{Ag}^+$
Bases – $\text{COO}^-$ , $\text{NH}_3$ , $\text{H}_2\text{O}$ , $\text{ROH}$ , $\text{OH}^-$ , $\text{F}^-$ , $\text{Cl}^-$ , $\text{NO}_3^{2-}$ , $\text{CO}_3^{2-}$ , $\text{PO}_4^{3-}$ , $\text{ClO}_4^-$	Bases – Pyridine, $\text{C}_6\text{H}_5\text{NH}_2$ , $\text{N}_2$ , $\text{N}_3^-$ , $\text{NO}_2^-$ , $\text{Br}^-$ , $\text{SO}_2$ , $\text{SO}_3$ $^{2-}$ , $\text{NO}^+$	Bases – Benzene, ethylene, $\text{CO}$ , $\text{CN}^-$ , $\text{S}^{2-}$ , $\text{RS}^-$ , $\text{SCN}^-$ , $\text{RSH}$ , $\text{R}_2\text{S}$ , $\text{I}^-$

## 1.4 Design strategies of CPs and MOFs

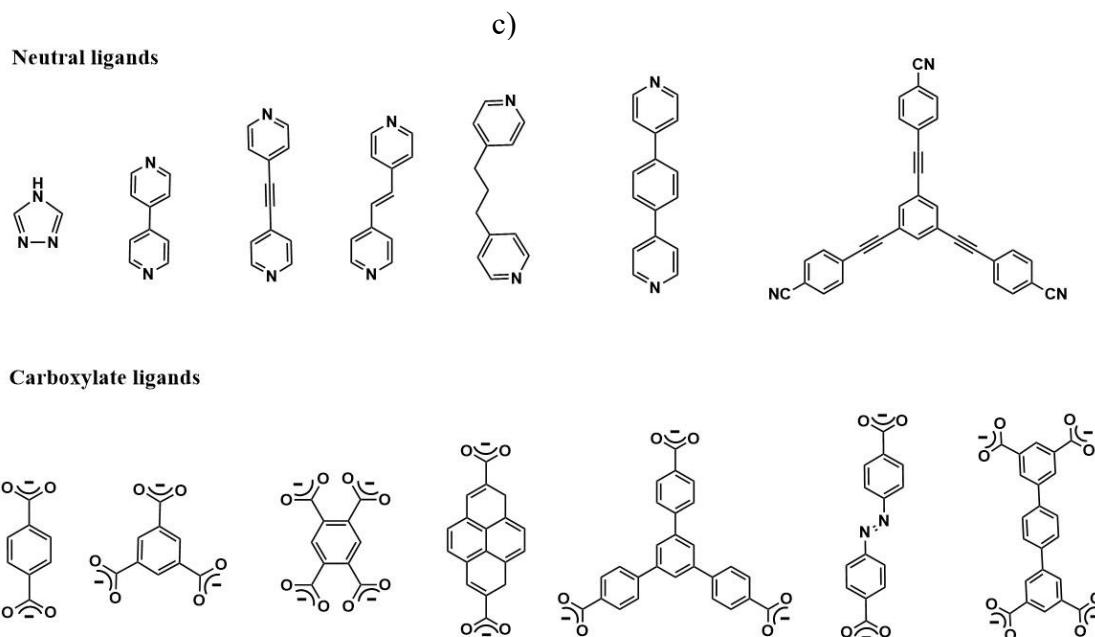
**1.4.1 Building blocks-** The building blocks *viz.* metal centers/connectors and organic ligands/linkers are the building bricks that self-assembles in a predetermined way to construct infinite one-, two-, and three-dimensional coordination frameworks depending upon the coordination geometry of the metal ions and the donocity of the ligand molecules [15].

- a) Metal ions or connectors – Metal ion has a great impact on the self-assembly process as it directs the coordination of ligand molecules in the crystal lattice. Thus, it affects the dimensionality of resulting coordination framework. The metal ion should have compatibility with the donor atoms of linker in terms of HSAB principles and must have vacant or labile coordination sites that can accommodate linker molecules to form a coordination network. In addition, the factors such as size, coordination geometries and crystal field effects of metal ion are also important. Most widely used connectors in the synthesis of CPs and MOFs correspond to transition metal ions owing to their coordination flexibility and versatile coordination geometries. These geometries are related to coordination numbers (CN): for instance, coordination number 2 can be named as linear and coordination number 7 as pentagonal-bipyramidal geometry. Different coordination geometries and corresponding coordination numbers are listed in Scheme III.

Frequently used transition metal ions are  $\text{Cu}^+$ ,  $\text{Ag}^+$ ,  $\text{Cu}^{+2}$ ,  $\text{Cd}^{+2}$ ,  $\text{Zn}^{+2}$ ,  $\text{Hg}^{+2}$  and  $\text{Ni}^{+2}$ . Among these,  $\text{Cu}^+$ ,  $\text{Ag}^+$ ,  $\text{Zn}^{+2}$ , and  $\text{Hg}^{+2}$  ions are labile and thus display coordination flexibility. For example,  $\text{Cu}^+$  display tetrahedral or trigonal geometries whereas tetrahedral, square pyramidal or trigonal-bipyramidal, and octahedral geometries are

observed for  $\text{Zn}^{+2}$  ion, depending on the reaction conditions i.e. solvent, counter anion and ligand used. Labile metal ions are often helpful in obtaining crystallized products due to the rearrangements i.e. reversible bond breaking/formation between metal ion and ligand molecule in the initially formed kinetic product to give a final thermodynamically favored product. In contrast, metal ions such as  $\text{Ni}^{+2}$  and  $\text{Cu}^{+2}$  stick to square planar and octahedral geometries (also square planar and square pyramidal due to Jahn-Teller distortions), respectively. Besides transition metal ions, lanthanide ions ( $\text{Ln}^{+3}$ ) with high coordination numbers from 7 to 10 can be used to construct variety of coordination networks with interesting network topologies. The advantage of using  $\text{Ln}^{+3}$  ions in coordination compounds especially MOFs is that coordinatively unsaturated vacant sites can be generated by the removal of coordinated solvent molecules that can be used for adsorption, sensing, and catalytic applications [16].

- b) Organic ligands or struts – These are rigid bridging units that forms connections between metal centers. Rigidity of organic ligands means prohibition of orientation freedom of the lone pairs on donor atoms. For instance, in 4,4'-bipyridine molecule, rotation about C-C bond does not affect mutual orientation of lone pairs on nitrogen atoms of pyridine rings. Besides, the rigidity could be attributed to absence of linkages containing  $\text{sp}^2$  oxygen or  $\text{sp}^3$  carbon atoms or both about which the molecule can bend. Apart from the rigidity, the bridging nature of ligand molecules, donicity (number of donor sites) and divergent character is required for possible infinite expansion of the framework. Most common ligand molecules used are neutral in nature with N-, O- or S-donors. The final topology of the coordination framework is dependent upon the shape (symmetric or chiral), length (number of carbons between donor atoms) and functionalities (aliphatic and aromatic backbones, presence of hetero atoms etc.) of the ligand. Scheme II summarizes the different types of organic linker that are often used in the fabrication of CPs and MOFs [15-16].



**Scheme II** – Examples of the ligand molecules used to synthesize coordination networks [15-16].

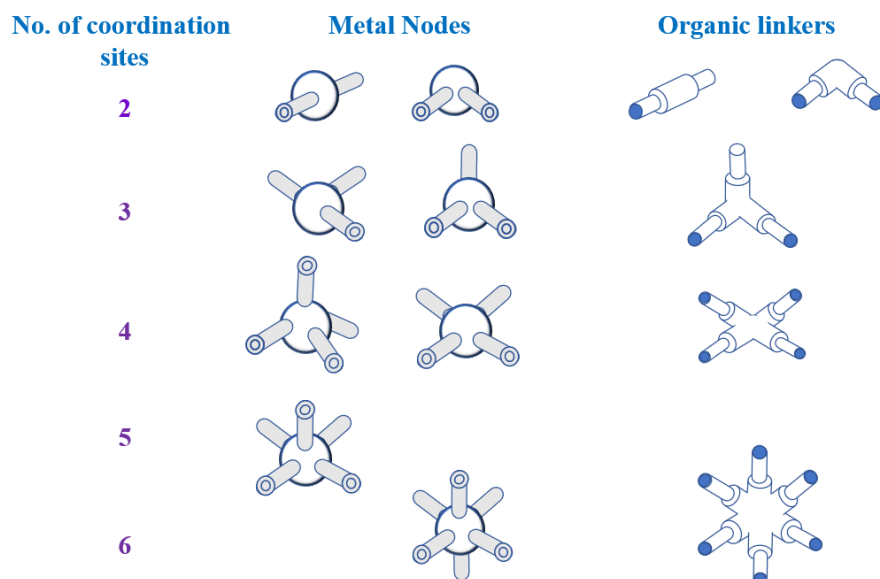
Sometimes counter ions forms bridges between adjacent metal centres to form anion driven coordination chains. Thus, they can help in extending the dimensionality of ligand driven coordination chains formed by bridging organic linkers. Most common anions that form bridges are halide ions *viz.*  $F^-$ ,  $Cl^-$ , and  $I^-$ . Some ions such as  $NO_3^-$ ,  $ClO_4^-$ ,  $CF_3SO^-$  etc. including halide ions can also direct the self-assembly of coordination complexes through hydrogen bonding. The counter ions or anions help in stabilization of the positive charge on metal ion either by coordination (such as halide ions) or by crystallizing as free anion (perchlorate, benzoate etc.). Furthermore, co-crystallized solvent molecules can also affect self-assembly process through hydrogen bonding. In case of MOFs, these molecules grant porosity to these materials by filling up the vacant spaces as space fillers between the polymer constructs and protects the framework from collapsing. The solvent molecules can then be removed once a final stabilized network is formed.

## 1.5 Motifs and dimensionality

Motif is a unique pattern formed by organization of connectors and linkers in the crystal structure. Depending upon on the connectors and linkers used, self-assembly of these building blocks process can lead to coordination network of various dimensionalities: 1D, 2D and 3D frameworks. Simplest representation of principal

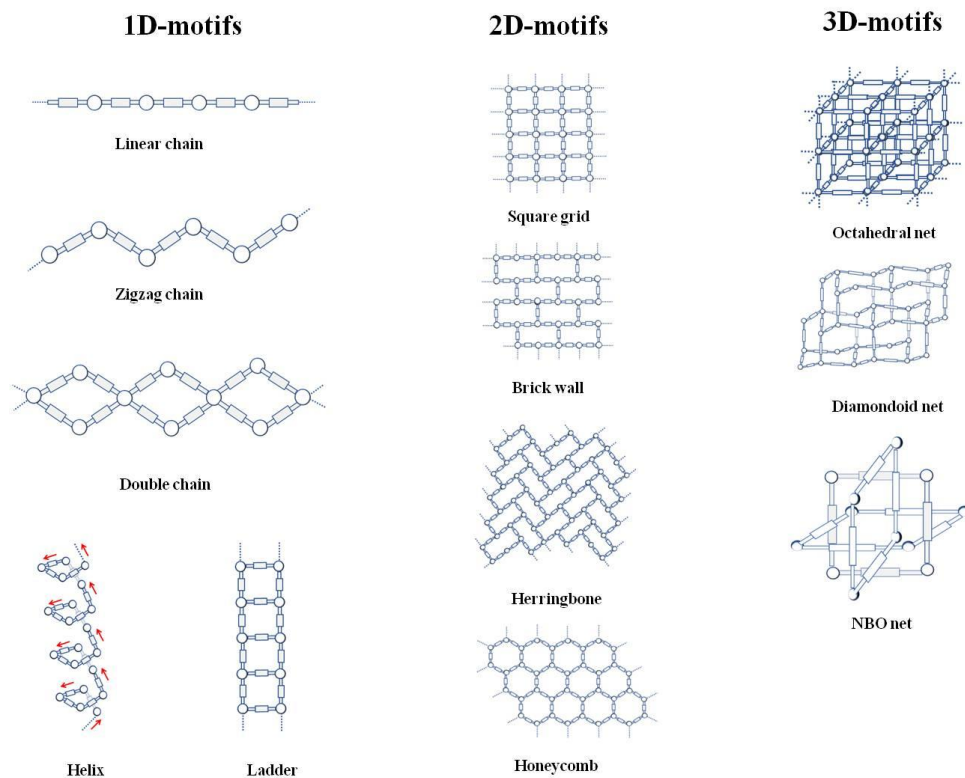


components with which the overall framework is constructed by self-assembly process is shown in scheme III [17]



**Scheme III** – Metal nodes and organic linkers used for the construction of coordination networks [17].

It is worth mentioning here that when the ligand/linker is linear, it is the metal centre (node) that determines the dimensionality of final coordination network: for instance, if the metal node is coordinated to two organic linkers, then an infinite 1D chain with alternate metal and ligand units is generated; a two dimensional sheet can be obtained if a metal node is coordinated to three or four linker molecules; three dimensional architectures can be obtained using the above combination but with higher coordination number (CN) of metal ion (CN: 4-6). Owing to the huge choice of metal ions with coordination diversity and variety of synthesizable organic ligands, a lot of different one-, two- and three-dimensional coordination architectures with complex topologies are possible (Scheme IV). To illustrate the better overview of design strategies of CPs and MOFs and the resulting motifs, we present herein the systems constructed using different types of connectors (with different geometries) and linear linker due to their simplicity [15].



**Scheme IV** – View of different motifs constructed using linear linkers with different types of connectors [15].

## 1.6 Synthetic routes for the synthesis of coordination polymers and MOFs

As mentioned previously, the design strategy involving the understanding of building blocks *viz.* functionality of multi-dentate organic linkers and metal coordination environment works well to predict the dimensionality of self-assembled network and associated topologies. However, the kinetics of crystallization involving the interactions between building blocks sometimes affects the appropriate nucleation and growth of the desired phase which in turn influences the structure of final self-assembled network. It is worth mentioning that besides coordination bonds or bonds with different degrees of covalency between the metal and the organic ligand, there are various non-covalent interactions that governs the assembly of these units in a crystal. The understanding of these interactions aids in predicting the way these molecules are arranged in a crystal lattice, which in turn helps in designing new solid materials with desired physical and chemical properties [18]. The ideology of “crystal engineering” [19] contains information on various intermolecular interactions that direct the self-assembly process in the molecular

solids and, therefore, serves well in guiding the design strategy of a material with desired properties [19].

From the above discussion, it is now clear that the understanding of crystal packing of molecules and associated intermolecular interactions involved can help in investigating the structure-property relationship of solid materials, but it is possible only if these materials are crystallized into a highly ordered crystal system. The crystal is then studied by single crystal X-ray diffraction (SCXRD), which is a primary tool to see the actual structure of coordination complexes. It is important to remember that with the same combination of a metal ion and an organic ligand, different crystallization techniques could result in different products. The common techniques that are used for the synthesis and crystallization of extended coordination networks (1D, 2D and 3D CPs) and/or MOFs are presented in the sub-sections 1.6.1 to 1.6.4 [15].

### **1.6.1 Saturation methods**

In this technique, a solution containing mixture of reactants is heated to saturation in a beaker or conical flask by increasing temperature. The beaker is then (partially) covered and kept for slow evaporation which can result in crystals. The quality and the size of crystals are dependent on the rate of cooling and on the rate of evaporation. This is a conventional method of growing crystals of simple compounds or ionic crystals and most of the time it is a successful technique in the synthesis of CPs.

### **1.6.2 Diffusion methods**

Sometimes reaction between metal salt and ligand in a given solvent is so fast that insoluble non- or polycrystalline products not suitable for diffraction studies are obtained. Two diffusion methods are available that involve slow contact of reacting species, which results in single crystals suitable for SCXRD. These methods are:

- a) Solvent or Liquid diffusion. This method is generally used in cases where an instant reaction between metal and organic ligand results in precipitation. In this method, each reactant is dissolved separately in two different solvents that are miscible to some extent. The solvent with the lighter density is then layered on the high-density solvent. The slow mixing of these solvents can then result in crystal formation at the interface because more time will be available for the mixing of reactants and for the crystallization process to get better quality crystals.

- b) Vapour diffusion. This method is used when the precipitate of metal complex is soluble in high density solvent such as DMF, DMSO etc. In this method, the powder product is dissolved in one of these solvents in a vial. This vial is then kept in a closed vessel in which vapours of low-density precipitant solvent are made to diffuse, resulting in crystal formation.

### 1.6.3 Hydrothermal/Solvothermal synthesis

In this method, the reaction between the metal salt and ligand takes place in closed vessels, for example, a capped dram vial or a bomb vessel under high pressure above the boiling point of the solvent in a temperature range of 120-150 °C. This method is mostly used for the synthesis of MOFs. The concept of high-temperature synthesis of these materials i.e. solvothermal and hydrothermal conditions, use of modulators or mineralizers, and microwave-assisted synthesis comes from their analogy with porous zeolites [20].

It should be noted that when water is used as synthesis medium then the reaction is called hydrothermal synthesis, while use of solvent other than water is solvothermal synthesis. In general, polar aprotic solvents viz. DMF, DMA, DEF etc. (N,N-dimethylformamide (DMF), N,N-dimethylacetamide (DMA), N,N-diethylformamide (DEF)) are often used in solvothermal synthesis because: 1) at room temperature they keep the reactants far apart owing to their high dielectric constant values thus limiting the chance of precipitation, 2) at high temperatures (above 120 °C) they generate an amine base that deprotonates the ligand molecules (especially carboxylic acid) to facilitate the formation of metal-organic complex, and 3) they keep the solution clear by dissolving all reaction components at higher temperatures to promote crystallization.

### 1.6.4 Other methods

These methods are: microwave, mechano-chemical, and ultra-sonication methods, which are used to improve the solubilities of reactants (by pulverization of particles to mm/nm levels) and to facilitate suitable reaction rates of kinetically inert systems. By optimizing the reaction conditions, a single crystal can be obtained in microwave synthesis.

Although these techniques illustrate better energy efficiency and a considerable reduction in reaction time, the main drawback is that the nano-sized crystals

obtained by these techniques do not diffract on the SCXRD machine. Conversely, they can be used in bulk synthesis of the compounds.

## 1.7 Structure property relationship

The ideology that structure and composition of a material reflects its properties is an important conception in chemistry and material sciences. For instance, properties like magnetism, catalysis, luminescence, adsorption etc. can be depicted by looking at framework structure and their associated components *viz.* type of the metal ion and organic ligand used. For example, a given material can show magnetic properties (paramagnetic, ferromagnetic, antiferromagnetic etc.) if it has transition metal ions with partially filled *d*-orbitals or trivalent lanthanide ions with partially filled *f*-orbitals. Likewise, luminescence properties from the material can be expected if it has highly conjugated system of aromatic rings and/or aliphatic chains, or luminescent trivalent lanthanide ions in its structure. These luminescent materials can be used as sensitizers, catalysts in the photodegradation of dyes, sensing probes in fluorescence sensing applications etc. [21-22].

Highly porous materials like MOFs are primarily used in gas adsorption, VOC (volatile organic compounds) and toxic metal ions adsorption applications [23-24], but depending upon the metal ion and organic ligand present in the framework they can be explored for diverse applications [25-27].

## 1.8 Pore tuning/modification in MOFs

The potential application of MOFs in the gas adsorption-separation applications is directly related to the pore size and porous surface area. These materials are so fascinating that even few grams of them have the surface area that could exceed the surface of a football ground [28].

Based on the pore size they can be classified into [29-31]:

- a. Micro-porous – pore diameter is  $< 20 \text{ \AA}$ .
- b. Meso-porous – pore diameter lies between  $20\text{-}500 \text{ \AA}$ .
- c. Macro-pores – pore diameter is greater than  $> 500 \text{ \AA}$ .

Besides MOFs, there are other classes of micro-porous inorganic materials known as zeolites or aluminosilicates containing  $\text{Na}^+$  or  $\text{K}^+$  ions in the cavities, which are also being used industrially as cation exchangers, selective catalysts and moisture absorbents or deodorizers [32a].

Although zeolites are cost effective, stable and have good adsorption capacity, lack of structural diversity (low pore size and pore geometry) and hence pore tuning to accommodate molecules with steric preference restricts their application. Conversely, the structure of MOFs and hence the pore size could be modulated hierarchically using different organic struts varying in length while maintaining the structure prototype (i.e the ligand connectivity and the over contour of the pore) thanks to the development of efficient methods of organic synthesis that permit the synthesis of analogous organic building blocks differing in overall length. The modulation of the pore size and hence the overall surface area of the compound could be studied using BET technique. BET stands for Brauner-Emmett-Teller, a model that assumes multi-layer adsorption of the inert gas specifically nitrogen gas on the surface of porous sample to determine the specific surface area including pore size measurement. In this method, the physisorption of the gas is depicted as a plot of the amount of gas adsorbed on the surface of the sample as a function of the relative pressure of the gas. The surface area of the sample obtained is expressed in  $\text{m}^2/\text{g}$  [32b].

In the MOF chemistry, a series of structures with the same topology but different pore sizes constructed using different derivatives of organic struts differing in length are called isorecticular MOFs. The initial work on the synthesis of isorecticular MOFs was pioneered by Yaghi *et al.* [30], in which a series of MOFs called IRMOFs were obtained by the coordination of BDC, BPDC, PDC, and TPDC linkers (defined in abbreviation section) differing in length to zinc oxo-cluster *viz.*  $\text{Zn}_4\text{O}(\text{CH}_3\text{COO})_6$  to give IRMOF-1, IRMOF-10, IRMOF-14, and IRMOF-16, respectively. It was observed that the pore diameter was transformed gradually from 3.8 Å to 28.8 Å without any change in shape of the pore, which in this case was cubic (Figure 1).

In another work, MOF-399 isorecticular to HKUST-1 [33] was prepared by Yaghi *et al.* [34]. Both were constructed using the unique building unit comprising paddlewheel  $\text{Cu}_2(\text{CO}_2)_4$ , and triangular *viz.* BTC anions in HKUST-1 and BBC anions in MOF-399, respectively, to yield a non-interpenetrated 3D framework with **tbo** topology. It was observed that inner diameter of the pore was increased from 11.1 Å in HKUST-1 to 43.2 Å in MOF-399 and the void volume was changed from 72% to 94% (Figure 1).

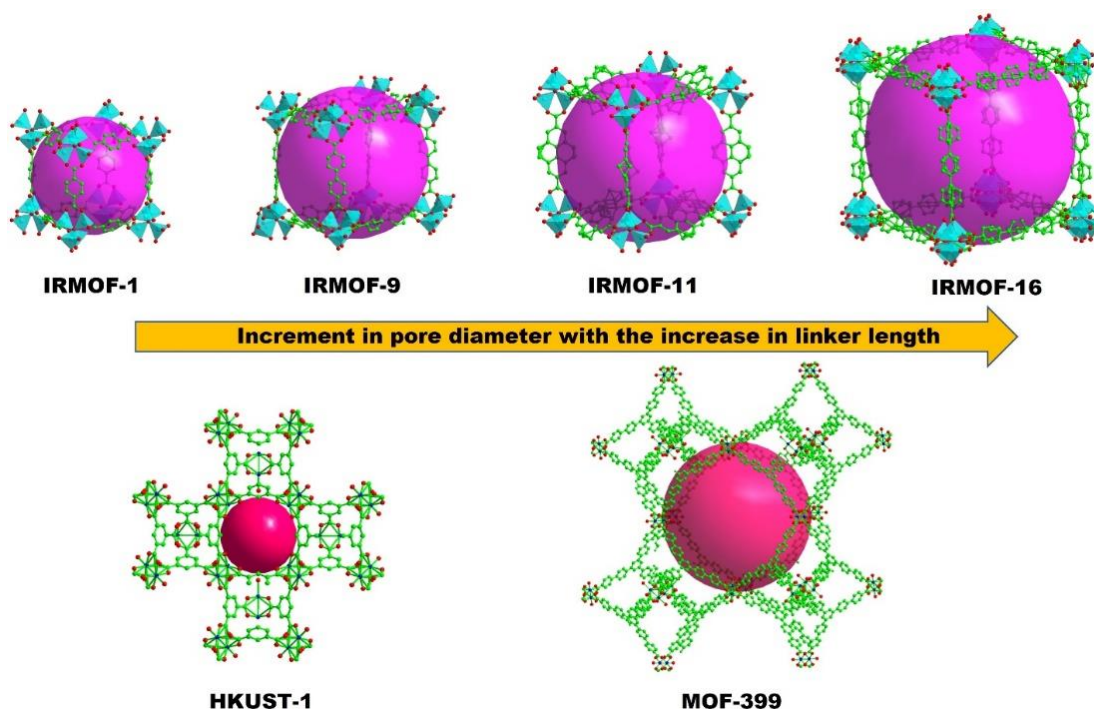


**Figure 1** – Change of pore diameter with the variation in the length of organic linkers [30, 33-34].

## 1.9 Activation of MOFs and classification

MOFs have been studied extensively for their gas adsorption and separation potential, but these materials could be used for such applications only if the entrapped solvent molecules (used during synthesis) are completely removed from the cavities without affecting the ruggedness of the framework to result in permanent porosity [35]. The process of isolating porous crystalline solids with accessible pores upon the removal of adsorbed solvents and other guest molecules is called activation of MOFs. However, most of the times the activation of MOFs result in the materials with low crystalline and collapsed pores following the solvent exchange and vacuum drying at certain temperatures. The rationale for this fact is that the coordination bond strength cannot withstand with the surface tension and capillary forces brought about by adsorbed molecules while transiting from liquid-to-gas phase [36]. There is an alternative way available to activate fragile MOFs using supercritical carbon dioxide (SCO) which involves its transition to gas phase under reduced pressure with minimal capillary forces exerted on the MOF framework [37]. Besides, sequential washing with low boiling solvents followed by activation under nitrogen flow could also results in the activation of MOFs.

On the contrary, not all MOFs are stable upon the removal of solvent molecules i.e. their framework collapses and thus cannot be used in adsorption applications. Based on the stability of the framework after the solvent evacuation, MOFs have been classified as follows [38-39]:

- a. 1<sup>st</sup> generation MOFs – These are micro-porous materials that show permanent decomposition of their framework following the removal of solvent molecule, yielding an amorphous solid. Besides, in some MOFs porosity is regained during the adsorption of guest molecules.
- b. 2<sup>nd</sup> generation MOFs – These materials have rigid framework; retain permanent porosity on the adsorption/desorption of the molecules of interest.
- c. 3<sup>rd</sup> generation MOFs – This class represents the present-day MOFs, which shows reversible deformation of their frameworks relative to external stimuli. This means that they can flexibly tune their pore size while keeping the crystalline nature. This dynamic character is not seen in zeolites, making MOFs versatile materials to be used in various applications such as catalysis, adsorption-separation, toxic metal ion sensing etc.

## **1.10 Analytical techniques for the characterization of organic and coordination compounds**

### **1.10.1 Single crystal X-ray diffraction (SCXRD)**

SCXRD is a non-destructive analytical tool, which gives a photograph of internal crystal lattice (reciprocal lattice) of a single crystal. Important information related to the crystal such as bond lengths, bond angles, unit cell dimensions, type of unit cell etc. can be obtained with precision [40]. Crystal lattice contains well-ordered sites called lattice points that are occupied by atoms and can diffract X-ray, thus specific crystal structure information can be obtained. X-ray diffraction is the result of constructive interference of monochromatic X-rays diffracted from the crystalline sample. The constructive interference takes place when the interaction of incident rays with the crystal sample satisfies Bragg's law, which is presented by equation 1 as-

$$(n\lambda = 2d\sin\theta) \quad \text{(equation 1)}$$

The Bragg's law is a mathematical expression that relates wavelength of incident radiation with diffraction angle ' $\sin\theta$ ' and interplanar spaces ' $d$ ' in the sample. The diffracted rays or reflections from the lattice points produce a



characteristic diffraction pattern, which is then detected and processed to get information about the spatial arrangement of atoms. Each reflection is designated by miller indices ' $hkl$ ' that indicate its position in the diffraction pattern. The X-ray single crystal diffraction (SCXRD) instrument is fabricated based on this theory and comprises the emitter, goniometer, and detector. The emitter is a cathode ray tube from which electrons are accelerated toward target materials most common of which are molybdenum and copper to generate  $\text{MoK}_\alpha = 0.71073 \text{ \AA}$  and  $\text{CuK}_\alpha = 1.5154 \text{ \AA}$  radiations, respectively. The sample used for SCXRD is a single crystal of regular shape without cracks and imperfections. A typical size of the crystal between 0.3 mm to 0.7 mm is reasonable. Details pertaining to the diffractometer used for the single crystal data acquisition of the compounds discussed in the thesis are given in the experimental section of Chapter 2, 3 and 5.

### 1.10.2 Powder X-ray diffraction

As the molecular structure obtained from single crystal diffraction studies corresponds only to the crystal used for analysis, the information about the homogeneity of the bulk sample relative to same structure is obtained by powder X-ray diffraction (PXRD). Powder X-ray diffraction is also a non-destructive analytical technique that follows the principles of Bragg's law and is used for the identification of phase purity in bulk sample [41]. Besides, information about lattice parameter, grain size, and interplanar spacing (Miller indices) can also be obtained. The most common X-ray source used is usually copper. PXRD differs from SCXRD in sample preparation and instrumentation. In contrast to SCXRD where a single crystal is used, a finely grounded homogenous powder sample is used in PXRD with a particle size less than  $\sim 10 \text{ }\mu\text{m}$  in diameter. Another difference is that the data from SCXRD is a bit easy to interpret because discrete diffraction peaks are observed in SCXRD whose positions can be transformed into meaningful series of coordinates to recuperate the related lattice dimensions, whereas powder sample tends to give continuous diffraction rings due to the diffraction from randomly oriented crystallites or crystal planes, which results in uncertainty in the data interpretation and thus needs different fitting to the reference data (Joint committee on powder diffraction standards database (JCPDS)) to obtain the final structure. Details pertaining to the

diffractometer used for the powder data acquisition of the compounds discussed in the thesis are given in the experimental section of Chapter 2, 3 and 5.

### 1.10.3 Infrared spectroscopy

Infrared spectroscopy is a technique utilized for qualitative analysis of different functional group in a given material. The prerequisite for a molecule to absorb IR radiations is that the bonds involved should have polarity or dipole moment. The basic principle of infrared spectroscopy involves shining the sample with IR radiations over a range of wavelengths and measuring the absorptions that correspond to the vibration of different bonds in the molecules. The IR spectrum spans 4000-600  $\text{cm}^{-1}$  region of the electromagnetic spectrum and is reported as plot of % transmittance vs. wave number. The IR region is further divided into a functional group region (4000-1430  $\text{cm}^{-1}$ ) and a fingerprint region (1400-700  $\text{cm}^{-1}$ ), and the corresponding vibrations in these regions are specific to a given compound [42]. Details pertaining to the IR spectrometer used in my research is given in the experimental section of Chapter 2, 3 and 5.

### 1.10.4 CHN elemental analysis

CHN analysis is an analytical technique that provides a precise and accurate measurement of the total carbon, hydrogen, and nitrogen percentage in a given sample [43]. These percentage compositions can then be compared to theoretical figures obtained from tentative structure in order to confirm whether the desired product is obtained or not. In addition, the information about additional solvent molecules, impurities etc. can also be obtained after careful comparison of the results. This information is sometimes used to calculate percentage yield of the product too. The elemental analysis involves combustion of the sample to a gaseous form in the furnace at a temperature as high as 1050 °C. The sample is combusted with the aid of oxygen gas and undergoes further catalytic redox processes to convert C, H, and N to  $\text{CO}_2$ ,  $\text{H}_2\text{O}$ , and  $\text{N}_2$  gases. These gases are sent to a chromatography column with an inert helium gas for separation followed by their detection. The carrier gas is helium (99.99% purity) and the combustion gas is oxygen (99.99% purity). The accepted accuracy of the results is  $\leq 0.4 - 0.5\%$ . Details pertaining to the CHN elemental analyzer used in my research is given in the experimental section of Chapter 2, 3 and 5.

### 1.10.5 Nuclear Magnetic Resonance

Nuclear magnetic resonance (NMR) spectroscopy is a powerful technique used to determine the structure of organic compounds and is based on the magnetic resonance of atomic nuclei with nuclear spin quantum number  $I \neq 0$  by the interaction with externally applied radiofrequency in the presence of variable magnetic field [44]. This interaction leads to exchange of energy resulting in flip of nuclear spin to excited state. The NMR spectra provide valuable information about magnetically equivalent nuclei, chemical environment around a NMR active nuclei (electronegative or electropositive atoms), functional groups in the molecule of a sample, coupling between nuclei, etc. with the aid of chemical shift values obtained relative to a reference material such as TMS (tetramethyl silane). The most common NMR analysis recorded are  $^1\text{H}$  and  $^{13}\text{C}$  spectra because principal elements of an organic compound are carbon and hydrogen whose nuclear spin values are  $I = \frac{1}{2}$ . The integration of peak areas in  $^1\text{H}$ -NMR gives information about the number of protons producing a respective signal.  $^{13}\text{C}$ -NMR spectra gives information about different types of carbon atoms in different chemical environment. Details pertaining to the NMR spectrometer used in my research is given in the experimental section of Chapter 2 and 3.

### 1.10.6 Thermo-gravimetric Analysis

Thermo-gravimetric analysis (TGA) is a technique that gives information about physical and chemical phenomenon involved as a function of mass loss on exposing the sample to an increased temperature [45]. These phenomena can be vaporization, sublimation, desolvation and decomposition. The common use of TGA involves characterization of material through its decomposition pattern, study of degradation mechanism, determination of organic and inorganic content of the sample. These processes are accompanied by sharp decline in the thermogravimetric curve of the sample, which corresponds to loss of solvent molecules, organic molecules etc. In case of MOFs, TGA can give valuable information about its thermal stability that can be used during their activation. Details pertaining to the TGA apparatus used in my research is given in the experimental section of each of Chapter 2 and 3.

### 1.10.7 Scanning electron Microscopy/Energy dispersive X-ray spectroscopy

Scanning electron Microscopy (SEM) is a technique used to produce the high-resolution images of the surface of a sample to see the surface morphology of the particles [46]. In the SEM analysis, very thin high-energy electron beam is used to scan the surface of a particular region of the sample that is mounted on a stub using a conductive adhesive material, which results in the generation of secondary electrons, Auger electrons, characteristic X-rays, and other microscopic particles. The secondary electrons usually come from 5-10 nm deep of the surface, have low energy, typically 1-10 eV, and can efficiently show the sample morphology. The SEM instrument is comprised of an electron gun, magnetic lens system, a vacuum system and a detector for signal collection. Most of the SEM equipment are equipped with Energy dispersive X-ray Spectroscopy (EDS) analysis that enables surface mapping and semi-quantitative analysis of the elemental composition of an area scanned of the material. The EDS analysis differs from SEM with the fact that X-rays emitted by sample are detected by an additional X-ray detector in contrast to secondary electrons in SEM. Details pertaining to the SEM used in my research is given in the experimental section of each Chapter 3.

### 1.11 Applications of CPs and MOFs

Prime interest in the synthesis of coordination polymers is the fabrication of new functional materials possessing properties of both metal ion and ligand molecule. Besides, the strength of coordination bond ranges from 50 kJ/mole in pyridyl complexes [47] to 180 kJ/mole in carboxylate complexes [48] of transition metal ions that makes these compounds appealing. Metal-organic lattices grant numerous advantages over sole organic counterparts, such as the periodic arrangement of alternate metal ions and ligand units, ordered organization of organic linkers in the framework, better mechanical strength, and the presence of catalytically active sites of metal ions. An attractive feature of coordination polymers is the availability of 90° (in case of 2, 5, and 6 metal coordination geometries) joints for constructing a polymeric network (in case of two- and three dimensional) with macrocyclic boxes [49-51] where interesting inter-play of non-covalent interactions between host-guest molecules can be observed. The metal centers can be thought of as template species that helps to organize and rigidify the organic ligand in a specific

orientation that otherwise is not possible in a free ligand molecule. Furthermore, coordination frameworks have numerous practical applications owing to the delocalization of the electron densities over the framework, which otherwise are concentrated on the unligated ligand molecules.

The popularity of these materials could be identified from different industrial applications of some MOFs. For instance, MOF-5 adsorbent has been commercialized successfully by TruPick in 2016 to limit the fruit ripening by storing and immediately releasing 1-methylcyclopropene (1-MCP) into the air, a competitive suppressor of naturally occurring ripening agent ethylene in fruits [52]. Besides, MOF-5 is also used in a cylinder system called ION-X by NuMat to store toxic dopant gases *viz.* arsine, phosphine, and boron trifluoride, which are used to mount dopants in the manufacture of electronics [53]. Likewise, HKUST-1 or Basolite C-300 by 'Sigma Aldrich' is used in stream crackers to separate 'C5 olefins from paraffin [54].

Although there is a colossal literature available on CPs and MOFs, and their practical applications, we will present a few examples of CPs and MOFs synthesized from ligands analogous to those we have used in our research. The coordination compounds discussed below are based on:

1. Mixed-ligand coordination complexes of transition metal ions comprising neutral ligands containing pyridine ring with secondary amide linkage (Figure 2), and carboxylic acid ligands.
  2. Lanthanide MOFs synthesized using terphenyl tetracarboxylic acid ligand.
- The ligands used in the synthesis of coordination complexes reviewed here are listed in Figure 2.

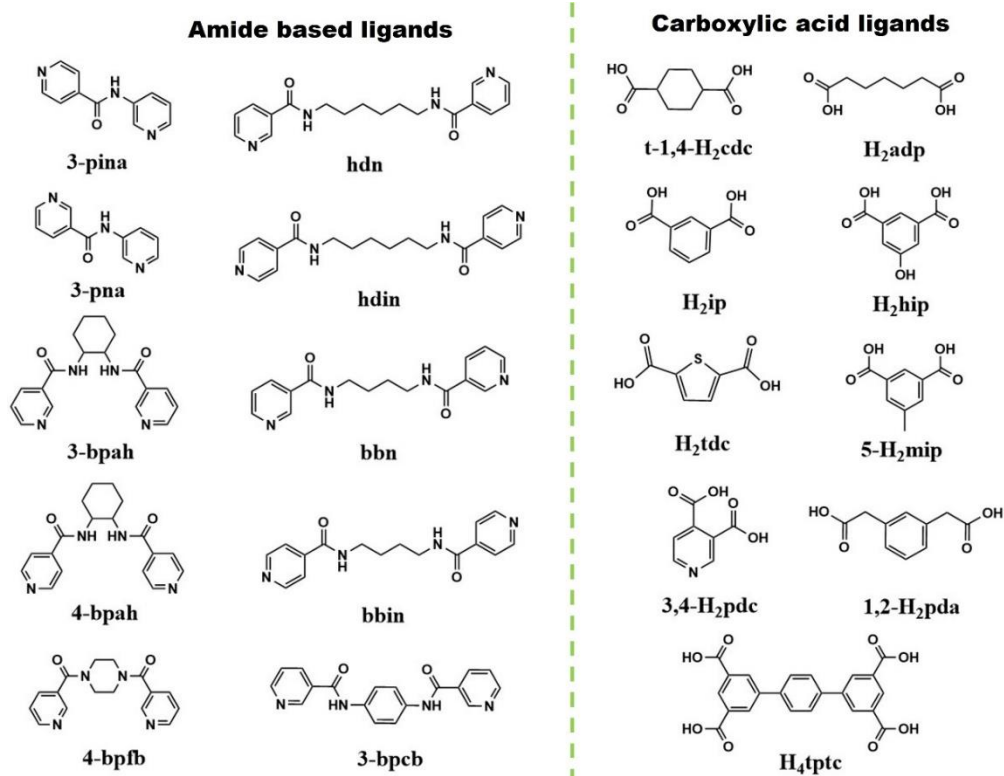


**Figure 2** – List of analogous ligands used in the synthesis of coordination compounds reported in the literature. Note: The protonated form of carboxylic acid ligands is shown above.

For simplification, these complexes are classified based on their applications, followed by a brief account on the molecular structure and the noteworthy results of their applications.

### 1.11.1 Magnetism

A 3D coordination polymer  $\{[\text{Cu}_2(\text{t-1,4cdc})_2(3\text{-pina})_2(\text{H}_2\text{O})]\cdot 5\text{H}_2\text{O}\}_n$  (**1**) has two different Cu(II)/1,4cdc chain motifs comprising two isolated square pyramidal Cu(II) ions (Cu1 and Cu2) in  $\{\text{Cu}_2\text{O}_2\}$  dimeric units (Figure 3a ). These dimeric units were linked together in a three-dimensional self-penetrated 4,6-connected binodal net by 3-pina molecules (Figure 3b). Conversely, a simple three-dimensional binodal 3,5-connected network was obtained in the complex  $[\text{Cu}(\text{t-1,4cdc})(3\text{-pna})]_n$  (**2**) containing isomeric 3-pna molecule [55].

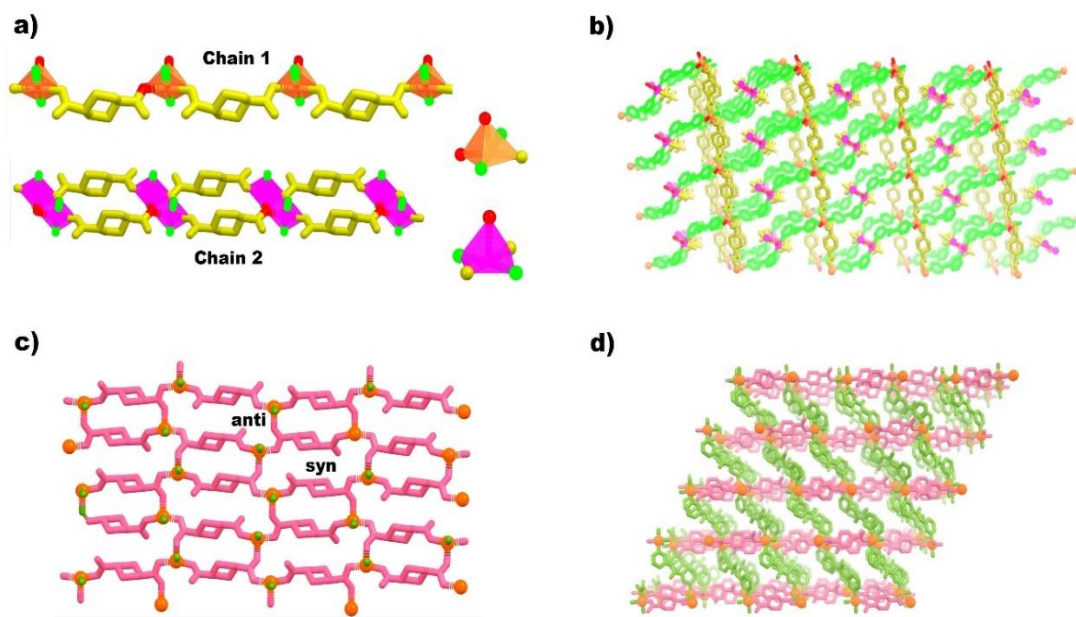


**Figure 3** – View of a) chain motifs of  $\{\text{Cu}_2\text{O}_2\}$  dimeric units of complex **1**, b) three-dimensional framework of complex **1**, c) 2D layer of complex **2** comprising *anti-syn* axial–equatorial bridged  $[\text{Cu}(\text{OCO})]_n$  motifs, and d) 2D layers pillared by 3-pna molecules to form a three-dimensional network in complex **2** [55]. (Note: t-1,4cdc ions are shown in yellow and magenta colour while 3-pina and 3-pna are shown in green colour).

The complex  $[\text{Cu}(\text{t-1,4cdc})(3\text{-pna})]_n$  contains  $\text{Cu}(\text{t-1,4cdc})_n$  layers comprising *anti-syn* axial–equatorial bridged  $[\text{Cu}(\text{OCO})]_n$  chain motifs (Figure 3c) that were pillared by anti-conformation 3-pna ligands to yield a 3D network (Figure 3d). The variable temperature magnetic studies reveal that the complex  $\{[\text{Cu}_2(\text{t-1,4cdc})_2(3\text{-pina})_2(\text{H}_2\text{O})] \cdot 5\text{H}_2\text{O}\}_n$  has weak anti-ferromagnetic coupling between Cu(II) ions within  $\{\text{Cu}_2\text{O}_2\}$  dimeric units with the values of characteristic parameters as  $g = 1.906(3)$ , and  $J = -3.4(3) \text{ cm}^{-1}$ . Whereas the complex  $[\text{Cu}(\text{t-1,4cdc})(3\text{-pna})]_n$  has shown weak ferromagnetic coupling among Cu(II) ions of dimeric units with the values of  $g = 2.01(1)$ ,  $J = 0.04(1) \text{ cm}^{-1}$  [55].

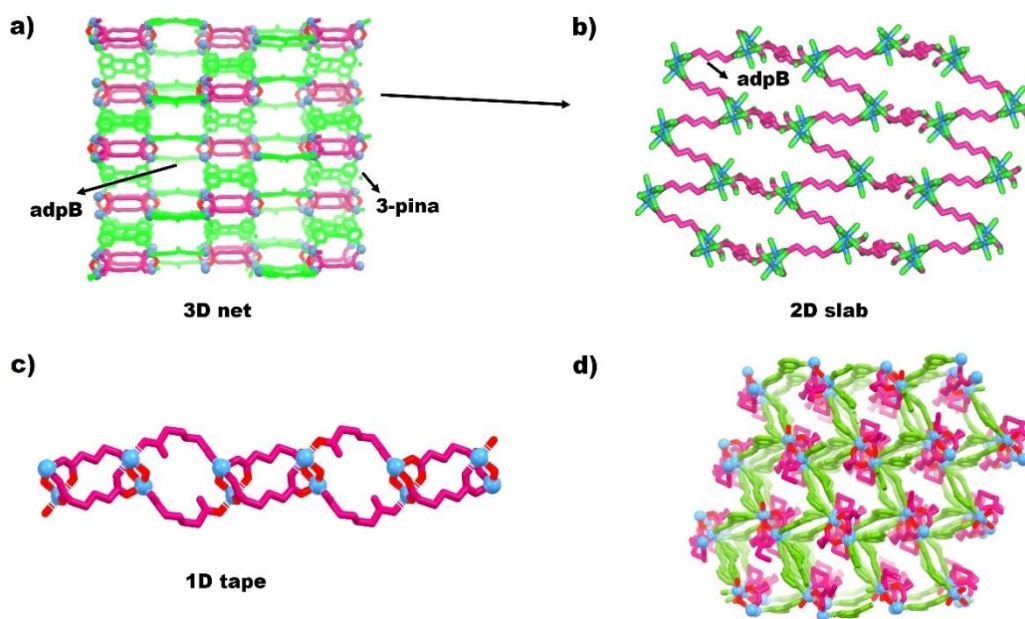


**Figure 4** – View of a) hybrid three-dimensional network formed by non-interpenetrated three-dimensional net and a two dimensional 7-connected slab of complex **3**, b) two-dimensional slab of complex **3**, c) one-dimensional tape of complex **4** containing adpA and adpB ions, and d) three-dimensional network of complex **4** [56]. (Note: adpB molecules are shown in magenta colour while 3-pina and 3-pna are shown in green colour).

In the similar study, Duca *et al.* synthesized two new Ni(II) coordination polymers using 3-pina and 3-pna molecules, and studied their magnetic behavior [56]. The complex  $\{[\text{Ni}_2(\text{adp})_2(3\text{-pina})_2(\text{H}_2\text{O})] \cdot 2\text{H}_2\text{O}\}_n$  (**3**) was a 3D coordination polymer (Figure 4a), hybrid of a non-interpenetrated three-dimensional net and a two dimensional 7-connected slab with pillared (3,6) triangular topology (Figure 4b). The molecular structure of complex **3** contains  $\{\text{Ni}_2(\mu_2\text{-H}_2\text{O})(\text{OCO})_2\}$  dimeric units in which octahedral Ni(II) ions were linked to each other by a bridged water, and exotetradentate adpA ions. These dimeric units were interconnected by major disordered component of adpB molecules in a bis(monodentate) fashion together with 3-pina molecules to form a 2-connected chain patterns resulting in a 3D cubic type **pcu** (primitive cubic) network (Figure 4a). Whereas the minor disordered component of adpB forms a 3-connected pattern, which results in 2D slab (Figure 4b). The molecular structure of the complex  $\{[\text{Ni}_2(\text{adp})_2(3\text{-pna})_2(\text{H}_2\text{O})] \cdot \text{H}_2\text{O}\}_n$  (**4**) contains  $\{\text{Ni}_2(\mu_2\text{-H}_2\text{O})(\text{OCO})_2\}$  dimeric units, bridged by a water molecules and exotetradenate adpA and adpB ions to form a 1D tape (Figure 4c). These tapes were



connected by 3-pna molecules to form a three-dimensional network (Figure 4d). These two complexes were further studied for variable temperature magnetism studies. Weak ferromagnetic coupling was observed among Ni(II) ions in the complex **3** with the values  $g = 2.034(7)$ ,  $J = 0.51(2) \text{ cm}^{-1}$ . On the contrary, anti-ferromagnetic coupling with the values  $g = 2.077(1)$ ,  $J = -0.36(1) \text{ cm}^{-1}$  was observed in complex **4** due to the change of the ligand molecule [56].

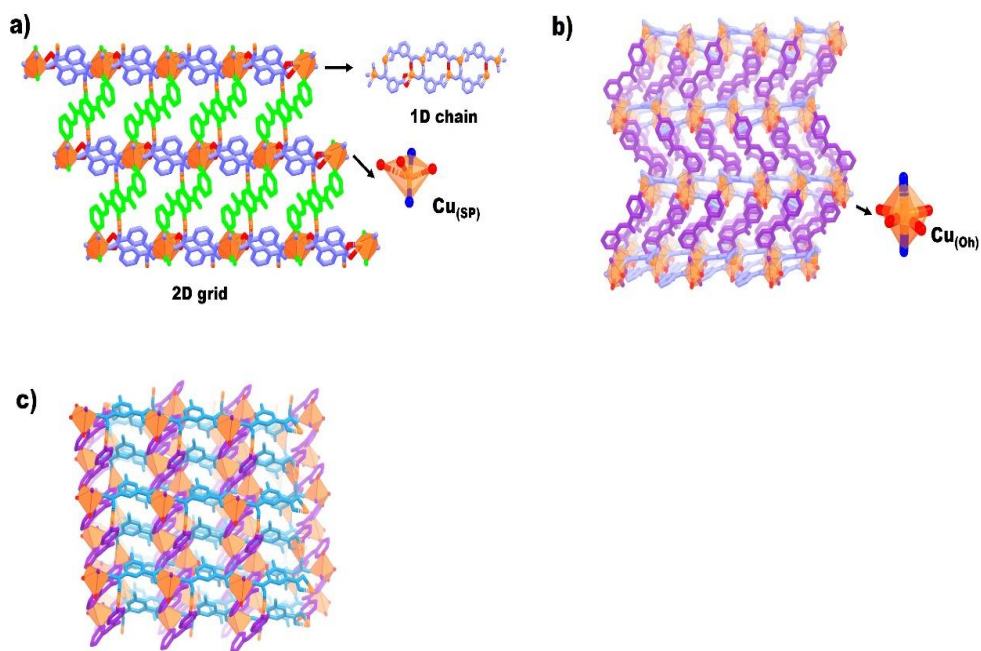


**Figure 5** – View of a) 1D chain (inset) and two-dimensional grid of complex **5**, b) three-dimensional framework of complex **6** with octahedral Cu(II) ions, and c) three-dimensional framework of complex **7** with **pcu** topology [57]. (Note: ip and hip ions are shown in light blue colour while 3-pina and 3-pna are shown in violet and green colours, respectively).

The effect of pyridyl nitrogen donor disposition in dipyridylamide ligand and the steric bulk of the substituent of the isophthalate aromatic ring on the final topologies of Cu(II) based coordination polymers have been studied [57]. In this pursuit, three Cu(II) based coordination polymers were synthesized *viz.*  $[\text{Cu}(\text{ip})(3\text{-pna})]_n$  (**5**),  $\{[\text{Cu}(\text{ip})(3\text{-pina})] \cdot \text{H}_2\text{O}\}_n$  (**6**), and  $[\text{Cu}(\text{hip})(3\text{-pina})]_n$  (**7**) differing in the position of pyridyl nitrogen in the dipyridylamide molecule, and the type of isophthalate anions used. The bridging of exotridentate isophthalate anions among adjacent Cu(II) centers in the complex  $[\text{Cu}(\text{ip})(3\text{-pna})]_n$  (**5**) has led to the formation of a one-

dimensional chain of square-pyramidal  $[\text{Cu}_2(\text{OCO})_2]$  dimeric units bridged by ip anions (inset, Figure 5a). These chains were linked into a two-dimensional (4,4) grid structure by bridged 3-pna molecules (4-connecting, Figure 5a). In contrast, a three-dimensional network with **cds** (cadmium sulphate) topology was obtained in the complex  $\{[\text{Cu}(\text{ip})(3\text{-pina})]\cdot\text{H}_2\text{O}\}_n$  (**6**) due to change in the position of nitrogen atom in one of the pyridyl ring (Figure 5b). Furthermore a 3D network with **pcu** topology was obtained in the complex  $[\text{Cu}(\text{hip})(3\text{-pina})]_n$  (**7**) using 3-pina ions (Figure 5c). The complex **5** was chosen as a representative of these complexes for variable temperature magnetism studies because all these complexes have same  $[\text{Cu}_2(\text{OCO})_2]$  dimeric units. The results display a weak anti-ferromagnetic coupling among Cu(II) ions in the dimeric units with the values of relevant characteristic parameters as  $J = -0.96(1) \text{ cm}^{-1}$  and  $g = 2.041(1)$  [57]

### 1.11.2 Sensing/Detection

A one-dimensional chain comprising  $[\text{Cd}(\text{tdc})(\text{H}_2\text{O})]_n$  chain motifs (Figure 6a) was constructed by bridged chelating/monodentate tdc ions in the complex  $\{[\text{Cd}(\text{tdc})(\text{hdin})(\text{H}_2\text{O})]\cdot\text{H}_2\text{O}\}_n$  (**8**) [58].

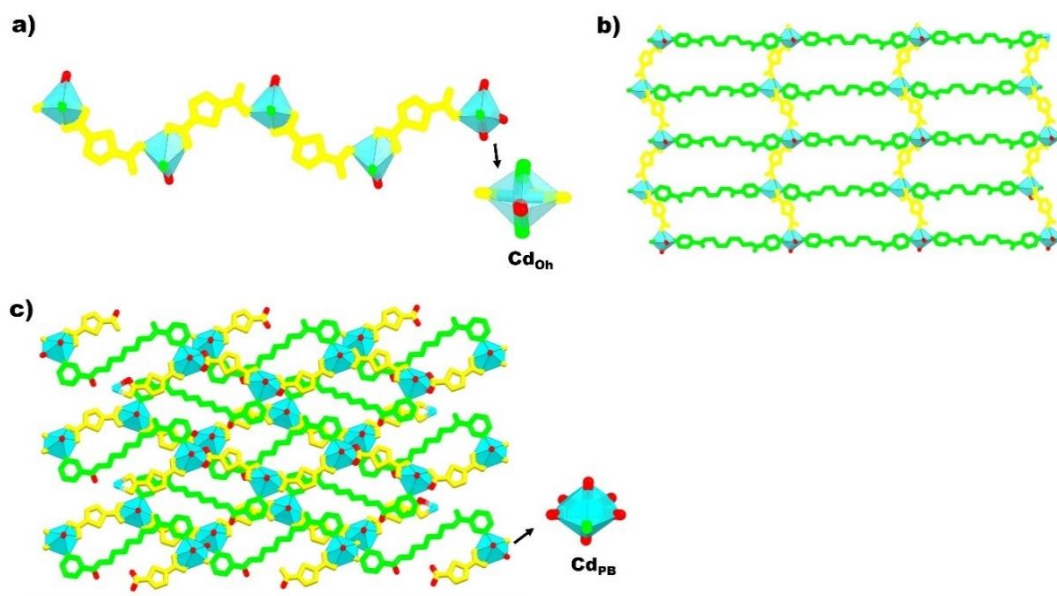


**Figure 6** – Pictorial depiction of a) 1D chain of octahedral Cd(II) ions of complex **8**, b) two-dimensional grid of complex **8**, and c) two-dimensional herringbone sheet of complex **9** with (6,3) grid motifs [58]. (Note: tdc ions are shown in yellow colour while hdin and hdn are shown in green colours.

These one-dimensional chains were pillared into a two-dimensional (4,4) grid sheet containing  $[\text{Cd}(\text{tdc})(\text{hdin})(\text{H}_2\text{O})]_n$  motifs by *hdin* ions oriented in a *gauche-anti-gauche* conformation relative to their six member aliphatic tethers (Figure 6b). On the contrary, a two-dimensional herringbone sheet with (6,3) grid motifs was obtained in the complex  $\{[\text{Cd}_2(\text{tdc})_2(\text{hdn})(\text{H}_2\text{O})_4] \cdot \text{H}_2\text{O}\}_n$  (**9**) with pentagonal bipyramidal Cd(II) ions using isomeric *hdn* ions (Figure 6c). Here, the hexamethylene tethers of *hdn* ions display *anti-anti-anti* conformation. These compounds were tested for the detection of nitrobenzene in ethanol/DMSO. The decrease in the emission intensity of these compounds on the addition of  $\mu\text{L}$  aliquots of nitrobenzene was ascribed to electron transfer from pyridyl ring of *hdin*/*hdn* ions to the LUMO of electron accepting nitro group. The values of quenching constant ' $K_{sv}$ ' obtained were  $6.4 \times 10^5$  and  $8.4 \times 10^5 \text{ M}^{-1}$  for the complexes **8** and **9**, respectively. The relatively high value of the later was attributed to stacked, non-interpenetrated, and non-interdigitated structure of the compound that permits best approach of the analyte molecules for electron transfer [58].

### 1.11.3 Adsorption and Photo-degradation of dyes

A Zn-MOF with the formula  $\{[\text{Zn}_2(\text{tptc})(\text{DMF})_3] \cdot 2\text{DMF} \cdot 2\text{H}_2\text{O}\}$  (**10**) was studied for the photocatalytic application towards degradation of organic dyes *viz.* MB and RhB [59].

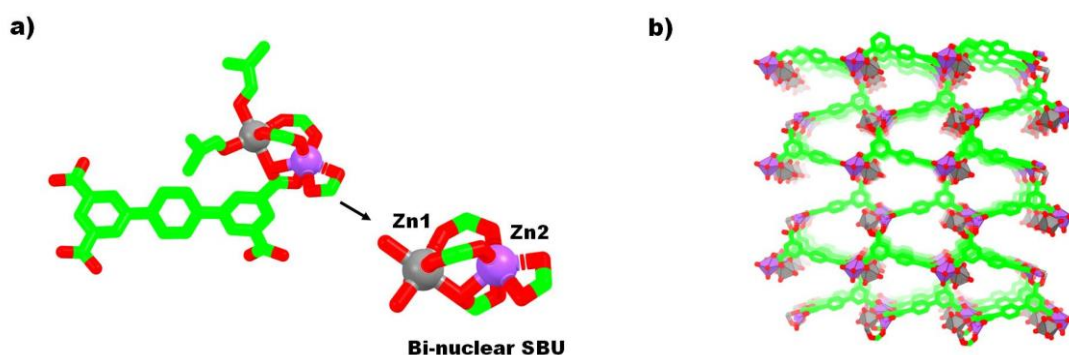


**Figure 7** – View of a) binuclear  $\{\text{Zn}_2(\text{CO}_2)_5\}$  molecular building blocks of complex **10** bridged by three carboxylate groups from three tptc anions, and b) three-dimensional framework of complex **10** [59].

The molecular structure of the complex contains binuclear  $\{\text{Zn}_2(\text{CO}_2)_5\}$  molecular building blocks in which octahedral Zn(II) ions were bridged by three carboxylate groups from three tptc anions (Figure 7a). These binuclear building blocks were connected to each other by bridged tptc anions to form a 3D framework with

elliptical channels of the dimensions  $11.5 \times 14.8 \text{ \AA}^2$  (Figure 7b). The overall topology of the framework was of the type uninodal 4-c lonsdaleite (**ion**). This compound has demonstrated a good degradation efficiency of 72.5% and 92.8% towards MB and RhB, respectively, within 100 min. The associated rate constants calculated for the photo-degradation using Langmuir–Hinshelwood model were  $1.67 \times 10^{-2}$  and  $2.12 \times 10^{-2} \text{ min}^{-1}$  for MB and RhB dyes, respectively [59].

Wang *et al.* reported a two-dimensional complex  $[\text{Cu}(4\text{-bpah})(5\text{-mip})(\text{H}_2\text{O})] \cdot \text{H}_2\text{O}$  (**11**) containing a 1D chain of square-pyramidal Cu(II) ions,

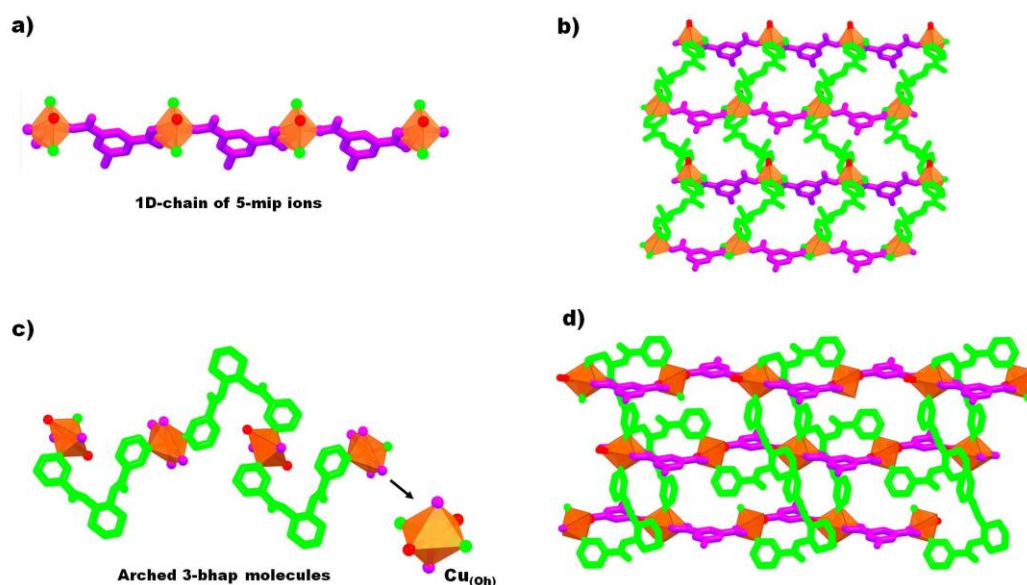


**Figure 8** – View of a) one-dimensional network formed by 5-mip and Cu(II) ions in complex **11**, b) two-dimensional (4,4) grid framework of complex **11**, c) one-dimensional meso-helical chain containing arched 3-bpah molecules in complex **12**, and d) two-dimensional (4,4) grid framework of complex **12** with different orientations of 5-mip ions relative to complex **11** [60]. (Note: 5-mip ions are shown in magenta colour while 3-bpah and 4-bpah are shown in green colour).

fabricated by 5-mip ions bridged in a bis(monodentate) mode between adjacent metal centers (Figure 8a) [60]. On the other hand, bridging 4-bpah molecules forms a left helical 1D chain with Cu(II) ions. These two different chains further weave an undulate 2D (4,4) network (Figure 8b). Likewise, a 2D (4,4) grid framework differing in the orientation of 5-MIP ions along with arched arrangement of 3-bpah molecules in the 1D meso-helical chain (Figure 8c and 8d) was obtained in the complex  $[\text{Cu}(3\text{-bpah})(5\text{-mip})] \cdot 2\text{H}_2\text{O}$  (**12**) synthesized using 3-bpah ligand. These complexes were tested for their photo-catalytic activity towards dye degradation

using methylene blue (MB), rhodamine (RhB) and methyl orange (MO) dyes. The results illustrate that 65-80% catalytic efficiencies were obtained in 240 minutes using these complexes [60].

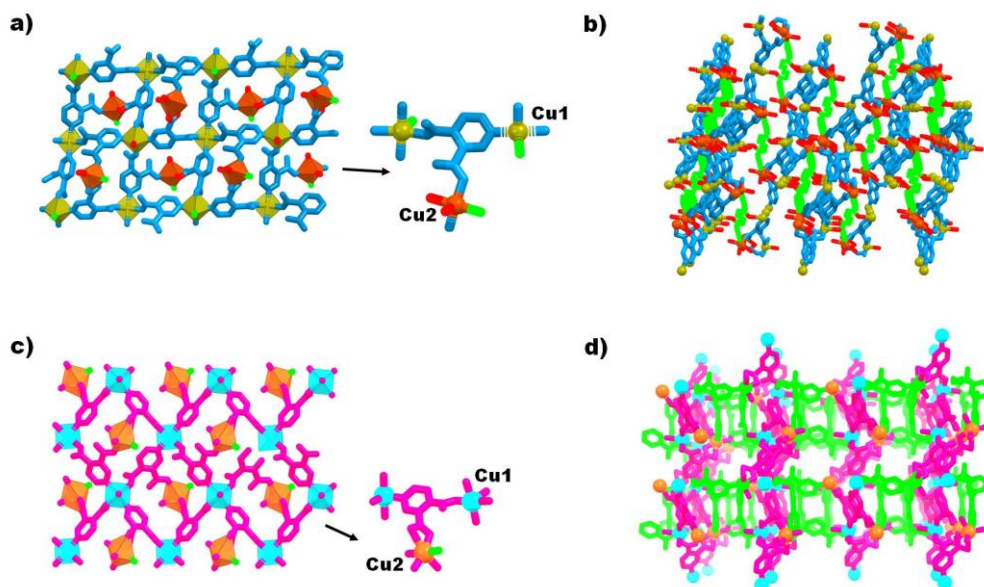


**Figure 9** – View of a) two-dimensional network of complex **13** comprising two different Cu(II) ions, b) three-dimensional framework of complex **13**, c) two-dimensional network of complex **14** comprising two different Cu(II) ions complex **14**, and d) three-dimensional framework of complex **14** [61]. (Note: 3,4-pdc ions are shown in light blue and magenta colour, whereas 3-bbn and bbin molecules are shown in green colour).

The complex  $[\text{Cu}_4(3,4\text{-pdc})_4(\text{bbin})(\text{H}_2\text{O})_4] \cdot 8\text{H}_2\text{O} \}_n$  (**13**) has two crystallographically independent square pyramidal Cu(II) ions, connected to each other by exotridentate (3-connected) 3,4-pdc ions in a two-dimensional layer motif  $[\text{Cu}_4(3,4\text{-pdc})_4(\text{H}_2\text{O})_4]_n$  (Figure 9a) [61]. These layers were aggregated by exotetradentate (4-connected) bbin ligands into a non-interpenetrated 3,3,4,5-connected three-dimensional coordination network (Figure 9b). While in complex  $[\text{Cu}_2(3,4\text{-pdc})_2(\text{bbn})(\text{H}_2\text{O})_2] \cdot 7\text{H}_2\text{O} \}_n$  (**14**), a non-interpenetrated 3,3,4 connected tri-nodal network was formed by bridged exotetradentate 3,4-pdc anions (Figure 9c) and bis(monodentate) bbn molecules (Figure 9d). These compounds were explored for their photocatalytic dye degradation using “Congo Red” and hydrogen peroxide. The results illustrate a 99% degradation of the dye using complex **13** after 120 min elapsed time, whereas it was 92% for complex **14** after 120 min [61].



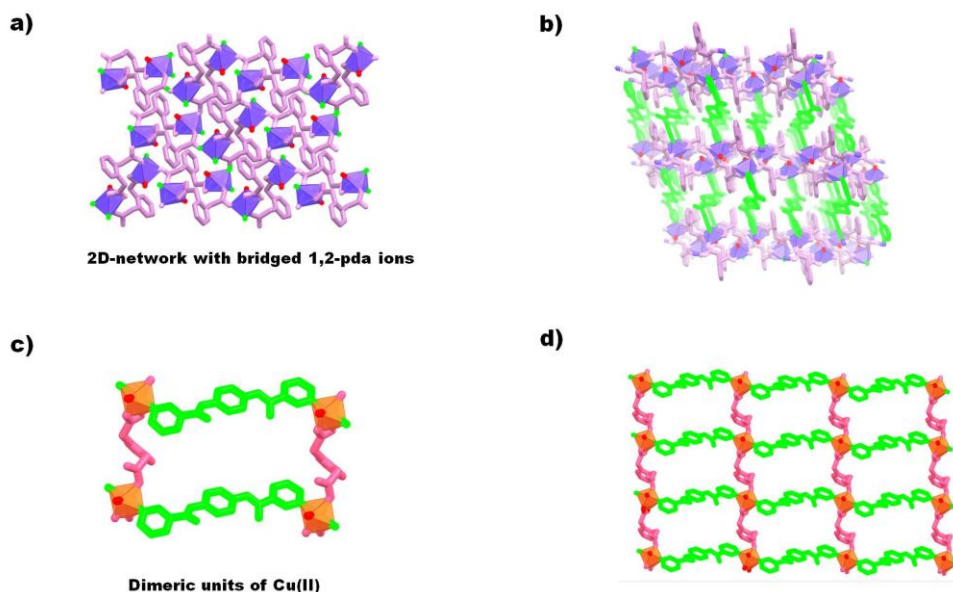


**Figure 10** – View of a) two-dimensional of complex **15** comprising bridged 1,2-pda ions, b) three-dimensional framework of complex **15**, c) dimeric units of Cu(II) ions formed by bridged 1,2-pda ions and 3-bpcb molecules, respectively in complex **16**, and d) two-dimensional network of complex **16** [62]. (Note: 1,2-pda ions are shown in light pink colour, whereas 3-bpcb and 4-bpfp molecules are shown in green colour).

In another work, Wang *et al.* reported two coordination polymers of Co(II) and Cu(II),  $[\text{Co}(\text{4-bpfp})_{0.5}(\text{1,2-pda})(\text{H}_2\text{O})]$  (**15**) and  $[\text{Cu}(\text{3-bpcb})(\text{1,2-pda})] \cdot 2\text{H}_2\text{O}$  (**16**), respectively, using bpfp and 3-bpcb ligands [62]. The complex **15** containing octahedral Co(II) ions was a three-dimensional coordination polymer, constructed by bridged tridentate 1,2-pda ions (3-connected linkers) that connect Co(II) centers (4-connected nodes) into a two-dimensional coordination sheet (Figure 10a). These two-dimensional sheets were linked to each other by bridged bpfp ligands to form a three-dimensional network with a 3,4-connected topology (Figure 10b). The complex **16** was also a two-dimensional coordination polymer with Cu(II) ions in a trigonal-bipyramidal geometry. The two-dimensional framework was formed because of the dimeric units of Cu(II), which were absent in Co(II) complex (Figure 10c). These dimeric units were linked to each other by 1,2-pda anions and 3-bpcb molecules (bridging bidentate) to form a 3,5-connected two-dimensional network (Figure 10d). These complexes were studied for their adsorption capacity towards

organic dyes such as Congo red, Methyl orange etc. The results illustrate that the Co(II) complex was a better adsorbent for these dyes than Cu(II) with good selectivity towards Congo red *ca.* 200 mg/g after 60 minutes [62.]

#### 1.11.4 Photoluminescence studies

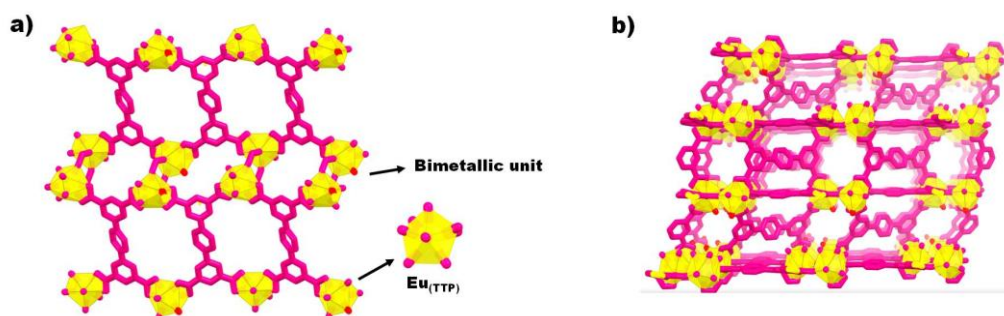


**Figure 11** – View of a) two-dimensional network of complex **17** comprising bimetallic Eu(III) units, and b) three-dimensional framework of complex **17** [63].

The complex  $\{[\text{DMF}]_2[\text{Eu}_2(\text{tptc})_2(\text{H}_2\text{O})(\text{DMF})].1.5 \text{ DMF}.7\text{H}_2\text{O}\}_n$  (**17**) synthesized using europium(III) sulfate with p-terphenyl-3,3',5,5'-tetracarboxylic acid ( $\text{H}_4\text{tptc}$ ) was a 3D coordination polymer [63]. The molecular structure of the complex **17** has two crystallographically independent Eu(III) ions each in a distorted tricapped-trigonal prism environment, which were linked into a bimetallic unit by a bridged tptc ions. These bimetallic units were cross-linked into a two- and then to a three-dimensional framework by bridged  $\mu_4$ -tptc anions (Figure 11a and 11b). The complex was studied for photoluminescence application, which show bright red luminescence from the complex owing to characteristic  $^5\text{D}_0 \leftarrow ^7\text{F}_J$  ( $J = 0-4$ ) transitions. In addition, the relevant quantum yield ' $\Phi$ ' observed was 16.

#### 1.11.5 Acetone Sensor

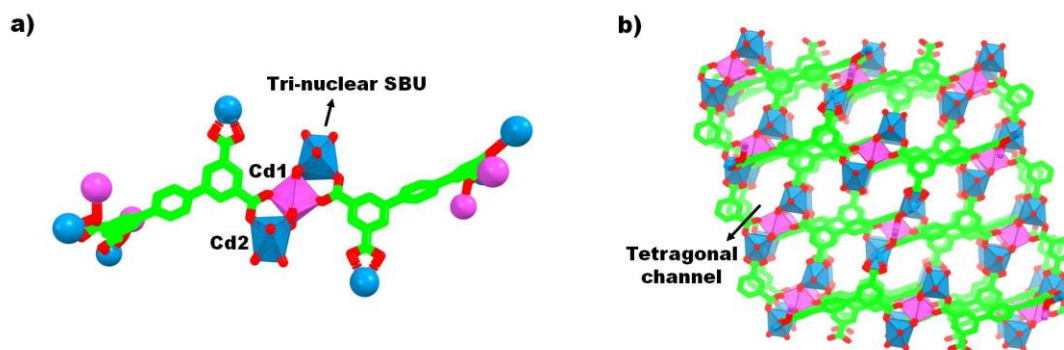


**Figure 12** – View of a) trinuclear secondary building unit (SBU) containing two different Cd(II) ions in complex **18**, and b) three-dimensional framework with tetragonal channels of complex **18** [64].

A three-dimensional Cd-MOF with the chemical formula  $\{[(\text{CH}_3)_2\text{NH}_2]_2\text{Cd}_3(\text{tptc})_2\}$  (**18**) was explored as a luminescent sensor for acetone and picric acid. Molecular structure of complex **18** shows two independent Cd(II) ions in the crystal lattice: an octahedral Cd1 and a decahedral Cd2 ion, connected by eight tptc ions to form a trinuclear  $[\text{Cd}_3(\text{COO})_8]^{2-}$  secondary building unit (SBU) (Figure 12a) [64]. The adjacent SBUs were connected to each other by  $\mu_7$ -bridged tptc ions to form a 3D framework with 1D square and tetragonal channel (Figure 12b). This compound was deposited on the paper to be used as a paper-based sensor in acetone sensing. The results show a good sensitivity towards acetone vapors at the detection limit of 86 ppm. Besides, it was also sensitive to picric acid even at nano-molar levels (200 nM) with good selectivity towards picric acid over other analytes *viz.* metal ions,  $\text{KMnO}_4$ ,  $\text{K}_2\text{Cr}_2\text{O}_7$ , other nitro-group containing compounds.

### 1.11.6 Gas separation

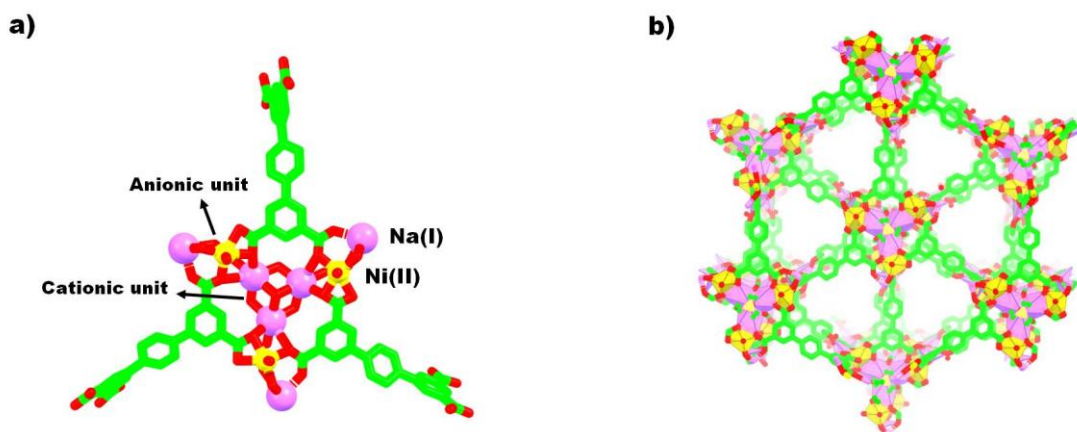


**Figure 13** – View of a) tri-nuclear  $[\text{Na}_3(\mu_2\text{-MeOH})_3(\mu_3\text{-DMSO})]^{3+}$  cationic unit surrounded by three binuclear  $[\text{NiNa}(\text{COO})_4]^-$  anionic unit in complex **19**, and b) three-dimensional framework of complex **19** [65].

Li *et al.* synthesized a enneanuclear bimetallic **NbU-2** Metal-organic framework *via* two-step crystallization involving post-synthetic uptake of Ni(II) ions by Na(I) based framework. The secondary building unit  $[\text{Ni}_3\text{Na}_6(\text{DMSO})(\text{MeOH})_6(\text{COO})_{12}]_n$  (**19**) was comprised of a trinuclear  $[\text{Na}_3(\mu_2\text{-MeOH})_3(\mu_3\text{-DMSO})]^{3+}$  cationic unit, and three binuclear  $[\text{NiNa}(\text{COO})_4]^-$  anionic unit connected by tptc anions (Figure 13a)



[65]. Topologically, the resulting 3D framework contains 3- and 9- connected nodes with the topology (3,9) connected network (Figure 13b). The N<sub>2</sub> gas adsorption studies showed the Langmuir surface area of 421.3 m<sup>2</sup> g<sup>-1</sup> with the pore size distribution in the range 5-7 Å. The studies involving the adsorption of CO<sub>2</sub> and CH<sub>4</sub> at 273 K have shown that the uptake of CO<sub>2</sub> by **NbU-2** is 5 times more than for CH<sub>4</sub> gas with the adsorption values of 58.2 and 12.5 cm<sup>3</sup> (STP) g<sup>-1</sup>, respectively.

### 1.12 Present work

In this thesis, I have compiled the results of my research work on the coordination compounds with intriguing molecular architectures used for metal-ion sensing and fluorescence/photoluminescence applications. In the fabrication of materials for the sensing and photoluminescence applications, I have meticulously chosen the metal-ligand combination by implementing the ideology of “crystal-engineering”. For the metal-ion sensing studies, I have opted mixed-ligand approach using carboxylate ion and dicarboxamide based ligands to introduce more sticky/interacting sites in the coordination framework to facilitate more sensor-analyte interactions during fluorescence titrations. Besides, Co(II) ion of 1<sup>st</sup> transition series was chosen to construct porous coordination framework because it is coordinatively flexible and thus can accommodate two different ligands. This strategy also worked well using Zn(II) ion that has resulted in an appealing porous framework, but the lack of stable fluorescence signal precludes its use for sensing studies. Finally, a three-dimensional coordination polymer is obtained using Ni(II), which is also interesting from structural viewpoint. The detailed description of this work is given in Chapter 2 of the thesis. I have also tried a mixed-ligand strategy using the same metal and carboxylate ion combination as mentioned above with a dicarboxamide ligand differing in the position of nitrogen atom in pendant pyridine ring to construct coordination compounds for the comparison of molecular structures and the resulting frameworks. Unfortunately, I got three isostructural one-dimensional coordination polymers containing Co(II), Cu(II) and Zn(II) ions, respectively. The reason for this result could be ascribed to the absence of steric effects owing to the *para* position of the pyridine nitrogen atom with respect to the amide group, which results in the coordination of solvent molecules at the remaining coordination sites of the metal ions thereby blocking the approach of carboxylate ions toward metal ions. This work is discussed in Chapter 3, which is completely dedicated to the characterization of these compounds using different techniques such as SCXRD,

XPS, EDS etc., and the comparison among the compounds. Moreover, DFT calculations are done on these complexes to have an information of the orbitals involved in the ground and excited states of the ligand and the complexes as well, and to understand the nature of metal-ligand bonds. Chapter 4 is a review article on the coordination chemistry and applications of the complexes of pyridine-based ligands containing fully substituted or tertiary amide moiety (-CONRR-). Library of ligands with diverse molecular structures are compiled and classified based on the position of pyridine ring in the ligand molecule. In addition, a critical discussion on the coordination chemistry and the relative applications has also been given. Chapter 5 includes a discussion on the room temperature photoluminescence studies of isomorphous coordination compounds of Ln(III) ions (Ln = Ho, Er, Tm, Yb) with a symmetric ligand *viz.* terphenyltetracarboxylic acid. Here again, I have implemented the ideas of “crystal-engineering” in fabricating self-assembled three dimensional networks (Ln-MOFs) containing the combination of photoluminescent Ln(III) ions and the photosensitizer ligand molecule containing fluorophore moieties. Single crystal X-ray diffraction studies have shown that these compounds are highly porous Metal-organic frameworks with solvent accessible voids volumes >50%. Although the characteristic peaks of Ln(III) ions are observed in the emission spectra of the corresponding compounds, the presence of a broad ligand-centered emission band (due to back energy transfer) relative to weak Ln(III) emissions illustrates that the terphenyl tetracarboxylic acid is not an ideal ligand to be used as an antenna molecule. Besides, the factors affecting the intensity and the broadness of emission bands are also discussed.

### 1.13 References

1. a) <http://goldbook.iupac.org/C01330.html>; b) G. B. Kauffman, Alfred Werner: *Founder of Coordination Chemistry. Springer Science & Business Media*: 2013.
2. S. R. Batten, N. R. Champness, X. Mi. Chen, J. G. Martinez, S. Kitagawa, L. Öhrström, M. O’Keeffe, M. P. Suhh, Jan Reedijk, *CrystEngComm*, 2012, **14**, 3001.
3. J. C. Bailar, Coordination Polymers, in: W. L. Jolly (Eds.), *Preparative Inorganic Reactions*, Vol. 1, Interscience, New York, 1964, pp. 1-25.
4. V. V. Adrabinska, *Coord. Chem. Rev.* 2007, **251**, 1987.

5. J. A. Rood, W. C. Boggess, B. C. Noll, K. W. Henderson, *J. Am. Chem. Soc.* **2007**, *129*, 13675.
6. C. Y. Li, C. S. Liu, J. R. Li, X. H. Bu, *Cryst. Growth Des.* 2007, **7**, 286.
7. C. T. Chen, K. S. Suslick, *Coord. Chem. Rev.*, 1993, **128**, 293.
8. a) B. F Hoskins and R. J. Robson, *Am. Chem. Soc.* 1989, **111**, 5962, b) B. F. Hoskins, R. J. Robson, *Am. Chem. Soc.* 1990, **112**, 1546.
9. O. M Yaghi, G. Li, H. Li, *Nature* 1995, **378**, 703.
10. H. Li, M. Eddaoudi, M O’Keeffe, O. M. Yaghi, *Nature* 1999, **402**, 276.
11. S. S. Y. Chui, S. M.F. Lo, J. P. H. Charmant, A. G. Orpen, I. D. Williams, *Science*, 1999, **283**, 1148.
12. M. H. Yap, K. L Fow, G. Z. Chen, *Green Energy Environ.* 2017, **2**, 218.
13. R. J. Kuppler, D. J Timmons, Q. R. Fang, J. R. Li, T. A. Makal, M. D Young, D. Yuan, D. Zhao, W. Zhuang, H.C. Zhou, *Coord. Chem. Rev.* 2009, **253**, 3042.
14. R G Pearson, *J. Am. Chem. Soc.*, 1963, **85**, 3533.
15. A. Y. Robin, K. M. Fromm, *Coord. Chem Rev.*, 2006, **250**, 2127
16. L. Pan, K. M. Adams, H. E. Hernandez, X.Wang, C. Zheng, Y.Hattori, K. Kaneko, *J. Am. Chem. Soc.* 2003, **125**, 3062, b) S. Kitagawa, S. Noro, *Compreh. Coord. Chem.* 2004, **7**, 231.
17. S. Kitagawa, R. Kitaura, S. Noro, *Angew.Chem. Int. Ed.*, 2004, **43**, 2334.
18. G. R Desiraju, *Crystal Engineering. The Design of Organic Solids*, Elsevier, Amsterdam, 1989.
19. G. R. Desiraju, *J. Am. Chem. Soc.* 2013, **135**, 9952.
20. C. S Cundy, P. A. Cox, *Chem. Rev.* 2003, **13**, 663.
21. S. L. Hou, J. Dong, X. L. Jiang, Z. H. Jiao, C. M. Wang, B. Zhao. *Analytical Chemistry*, 2018, **90**, 1516.
22. H. Xu, C. S. Cao, X. M.Kang and B. Zhao. *Dalton Transactions*, 2016, **45**, 18003.
23. N. D. Rudd, H.. Wang, E. M. A. F. Fernandez, S. J. Teat, Feng Chen, G. Hall, Y. J. Chabal, and J. Li. *ACS Applied Materials & Interfaces*, 2016, **8**, 30294.
24. Y. Takashima, V. M. Martínez, S. Furukawa, M. Kondo, S. Shimomura, H. Uehara, M. Nakahama, K. Sugimoto, and S. Kitagawa, *Nature Communications*, 2011, **2**, 168.
25. M. Liqing, A. Carter and L. Wenbin, *Chemical Society Reviews*, 2009, **38**, 1248.

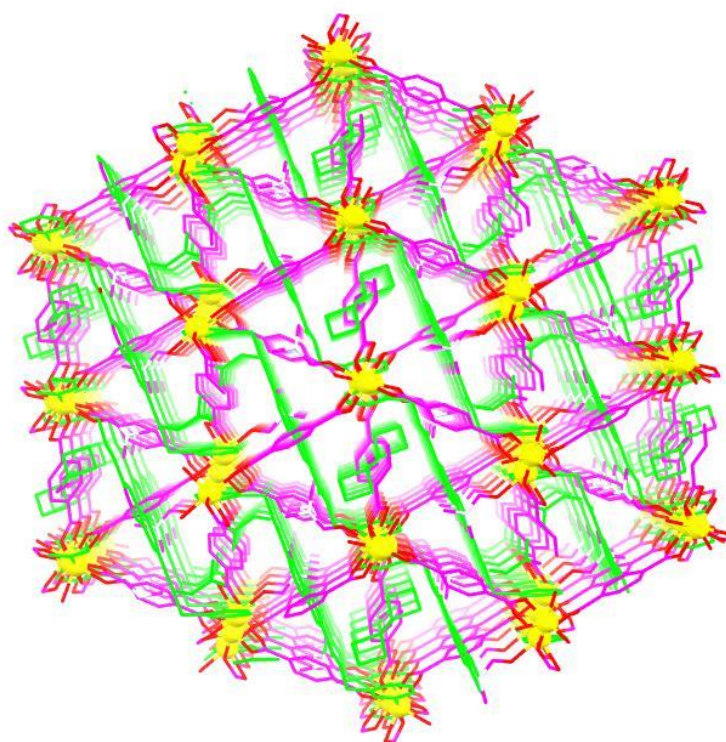
26. J. R. Li, R. J. Kuppler and H. C. Zhou, *Chemical Society Reviews*, 2009, **38**, 1477-1504.
27. J. Y. Lee, O. K. Farha, J. Roberts, K. A. Scheidt, S. B. T. Nguyena and J. T. Hupp, *Chemical Society Reviews*, 2009, **38**, 1450.
28. (a) Molecular Sieves, R. Szostak, Van Nostrand Reinhold, New York, 1989, 1;  
(b) Natural Zeolites, G. Gottardi and E. Galli, Springer-Verlag, Berlin, 1985, 1.
29. A.G. Wong-Foy, A.J. Matzger, *J. Am. Chem. Soc.* **2006**, 128, 3494–3495.
30. M. Eddaoudi, J. Kim, N. Rosi, D. Vodak, J. Wachter, M. O’Keeffe, O. M. Yaghi, *Science* 2002, **295**, 469.
31. C. P. Raptopoulou, *Materials*, 2021, **14**, 310.
32. a) H. R. Abid, M. R. Azhar, S. Iglauer, Z. H. Rada, A. Al-Yaseri, A. Keshavarz, *Heliyon*, 2024, **10**, e23840, and b) M. Jaroniec, M. Kruk, A. Sayari, *Studies in Surface Science and Catalysis*, 117, **1998**, 325-332.
33. S. S. Y. Chui, S. M. F. Lo, J. P. H. Charmant, A. G. Orpen, I. D. Williams, *Science*, 1999, **283**, 1148.
34. H. Furukawa, Y. B. Go, N. Ko, Y. K. Park, F. J. Uribe-Romo, J. Kim, M. O’Keeffe, O. M. Yaghi, *Inorganic Chemistry*, 2011, **50**, 9147.
35. M. Bosch, M. Zhang, H. C. Zhou, *Adv. Chem.* 2014, **2014**, e182327.
36. J. E. Mondloch, O. Karagiari, O. K. Farha, J. T. Hupp, *CrystEngComm* 2013, **15**, 9258.
37. A. P. Nelson, Farha, O. K.; Mulfort, K. L.; Hupp, J. T. Supercritical Processing as a Route to High Internal Surface Areas and Permanent Microporosity in Metal–Organic Framework Materials. *J. Am. Chem. Soc.* 2009, **131**, 458.
38. S. Horike, S. Shimomura, S. Kitagawa, *Nat. Chem.* 2009, **1**, 695.
39. J. H. Lee, S. Jeoung, Y. G. Chung, H. R. Moon, *Coord. Chem. Rev.*, 2019, **389**, 161.
40. [https://serc.carleton.edu/research\\_education/geochemsheets/techniques/SXD.html](https://serc.carleton.edu/research_education/geochemsheets/techniques/SXD.html); accessed 11-2024.
41. [https://serc.carleton.edu/research\\_education/geochemsheets/techniques/XRD.html](https://serc.carleton.edu/research_education/geochemsheets/techniques/XRD.html); accessed 11-2024.
42. <https://pubs.acs.org/doi/10.1021/acsreagents.2008>; accessed 11-2024.
43. [https://www.rsc.org/images/chns-elemental-analysers-technical-brief-29\\_tcm18-214833.pdf](https://www.rsc.org/images/chns-elemental-analysers-technical-brief-29_tcm18-214833.pdf); accessed 11-2024.

44. <https://www2.chemistry.msu.edu/faculty/reusch/virttxtjml/spectrpy/nmr/nmr1.htm>; accessed 11-2024.
45. [https://resources.perkinelmer.com/lab-solutions/resources/docs/faq\\_beginners-guide-to-thermogravimetric-analysis\\_009380c\\_01.pdf](https://resources.perkinelmer.com/lab-solutions/resources/docs/faq_beginners-guide-to-thermogravimetric-analysis_009380c_01.pdf); accessed 11-2024.
46. <https://www.nanoscience.com/techniques/scanning-electron-microscopy/>; accessed 11-2024.
47. A. N. Khlobystov, A. J. Blake, N. R. Champness, D. A. Lemenovskii, A. G. Majouga, N.V. Zyk, M.Schröder, *Coordination Chemistry Reviews*, 2001, **222**, 155.
48. A. Nimmermark, L. Öhrström, J. Reedijk, *Z. Kristallogr.* 2013, **228**, 311.
49. S. R. Batten, *CrystEngComm*, 2001, **3**, 67.
50. C. A Hunter, *Angew. Chem Int. Ed. Engl.*, 1995, **34**, 1079.
51. M. I. Khan, Y.-S. Lee, C. J. O'Connor, R. C. Haushalter, J. Zublea, *Chem. Mater.* 1994, **6**, 721.
52. Frameworks for Commercial Success, *Nat. Chem.* **8**, 2016, 987–987.
53. J. Arnó, O. K. Farha, W. Morris, P. W. Siu, G. M. Tom, M. H. Weston, P. E. Fuller, 2018 22nd International Conference on Ion Implantation Technology (IIT); 2018; pp 227–230.
54. G. Blanco-Brieva, J.M. Campos-Martin, S.M. Al-Zahrani, J.L.G. Fierro, *Fuels*, **113**, 2013, 216-220.
55. S. H. Qiblawi, A. L. Pochodylo, R. L. LaDuca, *CrystEngComm*, 2013, **15**, 8979.
56. C. L. White, R. L. L. Duca, *CrystEngComm*, 2016, **18**, 6789.
57. M. E. O. Donovan, A. R. Porta, M. D. T.Salgado, R. L. L. Duca. *Z. Anorg. Allg. Chem.* 2014, **640**, 2113.
58. J. J. Przybyla, Robert L. LaDuca, *Inorganica Chimica Acta*, 2019, **486**, 314.
59. J. C. Jin, J. Wu, Y. X. He, B. H. Li, J. Q. Liu, R. Prasad, A. Kumar, S.R. Batten, *CrystEngComm*, 2017, **19**, 6464.
60. X. L. Wang, J. Luan, H.Y. Lin, Q. L. Lu, M. Le, G. C. Liu, J. Y. Shao, *ChemPlusChem* 2014, **79**, 1691.
61. E. C. Jaddou, R. L. L. Duca *Polyhedron*, 2020, **180**, 114427.
62. X. Wang, J. Zhao, M. Le, H. Lin, G. Liu, X. Wang, *CrystEngComm*, 2016, **18**, 9316.

63. Y. L. Gai, F. L. Jiang, L. Chen, Y. Bu, K. Z. Su, S. A. A. Thabaiti, M. C. Hong, *Inorganic Chemistry*, 2013, **52**, 7658.
64. P. Ju, H. Yang, L. Jiang, M. Li, Y. Yu, E. Zhang, *Spectrochimica Acta Part A: Molecular and Biomolecular Spectroscopy*, 2021, **246**, 118962.
65. L. Jiang, J. Zhao, S. Chen, J. Li, D. Wu, Y. Li, *Inorg. Chem.*, 2019, **58**, 9425.

## Chapter – 2

# **An Insight into Sensitive Detection of Metal ions Using a Novel Cobalt MOF: Single Crystal, Photoluminescence, and Theoretical Studies**



Rana *et. al*, *CrystEngComm*, 2022, **24**, 5460-5473.

## 2.1 Introduction

From the past few years, industrial advancements have come up with a variety of new products and technologies that are beneficial to human beings, but the usage of chemicals has led to the devastating effects on the environment, including surge in the diseases in the flora and fauna. In almost all daily products, heavy metal-ions have been used quite frequently. The term “Heavy metals” is ascribed to non-biodegradable, high atomic weight elements whose density is relatively greater than water. Some transition metals, metalloids (As, Pb etc.), lanthanides and actinides belong to this category. Metal-ions such as  $\text{Fe}^{+2}$ ,  $\text{Fe}^{+3}$ ,  $\text{Cu}^{+2}$ ,  $\text{Hg}^{+2}$ ,  $\text{Cr}^{+5}$ ,  $\text{Pb}^{+2}$  etc. can be fatal beyond even at low concentrations, causing various detrimental health effects on humans. Although there are different analytical equipments available for the quantification of these ions along with good detection limits (ppm level), rapid quantification is not achieved using these techniques. Besides, requirement of large sample quantities (5 mL or more), costly stationary equipment and skilled staff are some associated drawbacks.

Coordination complexes especially porous Metal-Organic Frameworks (MOFs) with preorganized coordination sites around the cavities can be utilized as potential sensing material for rapid detection of analyte molecules using fluorescence technique. MOFs contain metal nodes and organic linkers both of which can be modulated to allow both fine chemical and structural control. Thus, various properties such as porosity, particle morphology, stability and photophysical properties can be tailored for desired applications. Owing to these features, these materials have become an interesting class for scientific community with ever-expanding practical application scope.

In a sensing experiment, greater sensitivity/or selectivity can be achieved with MOFs than the uncoordinated organic ligands because in the coordination framework of MOFs, the ligand molecules are immobilized and preorganized to facilitate more interactions with analyte molecules. Moreover, the porous framework of MOFs allows free passage to analytes, thus maximizing their interactions with preorganized organic functional groups around the pores. Hence, greater sensitivity can be achieved in detection experiments. Consequently, MOFs containing highly conjugated moieties or fluorophores also known as luminescent metal organic frameworks (LMOFs) have been used as potential chemo-sensing materials in fluorescence sensing. In this research work we have explored the novel Co-MOF, fabricated by the coordination of naphthalene anchored dicarboxamide ligand (**L1**) and benzene dicarboxalate ions



(BDC) to Co(II) ions to produce a porous 3D framework for the sensitive detection of toxic metal ions (detection at ppm levels). In addition factors that make this material more sensitive to some metal ions over others has also been investigated with the aid of DFT studies.

## 2.2 Objective

- Design and synthesis of novel transition metal-based coordination compounds using mixed ligand strategy for the sensitive detection of toxic metal ions using fluorescence.
- Implementation of the ideas of “Crystal engineering” while choosing the ligand/metal ions combinations to fabricate the coordination compounds for the sensing application.
- Meticulous selection of the ligands and the metal-ions to attain intriguing porous framework comprising sticky sites in the cavities to enhance sensor-analyte interactions.
- Investigation of the structural diversities obtained using different metal ions and the mixed ligand combinations.
- Characterization of the ligand and the related coordination compounds using single crystal x-ray diffraction technique, and its correlation with other analytical techniques *viz.* IR, NMR, CHN, TGA etc.

## 2.3 Authors contribution

- Conceptualization – Love Karan Rana
- Data curation – Love Karan Rana and Thierry Maris (SCXRD Data)
- Formal analysis – Love Karan Rana
- Funding acquisition – Dr. Adam Duong
- Investigation – Love Karan Rana
- Methodology – Love Karan Rana
- Supervision – Dr. Adam Duong
- Visualization – Love Karan Rana
- Writing - original draft – Love Karan Rana

- Writing – review and editing – Love Karan Rana, Prabhjot Kaur, and Dr. Adam Duong

## **2.4 Article**



Cite this: *CrystEngComm*, 2022, 24, 5460

## An insight into sensitive detection of metal ions using a novel cobalt MOF: single crystal, photoluminescence, and theoretical studies†

Love Karan Rana,<sup>a</sup> Prabhjyot Kaur,<sup>a</sup> Thierry Maris <sup>b</sup> and Adam Duong <sup>\*a</sup>

In this work, sensitive detection of various metal ions and anions using cobalt metal-organic frameworks has been studied. Furthermore, various sensor-analyte interactions that prompt changes in the fluorescence emission have been investigated and discussed in the realm of “crystal engineering”. In this pursuit, three novel mixed ligand coordination compounds with the molecular formula  $\{[\text{Co}_3(\text{L1})(\mu\text{-BDC})(\text{BDC})_2(\text{L1})(\text{DMF})_2]\cdot\text{DMF}\}_n$  (**1**),  $\{[\text{Zn}_8(\mu_2\text{-BTB})_3(\text{BTB})(\text{O})_2(\text{L1})(\text{DMF})_2]\cdot 4\text{DMF}\}_n$  (**2**) and  $\{[\text{Ni}(\text{L1})(\text{BDC})(\text{EtOH}/\text{DMF})_2]\cdot\text{EtOH}\}_n$  (**3**) have been synthesized using a new naphthalene dicarboxamide ligand **L1** (*N*<sup>2</sup>,*N*<sup>6</sup>-bis(pyridin-3-ylmethyl)naphthalene-2,6-dicarboxamide) and two carboxylic acid-based ligands, viz. **H<sub>2</sub>BDC** (1,4-benzene dicarboxylic acid) and **H<sub>3</sub>BTB** (1,3,5-tris(4-carboxyphenyl) benzene). Among these, **1** and **2** have solvent-accessible voids in the crystal structure but a single and stable fluorescence signal is observed only in the case of **1** and therefore it has been utilized for sensing studies. Various metal cations have been used in fluorescence titrations to test the sensing ability of **1**, which is also referred to as Co-MOF in the following discussion. It was found that **1** is highly responsive to  $\text{Fe}^{+3}$ ,  $\text{Ru}^{+3}$ ,  $\text{Pd}^{+2}$ , and  $\text{Hg}^{+2}$  ions and moderately responsive to  $\text{Pb}^{+2}$ ,  $\text{Cd}^{+2}$ ,  $\text{Ni}^{+2}$ ,  $\text{Co}^{+2}$ , and  $\text{Fe}^{+2}$  ions. Interestingly, **1** gave no response upon the addition of  $\text{Zn}^{+2}$ ,  $\text{Mn}^{+2}$ ,  $\text{Be}^{+2}$  and all alkaline earth metal ions. Fluorescence experiments were also performed using different salts of Fe(III) and Cu(II) ions with different counterions. Distinct trends in the decrease in fluorescence intensity of **1** on varying the counter anions prompted us to perform anion sensing experiments. Addition of  $\text{BF}_4^-$ ,  $\text{I}^-$ ,  $\text{NO}_3^-$ , and  $(\text{SO}_4)^{-2}$  ions have caused a slight decrease in the fluorescence intensity of **1**, while no response was observed towards  $\text{ClO}_4^-$ ,  $\text{Br}^-$ , and  $\text{SCN}^-$  ions. The potential mechanism of sensitive detection was proposed with the aid of DFT calculations performed on a model Co(II) complex, which illustrates that the excited state has a dominant contribution from naphthalene and carbonyl moieties and that the electron transfer can occur only if the analyte ions interact with either of the moieties or both. SCXRD reveals that compound **3** is a 3D coordination polymer with no solvent-accessible voids. Various characterization techniques, viz. NMR, SCXRD, PXRD, IR, TGA, and photoluminescence, were used to determine the structure and properties of **L1** and **1–3**.

Received 17th March 2022,  
Accepted 12th June 2022

DOI: 10.1039/d2ce00385f

rsc.li/crystengcomm

## Introduction

In the past few years, industrial advancements have come up with a variety of new products and technologies in multiple

fields, viz. domestic, agricultural, industrial, medical, etc.<sup>1,2</sup> Although these developments are beneficial to human beings, the usage of chemicals has led to devastating effects on the environmental system, including a surge in diseases in plants, humans, and animals. Among these, heavy metal ions have been used quite frequently in almost all daily products. “Heavy metals” are non-biodegradable elements with high atomic weight and relatively greater density than water. Some transition metals, metalloids (As, Pb etc.), lanthanides and actinides belong to this category. These toxicants pose adverse effects on humans even at lower concentrations.<sup>3,4</sup> They enter into biogeochemical cycles via industrial effluents and/or by leaching from the soil into water bodies.<sup>5</sup> Metal ions such as  $\text{Fe}^{+2}$ ,  $\text{Fe}^{+3}$ ,  $\text{Cu}^{+2}$ ,  $\text{Hg}^{+2}$ ,  $\text{Cr}^{+5}$ ,  $\text{Pb}^{+2}$  etc. can be fatal beyond certain concentrations, causing various detrimental health effects.<sup>6,7</sup> Presently, analytical methods reported for the

<sup>a</sup> Département de Chimie, Biochimie et Physique and Institut de Recherche sur l'Hydrogène (DuongLab), Université du Québec à Trois-Rivières, Trois-Rivières, Québec, G9A 5H7, Canada. E-mail: adam.duong@uqtr.ca

<sup>b</sup> Département de Chimie, Université de Montréal, Montréal, Québec, H3C 3J7, Canada

† Electronic supplementary information (ESI) available: ORTEP diagrams, Table S1 showing IR peak assignments, and Table S2 showing pertinent atomic parameters of compounds **1**, **2**, and **3** are given. In addition, <sup>1</sup>H NMR and <sup>13</sup>C NMR of **L1**, PXRD patterns of the complexes along with TGA plots and their description and some fluorescence graphs are shown. CCDC numbers 1982228, 2130355, 2130357 and 2127996. For ESI and crystallographic data in CIF or other electronic format see DOI: <https://doi.org/10.1039/d2ce00385f>

quantification of metal ion contaminants are inductively coupled plasma optical emission spectrometry (ICP-OES),<sup>8</sup> electrochemical detection,<sup>9</sup> or atomic absorption spectrophotometry (AAS).<sup>10</sup> These methods have good detection limits (ppm level), but the requirement of large sample quantities (5 mL or more), costly stationary equipment and skilled staff are some associated drawbacks. Moreover, rapid quantification is not achieved using these techniques. In contrast, coordination complexes especially porous metal-organic frameworks (MOFs) with preorganized coordination sites around the cavities can be utilized as potential sensing materials for rapid fluorescence detection of analyte molecules. MOFs are composed of metal nodes and organic linkers both of which can be modulated to allow both fine chemical and structural control. Thus, various properties such as porosity, particle morphology, stability and photophysical properties can be tailored for desired applications. Owing to these features, these materials have become an interesting class for the scientific community<sup>11–14</sup> with an ever-expanding practical application scope.

In a sensing experiment, greater sensitivity/or selectivity can be achieved with MOFs than the uncoordinated organic ligands or nonporous materials because analyte molecules can concentrate significantly towards the pores, maximizing their interactions with preorganized organic functional groups around the pores. Hence, greater sensitivity can be achieved in detection experiments. Consequently, MOFs containing highly conjugated moieties or fluorophores, also known as luminescent metal-organic frameworks (LMOFs), have been used as potential chemo-sensing materials<sup>15,16</sup> in fluorescence sensing. Since the emission intensity of MOFs is sensitive to solvent change and analyte concentrations, a noticeable change in fluorescence signal can be detected.<sup>17,18</sup> As a result, MOFs have potential applications in detection of heavy metals,<sup>19</sup> volatile organic carbons (VOCs),<sup>20</sup> and explosives.<sup>21</sup> There are plenty of reports in the literature on the use of mixed ligand MOFs for the detection of toxic metal ions, for instance, two mixed ligand Zn-MOFs, viz. UCMC-1 and NH<sub>2</sub>-UCMC-1 (comprising 4,4',4''-benzene-1,3,5-triyltribenzoic acid (BTB) and terephthalic acid (BDC) in UCMC-1 or 2-amino-1,4-benzene dicarboxylate (NH<sub>2</sub>-BDC) in NH<sub>2</sub>-UCMC-1), were explored as luminescent probes in metal ion sensing.<sup>22</sup> It was observed that high selectivity was achieved for Fe<sup>3+</sup> ions using amino functionalized MOFs (NH<sub>2</sub>-UCMC-1). In another work, a mixed ligand Zn-MOF containing tetrakis(4-pyridyloxymethylene)-methane (TPOM) and 2-aminoterephthalic acid (NH<sub>2</sub>-BDC) ligands was found to be selective for Cr<sup>3+</sup> ions through fluorescence enhancement and to Cr<sup>6+</sup> ions due to quenching of fluorescence.<sup>23</sup>

A mixed ligand Cu-MOF (TMU-48S) comprising S-linker (*N*<sup>1</sup>,*N*<sup>3</sup>-di(pyridine-4-yl) malonamide), H<sub>2</sub>oba (4,4'-oxybis(benzoic acid) and *N,N'*-bis-(4-pyridylformamide)-1,5-naphthalenediamine (bpfn) was synthesized using a solvent-assisted ligand exchange (SALE) technique. The material has shown high detection ability for Hg<sup>2+</sup> ions.<sup>24</sup> Apart from this, there are many reports in the literature on the use of MOFs

with one ligand system for metal ion detection. One such example is as an amine-free Zr<sup>4+</sup>-based MOF (UiO-66) containing one ligand, viz. 1,4-benzodicarboxylic acid, and [Zr<sub>6</sub>O<sub>4</sub>(OH)<sub>4</sub>] secondary building units (SBUs) that have shown selective and rapid reduction in fluorescence intensity upon the addition of Cu<sup>2+</sup> ions.<sup>25</sup>

A literature survey shows that the research is more dedicated to quantitative analysis of metal ions. Nevertheless, qualitative analysis is also equally important to provide an idea about the design of new materials for further development of MOF-based sensors. Currently, our research interest is twofold: (1) to study the versatility of compound **1** in the sensitive detection of various toxic metal ions using fluorescence studies and (2) to scrutinize the factors that make this material more sensitive to some metal ions over others. Compound **1** is fabricated by the coordination of **L1** and **BDC** (deprotonated form) to Co(II) ions to produce a porous 3D framework, which is explored as a sensing material to achieve rapid (<2 min) and sensitive (detection at ppm levels) toxic metal ion detection by fluorescence techniques. To the best of our knowledge, this type of Co(II) MOF with the ligand combination **L1**/**BDC** is unique and has never been utilized for such sensing applications. The observed solvent-accessible void volume of ca. 57 Å<sup>3</sup> (2% of unit cell volume)<sup>26</sup> is anticipated to provide free passage to analyte molecules through the material to allow sensor-analyte interactions to occur to attenuate the fluorescence of the material. The low void volume observed might be due to the diagonal coordination of flexible **L1** molecules to Co(II) ions in the adjacent 2D sheets (formed by Co(II) ions and **BDC** ligands) that has resulted in the low pore volume and hence small solvent-accessible voids (SAVs). The flexibility in **L1** stems from the free orientation of pyridine rings around sp<sup>3</sup> carbon atoms (next to amide nitrogen) while coordinating to Co(II) ions.

In this work, we have carefully implemented the ideas of “crystal engineering”<sup>27–29</sup> while choosing the ligand/metal ion combinations to fabricate the coordination compounds for sensing applications. The naphthalene dicarboxamide ligand (**L1**) was chosen because it can bestow sensing properties to coordination compounds to be used in fluorescence titrations with different metal ions due to potential M<sup>n+</sup>...O<sub>amide</sub> (Lewis base) and M<sup>n+</sup>...π interactions. Among these complexes, only Co-MOF (**1**) was explored in sensing experiments owing to its single/stable fluorescence emission along with its porous nature.

## Materials and methods

2,6-Naphthalenedicarboxylic acid, 3-(aminomethyl)pyridine, thionyl chloride, dimethylformamide (DMF), and the following ionic compounds were purchased from Sigma-Aldrich: NaOAc, NaNO<sub>3</sub>, NaClO<sub>4</sub>, NaBF<sub>4</sub>, CuBr, CuCl<sub>2</sub>, ZnCl<sub>2</sub>, NiCl<sub>2</sub>, FeCl<sub>2</sub>, FeCl<sub>3</sub>, Fe(NO<sub>3</sub>)<sub>3</sub>, Fe(ClO<sub>4</sub>)<sub>3</sub>, RuCl<sub>3</sub>, CdI<sub>2</sub>, MnCl<sub>2</sub>, PbI<sub>2</sub>, CuI, HgBr<sub>2</sub>, BeCl<sub>2</sub>, MgCl<sub>2</sub>, CaCl<sub>2</sub>, SrCl<sub>2</sub>, BaCl<sub>2</sub>, and Na<sub>2</sub>SO<sub>4</sub>. All materials were used as received without further



purification. Fluorescence experiments were performed on a Cary spectrofluorometer using a UV-quartz cuvette with a 1 cm path length. Thermogravimetric analysis for all compounds was done using a Diamond Pyris 6000 TGA/DTA apparatus from Perkin-Elmer from 30 °C to 850 °C under a N<sub>2</sub> flow at a heating rate of 5 °C min<sup>-1</sup>.

### Diffraction studies

Single-crystal data for **L1** were collected on a sealed tube Bruker APEX II CCD DIFFRACTOMETER equipped with a graphite monochromator. The single crystal data for **1** and **2**, respectively, was collected on a Bruker Venture Kappa geometry diffractometer equipped with a Gallium Liquid Metal Jet Source, a Photon 100 CMOS Detector, and a Helios MX mirror optics monochromator. The data collection for **L1** was done at 296 K using MoK $\alpha$  radiation ( $\lambda$  = 0.71073 Å), at 150 K for **2** using GaK $\alpha$  radiation ( $\lambda$  = 1.34139 Å) and at 100 K for **1** using CuK $\alpha$  radiation ( $\lambda$  = 1.54178 Å). The data were integrated with SAINT V8.38A and a multi-scan absorption correction using SADABS was applied. Diffraction data for **3** was collected on a Rigaku New Gemini four-circle diffractometer equipped with a fine-focus sealed X-ray tube and an EosS2 detector with a CCD plate. The data was integrated using CrysAlisPro 1.171.40.84a software and a multi-scan absorption correction was applied using spherical harmonics, implemented in SCALE3 ABSPACK scaling algorithm. The structures were solved with the SHELXT<sup>30</sup> structure solution program and refined with the SHELXL<sup>31</sup> refinement package using least squares minimization in a graphical user interface OLEX2.<sup>32</sup> All non-hydrogen atoms were refined with anisotropic displacement parameters, except atoms from the main framework that were disordered and atoms from disordered solvent molecules. The hydrogen atoms were refined isotropically on calculated positions using a riding model with their  $U_{iso}$  values constrained to 1.5 times the  $U_{eq}$  of their pivot atoms for terminal sp<sup>3</sup> carbon atoms and 1.2 times for all other carbon atoms. The sample selected for **1** turned out to be a two-component twin. The reflection data were integrated using both components. The best result was obtained with a single component integration dataset with an HKLF5 reflection file type generated using the TWINROTAT routine of PLATON<sup>26</sup> to account for the remaining second component contribution. One complete DMF molecule was located, but residual density sitting over the inversion centre in the middle of the unit cell could not be modelled properly. A solvent mask was calculated using the PLATON/SQUEEZE routine<sup>26</sup> adapted for twinned datasets, and 88 electrons were found in a volume of 324 Å<sup>3</sup> within a single void per unit cell. This is consistent with the presence of 2.2 DMF (C<sub>3</sub>H<sub>7</sub>NO) solvent molecules.

For compound **2**, some included DMF molecules were located and fully refined, but akin to **1**, the amount of residual electron density that cannot be properly modeled was accounted for by a solvent mask, which corresponds to

1441 electrons in a volume of 9906 Å<sup>3</sup> per unit cell. This is consistent with the presence of 36 DMF (C<sub>3</sub>H<sub>7</sub>NO) solvent molecules which account for 1440 electrons per unit cell.

In **3**, a disordered coordinated solvent position was assigned to EtOH and DMF molecules to give a total site occupancy of 1.0. Similarly, in the crystal lattice, an EtOH molecule has shown disorder, which was resolved by splitting and assigning the respective atoms two positions with a total site occupancy of 1.000. The thermal parameters and site occupancies for these disordered molecules were refined as free variables. Refinement of **3** showed a residual electron density peak of 1.35 e Å<sup>-3</sup> close to one of the methyl carbons of disordered ethanol molecules. An attempt to refine it as a methyl group of DMF molecules did not help as it led to an unstable refinement. Powder X-ray diffraction for **1**, before and after soaking in different metal ion solutions, was performed on a Bruker D8-Discover instrument ( $\theta$ - $\theta$  geometry) equipped with an XYZ platform and a HI-STAR gas detector. X-rays were generated using a conventional sealed-tube source with a copper anode producing CuK $\alpha$  radiation ( $\lambda$  = 1.54178 Å). The data collection involved acquisition of two different sections with increasing angular position, giving two different 2D frames. These frames were integrated and combined to produce the final 2D X-ray diffraction powder pattern. Powder patterns for **2** and **3** were recorded on a Rigaku New Gemini four-circle diffractometer equipped with a fine-focus sealed X-ray tube and an EosS2 detector with a CCD plate. CuK $\alpha$  radiation ( $\lambda$  = 1.54178 Å) was passed through a graphite monochromator for data collection. Powder patterns from single crystals were generated using Mercury software of the Cambridge Crystallographic Data Centre.<sup>33</sup> To verify the structural integrity of **1** after the sensing experiments, powder patterns were recorded after exposing to the highest concentration of some metal salts, which are given in Fig. S1† while the PXRD data for **2** and **3** are given in Fig. S2 and S3†. The BFDH morphologies showing the planes involved in the growth of crystal are given in Fig. S4† for **L1**, **1** and **2**.

### Photoluminescence studies

In all sensing experiments 1 mg of finely ground **1** was taken in 2 mL of DMF to minimize light scattering from the sample and to optimize the fluorescence signal. The mixture was sonicated for 40 minutes before being transferred to a UV-quartz cuvette with a 10 mm path length for analysis. For **L1**, 2 mL of 1 mM solution was taken for fluorescence studies. Emission spectra were acquired in the range 330 to 500 nm using an excitation wavelength of 265 nm on a Cary eclipse fluorescence spectrophotometer. The stability of the fluorescence signal manifests that the structural integrity of **1** was maintained in the presence of different analytes. To further verify that the material remains stable in the fluorescence titrations without any framework collapse, PXRD patterns were taken after subjecting **1** to the highest concentration of 10 mM solution of some metal salts for 10

minutes. The consistency of the PXRD peaks with as-synthesized material reveals the structural integrity of the material and hence no structure damage (Fig. S1†).

### Computational details

DFT calculations were performed using the ORCA quantum chemistry suite 4.2.1.<sup>34</sup> The geometry of **L1** and a model Co(II) complex was optimized using the hybrid PBE0 exchange–correlation function<sup>35</sup> with basis set def2-SVP.<sup>36</sup> The D3BJ empirical dispersion correction was used to evaluate the binding energies.<sup>37–39</sup> An additional polarized triple-zeta function def2-TZVP<sup>40</sup> with core effective potential was used for cobalt to account for relativistic effects. The auxiliary basis set used was def2/J.<sup>41</sup> Electrostatic potential was mapped on the electron isodensity surface of **L1** and Co(II) complex at 0.01 au using Avogadro software.<sup>42</sup>

### Synthesis of **L1**

In a 100 ml round bottom flask, a solution of 2,6-naphthalene dicarboxylic acid (4.6 mmol, 1.0 g) in  $\text{SOCl}_2$  (20 ml) was refluxed for 1 h at 90 °C. Dry toluene was added to the resulting clear solution and excess  $\text{SOCl}_2$  was removed by vacuum distillation. After the reaction mixture was cooled to room temperature, 3-aminomethyl pyridine (1000 mmol, 0.94 ml) and pyridine (731 mmol, 0.75 ml) were added to the reaction mixture and stirred for 1 h. The reaction mixture was left undisturbed for a few hours. The organic layer was washed with distilled water followed by a saturated solution of  $\text{NaHCO}_3$  five times and dried over  $\text{Na}_2\text{SO}_4$ . The crude product was recrystallized using MeOH, whereupon slow evaporation gave light colourless crystals of **L1**. Yield (82%). Anal. calc. for **L1** ( $396.4 \text{ g mol}^{-1}$ ), found (%): C, 72.79; H, 5.01; N, 14.19, requires (%): C, 72.71; H, 5.08; N, 14.13.  $^1\text{H}$  NMR (700 MHz, DMSO,  $\delta$  from TMS) (Fig. S5†):  $\delta_{\text{H}}$  9.35 (t, 1H,  $J = 5.9 \text{ Hz}$ ), 8.62 (s, 1H), 8.55 (s, 1H), 8.50 (m, 1H), 8.47 (m, 1H), 8.13 (d, 1H,  $J = 8.5$ ), 8.03 (dd, 1H,  $J = 8.5, 1.3$ ), 7.79 (d, 1H,  $J = 7.9$ ), 7.38 (dd, 1H,  $J = 7.8, 4.8$ ), 4.58 (d, 2H,  $J = 5.9$ ).  $^{13}\text{C}$  NMR (175 MHz, DMSO,  $\delta$  from TMS) (Fig. S6†):  $\delta_{\text{C}}$  166.74, 149.38, 149.34, 148.62, 148.58, 135.71, 135.48, 133.84, 133.45, 129.55, 127.80, 125.38, 124.00, 41.05. HRMS  $m/z$ , 396.167 [ $\text{M} + 1$ ]<sup>+</sup> (calc. 397.168). FT-IR ( $\text{cm}^{-1}$ ) (Fig. S7, Table S1†): 3105 (m), 1675 (s), 1575 (s), 1509 (s), 1171 (s), 727 (s).

### Synthesis of **1**, **2** and **3**

All the compounds were synthesized solvothermally in a capped dram vial. A mixture of **L1** (0.01 g, 0.025 mM for **1**, **2** and **3**), **H<sub>2</sub>BDC** (0.004 g, 0.025 mM for **1** and **3**) or **H<sub>3</sub>BDC** (0.011 g, 0.025 mM for **2**) and  $\text{Co}(\text{NO}_3)_2 \cdot 6\text{H}_2\text{O}$  (0.0184 g, 0.063 mM) for **1**,  $\text{Zn}(\text{NO}_3)_2 \cdot 6\text{H}_2\text{O}$  (0.0187 g, 0.063 mM) for **2**, and  $\text{Ni}(\text{NO}_3)_2 \cdot 6\text{H}_2\text{O}$  (0.0183 g, 0.063 mM) for **3** in 3 ml DMF was sealed in a 5 ml dram vial for 1 day in a normal heating oven at 80 °C. Next day, dark pink crystals for **1** (yield 76%), colourless crystals for **2** (yield 83%), and light green crystals for **3** (yield 59%) were obtained. All the samples were washed

with fresh DMF at least four times before doing further analysis.

Anal. calc. for **1** ( $1284.85 \text{ g mol}^{-1}$ ) found (%): C, 53.38; H, 4.07; N, 7.72, requires (%): C, 53.28; H, 4.16; N, 7.63. For **2** ( $3131.53 \text{ g mol}^{-1}$ ) found (%): C, 57.73; H, 3.73; N, 4.56, requires (%): C, 57.53; H, 3.93; N, 4.47. For **3** ( $816.30 \text{ g mol}^{-1}$ ) found (%): C, 59.41; H, 6.15; N, 7.53, requires (%): C, 59.53; H, 6.04; N, 7.65. FT-IR ( $\text{cm}^{-1}$ ) (Fig. S7, Table S1†): 3298 (m), 2936 (w), 1677 (s), 1509 (s), 1419 (s). For **2** (Fig. S8, Table S1†): 3057 (w), 1661 (s), 1591(w), 1520 (s), 1523 (s). For **3** (Fig. S7, Table S1†): 3343 (m), 1644 (s), 1587 (w), 1520 (s), 1440 (m), 1397 (w).

## Results and discussion

### Selection of the ligands

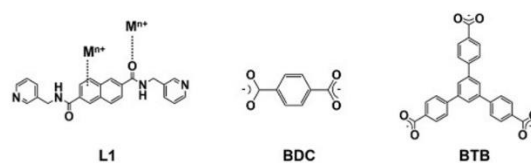
The rationale of using a mixed ligand system is twofold: (1) **L1** ligand has been chosen because it can potentially interact with the analytes through cation– $\pi$  (naphthalene ring) interactions and/or through amide oxygen (–CONH–) which would either lead to quenching or enhancement in fluorescence signal of the sensor (Scheme 1). In addition, **L1** imparts fluorescence properties to **1**, which renders this material useful in photoluminescence studies. Apart from this, the flexible nature of **L1** due to the presence of  $\text{sp}^3$  carbons (–CH<sub>2</sub>–) can render free orientation of the ligand to facilitate more sensor–analyte interactions. On the other hand, **H<sub>2</sub>BDC**/**H<sub>3</sub>BTB** ligands on deprotonation stabilize the +2 charge on metal ions, provide rigidity to the framework and extend its dimensionality (Scheme 1).

### Coordination modes of ligands

The coordination modes shown by the above ligands in the complexes discussed in this work are shown in Scheme 2.

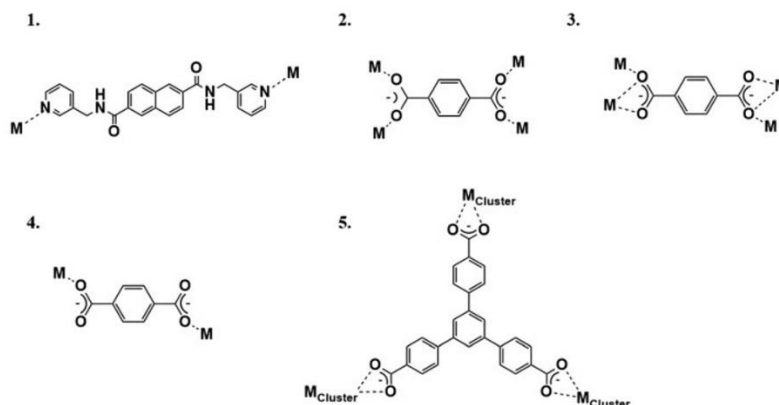
### Structure of **L1**

The crystal structure shows that **L1** is centrosymmetric with the centre of inversion lying on a C–C bond naphthalene ring (Fig. S9a†). The amide side arms are slightly twisted out of plane with respect to the naphthalene ring as apparent from a dihedral angle of 37° (Fig. S9b†). In the crystal lattice, pyridine and amide moieties undergo extensive hydrogen bonding using  $\text{R}_2^2(22)$ ,  $\text{R}_2^1(7)$ , and  $\text{R}_2^3(8)$  synthons and  $\text{C}_2^2(22)$  graph set to yield a 3D framework (Fig. 1).



Scheme 1 Molecular structures of ligand **L1** and deprotonated forms of carboxylic ligands with corresponding codes.





**Scheme 2** Coordination modes shown by the ligands (1) ( $\mu_2\text{-}\kappa^2\text{-}\eta^1\text{-}\eta^1$ ) in all complexes, (2) ( $\mu_4\text{-}\kappa^4\text{-}\eta^1\text{-}\eta^1\text{-}\eta^1\text{-}\eta^1$ ) in complex **1**, (3) ( $\mu_4\text{-}\kappa^4\text{-}\eta^1\text{-}\eta^1\text{-}\eta^2\text{-}\eta^2$ ) in complex **1**, (4) ( $\mu_2\text{-}\kappa^2\text{-}\eta^1\text{-}\eta^1$ ) in complex **3**, and ( $\mu_3\text{-}\kappa^6\text{-}\eta^1\text{-}\eta^1\text{-}\eta^1\text{-}\eta^1\text{-}\eta^1\text{-}\eta^1$ ) in complex **2**.

### Structure of 1

Single-crystal analysis illustrated a three-dimensional coordination framework of **1**. The asymmetric unit of **1** contains two dimeric units composed of four unique Co(II) ions, viz. Co1, Co2, Co3 and Co4 (Fig. 2a and S10†).

In the first unit, Co(II) ions (Co3 and Co4) are linked by two unique and a centrosymmetric BDC ligand, while in the second unit, Co1 and Co2 are connected by two BDC ligands, a unique and a centrosymmetric ligand (Fig. 2a). These dimeric units are further held together by a  $\mu_4$ -bridged BDC molecule to form a Co<sub>4</sub> (BDC) metallic unit (Fig. 2a). Within each metallic unit, a centre of inversion is present on Co1 and Co3 ions, which resulted in the transformation of dimeric units (composed of Co1 or Co3) to centrosymmetric trimeric units (Fig. 2b). These trimeric units are further linked to nearby units by L1 and BDC molecules in the framework (Fig. 2b). In each trimeric unit, Co(II) ions are in a distorted octahedral environment granted by six BDC molecules in the case of Co1 and Co3, whereas three BDC

molecules, L1 and a DMF molecule grant a distorted octahedral geometry to Co2 and Co4 ions (Fig. 2c). A 2D sheet of trimeric units is formed by  $\mu_4$ -bridged BDC molecules (Fig. 2d), which is connected to adjacent sheets by a  $\mu_2$ -bridged L1 molecule to form a 3D framework (Fig. 3a and b). Topologically,<sup>43</sup> the framework has a 4-nodal net with stoichiometry (4-c)(4-c)2(4-c)2(6-c) (Fig. 3c).

### Structure of 2

Eight unique Zn atoms present in an asymmetric unit with Zn1, Zn2, Zn3 and Zn4 form a tetranuclear cluster, which is connected to neighbouring Zn5, Zn6, Zn7 and Zn8 ions by three BTB molecules (Fig. S11†). The crystal structure of **2** is composed of two tetranuclear clusters, i.e. cluster 1 comprising Zn1, Zn2, Zn3 and Zn4 ions and cluster 2 with Zn5, Zn6, Zn7 and Zn8 ions, which are linked to each other by six  $\mu_3$ -bridged BTB molecules and one  $\mu_2$ -bridged L1 molecule (Fig. S11†). Among the Zn(II) ions, Zn1, Zn2, Zn3,

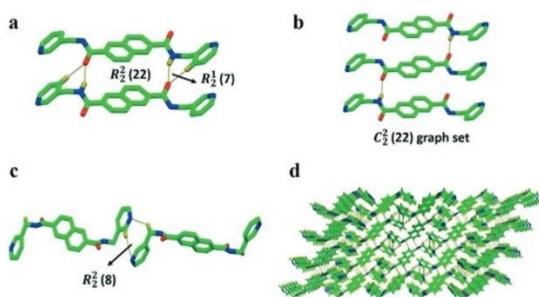


**Fig. 1** Pictorial presentation of (a) ring synthons involving amide moieties, (b) catemer synthons, (c) ring synthons involving pyridine rings and (d) 3D hydrogen bonded framework in L1. Colour codes – carbon: green, nitrogen: blue, oxygen: red.

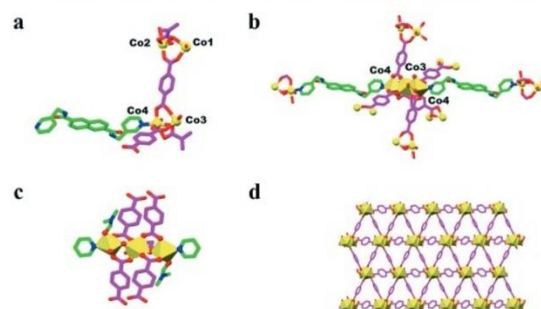


**Fig. 2** Pictorial depiction of (a) asymmetric unit in the structure of **1**, (b) trimeric unit surrounded by L1 and BDC molecules, (c) coordination environment around Co3 and Co4 and (d) pictorial depiction of 2D coordination sheet of trimeric units. Colour codes in L1, carbon: green, and in BDC, carbon: magenta and nitrogen: blue, oxygen: red, cobalt: yellow.

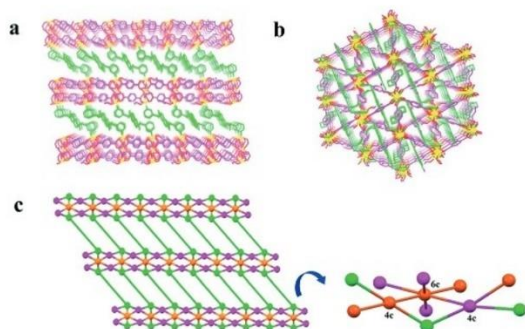


Fig. 3 Perspective view of 3D framework parallel to (a) the *bc* plane and (b) the *ac* plane and (c) the topological view of the framework of complex 1. Colour codes – L1: green, BDC: magenta, and cobalt in yellow/orange in the topology picture (c).

Zn7 are tetracoordinated (orange colour), whereas Zn5, Zn6 and Zn8 are pentacoordinated (cyan) (Fig. 4a). Zn4 is the only ion that is hexacoordinated (yellow, Fig. 4a). The octahedral coordination environment around Zn4 can be described as follows. The square planar arrangement around Zn4 is provided by three unique BTB molecules using O3, O4 and O7 atoms and an O10 atom of a DMF molecule, while the axial sites are occupied by an O1 atom which is bridged in a tetramer formed by four Zn atoms and a pyridinic N4 atom of an L1 molecule. The coordination environment around the Zn5 ion is trigonal bipyramidal ( $\tau = 0.8$ ), whereas it is square pyramidal in Zn6 and Zn8 (cyan) ( $\tau = 0.53, 0.39$ ). Two different cyclic chains generating metallacycles, viz. 62 ( $\sim 23 \times 24$  Å) and 72 ( $\sim 16 \times 32$  Å) membered, grant a twofold interpenetrated net-type structure to Zn-CP (Fig. 4b and c). In the crystal lattice, the tetranuclear clusters are linked to each

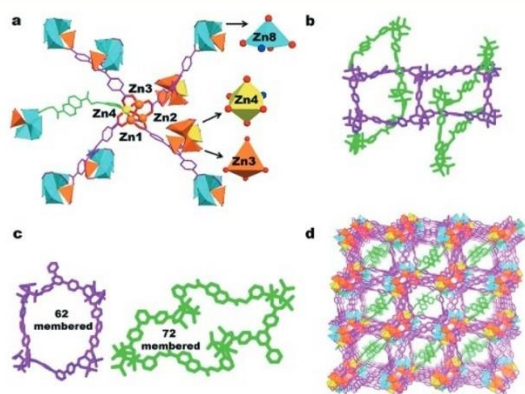


Fig. 4 (a) Different coordination geometry around Zn(II) ions, (b) and (c) interpenetrated chains and corresponding macrocycles generated along the framework, and (d) pictorial presentation of 3D framework of complex 2. Colour codes – L1: green, BTB: purple and zinc in yellow (octahedral), cyan (square pyramidal or trigonal bipyramidal) and orange (tetrahedral).

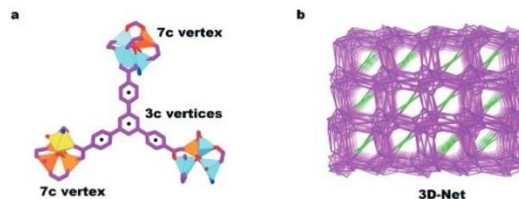


Fig. 5 (a) 3- and 7-branch points and (b) topological view of the 3D net of complex 2

other by L1 and BTB molecules to form a 3D coordination framework (Fig. 4d).

Topological analysis shows that the structure consists of a tritopic ligand BTB with four 3-c branch points or the linker with four 3-c nodes linked to two  $\text{Zn}_4\text{O}(\text{CO})_6\text{N}$  metal SBUs with seven points of extension to give a (3,7)-c net. The topology<sup>43</sup> can be best described as a 7-c vertex linked to 6 (3-c) vertices and one 7-c vertex with minimum transitivity (3,2) (Fig. 5a). Topologically, the 3D framework is a 3,7-c net in clusters which is the representation of valence-bonded MOFs having stoichiometry (3-c)2(7-c). The point symbol for the net is  $\{4^2\cdot 2\cdot 6\}2\{4^4\cdot 6^6\cdot 8^8\cdot 10\cdot 10\}$ . The topographic view of the framework parallel to the *ab* plane is shown in Fig. 5b.

### Structure of 3

The crystal structure of 3 shows that in the asymmetric unit, the Ni(II) ion is coordinated to a half L1, half BDC, and a disordered solvent molecule (DMF/EtOH with a total sof of 1) (Fig. S12†). A disordered ethanol molecule is crystallized as solvent of crystallization. In addition to this, a centre of inversion is passing through a Ni(II) ion, a naphthalene ring of L1 and a benzene ring of BDC ligand about which a centrosymmetric complex is generated comprising three symmetry-related Ni(II) ions connected to each other by  $\mu_2$ -bridged L1 and BDC ligands (Fig. 6a). The octahedral coordination geometry around each Ni(II) ion is granted by symmetry-related L1, BDC and a disordered solvent molecule (DMF/EtOH). In the crystal lattice, adjacent Ni(II) ions are connected in a 1D chain by BDC molecules, which act as a 2c linker. The neighbouring 1D chains are further interlinked to each other by L1 (2c linker) molecules in a pattern – chain 1 of row 1 to chain 2 of row 3 and so on – to weave a 3D coordination framework. Topological analysis illustrates that the structure consists of (1 2  $\bar{1}$ ) layers containing 4c-uninodal metal nodes with point symbol  $\{4^4\cdot 6^6\cdot 2\}$  and sql/Shubnikov tetragonal plane net-type topology. Pertinent bond lengths and angles for all these complexes are given in Table S2.†

A summary of the metal–ligand combination used, coordination mode of the ligands and the related framework topologies are tabulated in Table 1.

### Thermal stability

The thermal stabilities of compounds 1–3 and ligand (L1) were studied in the temperature range from 30 °C to 850 °C



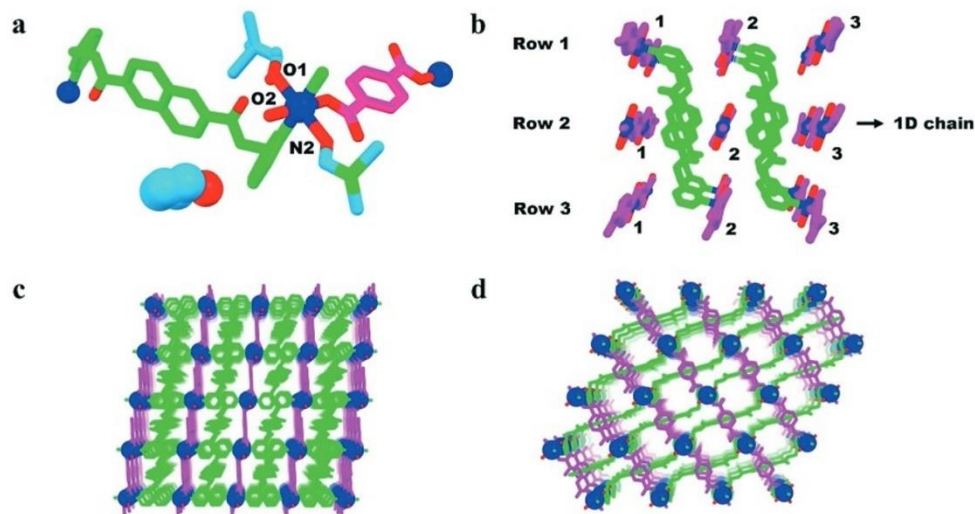


**Fig. 6** (a) Picture showing a centrosymmetric unit of **3**, (b) pictorial presentation of the linkage of 1D chains, (c) perspective view of 3D coordination framework parallel to the *ab*- and (d) *ac*-planes. Colour codes – L1: green, BDC: magenta, nickel: blue.

**Table 1** Summary of the metal–ligand combination used, coordination mode of the ligands and the related framework topologies of complexes **1–3**

Compound	Ligand 1	Ligand 2	Coordination modes	Dimensionality	Topology
1			2-C, 4-C	3D	4-Nodal net
2			2-C, 3-C	3D	3,7-c net
3			2-C, 2-C	3D	4c-Uninodal

using thermogravimetric analysis (TGA) (Fig. S13†). The thermal decomposition curve for **L1** shows 9% weight loss around 90 °C that corresponds to the loss of one methanol molecule (theoretical loss 8.2%) followed by complete decomposition at 425 °C. Compound **1** was stable up to ~150 °C with the first weight loss of 17.5% at 203 °C corresponding to the loss of two coordinated and a lattice DMF molecule (theoretical loss 17.3%). Next, the weight loss of 9.6% till 389 °C can be attributed to loss of one **BDC**

molecule followed by complete decomposition at ~600 °C leading to the formation of cobalt oxide residues. In the case of **2**, gradual decomposition was observed from 50 °C onwards with 28.8% weight loss at 125 °C corresponding to the loss of six DMF molecules and an **L1** molecule (theoretical loss ~27.5%). Following this, complete decomposition was observed at 585 °C. Compound **3** has started decomposing at 70 °C to give a weight loss of 24% at 295 °C that corresponds to the loss of coordinated DMF

molecules and a lattice ethanol molecule (theoretical loss ~23.5%). The next weight loss of 13% at 375 °C might be due to the decomposition of a BDC molecule. Following this, complete decomposition of the complex takes place at 600 °C to yield nickel oxide residues.

### Photophysical studies

To probe the ion sensing ability of Co-MOF (**1**) towards various cations and anions, fluorescence experiments were performed.<sup>44</sup> In the sensing experiments, homogenous dispersion of the sample, its long-term stability in the solvent and consistency in its fluorescence emission are some important factors that need to be considered. In addition, the emission from the fluorophores is sensitive to the polarity of the solvent.<sup>45</sup> Thus, to ascertain the effect of different solvents on the emission signal of **1** and its stability and to find out the optimal solvent for sensing, we performed the initial screening using different solvents (Fig. 7). Prior to screening, the material was soaked in different solvents for a few hours and after that the emission was measured. It was observed that only in strongly coordinating solvents, *viz.* ACN and DMF, a characteristic emission peak at 368 nm was observed (Fig. 7). Among these, DMF was chosen for the experiments owing to even dispersion of **1** and long-term stability of its suspension (>10 min). Conversely, in the case of dichloromethane, chloroform and ethyl acetate, multiple different emission wavelengths were observed, suggesting that fluorescence occurred *via* multiple relaxation pathways. No emission was observed in the case of benzene and toluene (Fig. 7) because the sample was not well dispersed (based on the visual observation). Alcoholic solvents and water as well were excluded for such studies because leaching of Co(II) ions was observed, which led to decomposition of the framework.

Emission spectra of **L1** and **1** were acquired from 330 to 500 nm using an excitation wavelength of 265 nm on a Cary

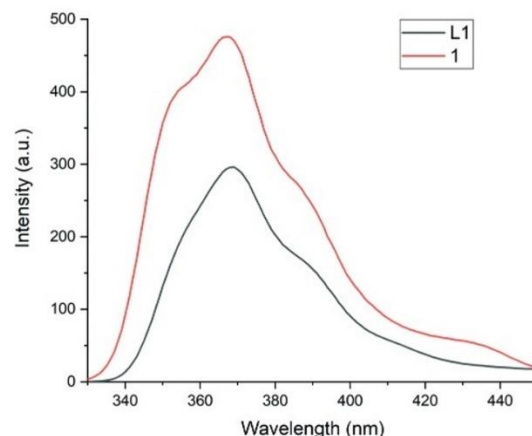


Fig. 8 Emission spectra of **L1** and **1**.

Eclipse fluorescence spectrophotometer. For **L1**, the spectrum was recorded in the solution state because it is soluble in DMF (Fig. 8). The emission spectra of **L1** showed two peaks, an intense peak at 368 nm due to intraligand  $\pi-\pi^*$  transitions and a weak shoulder at 392 nm due to  $n-\pi^*$  transitions. Compound **1** has shown similar emission, demonstrating that the emission is dominated by the **L1** ligand when it is excited at 265 nm (Fig. 8). In addition, an increase in fluorescence intensity was observed because immobilization of **L1** prevents energy losses due to its rotational and/or translational motions resulting in fluorescence enhancement of **1**.

### Theoretical studies

To further investigate the frontier molecular orbitals (FMOs) involved in electronic transitions, we have performed DFT calculations on **L1** and a model Co(II) complex containing a combination of **L1** and protonated **HBDC** molecules. Due to the complexity of **1**, the model complex was chosen to simplify the system, to speed up the calculation and to obtain information about the excited state involved in electronic transitions (Fig. 9). It is apparent from Fig. 9 that the excited state of **L1** is dominated by naphthalene and carbonyl moieties, while the ground state involves only the naphthalene moiety. The corresponding bandgap between the excited and the ground state was found to be 4.8 eV, which corresponds to the absorption by **L1** at 265 nm. In the case of the model complex, the excited state is dominated by both naphthalene and carbonyl moieties akin to **L1**. The bandgap calculated for this system was 4.27 eV. These results can be assumed to support the trend observed in fluorescence studies that the excited state of **1** from which emission takes place after excitation at ~265 nm is primarily dominated by **L1** molecules. These findings can be utilized to illustrate that after the addition, the analyte ions can interact with Co-MOF (**1**) at the naphthalene and carbonyl moieties of

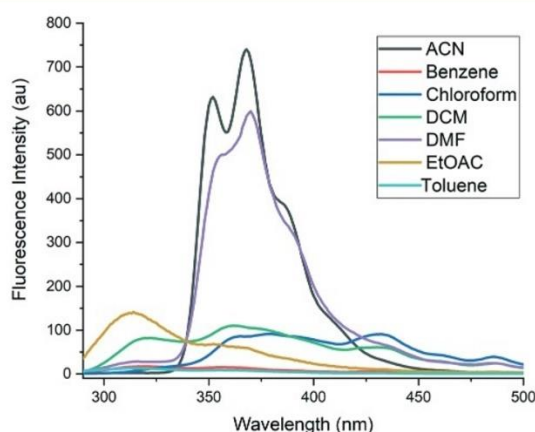


Fig. 7 Fluorescence emission of **1** in different solvents.

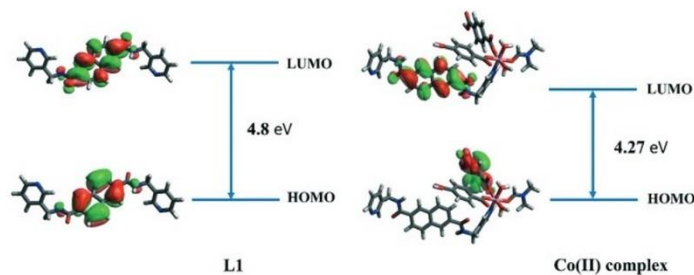


Fig. 9 Frontier molecular orbitals of **L1** and the model Co(II) complex, respectively, and the associated bandgaps.

**L1** to cause fluorescence quenching. The MEP plot (Fig. S14a†) for **L1** shows that the regions of high electron density (red colour) are located on the amide oxygen and the naphthalene ring, indicating that metal cations (electrophiles) can potentially interact with these electron-

rich sites. Thus, it may be concluded that compound **1** can interact with  $M^{n+}$  ions probably through **L1** via cation- $\pi$ <sub>naphthalene</sub> or  $M^{n+} \cdots O_{\text{amide}}$  interactions or both. The MEP plot of the model Co(II) complex with the respective regions of electron densities is shown in Fig. S14b.†

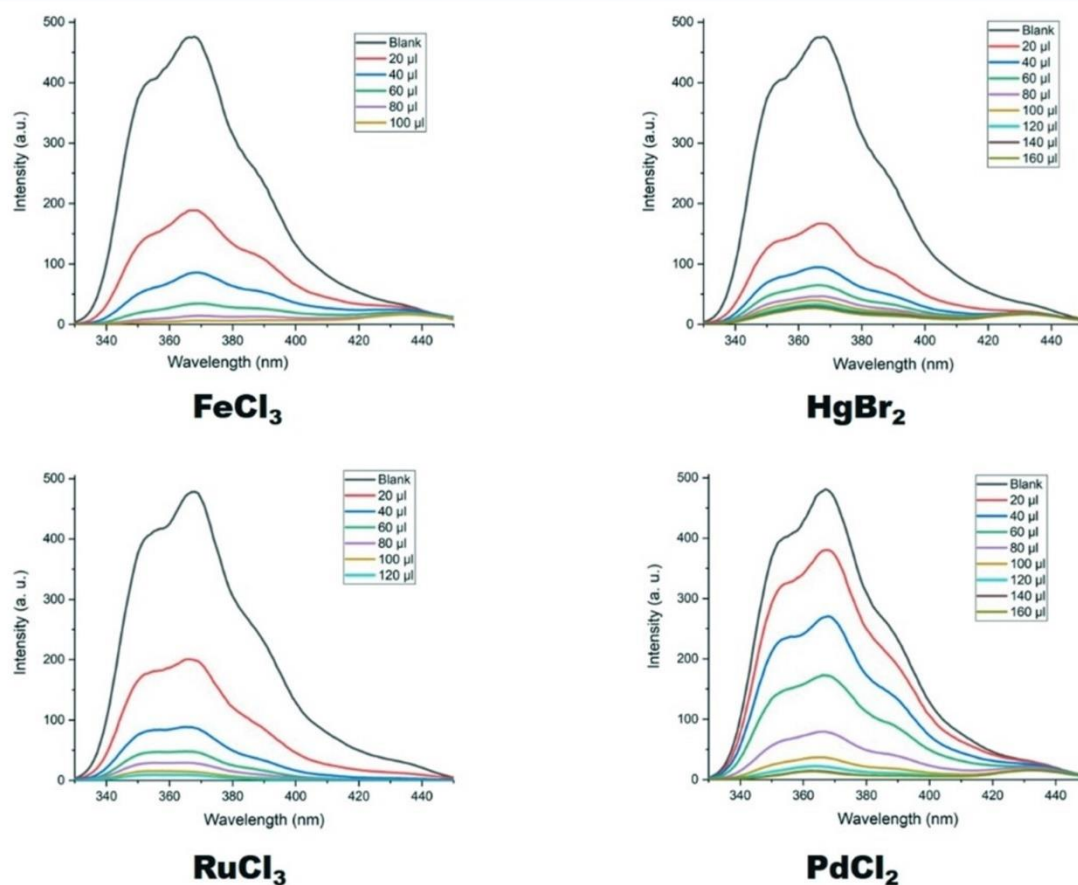


Fig. 10 Quenching of fluorescence intensity of **1** by different metal ions (note: blank refers to the emission from **1** before the addition of analytes).



## Sensing experiments

To explore the sensitivity of **1** towards different metal ions, suspension steady-state photoluminescence (PL) studies were performed. To further investigate if the associated counter anions interfere with the changes in emission intensity of the material, fluorescence studies were performed using different counter anions. In all experiments, 1 mg of **1** in 2 ml of DMF was taken to minimize light scattering because of its solid nature. The heterogeneous solution was sonicated for at least 40 minutes to obtain evenly dispersed particles of compound **1** which was then transferred to a quartz cuvette. Solutions at 10 mM concentration of different  $M^{n+}$  ions (where  $M = \text{Fe}, \text{Cu}, \text{Na}, \text{Be}$  and so on, and  $n = \text{oxidation state}, +1, +2 \text{ and } +3$ ) in DMF were titrated with the suspension of **1** successively in 20, 40, 60, 80, 100, 120, 140  $\mu\text{L}$  aliquots and so on, and the changes in fluorescence intensity were observed. After the addition of analyte to the suspension of **1**, the mixture was agitated. The whole process of addition, agitation and detection took approximately 2 minutes; thus the detection was rapid. Apart from these experiments, the **L1** molecule was also tested with different metal ions for comparison. Various interactions between the sensor and the analytes that are responsible for the observed trends in variation of fluorescence intensity are explained using the concept of "crystal engineering".<sup>27–29</sup>

Metal  $M^{n+}$  sensing using PL studies

$M^{n+}$  salts used for sensing are  $\text{BeCl}_2$ ,  $\text{FeCl}_2$ ,  $\text{FeCl}_3$ ,  $\text{Fe}(\text{NO}_3)_3$ ,  $\text{Fe}(\text{ClO}_4)_3$ ,  $\text{NiCl}_2$ ,  $\text{MnCl}_2$ ,  $\text{CuCl}_2$ ,  $\text{Cu}(\text{NO}_3)_2$ ,  $\text{CuBr}$ ,  $\text{PbCl}_2$ ,  $\text{ZnCl}_2$ ,  $\text{CdI}_2$ ,  $\text{Cd}(\text{NO}_3)_2$ ,  $\text{HgBr}_2$ ,  $\text{RuCl}_3$  and some alkaline earth metals.

On addition of a 20  $\mu\text{L}$  aliquot of analyte, a decrease in the intensity of the fluorescence signal was observed for  $\text{Cu}^{+2}$ ,  $\text{Co}^{+2}$ ,  $\text{Cu}^{+1}$ ,  $\text{Fe}^{+2}$ ,  $\text{Pb}^{+2}$ , and  $\text{Cd}^{+2}$  ions (Fig. S15†), but it was much pronounced for  $\text{Pd}^{+2}$ ,  $\text{Fe}^{+3}$ ,  $\text{Ru}^{+3}$ , and  $\text{Hg}^{+2}$  ions (Fig. 10). Subsequent addition of analytes in the 40, 60, 80, 100, 120, 140, 160, 180  $\mu\text{L}$  aliquots and so on resulted in rapid and complete turn off in fluorescence intensity for  $\text{Fe}^{+3}$  and  $\text{Ru}^{+3}$  ions at  $\sim 100 \mu\text{L}$  and 96% for  $\text{Hg}^{+2}$  at 160  $\mu\text{L}$  and 98% for  $\text{Pd}^{+2}$  at 160  $\mu\text{L}$  (Fig. 10), whereas 98% fluorescence quenching for the  $\text{Cu}^{+2}$  ion,  $\sim 93\%$  for  $\text{Cd}^{+2}$  and  $\text{Pb}^{+2}$  ions and 85% for the  $\text{Cu}^{+1}$  ion at  $\sim 300 \mu\text{L}$  was observed (Fig. S15†). Although these ions are potentially good at quenching and have shown excellent quenching efficiency ( $>85\%$ ), the volume of the analyte required was very large when compared to  $\text{Pd}^{+2}$ ,  $\text{Fe}^{+3}$ ,  $\text{Ru}^{+3}$ , and  $\text{Hg}^{+2}$  ions. Thus, it can be inferred that **1** is highly sensitive to the latter ions and hence can be used for rapid detection of the same.

This trend can be visualized by comparing the quenching efficiencies of different analytes after five additions (100  $\mu\text{L}$ ) of 20  $\mu\text{L}$  each (Fig. 11). Based upon these findings, the Stern–Volmer equation was used to calculate  $K_{\text{sv}}$  values for **1** towards  $\text{Fe}^{+3}$ ,  $\text{Ru}^{+3}$ , and  $\text{Hg}^{+2}$  ions in the concentration range of 20 to 260 ppm, which were found to be 9126, 8987 and 7219  $\text{M}^{-1}$ , respectively (Fig. S16†). For  $\text{Ni}^{+2}$ ,  $\text{Fe}^{+2}$ , and  $\text{Co}^{+2}$

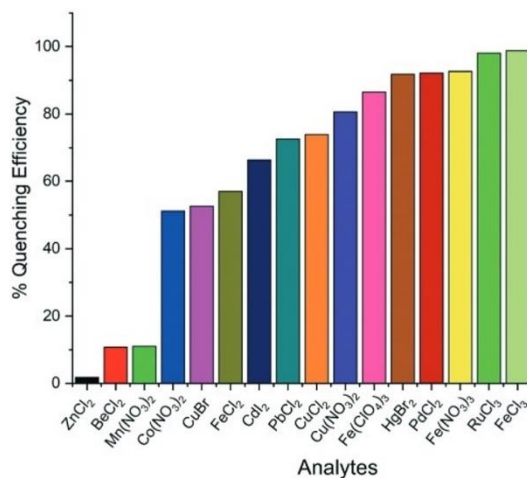


Fig. 11 Comparison of quenching efficiency of analytes after the first five additions to the suspension of **1**.

ions, saturation in quenching efficiency at 57%, 79% and 64%, respectively, was observed (Fig. S15 and S17†), while negligible or no response was observed for  $\text{Be}^{+2}$ ,  $\text{Zn}^{+2}$  and  $\text{Mn}^{+2}$  ions, suggesting that **1** is insensitive to these ions (Fig. S17†). Relative quenching efficiencies of different analytes are summarized in the graph of % quenching efficiency vs. volume of analyte (in  $\mu\text{L}$ ) (Fig. 12).

Anion  $A^{n-}$  sensing using PL studies

In the metal ion sensing studies, especially for  $\text{Fe}(\text{III})$  and  $\text{Cu}(\text{II})$  ions, different metal salts were studied in order to probe the effect of counter anions on the fluorescence quenching of **1** (Fig. S18†). After the first addition of 20  $\mu\text{L}$ , it was found that 30% to 60% quenching was observed on

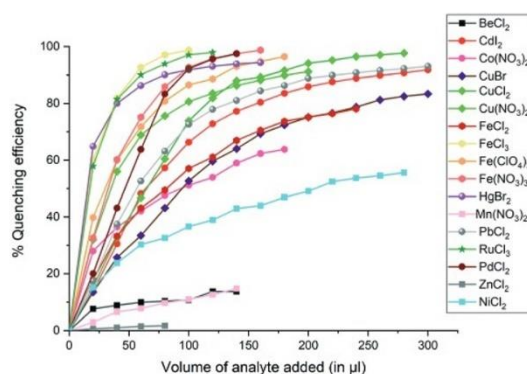


Fig. 12 Percent quenching efficiency of various analytes after some additions. Note that the sample was excited at 265 nm and the emission was observed at 378 nm.

## Paper

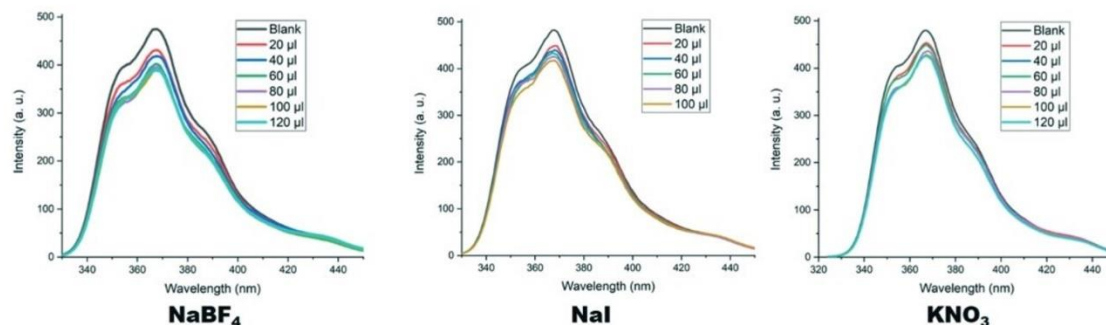


Fig. 13 Fluorescence intensity change upon addition of  $\text{NaBF}_4$ ,  $\text{NaI}$  and  $\text{KNO}_3$  to a suspension of **1** (note: blank corresponds to the emission from **1** before the addition of analytes).

varying the  $\text{Fe(III)}$  metal salts with 33% quenching using  $\text{NO}_3^-$ , 40% using  $\text{ClO}_4^-$ , and 60% with  $\text{Cl}^-$  salts (Fig. S18†). Similarly, 15% and almost double (32%) quenching in fluorescence signal was observed by using  $\text{Cl}^-$  and  $\text{NO}_3^-$  salts, respectively, of  $\text{Cu(II)}$  ions (Fig. S18†). These results indicate that the counter anions can affect the quenching of the fluorescence intensity of **1**, which encouraged us to perform sensing studies with anions. We have chosen some salts of sodium and potassium as anion sources, *viz.*  $\text{NaNO}_3$ ,  $\text{NaBF}_4$ ,  $\text{NaI}$ ,  $\text{Na}_2\text{SO}_4$ ,  $\text{NaClO}_4$ ,  $\text{KNO}_3$ ,  $\text{KBr}$ , and  $\text{KSCN}$ , for fluorescence titration experiments. The concentration of these ion-containing solutions in DMF was set to 10 mM, and a small (less than 200  $\mu\text{L}$ ) amount of water was also used to dissolve the salts. For these experiments too, 1 mg of **1** in 2 mL DMF was sonicated for 40 minutes, and the suspension was carefully pipetted into a new vial for further use. Next, these solutions were titrated in the following aliquots: 20, 40, 60, 80, 100 and 120  $\mu\text{L}$ . A noticeable decrease in fluorescence intensity was observed upon the addition of  $\text{BF}_4^-$ ,  $\text{I}^-$ , and  $\text{NO}_3^-$  ions (Fig. 13), whereas negligible to no response was observed using  $\text{ClO}_4^-$ ,  $\text{Br}^-$ ,  $\text{SCN}^-$ , and  $\text{SO}_4^{2-}$  ions (Fig. S19†).

#### Metal ion sensing using **L1**

Fluorescence studies have illustrated that the emission from **1** is dominated by the **L1** molecule, which signifies that sensor-analyte interactions could take place principally at the **L1** molecule. Thus, it is preferable to study the behaviour of the ligand molecule alone towards various analytes and see how the ligand behaves when it is free or uncoordinated. We have tested  $\text{FeCl}_3$ ,  $\text{HgBr}_2$ ,  $\text{CuCl}_2$ , and  $\text{CdI}_2$  salts for the fluorescence titrations with **L1** solution. Among these  $\text{M}^{n+}$  salts, a consecutive decrease in intensity was observed with the addition of  $\text{Fe}^{+3}$  ions that led to 50% quenching of intensity after the first five additions in the 20, 40, 60, 80 and 100  $\mu\text{L}$  aliquots (Fig. 14). The addition of  $\text{Hg}^{+2}$ ,  $\text{Cu}^{+2}$ , and  $\text{Cd}^{+2}$  ions does not cause a drastic change in fluorescence intensity, which is  $\sim 15\%$  at 100  $\mu\text{L}$  addition (Fig. 14). Although like **1**, the ligand is also responsive to  $\text{Fe}^{+3}$  ions than other ions, the number of additions required were more

( $\sim 100 \mu\text{L}$ ) in the case of **L1**. In contrast, an extensive decrease in fluorescence intensity was observed for **1** than **L1** after the first addition (20  $\mu\text{L}$ ). The highly responsive nature of **1** towards  $\text{Fe}^{+3}$  ions can be explained by the fact that after coordination to  $\text{Co(II)}$  ions, the ligand molecules (**L1**) are immobilized in a favourable orientation in the framework, which maximizes interactions with analyte ions.

Thus, it can be concluded that the observed rapid response of **1** towards  $\text{Fe}^{+3}$  ions might be due to the very responsive nature of **L1** molecules towards these ions.

#### Proposed mechanism of sensor-analyte interactions affecting fluorescence intensity

Metal ion sensing experiments illustrated that **1** is responsive to most of the metal ions, therefore it can be considered as a versatile chemo-sensor material. The responsive nature of **1** toward various analytes can be explained based on hard-soft acid and base (HSAB) principles, which illustrate that hard acid prefers to interact with hard base and soft acid with soft base.<sup>46</sup> Compound **1** contains **L1** and **BDC**, and within these ligands the core motifs, *viz.* benzene ring, naphthalene ring and carbonyl groups of amide and carboxylic groups, are borderline Lewis bases. Because of the presence of these borderline bases, **1** is sensitive to most of the metal ions and hence acts as a versatile chemo-sensor. Moreover, theoretical and fluorescence studies have elucidated that the excited state and the emission from **1** is dominated by **L1**. Hence, diminished fluorescence intensity of **1** after the addition of different metal ions is supposed to occur by the interaction of different metal ions with carbonyl or naphthalene moieties or both of **L1**. Due to their flexible nature, the adjacent **L1** molecules in the framework orient themselves in a way so as to have concomitant  $\text{M}^{n+} \cdots \text{O}_{\text{amide}}$  (Lewis-base) and  $\text{M}^{n+} \cdots \pi$  interactions<sup>24</sup> with different metal ions (Fig. 15), which alters the fluorescence signal of **1**. The highly sensitive nature of **1** towards  $\text{Fe}^{+3}$ ,  $\text{Ru}^{+3}$ , and  $\text{Hg}^{+2}$  ions than other ions might be due to the high affinity of its recognition sites (**L1** molecules) for these ions, which led to high influx or diffusion of them even at low concentrations towards accessible parallelogram-



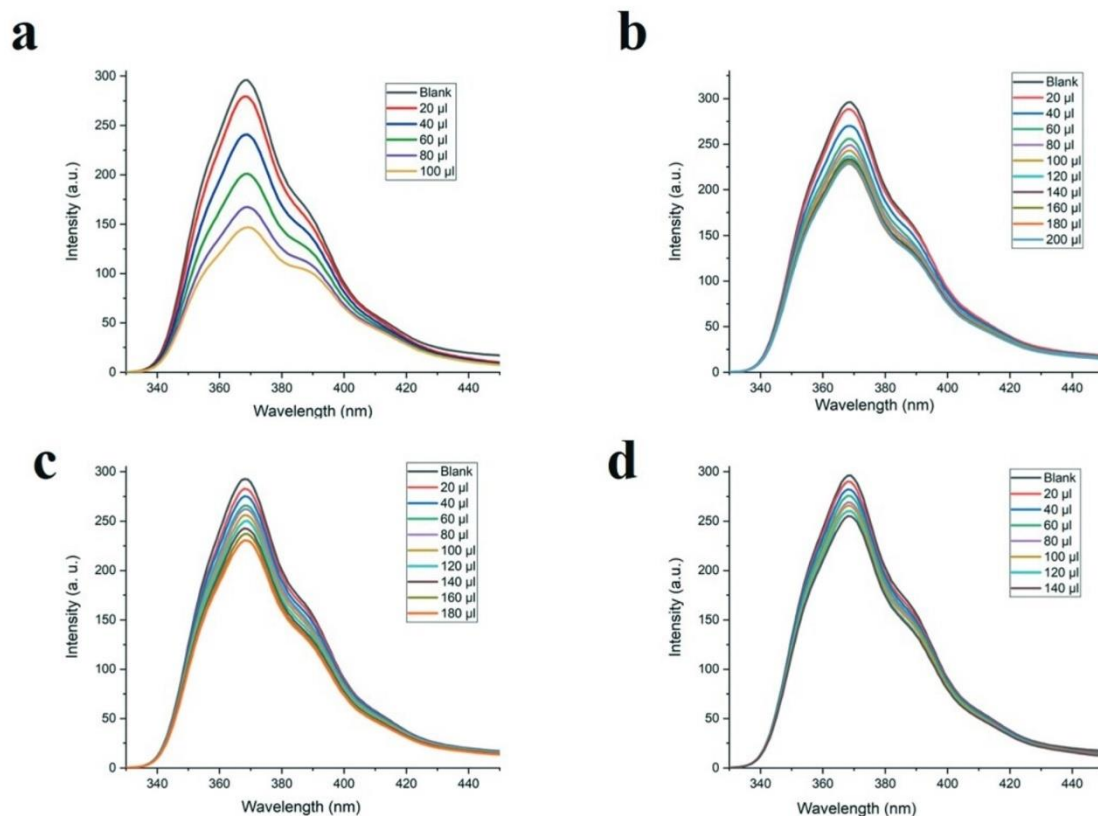


Fig. 14 Fluorescence intensity change upon addition of (a)  $\text{FeCl}_3$ , (b)  $\text{HgBr}_2$ , (c)  $\text{CuCl}_2$ , and (d)  $\text{CdI}_2$  to **L1** solution (note: blank corresponds to the emission from **1** before the addition of analytes).

shaped pores to concentrate ions to a high level. These trapped ions can now interact with **1** via the aforementioned

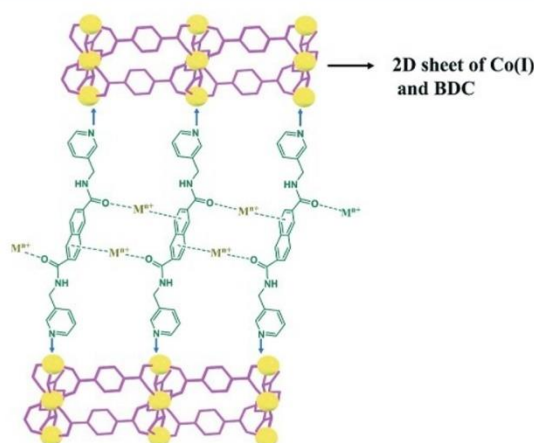


Fig. 15 Tentative mechanism of the sensor-analyte interactions proposed for **1** with different metal ions.

interactions, resulting in the quenching of the fluorescence signal. In the case of  $\text{Pd}^{+2}$ ,  $\text{Cu}^{+2}$ ,  $\text{Cd}^{+2}$ ,  $\text{Pb}^{+2}$  etc., the diffusion of ions increases at high concentration of analytes as apparent from the large number of additions,  $\sim 160 \mu\text{l}$  for  $\text{Pd}^{+2}$  and  $280 \mu\text{l}$  for the rest. Saturation in the fluorescence quenching was observed in the case of  $\text{Ni}^{+2}$ ,  $\text{Co}^{+2}$ , and  $\text{Fe}^{+2}$ , indicating that the accessible volume of **1** is fully drenched with ions while not a very negligible response was observed towards  $\text{Be}^{+2}$ ,  $\text{Mn}^{+2}$ , and  $\text{Zn}^{+2}$  ions.

In **1**, trimeric units with two coordinatively unsaturated  $\text{Co(II)}$  sites (occupied by DMF molecules) can be assessed by anions in a fluorescence titration experiment. The interaction of anions with the open coordination sites of  $\text{Co(II)}$  ions can be explained on the basis of polarizability and anisotropy in the distribution of electron densities on  $\text{Co(II)}$  ions. It is a well-known fact that metal ions with partially filled d-orbitals can undergo electronic interaction with organic linkers by participating in ligand to metal charge transfer (LMCT)-based transitions, which intensifies the electron densities on the metal ion. Conversely, the displacement of these electron densities towards ligand (or  $\pi$ -acceptor) molecules generates partially electron-deficient sites on the  $\text{Co(II)}$  ions, which can

## Paper

then lure anions. Thus, minor changes in the fluorescence signal of **1** upon addition of different anions can be attributed to the same reason. In general, the most reasonable hypothesis for fluorescence quenching is either (1) the energy transfer from donor (compound **1**) to acceptor in a bimolecular excited state or (2) bimolecular excited states involving electron or energy transfer from excited donor to nonexcited analyte ions or quenchers.<sup>47</sup>

## Conclusion

In the present study, three new mixed ligand coordination compounds of Co(II) **1**, Zn(II) **2** and Ni(II) **3** were synthesized using solvothermal methods and characterized by various analytical techniques. Due to the presence of some pores (SOVs) and stable fluorescence emission, compound **1** was investigated for its sensing ability. Although **1** has shown some response to different metal ions during fluorescence titrations, the response is much more pronounced for Hg<sup>2+</sup>, Fe<sup>3+</sup>, and Ru<sup>3+</sup> ions. The highly sensitive nature of **1** towards these ions than others might be due to its high affinity, which leads to high influx or diffusion of these ions at even low concentrations towards accessible pores to have more M<sup>n+</sup>...O<sub>amide</sub> (Lewis base) and M<sup>n+</sup>... $\pi$  interactions with metal ions, resulting in drastic changes in fluorescence signal. Theoretical studies were performed on a model Co(II) complex to determine the active orbitals involved in the excited state. The results illustrated that the excited state is dominated by naphthalene and carbonyl moieties of **L1**, and thus after the excitation of **1**, electron transfer to the analyte ions can take place only if the ions interact with either of the moieties or both. Fluorescence titrations were also performed with different anions following distinct quenching patterns observed with different Fe(III) and Cu(II) salts. The studies have shown that only slight changes were observed on the addition of BF<sub>4</sub><sup>-</sup>, I<sup>-</sup>, NO<sub>3</sub><sup>-</sup>, and (SO<sub>4</sub>)<sup>2-</sup> ions. Compound **1** is also interesting from a structural point of view because it has a new topology (4-c)(4-c)2(4-c)2(6-c) with a 4-nodal net. In addition, a structure containing Co(II) ions in a trinuclear system has never been reported. Similarly, **2** has a novel 3D framework with a (3,7)-c net topology that contains interesting tetranuclear Zn(II) clusters with four different coordination geometries around Zn(II) ions. Compound **3** has also shown an interesting pattern of interlinking of adjacent 1D chains to give a 3D framework of a sql/Shubnikov tetragonal plane net-type topology having the point symbol {4<sup>4</sup>·4·6<sup>2</sup>}.

## Conflicts of interest

There are no conflicts to declare.

## Acknowledgements

We are grateful to the Natural Sciences and Engineering Research Council of Canada (DDG-2022-00002), the Canadian Queen Elizabeth II Diamond Jubilee Scholarships,

the Fonds de recherche du Québec – Nature et technologies, The Canadian Foundation for Innovation (37843), Mitacs and the Université du Québec à Trois-Rivières. We are thankful to Prof. Geeta Hundal, Department of Chemistry, Guru Nanak Dev University, Amritsar, India, for single-crystal data of **L1**.

## References

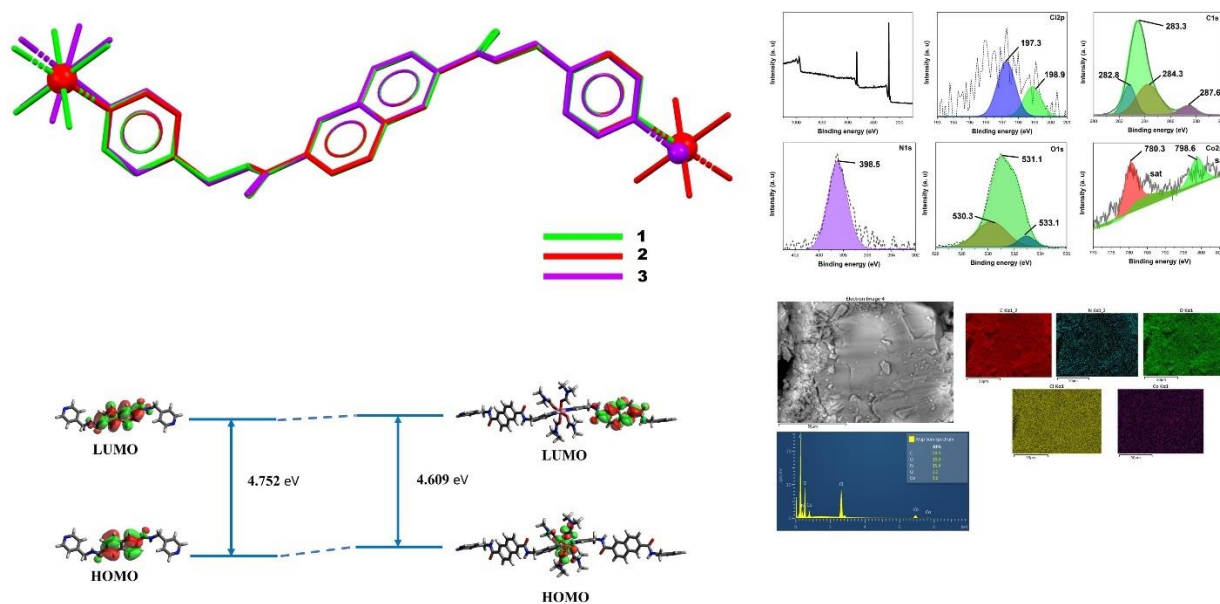
- 1 H. Bradl, *Heavy Metals in the Environment: Origin, Interaction and Remediation*, Academic Press, London, 2005.
- 2 Z. L. He, X. E. Yang and P. J. Stoffella, *J. Trace Elem. Med. Biol.*, 2005, **19**, 125.
- 3 P. B. Tchounwou, C. G. Yedjou, A. K. Patlolla and D. J. Sutton, *Exper. Suppl.*, 2012, **101**, 133.
- 4 G. F. Nordberg, B. A. Fowler, M. Nordberg and L. T. Friberg, *Handbook on the Toxicology of Metals*, Academic Press, London, 2007.
- 5 R. Singh, N. Gautam, A. Mishra and R. Gupta, *Indian J. Pharmacol.*, 2011, **43**, 246.
- 6 S. J. Stohs and D. Bagchi, *Free Radical Biol. Med.*, 1995, **18**, 321.
- 7 G. Flora, D. Gupta and A. Tiwari, *Interdiscip. Toxicol.*, 2012, **5**, 47.
- 8 United States Environmental Protection Agency online, <https://www.epa.gov/esam/method-2007-determination-metals-and-trace-elements-water-and-wastes-inductively-coupled-plasma>, (accessed 1994).
- 9 B. K. Bansod, T. Kumar, R. Thakur, S. Rana and I. Singh, *Biosens. Bioelectron.*, 2017, **94**, 443.
- 10 Agilent Technologies online, <https://www.agilent.com/cs/library/applications/si-01638.pdf>, (accessed, February 2012).
- 11 M. Eddaoudi, J. Kim, N. Rosi, D. Vodak, J. Wachter, M. O'Keeffe and O. M. Yaghi, *Science*, 2002, **295**, 469.
- 12 R. Banerjee, A. Phan, B. Wang, C. Knobler, H. Furukawa, M. O'Keeffe and O. M. Yaghi, *Science*, 2008, **319**, 939.
- 13 H. Furukawa, N. Ko, Y. B. Go, N. Aratani, S. B. Choi, E. Choi, A. O. Yazaydin, R. Q. Snurr, M. O'Keeffe, J. Kim and O. M. Yaghi, *Science*, 2010, **329**, 424.
- 14 S. Biswas and N. Stock, *Chem. Rev.*, 2012, **112**, 933.
- 15 S. L. Hou, J. Dong, X. L. Jiang, Z. H. Jiao, C. M. Wang and B. Zhao, *Anal. Chem.*, 2018, **90**, 1516.
- 16 H. Xu, C. S. Cao, X. M. Kang and B. Zhao, *Dalton Trans.*, 2016, **45**, 18003.
- 17 L. E. Kreno, K. Leong, O. K. Farha, M. Allendorf, R. P. V. Duyne and J. T. Hupp, *Chem. Rev.*, 2012, **112**, 1105.
- 18 H. Xu, C. S. Cao and B. Zhao, *Chem. Commun.*, 2015, **51**, 10280.
- 19 N. D. Rudd, H. Wang, E. M. A. F. Fernandez, S. J. Teat, F. Chen, G. Hall, Y. J. Chabal and J. Li, *ACS Appl. Mater. Interfaces*, 2016, **8**, 30294.
- 20 Y. Takashima, V. M. Martínez, S. Furukawa, M. Kondo, S. Shimomura, H. Uehara, M. Nakahama, K. Sugimoto and S. Kitagawa, *Nat. Commun.*, 2011, **2**, 168.
- 21 J. L. Du, X. Y. Zhang, C. P. Li, J. P. Gao, J. X. Hou, X. Jing, Y. J. Mu and L. J. Li, *Sens. Actuators, B*, 2018, **257**, 207.
- 22 Z. Xiang, C. Fang, S. Leng and D. Cao, *J. Mater. Chem. A*, 2014, **2**, 7662.

- 23 R. Lv, J. Wang, Y. Zhang, H. Li, L. Yang, S. Liao, W. Gu and X. Liu, *J. Mater. Chem. A*, 2016, **4**, 15494.
- 24 L. Esrafil, M. Gharib and A. Morsali, *New J. Chem.*, 2019, **43**, 18079.
- 25 L. Wu, X. F. Zhang, Z. Q. Li and F. Wu, *Inorg. Chem. Commun.*, 2016, **74**, 22.
- 26 A. L. Spek, *J. Appl. Crystallogr.*, 2003, **36**, 7.
- 27 G. R. Desiraju, J. J. Vittal and A. Ramanan, *Crystal Engineering, A Textbook*, World Scientific Publishing Co. Pte. Ltd., Singapore, 2011.
- 28 L. K. Rana, S. Sharma and G. Hundal, *Cryst. Growth Des.*, 2016, **16**, 92.
- 29 L. K. Rana, S. Sharma and G. Hundal, *J. Mol. Struct.*, 2018, **1153**, 324.
- 30 G. M. Sheldrick, *Acta Crystallogr., Sect. A: Found. Adv.*, 2015, **71**, 3.
- 31 G. M. Sheldrick, *Acta Crystallogr., Sect. C: Struct. Chem.*, 2015, **71**, 3.
- 32 O. V. Dolomanov, L. J. Bourhis, R. J. Gildea, J. A. K. Howard and H. Puschmann, *J. Appl. Crystallogr.*, 2009, **42**, 339.
- 33 C. F. Macrae, I. Sovago, S. J. Cottrell, P. T. A. Galek, P. McCabe, E. Pidcock, M. Platings, G. P. Shields, J. S. Stevens, M. Towler and P. A. Wood, *J. Appl. Crystallogr.*, 2020, **53**, 226.
- 34 F. Neese, F. Wennmohs, U. Becker and C. Riplinger, *J. Chem. Phys.*, 2020, **152**, 224108.
- 35 J. P. Perdew, K. Burke and M. Ernzerhof, *Phys. Rev. Lett.*, 1996, **77**, 3865.
- 36 F. Weigend and R. Ahlrichs, *Phys. Chem. Chem. Phys.*, 2005, **7**, 3297.
- 37 L. Goerigk, A. Hansen, C. Bauer, S. Ehrlich, A. Najibi and S. Grimme, *Phys. Chem. Chem. Phys.*, 2017, **19**, 32184.
- 38 S. Grimme, S. Ehrlich and L. Goerigk, *J. Comput. Chem.*, 2011, **32**, 1456.
- 39 S. Grimme, J. Antony, S. Ehrlich and H. Krieg, *J. Chem. Phys.*, 2010, **132**, 154104.
- 40 F. Weigend and R. Ahlrichs, *Phys. Chem. Chem. Phys.*, 2005, **7**, 3297.
- 41 F. Weigend, *Phys. Chem. Chem. Phys.*, 2006, **8**, 1057.
- 42 M. D. Hanwell, D. E. Curtis, D. C. Lonie, T. Vandermeersch, E. Zurek and G. R. Hutchison, *J. Cheminf.*, 2012, **4**, 17.
- 43 V. A. Blatov, A. P. Shevchenko and D. M. Proserpio, *Cryst. Growth Des.*, 2014, **14**, 3576.
- 44 N. Singh, N. Kaur, J. Dunn, M. MacKay and J. F. Callan, *Tetrahedron Lett.*, 2009, **50**, 953.
- 45 J. R. Lakowicz, *Principles of Fluorescence Spectroscopy*, Springer, Boston, MA, 1983.
- 46 R. G. Pearson, *J. Am. Chem. Soc.*, 1963, **85**, 3533.
- 47 J. Kalinowski, *Mater. Sci.-Pol.*, 2009, **27**, 735.



## Chapter – 3

# Isostructural coordination polymers of tethering naphthalene anchored bis(2-methylpyridinecarboxamide) ligand: Single crystal, XPS, EDS and theoretical studies.



Rana *et al*, *New J. Chem.*, 2023, **47**, 5477-5487

### 3.1 Introduction

Coordination polymers (CPs) have received immense attention from the scientific community during the past few decades owing to their interesting structures and properties. The properties of CPs are directly related to the type of the metal ion and organic ligand present: for instance, magnetism can be obtained using metal ions with partially filled *d* or *f*-orbitals, while luminescence properties could be related to the degree of unsaturation in the aliphatic/aromatic systems of the ligand and/or the presence of chromophores and/or auxochromes. It is always challenging to anticipate the structures of the coordination networks because the parameters such as the coordination modes of ligands, the geometric preferences of the metal ions, the solvent systems, pH values and the counter anions affect the self-assembly process.

Although there are plenty of reports in the literature on 1D coordination polymers synthesized using different classes of organic ligands containing divergent coordination sites, the compounds synthesized using dicarboxamide ligands containing secondary amide nitrogen (R-CONH-) with pendent pyridyl group are interesting owing to their ability to govern the self-assembly of coordination networks by virtue of their strong coordination potential alongside non-covalent interactions such as hydrogen bonding, and  $\pi \cdots \pi$  interactions to yield molecular networks of different dimensionalities. Also, the amide group is known to regulate the orientation of ligand molecules to direct the coordination to metal ions, and hence to control the primary structure in the solid state. These structures are further reorganized into supramolecular networks (secondary structure) through various non-covalent interactions (e.g., metallophillic and metal $\cdots$ halogen interactions, ligand-based interactions), which in turn depend upon the functionalities present in the ligand molecules.

In view of the above discussion, we have reported the synthesis of a symmetric dicarboxamide ligand (**L1**) containing a naphthalene core appended to two methyl pyridyl groups at 2,6-positions. Moreover, a series of coordination compounds have been synthesised by reacting **L1** molecule with  $\text{MX}_2$  salts ( $\text{M} = \text{Cu(II)}, \text{Co(II)}$  and  $\text{Zn(II)}$ ,  $\text{X} = \text{ClO}_4^-$ ). The diffraction studies reveal that these compounds are isostructural, which is also confirmed by dissimilarity index measurement using XPac software. In addition, the oxidation states of metal ions in the relative complexes have been investigated by XPS (X-ray photoelectron spectra) analysis. Moreover, information on the different chemical environments of non-metals (e.g., C, N, O and

Cl) has been obtained using the same technique. Besides, EDS (Energy-dispersive X-ray spectroscopy) analysis was performed to see the elemental composition of bulk samples. At last, DFT (Density Functional theory) calculations are performed on the L1 and complexes to see the orbitals composition of ground and excited states. Also, the total energy ( $E_{Total}$ ) of metal ligand coordination bond in the complexes is calculated and its decomposition into different energies viz.  $E_{Pauli}$ ,  $E_{electrostatic}$ ,  $E_{dispersion}$  etc. is done. The results obtained show that the energy of metal-ligand bond in the copper complex is more negative than others, which can be attributed to prevalent Jahn-Teller distortions that results in shorter metal-ligand bond distance. These observations are also in good agreement with the metal-ligand bond distances obtained from single crystal x-ray diffraction. Furthermore, the crystal structure of the ligand and the corresponding complexes discussed in this research are novel and have never been reported in the literature, which further adds value to this thesis.

### 3.2 Objective

- Design and synthesis of isostructural one-dimensional coordination polymers (1D-CP) using transition metal-ions and the naphthalene dicarboxamide ligand, differing from the one discussed in the Chapter 1 in the position of the pyridine nitrogen with respect to amide group.
- Characterization of the coordination compounds using different analytical techniques such as SCXRD, XPS, EDS etc. and establishing critical correlation among them.
- Chemical state identification of the transition metal-ions, and the information on chemical environments on different elements using XPS analysis.
- Investigation of bulk elemental composition of these compounds using EDS analysis.
- Investigation of the effect of DMF molecules on the HOMO-LUMO energy gap of these compounds using DFT studies.
- Theoretical studies to examine the strength of metal-ligand bond with the change in the metal-ion.

### 3.3 Authors contribution

- Conceptualization – Love Karan Rana

- Data curation – Love Karan Rana, Gurpreet Singh Selopal (XPS) and Alborz Bavandsavadkouhi (TGA)
- Formal analysis – Love Karan Rana
- Funding acquisition – Dr. Adam Duong
- Investigation – Love Karan Rana
- Methodology – Love Karan Rana
- Supervision – Dr. Adam Duong
- Visualization – Love Karan Rana
- Writing - original draft – Love Karan Rana
- Writing – review and editing – Love Karan Rana and Prabhjot Kaur, and Dr. Adam Duong

### **3.4Article**



Cite this: *New J. Chem.*, 2023, 47, 5477

## Isostructural coordination polymers of the tethering naphthalene anchored bis(2-methylpyridinecarboxamide) ligand: single crystal, XPS, EDS and theoretical studies†

Love Karan Rana,<sup>a</sup> Prabhjyot Kaur,<sup>a</sup> Alborz Bavandsavadvkouhi,<sup>a</sup> Gurpreet Singh Selopal<sup>b</sup> and Adam Duong<sup>a</sup>

This research work reports the synthesis of three novel coordination compounds with the formula  $\{[M(L1)(C_3H_7NO)_4](ClO_4)_2\}_n$  ( $M = Cu(II)$  **1**,  $Co(II)$  **2**, and  $Zn(II)$  **3**), using  $M(ClO_4)_2 \cdot 6H_2O$  metal salt with **L1** (where **L1** =  $(N^2,N^6$ -bis(pyridin-4-ylmethyl)naphthalene-2,6-dicarboxamide). Diffraction study shows that these compounds are isostructural 1D coordination polymers which is also confirmed using XPac 2.0 software. In addition, information on the chemical state of metal ions, and chemical environments around different elements viz. C, N, O and Cl was obtained by the XPS analysis of these compounds. EDS analysis was done on these compounds, which further supports the findings of XPS and single crystal diffraction studies by showing the presence of respective elements of the ligand, perchlorate ion, and metal ions in the bulk samples. DFT studies on **L1** and compounds **1–3** were performed considering the effect of solvent molecules on the HOMO–LUMO energy gap, which shows the order of 4.609 eV (**2**) < 4.737 eV (**3**) < 4.742 eV (**1**) < 4.752 eV (**L1**). Furthermore, the total energy ( $E_{Total}$ ) of the metal ligand coordination bond in the compounds **1–3** is calculated, which is further decomposed into various contributing energies. A more negative value of  $E_{Total}$  in **1** reflects the effect of Jahn–Teller distortions and is in good agreement with the crystallographic metal ligand bond distance. Besides, various analytical techniques viz. NMR, IR, etc. were used to characterize the ligand and compounds as well. The phase purity of these compounds was determined using PXRD.

Received 3rd January 2023,  
Accepted 1st February 2023

DOI: 10.1039/d3nj00038a

rsc.li/njc

## Introduction

Coordination polymers (CPs) are non-porous inorganic–organic hybrid materials comprising an infinite array of metal nodes tethered by organic struts to give repeating coordination motifs extending in one, two and three dimensions.<sup>1</sup> They represent an important interface between synthetic chemistry and materials science with interesting structures and properties<sup>2–7</sup> due to which they have received attention from the scientific

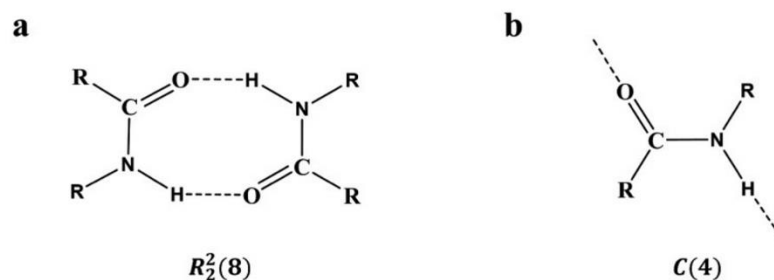
community for the past few decades. A careful selection of metal ions and a meticulously designed ligand can impart desired properties to materials (CPs); for instance, magnetic properties can be invoked in coordination polymers by incorporating transition metal ions with partially filled d orbitals such as  $Mn(II)$ ,<sup>8</sup>  $Co(II)$ ,<sup>8,9</sup>  $Ni(II)$ ,<sup>10</sup>  $Cu(II)$ <sup>11</sup> and some rare earth metal ions.<sup>12,13</sup> However, for the applications such as luminescence, photodegradation of dyes *etc.*, characteristics like degree of unsaturation in the aromatic rings and the presence of auxochromes, in the organic ligand imparts absorption/emission characteristics to the coordination polymers.<sup>14–16</sup>

Despite the immense progress that has been made in the design and synthesis of CPs, it is still a challenge to anticipate the structures of the resultant frameworks<sup>17,18</sup> because the crystallization process of coordination polymers is affected by parameters, such as the coordination modes of ligands, metal ions, solvent systems, pH values and counter anions.<sup>19–21</sup> In general, the outcome and topology of the product self-assembled from an inorganic metal centre and organic spacers depends on the (1) functionality of the ligand which involves flexibility, length, and symmetry of organic ligands,

<sup>a</sup> Département de Chimie, Biochimie et physique, Institut de Recherche sur l'Hydrogène and Laboratory of Functional Materials for Energy and Nanotechnology (DuongLab), Université du Québec à Trois-Rivières, Trois-Rivières, Québec, G9A 5H7, Canada. E-mail: love.karan@uqtr.ca

<sup>b</sup> Institut national de la recherche scientifique, Montréal, Québec, H2X 1E3, Canada  
† Electronic supplementary information (ESI) available: ORTEP diagrams, Tables S1 showing IR peaks assignments, and Tables S2–S5 showing information on hydrogen bonding in **L1** and compounds **1–3**. In addition, the <sup>1</sup>H NMR and <sup>13</sup>C NMR spectra of **L1** and the PXRD patterns of the compounds. Furthermore, XPS, SEM and EDS spectra of **2** and **3**. CCDC numbers are 2236996 (**L1**), 2190880 (**1**), 2045249 (**2**) and 2063340 (**3**). For ESI and crystallographic data in CIF or other electronic format see DOI: <https://doi.org/10.1039/d3nj00038a>





Scheme 1 Typical hydrogen bonded motifs in primary amides, (a) ring and (b) catemer synthon.

and (2) valences and the geometric needs of the metal ions used.<sup>22</sup>

There are plenty of reports in the literature on 1D coordination polymers, synthesized using different organic ligands with divergent coordination sites.<sup>23</sup> Among these, the dicarboxamide ligand containing secondary amide nitrogen (R-CONH-) with pendent pyridyl groups<sup>24,25</sup> is of particular interest due to its ability to direct the self-assembly of coordination networks by the virtue of its strong coordination potential and different non-covalent interactions such as hydrogen bonding and  $\pi \cdots \pi$  interactions to yield molecular networks of different dimensionalities. The amide group with well-known patterns of self-assembly (Scheme 1) has the potential to regulate the orientation of ligand molecules to govern the coordination to metal ions, thus affecting the primary structure in the solid state.<sup>26–38</sup> These structures are further reorganized into supramolecular networks (secondary structure) using various non-covalent interactions involving metallophilic and metal  $\cdots$  halogen interactions, and ligand-based interactions depending on the functionalities present in ligand molecules.<sup>26,39–45</sup>

In view of the above discussion, we have synthesized a new dicarboxamide ligand **L1** containing a naphthalene core appended to two methyl pyridyl groups at the 2,6-position and used it to obtain a series of 1D coordination compounds with  $MX_2$  salts ( $M = Cu(II), Co(II)$  and  $Zn(II)$ ,  $X = ClO_4^-$ ). The SCXRD analysis reveals that they are isostructural in nature, which is also confirmed by the dissimilarity index measurement using XPac software.<sup>46–48</sup> In addition, XPS analysis was performed on these compounds to see the oxidation state of metal ions and to investigate the influence on chemical environments of different elements of **L1** and the perchlorate ion after coordination to metal ions. Besides, the EDS analysis was performed on these compounds to see the elemental composition of bulk samples with respect to **L1**, the perchlorate ion and the metal ion. The results obtained supplement the information obtained by single crystal diffraction and XPS studies. Finally, DFT calculations were performed on **L1** and compounds **1–3** by taking into account solvent effects to study the orbital compositions of the HOMO and LUMO states and the effect of a solvent (DMF) on these states. We would like to mention here that although the ligand has been used elsewhere,<sup>49–51</sup> the crystal structure of the same and the corresponding compounds

included in this article have never been reported, which makes the present work novel.

## Materials and methods

All materials *viz.* 2,6-naphthalenedicarboxylic acid, 3-(aminomethyl)pyridine, thionyl chloride, dimethylformamide (DMF), pyridine and all perchlorate salts  $M(ClO_4)_2 \cdot 6H_2O$  ( $M = Co(II), Cu(II)$ , and  $Zn(II)$ ) were procured from Sigma-Aldrich and were used as received without further purification. The NMR data of **L1** was recorded using a Varian Oxford 200 MHz instrument. X-ray photoelectron spectra (XPS) was acquired using a VG Scientific Escalab 220i XL system, equipped with an aluminum monochromatic source of 1486.6 eV energy. Casa XPS and origin software were utilized for the elemental analysis and interpretation of characteristic binding energies. The thermogravimetric analysis of all compounds was performed using a Diamond Pyris 6000 TGA/DTA apparatus from Perkin-Elmer from 30 °C to 850 °C under a  $N_2$  flow at a heating rate of 5 °C min<sup>-1</sup>.

## Diffraction studies

The single crystal data for **L1** was collected using an Agilent Supernova, dual four circle diffractometer equipped with a mirror monochromator. The diffraction data for **1–3** were collected using a Rigaku New Gemini, four-circle diffractometer equipped with a fine-focus sealed X-ray tube and an EosS2 detector with a CCD plate. The data were integrated with CrysAlisPro 1.171.40.84a and a multi-scan absorption correction was applied using spherical harmonics, implemented in the SCALE3 ABSPACK scaling algorithm. The structure of compound **1** was solved using the SIR-92<sup>52a</sup> structure solution program and the structure of **L1** and compounds **2** and **3** using SHELXT.<sup>52b</sup> The data were refined with the SHELXL<sup>53</sup> refinement package using least squares minimization in a graphical user interface Olex2.<sup>54</sup> All non-hydrogen atoms were refined anisotropically. The hydrogen atoms were refined isotropically on calculated positions using a riding model with their Uiso values constrained to 1.5 times the Ueq of their pivot atoms for terminal  $sp^3$  carbon atoms and 1.2 times for all other carbon atoms. In compound **1**, the high thermal parameter of atoms in coordinated DMF molecules is fixed by splitting the respective atoms

Table 1 Crystallographic parameters for **L1** and compounds **1–3**

Identification code	<b>L1</b>	<b>1</b>	<b>2</b>	<b>3</b>
Empirical formula	C <sub>24</sub> H <sub>20</sub> N <sub>4</sub> O <sub>2</sub>	C <sub>36</sub> H <sub>48</sub> Cl <sub>2</sub> Cu N <sub>8</sub> O <sub>14</sub>	C <sub>36</sub> H <sub>48</sub> Cl <sub>2</sub> Co N <sub>8</sub> O <sub>14</sub>	C <sub>36</sub> H <sub>48</sub> Cl <sub>2</sub> Zn N <sub>8</sub> O <sub>14</sub>
Formula weight	396.44	951.27	946.65	953.11
Temperature	150 K	150 K	150 K	150(2) K
Wavelength	0.71073 Å	1.54184 Å	1.54184 Å	1.54184 Å
Crystal system	Triclinic	Triclinic	Triclinic	Triclinic
Space group	<i>P</i> $\bar{1}$	<i>P</i> $\bar{1}$	<i>P</i> $\bar{1}$	<i>P</i> $\bar{1}$
Unit cell dimensions	<i>a</i> = 9.779(9) Å $\alpha$ = 103.64° <i>b</i> = 10.072(10) Å $\beta$ = 98.53° <i>c</i> = 11.6525(15) Å $\gamma$ = 113.08°	<i>a</i> = 9.249(8) Å $\alpha$ = 95.50(7)° <i>b</i> = 10.877(8) Å $\beta$ = 107.674(8)° <i>c</i> = 11.2251(10) Å $\gamma$ = 100.68(7)°	<i>a</i> = 9.1612(6) Å $\alpha$ = 95.171(5)° <i>b</i> = 10.9721(8) Å $\beta$ = 105.936(5)° <i>c</i> = 11.5145(4) Å $\gamma$ = 103.407(6)°	<i>a</i> = 9.196(4) Å $\alpha$ = 95.18(4)° <i>b</i> = 10.976(6) Å $\beta$ = 106.101(4)° <i>c</i> = 11.4963(4) Å $\gamma$ = 103.357(4)°
Volume	988.1(2) Å <sup>3</sup>	1043.3(2) Å <sup>3</sup>	1067.87(12) Å <sup>3</sup>	1069.8(9) Å <sup>3</sup>
Z	2	1	1	1
Density (calculated)	1.332 Mg m <sup>-3</sup>	1.514 Mg m <sup>-3</sup>	1.472 Mg m <sup>-3</sup>	1.479 Mg m <sup>-3</sup>
Absorption coefficient	0.087 mm <sup>-1</sup>	2.574 mm <sup>-1</sup>	4.943 mm <sup>-1</sup>	2.587 mm <sup>-1</sup>
<i>F</i> (000)	416	495	493	496
Crystal size	0.23 × 0.19 × 0.11 mm <sup>3</sup>	0.15 × 0.14 × 0.12 mm <sup>3</sup>	0.21 × 0.19 × 0.17 mm <sup>3</sup>	0.20 × 0.18 × 0.16 mm <sup>3</sup>
Theta range for data collection	3.162 to 25°	4.189 to 72.451°	4.048 to 72.405°	4.058 to 71.866°
Index ranges	−11 ≤ <i>h</i> ≤ 11, −11 ≤ <i>k</i> ≤ 11, −12 ≤ <i>l</i> ≤ 13	−11 ≤ <i>h</i> ≤ 11, −13 ≤ <i>k</i> ≤ 11, −13 ≤ <i>l</i> ≤ 13	−11 ≤ <i>h</i> ≤ 11, −13 ≤ <i>k</i> ≤ 12, −14 ≤ <i>l</i> ≤ 9	−10 ≤ <i>h</i> ≤ 11, −13 ≤ <i>k</i> ≤ 13, −14 ≤ <i>l</i> ≤ 8
Reflections collected/unique	7397/3465 [R(int) = 0.0547]	7014/4000 [R(int) = 0.0345]	7666/4109 [R(int) = 0.0288]	7064/4059 [R(int) = 0.0235]
Completeness to theta full	99.7%	99.8%	99.6%	99.0%
Absorption correction	Semi-empirical from equivalents	Semi-empirical from equivalents	Semi-empirical from equivalents	Semi-empirical from equivalents
Max. and min. transmission	0.7456 and 0.6352	1 and 0.89999	1 and 0.60350	1 and 0.72216
Refinement method	Full-matrix least-squares on <i>F</i> <sup>2</sup>	Full-matrix least-squares on <i>F</i> <sup>2</sup>	Full-matrix least-squares on <i>F</i> <sup>2</sup>	Full-matrix least-squares on <i>F</i> <sup>2</sup>
Data/restraints/parameters	3465/0/271	4000/110/396	4109/0/281	4059/0/281
Goodness-of-fit on <i>F</i> <sup>2</sup>	1.064	1.029	1.026	1.057
Final R indices [I > 2σ(I)]	<i>R</i> <sub>1</sub> = 0.0911, <i>wR</i> <sub>2</sub> = 0.3047	<i>R</i> <sub>1</sub> = 0.0545, <i>wR</i> <sub>2</sub> = 0.1457	<i>R</i> <sub>1</sub> = 0.0434, <i>wR</i> <sub>2</sub> = 0.1155	<i>R</i> <sub>1</sub> = 0.0388, <i>wR</i> <sub>2</sub> = 0.1026
R indices (all data)	<i>R</i> <sub>1</sub> = 0.1365, <i>wR</i> <sub>2</sub> = 0.3399	<i>R</i> <sub>1</sub> = 0.0654, <i>wR</i> <sub>2</sub> = 0.1558	<i>R</i> <sub>1</sub> = 0.0461, <i>wR</i> <sub>2</sub> = 0.1184	<i>R</i> <sub>1</sub> = 0.0456, <i>wR</i> <sub>2</sub> = 0.1070
Largest diff. peak and hole	0.467 and 0.405 e Å <sup>-3</sup>	0.628 and 0.438 e Å <sup>-3</sup>	0.454 and 0.429 e Å <sup>-3</sup>	0.511 and 0.344 e Å <sup>-3</sup>
CCDC	2236996	2190880	2045249	2063340

into two positions to give a total site occupancy of 1.000 for each DMF molecule. The respective site occupancies and *U*<sub>iso</sub> values were refined as free variables. In addition, the disorder in perchlorate ion was resolved by splitting the respective oxygen atoms into two positions with a total site occupancy factor of 1. The powder diffraction patterns (PXRD patterns) of all compounds (Fig. S1–S3, ESI†) were obtained using a D8 Focus Bruker X-ray powder diffractometer with Cu K $\alpha$  radiation ( $\lambda$  = 1.54178 Å). Powder patterns from single crystals were generated using the Mercury software of the Cambridge Crystallographic Data Centre.<sup>55</sup> The crystallographic information of all compounds is shown in Table 1. The BFDH morphologies showing the planes involved in the crystal growth are given in Fig. S4 (ESI†) for **L1** and **1**.

### Computational details

DFT calculations of **L1** and all compounds were performed using the ORCA quantum chemistry suite 4.2.1.<sup>56</sup> by taking into account solvent effects of DMF using a conductor like polarizable continuum model (CPCM).<sup>57</sup> In the case of compounds **1–3**, geometry optimization was performed considering the fragment [M(**L1**)<sub>2</sub>(DMF)<sub>4</sub>] (M = Co(II), Cu(II) and Zn(II)) as the

representative unit, in which the coordinates of respective elements were directly taken from the respective cif files. The geometries of **L1** and **1–3** were optimized using a hybrid PBE0 exchange–correlation function<sup>58</sup> with a basis set def2-SVP.<sup>59</sup> The empirical dispersion correction D3BJ was used to evaluate the binding energies.<sup>60–62</sup> Besides, a polarized triple-zeta function def2-TZVP<sup>63</sup> with core effective potential was used for metal ions to account for relativistic effects. In addition, the auxiliary basis set used was def2/J.<sup>64</sup> The energy decomposition analysis (EDA)<sup>65</sup> was performed using the fragment [M(**L1**)<sub>2</sub>(DMF)<sub>4</sub>] to obtain a better understanding of metal–ligand coordination bond energies in **1–3** and interaction energies involved in hydrogen bonded fragments of **L1**. Decomposition of total binding energies was computed using the BLYP exchange–correlation function<sup>66</sup> with a D3 empirical dispersion correction.<sup>62</sup> In addition, all electron triple-zeta basis set with two polarization functions, TZ2P, has been applied to all atoms. Core electrons were treated by frozen core approximation. Scalar relativistic effects were considered by zeroth-order regular approximation (ZORA).<sup>67</sup> Fragments considered for this analysis were directly taken from the cif file without further optimization.



### Synthesis of L1

A mixture of 2,6-naphthalene dicarboxylic acid (4.6 mmol, 1.0 g) in  $\text{SOCl}_2$  (20 ml) was refluxed for 1 h at 90 °C in a 100 ml round bottom flask. Following this, dry toluene was added to the resulting clear solution and the excess of  $\text{SOCl}_2$  was removed by vacuum distillation. The reaction mixture was cooled down to room temperature and then 4-aminomethyl pyridine (1000 mmol, 0.94 ml) and pyridine (731 mmol, 0.75 ml) were added to the reaction mixture followed by stirring for 1 h. The reaction mixture was left undisturbed for few hours. The organic layer was washed with distilled water followed by a saturated solution of  $\text{NaHCO}_3$  five times and dried over  $\text{Na}_2\text{SO}_4$ . The crude product was recrystallized using MeOH whereupon slow evaporation gave light-colourless crystals of **L1** (yield: 0.75 g, 75%). Although the molecular structure of **L1** was obtained from one of these crystals, the data quality was not good as apparent from the deviation of data from the straight line in the Wilson plot and a low signal-to-noise ratio at higher angles (beyond  $2\theta = 43^\circ$ ), even though a high exposure time of 25 second per frame with a scan width of 1 was used. This can be related to the intrinsic nature of the crystal. The associated graphs illustrating weak diffraction data are shown in the ESI† (Fig. S5). Anal. calc for **L1**,  $\text{C}_{24}\text{H}_{24}\text{N}_4\text{O}_4$  (%): C, 66.65; H, 5.59; N, 12.95. Found: C, 66.70; H, 6.39; N, 12.79.  $^1\text{H}$  NMR (200 MHz, DMSO,  $\delta$  from TMS), (Fig. S6, ESI†):  $\delta_{\text{H}}$  9.38 (s, 2H), 8.58 (s, 2H), 8.52 (s, 2H), 8.14 (s, 2H), 7.36 (s, 4H), 4.57 (s, 4H).  $^{13}\text{C}$  NMR (200 MHz, DMSO,  $\delta$  from TMS), (Fig. S7, ESI†):  $\delta_{\text{C}}$  (200 MHz, DMSO) 166.60, 149.78, 148.70, 133.63, 133.13, 129.36, 127.61, 125.14, 122.39, 42.10. FT-IR ( $\text{cm}^{-1}$ ) (Fig. S8 and Table S1, ESI†) 3272 (s), 3068 (w,b), 1639 (s), 1597 (s), 1533 (b), 2937 (m), 1487 (w)

### Synthesis of 1–3

All the compounds were synthesized by the vapour diffusion method of crystallization. Mixture of **L1** (0.01 g, 0.025 mM) and  $\text{Cu}(\text{ClO}_4)_2 \cdot 6\text{H}_2\text{O}$  (0.0187 g, 0.050 mM) for compound **1**, **L1** (0.01 g, 0.025 mM) and  $\text{Co}(\text{ClO}_4)_2 \cdot 6\text{H}_2\text{O}$  (0.0185 g, 0.050 mM) for compound **2**, and **L1** (0.01 g, 0.025 mM) and  $\text{Zn}(\text{ClO}_4)_2 \cdot 6\text{H}_2\text{O}$  (0.0188 g, 0.050 mM) for compound **3** was dissolved in DMF at room temperature. Next, the solution of **1** was exposed to ethyl acetate, whereas EtOH was used as a diffusion solvent for **2**

and **3**. Light blue and pink crystals were obtained for **1** and **2**, respectively, while colourless crystals were obtained for **3**. All the samples were washed with fresh DMF for at least four times before performing further analysis.

Yield for **1**: 0.0080 g (80%). Anal. calc for **1**,  $\text{C}_{36}\text{H}_{48}\text{N}_8\text{O}_{14} \cdot \text{Cl}_2\text{Cu}$  (%): C, 46.22; H, 4.48; N, 12.52. Found: C, 45.45; H, 5.09; N, 11.78. FT-IR ( $\text{cm}^{-1}$ ), (Fig. S8 and Table S1, ESI†) 3076 (w), 2932 (vw), 1645 (s), 1615 (w), 1532 (m, b), 1494 (w), 1105 (w), 1081 (m), 1060 (w).

Yield for **2**: 0.0088 g (88%). Anal. calc for **2**,  $\text{C}_{36}\text{H}_{48}\text{N}_8\text{O}_{14} \cdot \text{Cl}_2\text{Co}$  (%): C, 45.68; H, 5.11; N, 11.84. Found: C, 45.43; H, 4.98; N, 11.45. FT-IR ( $\text{cm}^{-1}$ ), (Fig. S8 and Table S1, ESI†) 3069 (w), 2940 (vw), 1640 (s), 1611 (w), 1533 (s), 1493 (w), 1112 (w), 1058 (w), 1019 (w).

Yield for **3**: 0.0073 g (73%). Anal. calc for **3**,  $\text{C}_{36}\text{H}_{48}\text{N}_8\text{O}_{14} \cdot \text{Cl}_2\text{Zn}$  (%): C, 45.37; H, 5.08; N, 11.76. Found: C, 45.12; H, 4.92; N, 11.34. FT-IR ( $\text{cm}^{-1}$ ), (Fig. S8 and Table S1, ESI†) 3071 (w), 2935 (vw), 1643 (s), 1612 (w), 1529 (s), 1492 (w), 1114 (w), 1061 (w), 1021 (w).

## Results and discussion

### Crystal structure of L1

The crystal structure of **L1** shows a unique ligand molecule in the asymmetric unit (Fig. 1a and Fig. S9, ESI†). Within the molecule, amide moieties are slightly oriented with respect to the naphthalene ring as apparent from a dihedral angle of  $35.5^\circ$  between naphthalene and amide planes (Fig. S10, ESI†). The adjacent **L1** molecules are held together by  $R_2^1(6)$  synthons<sup>68–70</sup> involving naphthalene and pyridine moieties to form a 1D chain of hydrogen bonded ligands (Fig. 1b). A 2D sheet is formed by hydrogen bonding between neighbouring 1D chains *via*  $R_2^2(10)$  synthons composed of naphthalene and amide moieties (Fig. 1c). The adjacent 2D sheets are piled upon one another by  $R_2^1(7)$  and  $R_2^2(10)$  synthons to form a 3D framework (Fig. 1d).

### Crystal structure of compound 1

As all three compounds are iso-structural 1D coordination polymers, the crystal structural description of only **1** is given below. The details of hydrogen bonds of **1–3** are given in Tables S3–S5 (ESI†). The ORTEP diagrams of **1–3** are shown in the ESI†

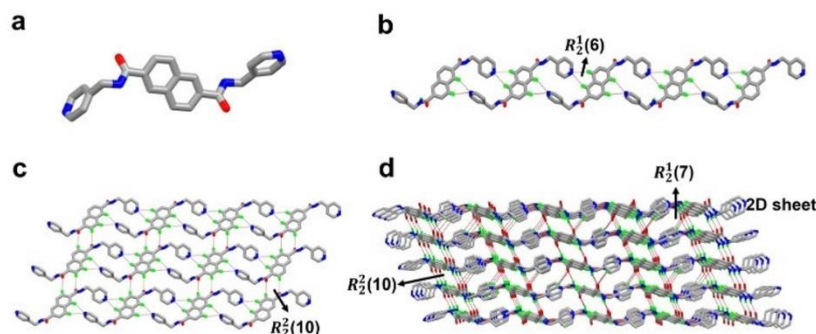


Fig. 1 (a) Asymmetric unit of the ligand. Pictorial presentations of the (b) 1D chain, (c) 2D sheet and (d) 3D hydrogen bonded framework.



(Fig. S11–S13). In the asymmetric unit of the compound (Fig. S11, ESI†), the Cu(II) ion is coordinated to a half **L1** and two unique DMF molecules with the centre of inversion present on the metal centre and the naphthalene ring of the ligand as well. Besides, perchlorate ions are crystallized as counter anions outside the coordination sphere. A unique coordination unit containing Cu(II) ion octahedrally coordinated to a complete **L1** molecule and symmetry related DMF molecules is generated around these centres of inversion (Fig. 2a). The octahedral geometry around the Cu(II) ion is granted by pyridine nitrogen atoms of two symmetry related **L1** and oxygen atoms of four DMF molecules, two unique and two symmetry related. In all compounds, the amide moieties of **L1** molecules are twisted out of the plane with respect to the plane of the naphthalene rings by  $25.5^\circ$  (the dihedral angle between the naphthalene plane and the amide plane). Whereas pyridine rings are oriented at  $62.5^\circ$  relative to the plane of the naphthalene ring. The amide and pyridine moieties of **L1** molecules exhibit the same orientation in all compounds as apparent from the overlay diagram (Fig. 2b). Due to the divergent/bridging nature of **L1**, the adjacent metal centres are connected to each other by  $\mu_2$ -bridged **L1** molecules to generate a 1D coordination chain (Fig. 2a). These chains are further extended to 2D and 3D hydrogen bonding networks (Fig. 2c and d) via extensive hydrogen bonding between perchlorate anions and, the naphthalene and amide moieties of **L1**, and coordinated DMF molecules. In the 3D network, the metal ions are arranged in such a way to give an arrangement of edge sharing multiple parallelograms (Fig. 2d). The respective ring synthons that hold the hydrogen bonding networks are shown in Fig. S14a and 14b (ESI†).

#### Isostructurality of compounds 1–3

The degree of similarity among **1**, **2** and **3** based on their subassemblies or “supramolecular construct” (SC) was investigated using XPac 2.0 software.<sup>46–48</sup> Supramolecular constructs are the subcomponents of crystal structures that have

geometrical closeness with respect to the geometrical conformation and position of molecules. The comparison of the structures is merely based on the geometrical basis that takes an account of angular, planar, and distance relationships between the kernel molecule (central molecule) and cluster molecules (surrounding molecules) of a given coordination sphere of molecules generated around a central molecule by relative symmetry operations of space groups of each structure considered for comparison. For comparison, the template structure was generated using compound **3**, which was then used to define equivalent atoms in **1** and **2** to be compared. The XPac dissimilarity index ( $X$ )<sup>48</sup> calculated for a coordination sphere comprising a kernel (central molecule) and 18 shell molecules shows 3D similarity between **1** and **3** with a value ( $X$ ) of 4. Likewise, compounds **2** and **3** have 3D similarity to a dissimilarity index ( $X$ ) value of 0.3. The pertinent values of geometrical parameters *i.e.* angles [ $\alpha$ ] and planes [ $\rho$ ] used to calculate ' $X$ ' for **1** and **3** are  $1.7^\circ$  and  $3.7^\circ$ , respectively, whereas these values are  $0.1^\circ$  and  $0.2^\circ$ , respectively, for **2** and **3**. In addition, interesting information can be derived from the graphs as shown in Fig. 3a and b. In the plot of  $\delta\rho$  ( $^\circ$ ) vs  $\delta\alpha$  ( $^\circ$ ) (Fig. 3a), more data points close to the origin (*i.e.* data points at lower angles [ $\alpha$ ]) signify more similarity among the crystal structure. Thus, compound **2** is more alike compound **3** than compound **1**.

In addition to this, the plot of  $X$  vs  $\delta d$  (Å) gives the stretch parameter ' $D$ ' that signifies the extent of stretching in one structure relative to other. Lower the value of ' $D$ ', more will be the similarity that again illustrates that compounds **2** and **3** are structurally very similar (Fig. 3b). The values obtained are 0.22 Å and 0.02 Å, respectively, for the comparison between **1** and **3** (Fig. 3a) and **2** and **3** (Fig. 3b).

#### XPS and EDS analyses

The chemical state identification and the investigation of electronic states of different elements have been studied using XPS.

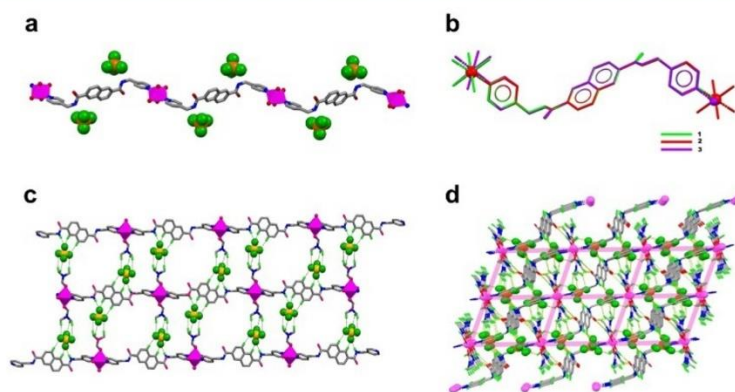


Fig. 2 (a) 1D coordination chain of **1**. (b) Overlay diagram showing the orientation of **L1** in all compounds. Pictorial presentations of the (c) 2D sheet and (d) 3D hydrogen bonding networks of **1**.

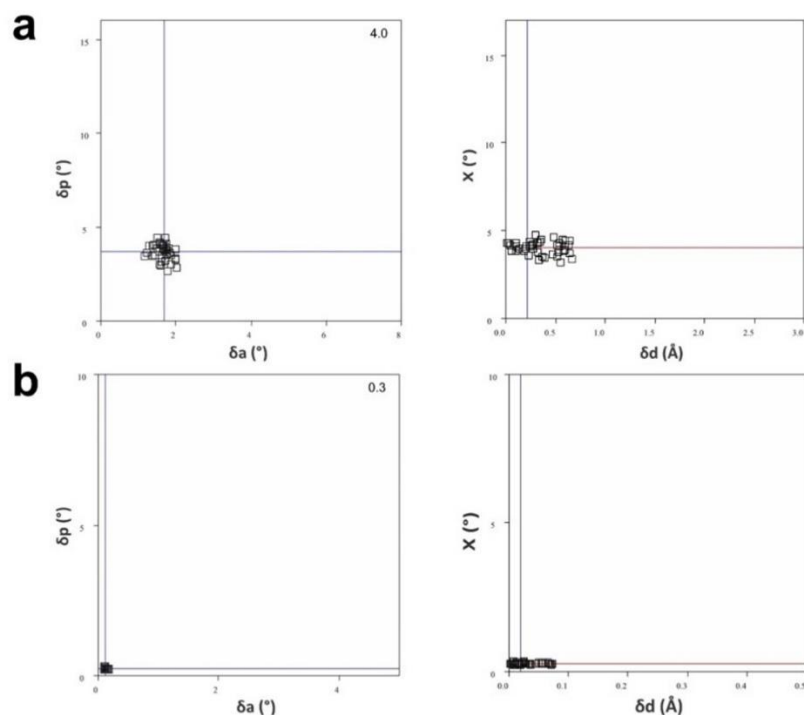


Fig. 3 (a) and (b) Plots of  $\delta a$  ( $^{\circ}$ ) vs  $\delta p$  ( $^{\circ}$ ) and  $X$  vs.  $\delta d$  ( $^{\circ}$ ) for the comparison of the structures of **1** and **3** and **2** and **3**.

In the XPS spectra of compound **1** (Fig. 4 and Table 2), the Cu bands  $2P_{3/2}$  at 933.8 eV with a charge transfer satellite peak at 942.6 eV and  $2P_{1/2}$  at 953.9 eV with a charge transfer satellite

peak at 962.1 eV illustrate the presence of the divalent copper ion.<sup>71</sup> The low intensity peaks at 575 eV and 649 eV, respectively, corresponding to the Auger LMM transition of the Cu(II) ion,<sup>72</sup>

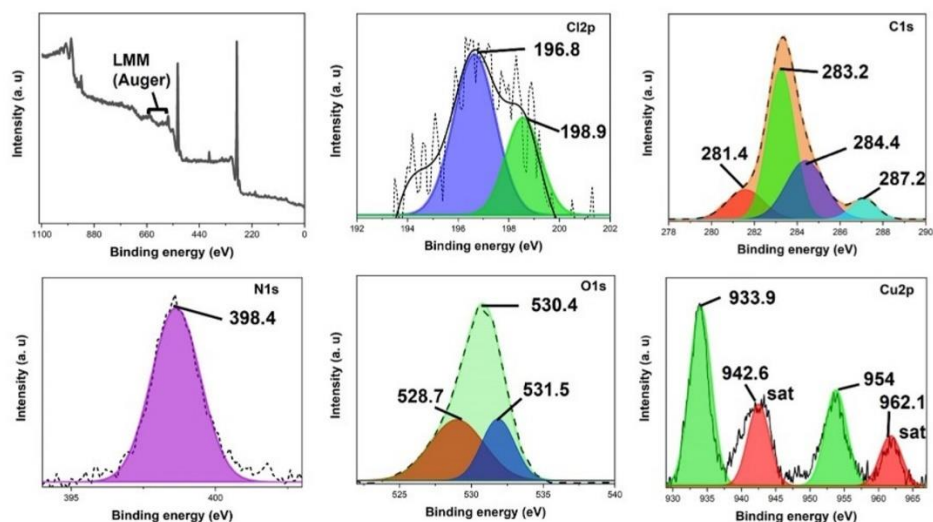


Fig. 4 Characteristic binding energies (eV) of the respective elements present in compound **1**.

are also observed (Fig. 4, Table 2). Apart from this, the  $sp^2$  hybridized N 1s core level binding energy observed at 398.4 eV shows the presence of the coordinated pyridine nitrogen atom.

The peak is slightly shifted towards a lower energy<sup>73</sup> (0.3 eV) because of the delocalization of electrons towards the pyridine ring due to  $M \rightarrow L$  back bonding. For Cu–O bonds (DMF), the O 1s peak at 530.4 eV is observed at a lower binding energy<sup>71</sup> due to either  $M \rightarrow L$  back bonding or the displacement of electron density towards the carbonyl group by electron releasing methyl groups attached to amide nitrogen of DMF molecules. The fully resolved Cl 2p peaks *viz.* 2P<sub>3/2</sub> at 196.8 eV and 2P<sub>1/2</sub> at 198.9 eV for O 1s at 531.5 eV confirm that ClO<sub>4</sub><sup>−</sup> ions are present in the material as counter anions. The shift in the position of the Cl 2P<sub>3/2</sub> peak towards a lower binding energy (~11 eV) with respect to NaClO<sub>4</sub><sup>−</sup> (208.9 eV for Cl 2P<sub>3/2</sub>)<sup>74</sup> might be due to strong electrostatic interactions between electron deficient Cu(II) ions (due to back bonding) and one of the oxygen atom of perchlorate ions. These interactions cause the scarcity of electrons on the chlorine atom resulting in the displacement of electron density from the rest of oxygen atoms towards chlorine, thus making it electron rich and tunes the effective nuclear charge. Thus, a shift towards lower binding energy is observed. This trend is further supported by a shift of 2 eV (533.5 eV)<sup>74</sup> at the position of the O 1s peak (Cl–O...Cu) towards lower binding energy due to the displacement of electron cloud from chlorine towards oxygen.

As it is a well-known fact that the local physical/chemical environment and the hybridization of the element have a significant effect on the binding energies. Analogous trends have been observed in a broad C 1s region encompassing several peaks *viz.* 281, 283.8 and 287.2 eV assigned to methylene ( $sp^3$ ), aromatic ( $sp^2$ ) and amide carbons (attached to N and O atoms), respectively.<sup>75</sup> Furthermore, in compound 2, the XPS bands 2P<sub>3/2</sub> at 780.3 eV and 2P<sub>1/2</sub> 798.6 eV<sup>71,76</sup> with corresponding satellite peaks at 785.2 and 802.3 eV, respectively, illustrate the presence of divalent Co(II) ions (Fig. S15, ESI† and Table 2). Conversely, the well resolved 2P<sub>3/2</sub> and 2P<sub>1/2</sub> bands at 1021.2 eV and 1044.5 eV, respectively, confirm the presence of Zn(II) ions in compound 3 and are in accordance with the reported values in the literature (Fig. S16, ESI† and Table 2).<sup>77,78</sup> The binding energies associated with different

elements of L1 and the perchlorate ion in 2 and 3 are tabulated in Table 2.

Besides XPS, the EDS analysis was performed to see the elemental composition in the bulk samples of 1 (Fig. 5), 2 and 3 (Fig. S17 and S18, ESI†). Besides, the intention behind the analysis is to see if all the elements and the metal ions are present in the bulk samples as observed in their crystal structure. The results obtained support the findings of SCXRD and XPS studies. The relevant SEM images and the corresponding percentage of different elements in these compounds obtained after surface mapping at 100  $\mu$ m are shown in Fig. 5 for 1, and Fig. S17 and S18 (ESI†) for 2 and 3, respectively.

### Thermal stability

Thermal stability studies were performed in the temperature range 30 to 850 °C for L1 and all compounds as well (Fig. S19, ESI†). The thermal decomposition curve for L1 illustrates its stability up to 110 °C, beyond which a steady weight loss takes place with a complete loss was observed at ~450 °C. The gradual decomposition after 90 °C was observed for 1 with 70% weight loss at ~280 °C, corresponding to decomposition of L1 and three DMF molecules (theoretical wt. loss 68.4%). The compound was decomposed completely at around 750 °C. Compound 2 has shown the highest thermal stability up to 230 °C, followed by irregular trends in decomposition patterns. Compound 3 was stable up to 115 °C with first 15% weight loss at 265 °C corresponds to the loss of two DMF molecules (theoretical wt. loss 15.4%). Following this, the gradual decomposition was observed.

### Theoretical studies

Before discussing the results of DFT calculations in detail, we would like to mention that the HOMO–LUMO energy gaps calculated here cannot be used to rationalize the colours of compounds 1–3, which is light green for compound 1, light burgundy for 2, and colorless for 3. The rationale for this is that all the calculations were performed considering the effect of DMF molecules on the HOMO–LUMO states of these compounds, due to which anomalies in the energy gap values are observed with an energy value of the Zn(II) compound (3) being little bit less than that of the Cu(II) compound (1) that otherwise should have shown the reverse trend in the absence of solvent effects. The geometry

**Table 2** Values of the core level binding energies of different elements involved in 1, 2 and 3

Compound	M <sup>n+</sup> ion	Metal 2p peaks	Peak assignment	N 1s peak	Peak assignment	O 1s peak	Peak assignment	Cl 2p peaks	Peak assignment	C 1s peaks	Peak assignment
1	Cu <sup>+2</sup>	933.8 eV	Cu 2P <sub>3/2</sub>	398.4 eV	Pyridine nitrogen	528.7 eV	Amide (C=O)	196.8 eV	Cl 2P <sub>3/2</sub>	281.4 eV	Methylene
		942.6 eV	Cu (+2) satellite			530.4 eV	Coordinated DMF	198.9 eV	Cl 2P <sub>1/2</sub>	283.2 eV	Aromatic
		953.9 eV	Cu 2P <sub>1/2</sub>							284.4 eV	Pyridine
		962.1 eV	Cu (+2) satellite			531.5 eV	Perchlorate ion			287.2 eV	Amide
2	Co <sup>+2</sup>	780.3 eV	Co 2P <sub>3/2</sub>	398.5 eV	Pyridine nitrogen	530.3 eV	Amide (C=O)	197.3 eV	Cl 2P <sub>3/2</sub>	282.8 eV	Methylene
		785.2 eV	Co (+2) satellite			531.1 eV	Coordinated DMF			283.3 eV	Aromatic
		798.6 eV	Co 2P <sub>1/2</sub>					198.9 eV	Cl 2P <sub>3/2</sub>	284.3 eV	Pyridine
		802.3 eV	Cu (+2) satellite			533.1 eV	Perchlorate ion			287.6 eV	Amide
3	Zn <sup>+2</sup>	1021.4 eV	Zn 2P <sub>3/2</sub>	398.8 eV	Pyridine nitrogen	529.7 eV	Amide (C=O)	197.1 eV	Cl 2P <sub>3/2</sub>	280.5 eV	Methylene
						531.1 eV	Coordinated DMF			283.4 eV	Aromatic
		1044.6 eV	Zn 2P <sub>1/2</sub>					198.8 eV	Cl 2P <sub>1/2</sub>	284.5 eV	Pyridine
						532.5 eV	Perchlorate ion			287.4 eV	Amide



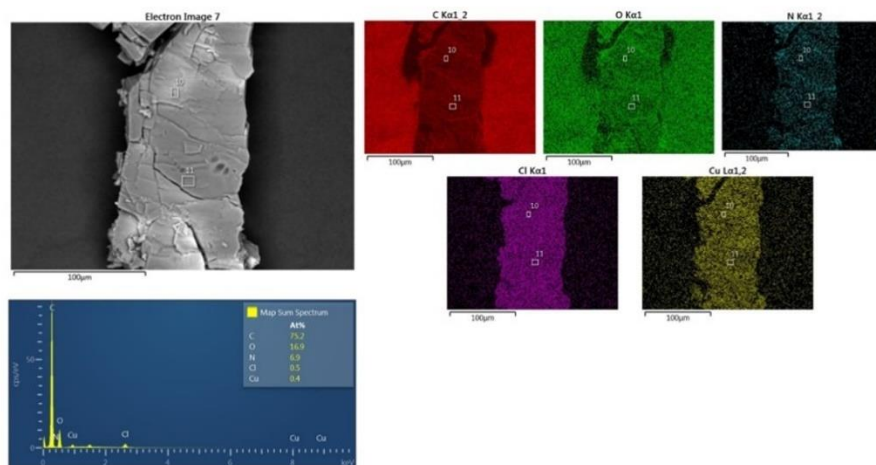


Fig. 5 Results of the SEM and EDS analyses of **1**.

optimization of the ligand and compounds **1–3** using DFT studies (Fig. 6 and Fig. S20, ESI†) shows that the energy gap between the HOMO and LUMO states follows the order 4.609 eV (**2**) < 4.737 eV (**3**) < 4.742 eV (**1**) < 4.752 eV (**L1**), which can be attributed to (1) the tuning of electron densities in the ligand molecule upon coordination to metal ions, and (2) the effect on the energies of these states due to the interaction with DMF molecules (solvent effect).

The variation in the energies of the HOMO–LUMO states of these compounds relative to the HOMO–LUMO of **L1** has been tabulated below (Table 3). The irregularity in the HOMO–LUMO energy gap between compounds **1** and **3** could be explained by referring to the information given in Table 3. Owing to the interaction of HOMO–LUMO states with DMF molecules, the energy of the HOMO state is increased by 0.07 eV in case of **3** (Zn(II) compound) relative to **L1**. Whereas, it is 0.064 eV in **1** (Cu(II) compound). Similarly, the increase in the energy of LUMO state is 0.054 eV in **3** and 0.053 eV in **1**. Considering

these trends, it can be concluded that the energy of the HOMO state is uplifted in the Zn(II) compound than the Cu(II) compound by 0.006 eV than the energy of the LUMO, which is just increased by 0.001 eV than the Cu(II) compound resulting in a little decrease in the energy gap of the Zn(II) compound. In contrast, the solvent effects in the compound containing the Co(II) ion (**2**) have resulted in a lower HOMO–LUMO gap of 4.609 eV, owing to the increase in the energy of the HOMO by a value of 0.194 eV than its LUMO (0.05 eV) as shown in Table 3.

Furthermore, to gain better understanding of binding energies involved in the metal–ligand coordination bond of all compounds and in hydrogen bonded **L1** fragments, the energy decomposition analysis (EDA) was performed at the BLYP-D3/TZ2P level.<sup>61,65</sup> In this regard, the total interaction energy was decomposed into various contributions of electrostatic interactions, orbital interactions, Pauli repulsion, and dispersion interactions in accordance with the framework of Kohn–Sham molecular orbital theory. The results of the analysis are shown

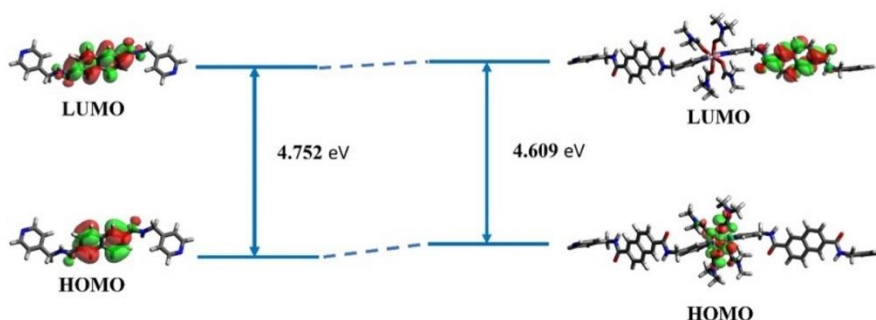


Fig. 6 View of the increase in energies of the HOMO–LUMO states of **2** affected by the interaction with solvent molecules relative to the HOMO–LUMO states of **L1**. (Note – Fig. 6 shows the speculative extent to which the HOMO–LUMO states of **2** are affected by solvent effects relative to the HOMO–LUMO states of **L1**. In compound **2**, the solvent effect of DMF has led to an increase in energy of the HOMO by 0.194 eV than that of the LUMO (0.05 eV)).

Table 3 Variation in the HOMO–LUMO energies of compounds 1–3 relative to L1

Compound	HOMO (eV)	LUMO (eV)	$E_{\text{gap}}$ (eV)	Increase in the energy of HOMO relative to L1	Increase in the energy of LUMO relative to L1
L1	−6.862	−2.109	4.752	—	—
1 (Cu(II) compound)	−6.798	−2.056	4.742	0.064	0.053
2 (Co(II) compound)	−6.668	−2.059	4.609	0.194	0.05
3 (Zn(II) compound)	−6.792	−2.055	4.737	0.07	0.054

Table 4 Energy decomposition analysis on L1 and 1–3

Compound	Type of bond/interaction	M–N <sub>Pyridine</sub> (L) bond length	$E_{\text{Total}}$ (Kcal mol <sup>−1</sup> )	$E_{\text{Total}}$ decomposition into associated components (Kcal mol <sup>−1</sup> )
L1	L···L (Hydrogen bond)	—	−7.17	$E_{\text{Pauli}} = 4.57$ $E_{\text{Electrostatic}} = -3.63$ $E_{\text{Orbital}} = -2.13$ $E_{\text{Dispersion}} = -5.98$
1	Cu ← N <sub>Pyridine</sub> (L)	2.018 (3)	−110.01	$E_{\text{Pauli}} = 123.57$ $E_{\text{Electrostatic}} = -96.76$ $E_{\text{Orbital}} = -121.25$ $E_{\text{Dispersion}} = -15.58$
2	Co ← N <sub>Pyridine</sub> (L)	2.1601 (18)	−52.34	$E_{\text{Pauli}} = 71.49$ $E_{\text{Electrostatic}} = -63.63$ $E_{\text{Orbital}} = -47.48$ $E_{\text{Dispersion}} = -12.72$
3	Zn ← N <sub>Pyridine</sub> (L)	2.1640 (19)	−24.09	$E_{\text{Pauli}} = 67.89$ $E_{\text{Electrostatic}} = -61.50$ $E_{\text{Orbital}} = -17.65$ $E_{\text{Dispersion}} = -12.83$

in Table 4, which shows that among all compounds, the total bonding energy ( $E_{\text{Total}}$ ) is more negative for 1 than those for compounds 2 and 3. This trend can be attributed to Jahn–Teller distortions that are more prevalent in compound 1. In contrast, between compounds 2 and 3, more negative total bonding energies in 2 are due to significant M → L back-bonding than those in 3. The energy values obtained for M–N<sub>Pyridine</sub> coordination bonds are in good agreement with corresponding bond lengths (Table 4) obtained from the crystal structures of these compounds. It is worth mentioning that the orbital interaction component ( $E_{\text{Orbital}}$ ) is the largest attractive term in 1 that plays an important role in the stabilization of the Cu ← N<sub>Pyridine</sub> (L1) coordination bond, whereas it is the electrostatic component ( $E_{\text{Electrostatic}}$ ) in 2 and 3.

## Conclusion

Three new 1D coordination polymers synthesized using L1 struts are characterized by SCXRD. The diffraction studies showed that these compounds are isostructural in nature, which is further confirmed from 'X', a dissimilarity index, using XPac 2.0 software. The single crystal structure of L1 illustrates that hydrogen bonding networks are strengthened by non-covalent interactions such as  $\pi \cdots \pi$  and H···H. Similarly, extensive hydrogen bonding is observed in these compounds between 1D chains and perchlorate anions in a hydrogen bonded 2D sheet and a 3D framework. The XPS studies illustrate that divalent metal ions are present in these compounds

and also provided the information about chemical environments of various non-metals present. The elemental composition obtained by EDS studies further supplements the information obtained by single crystal diffraction and XPS studies. DFT studies have shown a strange trend in the HOMO–LUMO energy gaps of compounds 1 and 3, which can be attributed to solvent effects on these states, which are more in compound 3 than in compound 1. The total bonding energy  $E_{\text{Total}}$  (Kcal mol<sup>−1</sup>) values obtained from the energy decomposition analysis on representative molecular fragment, [M(L1)<sub>2</sub>(DMF)<sub>4</sub>] shows that Jahn–Teller distortions are more prevalent in compound 1, which resulted in a more negative value. However, between compounds 2 and 3, metal to ligand back bonding M → N<sub>Pyridine</sub> (L) is dominant in 2 than 3, resulting in a more negative energy value. These results are in good agreement with the observed crystallographic M–N<sub>Pyridine</sub> (L1) bond lengths of respective complexes.

## Conflicts of interest

There are no conflicts to declare.

## Acknowledgements

We are grateful to the Natural Sciences and Engineering Research Council of Canada (DDG-2022-00002), the Canadian Queen Elizabeth II Diamond Jubilee Scholarships, the Fonds de recherche du Québec – Nature et technologies, The Canadian Foundation for Innovation (37843), Mitacs and the Université

du Québec à Trois-Rivières. We are thankful to Mr. Parveen Nasa, Department of chemistry, IISER Pune, India, for the single crystal data of **L1**.

## References

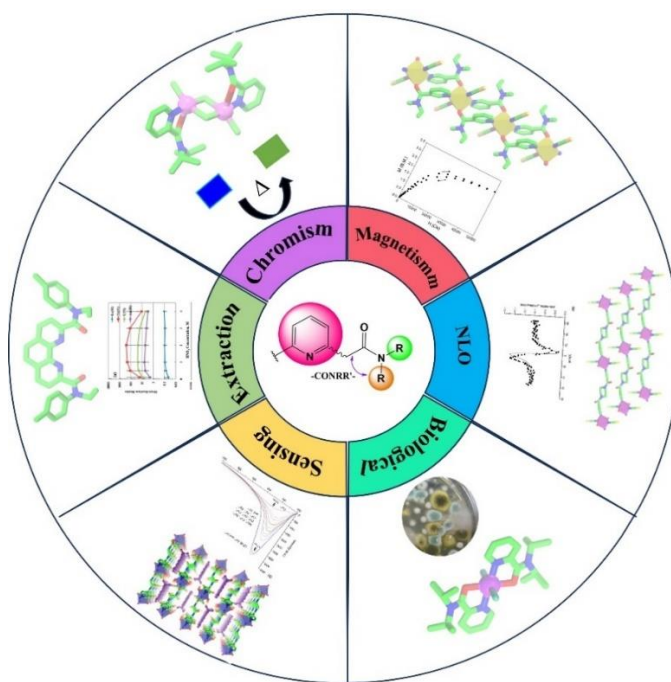
- 1 S. R. Batten and R. Robson, *Angew. Chem., Int. Ed.*, 1998, **37**, 1460.
- 2 Y. Gong, Z. Hao, J. L. Sun, H. F. Shi, P. G. Jiang and J. H. Lin, *Dalton Trans.*, 2013, **42**, 13241.
- 3 Y. Gong, T. Wua and J. H. Lin, *CrystEngComm*, 2012, **14**, 3727.
- 4 Y. Niu, Y. Song, T. Chen, Z. Xue and X. Xin, *CrystEngComm*, 2001, **3**, 152.
- 5 Y. Liu, G. Li, X. Li and Y. Cui, *Angew. Chem., Int. Ed.*, 2007, **46**, 6301.
- 6 L. Wang, M. Yang, G. H. Li, Z. Shi and S. H. Feng, *Inorg. Chem.*, 2006, **45**, 2474.
- 7 H. A. Habib, A. Hoffmann, H. A. Hoppea and C. Janiak, *Dalton Trans.*, 2009, 1742.
- 8 S. Goswami, G. Leitus, B. K. Tripuramallu and I. Goldberg, *Cryst. Growth Des.*, 2017, **17**, 4393.
- 9 A. P. S. Pannu, P. Kapoor, G. Hundal, R. Kapoor, M. Corbella, N. A. Alcalde and M. S. Hundal, *Dalton Trans.*, 2011, **40**, 12560.
- 10 H. Miyasaka, M. Julve, M. Yamashita and R. Clérac, *Inorg. Chem.*, 2009, **48**, 3420.
- 11 X. M. Zhang, Y. Q. Wang, Y. Song and E. Q. Gao, *Inorg. Chem.*, 2011, **50**, 7284.
- 12 J. Yang, Q. Yue, G. D. Li, J. J. Cao, G. H. Li and J. S. Chen, *Inorg. Chem.*, 2006, **45**, 2857.
- 13 B. S. Sran, S. Sharma, F. Pointillart, O. Cador and G. Hundal, *Inorg. Chem.*, 2021, **60**, 3479.
- 14 M. Li, L. Liu, L. Zhang, X. Lv, J. Ding, H. Hou and Y. Fan, *CrystEngComm*, 2014, **16**, 6408.
- 15 J. M. Hao, B. Y. Yu, K. V. Hecke and G. H. Cui, *CrystEngComm*, 2015, **17**, 2279.
- 16 H. J. Du, C. H. Wang, Y. Li, Z. C. Yue, L. R. Zhang, L. Li, W. L. Zhang, Y. Y. Niu and H. W. Hou, *Inorg. Chim. Acta*, 2015, **430**, 46.
- 17 Y. Qi, F. Luo, Y. X. Che and J. M. Zheng, *Cryst. Growth Des.*, 2008, **8**, 606.
- 18 O. D. Friedrichs, M. O'Keeffe and O. M. Yaghi, *Acta Crystallogr., Sect. A: Found. Crystallogr.*, 2003, **59**, 22.
- 19 T. L. Hennigar, D. C. MacQuarrie, P. Losier, R. D. Rogers and M. J. Zaworoko, *Angew. Chem., Int. Ed.*, 1997, **36**, 972.
- 20 S. L. James, *Chem. Soc. Rev.*, 2003, **32**, 276.
- 21 S. L. Huang, L. H. Weng and G. X. Jin, *Dalton Trans.*, 2012, **41**, 11657.
- 22 A. Morsali and M. Y. Masooumi, *Coord. Chem. Rev.*, 2009, **253**, 1882.
- 23 W. L. Leong and J. J. Vittal, *Chem. Rev.*, 2011, **111**, 688.
- 24 T. J. Burchell, D. J. Eisler and R. J. Puddephatt, *Inorg. Chem.*, 2004, **43**, 5550.
- 25 B. C. Tzeng, T. H. Chiu, B. S. Chen and G. H. Lee, *Chem. – Eur. J.*, 2008, **14**, 5237.
- 26 S. Muthu, J. H. K. Yip and J. J. Vittal, *J. Chem. Soc., Dalton Trans.*, 2002, **24**, 4561.
- 27 S. Muthu, J. H. K. Yip and J. J. Vittal, *J. Chem. Soc., Dalton Trans.*, 2001, **24**, 3577.
- 28 C. L. Schauer, E. Matwey, F. W. Fowler and J. W. Lauher, *J. Am. Chem. Soc.*, 1997, **119**, 10245.
- 29 C. B. Aakeroy, *Chem. Commun.*, 1998, 1067.
- 30 C. B. Aakeroy, A. M. Beatty, J. Desper, M. O'Shea and J. V. Martinez, *Dalton Trans.*, 2003, 3956.
- 31 Z. Qin, M. C. Jennings and R. J. Puddephatt, *Chem. – Eur. J.*, 2002, **8**, 735.
- 32 Z. Qin, M. C. Jennings and R. J. Puddephatt, *Inorg. Chem.*, 2001, **40**, 6220.
- 33 Z. Qin, M. C. Jennings and R. J. Puddephatt, *Chem. Commun.*, 2001, 2676.
- 34 X. Xu, S. L. James, D. M. P. Mingos, A. J. P. White and D. J. Williams, *J. Chem. Soc., Dalton Trans.*, 2000, **21**, 3783.
- 35 C. J. Kuehl, F. M. Tabellion, A. M. Arif and P. Stang, *J. Organometallics*, 2001, **20**, 1956.
- 36 T. J. Burchell, D. J. Eisler, M. C. Jennings and R. J. Puddephatt, *Chem. Commun.*, 2003, 2228.
- 37 T. J. Burchell, D. J. Eisler and R. J. Puddephatt, *Chem. Commun.*, 2004, 944.
- 38 G. Li, Y. Song, H. Hou, L. Li, Y. Fan, Y. Zhu, X. Meng and L. Mi, *Inorg. Chem.*, 2003, **42**, 913.
- 39 L. Raehm, L. Mimassi, C. G. Duhayon and H. Amouri, *Inorg. Chem.*, 2003, **42**, 5654; S. Sailaja and M. V. Rajasekharan, *Inorg. Chem.*, 2003, **42**, 5675.
- 40 B. R. Bhogala, P. K. Thallapally and A. Nangia, *Cryst. Growth Des.*, 2004, **4**, 215.
- 41 M. L. Tong, Y. M. Wu, J. Ru, X. M. Chen, H. C. Chang and S. Kitagawa, *Inorg. Chem.*, 2002, **41**, 4846.
- 42 Z. Qin, M. C. Jennings and R. J. Puddephatt, *Inorg. Chem.*, 2002, **41**, 5174.
- 43 L. Brammer, J. C. M. Rivas, R. Atencio, S. Fang and F. C. Pigge, *J. Chem. Soc., Dalton Trans.*, 2000, **21**, 3855.
- 44 C. B. Aakeroy, A. M. Beatty and K. R. Lorimer, *J. Chem. Soc., Dalton Trans.*, 2000, **21**, 3869.
- 45 J. C. MacDonald, P. C. Dorrestein, M. M. Pilley, M. M. Foote, J. L. Lundburg, R. W. Henning, A. J. Schultz and J. L. Manson, *J. Am. Chem. Soc.*, 2000, **122**, 11692.
- 46 T. Gelbrich and M. B. Hursthouse, *CrystEngComm*, 2005, **7**, 324.
- 47 T. Gelbrich and M. B. Hursthouse, *CrystEngComm*, 2006, **8**, 448.
- 48 F. P. A. Fabbiani, B. Dittrich, A. J. Florence, T. Gelbrich, M. B. Hursthouse, W. F. Kuhs, N. Shankland and H. Sowa, *CrystEngComm*, 2009, **11**, 1396.
- 49 P. Rani, Gauri, A. Hussain, K. K. Bhasin and G. Kumar, *Cryst. Growth Des.*, 2020, **20**, 7141.
- 50 P. Rani, Gauri, A. Hussain, K. K. Bhasin and G. Kumar, *Chem. Asian Journal*, 2022, **17**, DOI: [10.1002/asia.202101204](https://doi.org/10.1002/asia.202101204).
- 51 P. Rani, Gauri, A. Hussain, K. K. Bhasin and G. Kumar, *Inorg. Chem.*, 2022, **61**, 6977.
- 52 (a) A. Altomare, G. L. Casciarano, C. Giacovazzo and A. Guagliardi, *J. Appl. Crystallogr.*, 1993, **26**, 343; (b) G. M. Sheldrick, *Acta Cryst.*, 2015, **A71**, 3.



- 53 G. M. Sheldrick, *Acta Cryst.*, 2015, **C71**, 3.
- 54 O. V. Dolomanov, L. J. Bourhis, R. J. Gildea, J. A. K. Howard and H. Puschmann, *J. Appl. Crystallogr.*, 2009, **42**, 339.
- 55 C. F. Macrae, I. Sovago, S. J. Cottrell, P. T. A. Galek, P. McCabe, E. Pidcock, M. Platings, G. P. Shields, J. S. Stevens, M. Towler and P. A. Wood, *J. Appl. Crystallogr.*, 2020, **53**, 226.
- 56 F. Neese, F. Wennmohs, U. Becker and C. Riplinger, *J. Chem. Phys.*, 2020, **152**, 224108.
- 57 A. V. Marenich, C. J. Cramer and D. G. Truhlar, *J. Phys. Chem. B*, 2009, **113**, 6378.
- 58 J. P. Perdew, K. Burke and M. Ernzerhof, *Phys. Rev. Lett.*, 1996, **77**, 3865.
- 59 F. Weigend and R. Ahlrichs, *Phys. Chem. Chem. Phys.*, 2005, **7**, 3297.
- 60 L. Goerigk, A. Hansen, C. Bauer, S. Ehrlich, A. Najibi and S. Grimme, *Phys. Chem. Chem. Phys.*, 2017, **19**, 32184–32215.
- 61 S. Grimme, S. Ehrlich and L. Goerigk, *J. Comput. Chem.*, 2011, **32**, 1456–1465.
- 62 S. Grimme, J. Antony, S. Ehrlich and H. Krieg, *J. Chem. Phys.*, 2010, **132**, 154104.
- 63 F. Weigend and R. Ahlrichs, *Phys. Chem. Chem. Phys.*, 2005, **7**, 3297–3305.
- 64 F. Weigend, *Phys. Chem. Chem. Phys.*, 2006, **8**, 1057.
- 65 G. T. Velde, F. M. Bickelhaupt, E. J. Baerends, C. F. Guerra, S. J. A. V. Gisbergen, J. G. Snijders and T. Ziegler, *J. Comput. Chem.*, 2001, **22**, 931.
- 66 (a) A. D. Becke, *Phys. Rev.*, 1988, **38**, 3098; (b) C. Lee, W. Yang and R. G. Parr, *Phys. Rev. B: Condens. Matter Mater. Phys.*, 1988, **37**, 785.
- 67 E. Lenthe, A. Ehlers and E. J. Baerends, *J. Chem. Phys.*, 1999, **110**, 8943.
- 68 G. R. Desiraju, J. J. Vittal and A. Ramanan, *Crystal Engineering, A Textbook*, World Scientific Publishing Co. Pte. Ltd., Singapore, 2011.
- 69 L. K. Rana, S. Sharma and G. Hundal, *Cryst. Growth Des.*, 2016, **16**, 92.
- 70 L. K. Rana, S. Sharma and G. Hundal, *J. Mol. Struct.*, 2018, **1153**, 324.
- 71 Y. A. Torres, L. Huerta and N. B. Behrens, *J. Chem.*, 2013, **2013**, 1.
- 72 M. Jo and A. Tanaka, *Appl. Surf. Sci.*, 1996, **100**, 11.
- 73 K. Artyushkova, *J. Vac. Sci. Technol.*, 2020, **A38**, 031002.
- 74 B. C. Beard, *Surf. Sci. Spectra*, 1993, **2**, 97.
- 75 <https://www.eag.com/resources/appnotes/xps-chemical-shift-and-valence/>.
- 76 Y. G. Borod'ko, S. I. Vetchinkin, S. L. Zimont, I. N. Ivleva and Yu. M. Shul'ga, *Chem. Phys. Lett.*, 1976, **42**, 264.
- 77 S. Evans, *Surf. Interface Anal.*, 1985, **7**, 299.
- 78 B. R. Strohmeier, *Surf. Sci. Spectra*, 1994, **3**, 128.

## Chapter – 4

# Fascinating Tertiary Carboxamide Ligands and Their Coordination Complexes: An Account on Structural Chemistry and Practical Applications



Rana *et. al*, *Coord. Chem. Rev.*, **Manuscript No.- CCR-D-24-00580**



## 4.1 Introduction

Pyridine ring is a popular coordination moiety used in ligands to synthesize a variety of coordination complexes with different metal ions. Among these, ligands with carboxamide secondary (CONHR)/tertiary (CORR) linker moiety have been widely used in the fabrication of a variety of metal complexes owing to: 1) biological importance (construction unit of primary structure of proteins) and 2) medicinal properties (antifungal, antitumor, and anticancer activities) of bioactive compounds containing the amide group. Besides, some metal complexes pertaining to this class of ligands have been explored as bio-mimetic structural models of several metallo-enzymes *viz.* nitrile hydratase, nickel superoxide dismutase etc. This review discusses the coordination chemistry of carboxamide ligands with fully substituted amide nitrogen atom (-CONRR), in which pyridine ring is either an anchor moiety or part of it, or a free pendent group appended to anchor moiety, or both. Literature reports some review articles on pyridine carboxamide ligands with secondary nitrogen atoms (-CONHR-), however, to the best of our knowledge, there has been no discussion or report so far on the carboxamide/dicarboxamide ligands containing pyridine ring and tertiary amide nitrogen atoms and their complexes, which makes this review article a pioneer in the field. Besides, in this article, structure chemistry and applications of only those coordination complexes (along with the ligands) are discussed whose crystal data details are available in CSD database, right from the first entry up to the most recent one. While the ligand molecules have been systematically classified based on the position of pyridine moiety, the relevant complexes have been segregated based upon the dimensionality of the coordination networks.

## 4.2 Objective

- To give a brief account on the coordination chemistry of carboxamide ligands with fully substituted amide nitrogen atom (-CONRR), in which pyridine ring is either an anchor moiety or part of it, or as a free pendent group appended to anchor moiety, or both.
- To provide a better overview to the researchers about the above-mentioned interesting ligand designs and the application of their coordination complexes.

### **4.3 Authors contribution**

- Conceptualization – Love Karan Rana
- Investigation – Love Karan Rana
- Supervision – Love Karan Rana
- Visualization – Love Karan Rana
- Writing - original draft – Love Karan Rana
- Writing – review and editing – Love Karan Rana and Prabhjot Kaur

### **4.4 Article**

# Fascinating Tertiary Carboxamide Ligands and Their Coordination Complexes: an Account on Structural Chemistry and Practical Applications

Love Karan Rana<sup>1</sup> and Prabhjyot Kaur<sup>1</sup>

<sup>1</sup>*Département de Chimie, Biochimie et physique and Institut de Recherche sur l'Hydrogène, Université du Québec à Trois-Rivières, Trois-Rivières, Québec, G9A 5H7, Canada*

\*To whom correspondence should be addressed. E-mail: [love.karan@uqtr.ca](mailto:love.karan@uqtr.ca)

**Abstract** – Pyridine ring is the popular coordination moiety after carboxylic group, frequently used in the ligands to synthesize a variety of coordination complexes with different metal ions. Among these, ligands with carboxamide secondary (CONHR)/tertiary (CORR) linker moiety have been widely used in the fabrication of a variety of metal complexes. Profuse interest in new ligand designs comprising amide motifs as a structural unit could be credited to its 1) biological importance as it serves as main construction unit of primary structure of proteins, and 2) medicinal properties as it is a common structural motif of various bioactive compounds displaying antifungal, antitumor, and anticancer activities. Besides, some metal complexes pertaining to this class of ligands have been explored as bio-mimetic structural models of several metallo-enzymes *viz.* nitrile hydratase, nickel superoxide dismutase etc. This review discusses the coordination chemistry of carboxamide ligands with fully substituted amide nitrogen atom (-CONRR), in which pyridine ring is either an anchor moiety or part of it, or a free pendent group appended to anchor moiety, or both. A considerable amount of research has been conducted using these ligands owing to the fascinating coordination networks formed by their complexes and their remarkable applications all of which has been compiled and presented in this present review. Literature reports some review articles on pyridine carboxamide ligands with secondary nitrogen atoms (-CONHR-), however to the best of our knowledge there has been no discussion or report so far on the carboxamide/dicarboxamide ligands containing pyridine ring and tertiary amide nitrogen atoms and their complexes, which makes this review article a pioneer in the field. Besides, in this article, structure chemistry and

applications of only those coordination complexes (along with the ligands) are discussed whose crystal data details are available in CSD database, right from the first entry up to the most recent one. While the ligand molecules have been systematically classified based on the position of pyridine moiety, the relevant complexes have been segregated based upon the dimensionality of the coordination networks. The CSD version 2021.3 was used to conduct crystal data search. This work is intended to compile interesting ligand designs to keep the researchers aware of the library of ligands available along with the development made in this field vis-à-vis coordination complexes and relevant applications. We believe that researchers will get a better insight into the work that has already been done in this field, which will help them to come up with novel ideas of what else could possibly be done that could help in further advancements from both synthetic and practical point of view.

### Designation of Ligands

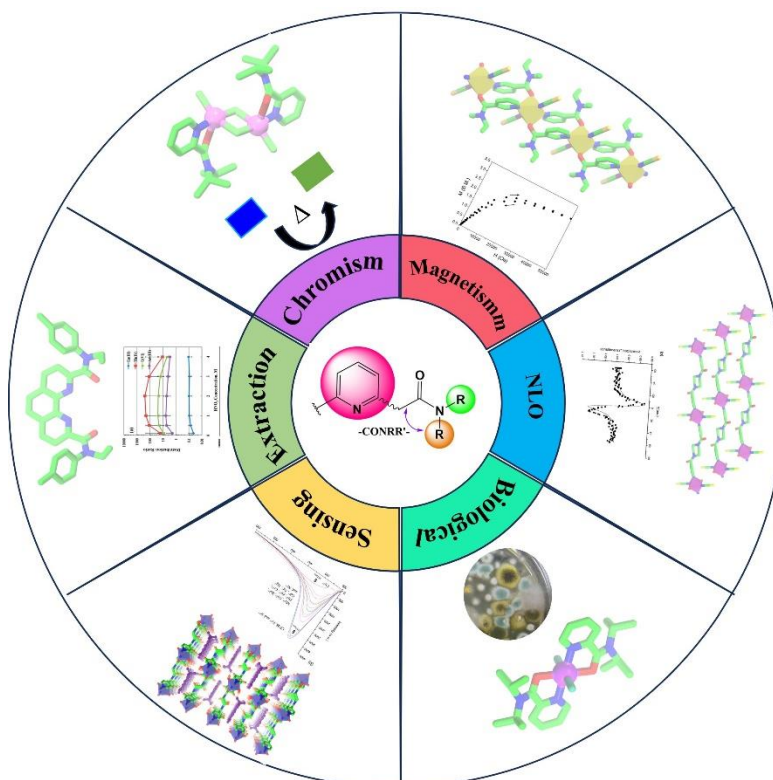
**L<sup>1</sup>:** N,N-diisopropylpyridine-2-carboxamide, **L<sup>2</sup>:** N,N-diisobutylpyridine-2-carboxamide, **L<sup>3</sup>:** N,N-diethylpyridine-3-carboxamide (nicotinamide), **L<sup>4</sup>:** N,N-diisopropylpyridine-4-carboxamide, **L<sup>5</sup>:** N,N-diisobutylpyridine-4-carboxamide, **L<sup>6</sup>:** N,N,N',N'-tetramethylpyridine-2,6-dicarboxamide, **L<sup>7</sup>:** N,N,N',N'-tetraethylpyridine-2,6-dicarboxamide, **L<sup>8</sup>:** N,N,N',N'-tetrabutylpyridine-2,6-dicarboxamide, **L<sup>9</sup>:** N,N,N',N'-tetraisopropylpyridine-2,6-dicarboxamide, **L<sup>10</sup>:** N,N,N',N'-tetraisobutylpyridine-2,6-dicarboxamide, **L<sup>11</sup>:** N,N,N',N'-tetrabenzylpyridine-2,6-dicarboxamide, **L<sup>12</sup>:** N,N'-dimethyl-N,N'-diphenylpyridine-2,6-dicarboxamide, **L<sup>13</sup>:** N,N'-diethyl-N,N'-diphenylpyridine-2,6-dicarboxamide, **L<sup>14</sup>:** N,N'-diethyl-N,N'-ditolylpyridine-2,6-dicarboxamide, **L<sup>15</sup>:** N,N,N',N'-tetraisopropylpyridine-3,5-dicarboxamide, **L<sup>16</sup>:** N,N,N',N'-tetraisobutylpyridine-3,5-dicarboxamide, **L<sup>17</sup>:** N,N,N',N'-tetraisopropylpyridine-3,4-dicarboxamide, **L<sup>18</sup>:** N,N,N',N'-tetraisobutylpyridine-3,4-dicarboxamide, **L<sup>19</sup>:** N,N'-bis(3-pyridylformyl) imidazolidine-2-thione, **L<sup>20</sup>:** N,N'-bis(4-pyridylformyl) imidazolidine-2-thione, **L<sup>21</sup>:** N,N'-bis(3-pyridylcarbonyl)piperazine, **L<sup>22</sup>:** N,N'-bis(4-pyridylcarbonyl)piperazine, **L<sup>23</sup>:** N,N'-diethyl-N,N'-bis(R-phenyl)-[2,2'-bipyridine]-6,6'-dicarboxamides, **L<sup>24</sup>:** N,N'-diethyl-N,N'-bis(R-3,5-diMephenyl)-[2,2'-bipyridine]-6,6'-dicarboxamides, **L<sup>25</sup>:** N,N'-diethyl-N,N'-bis(R-2,5-diMephenyl)-[2,2'-bipyridine]-6,6'-dicarboxamides, **L<sup>26</sup>:** N,N'-diethyl-N,N'-bis(4-ethylphenyl)-1,10-phenanthroline-2,9-dicarboxamide, **L<sup>27</sup>:** N,N'-diethyl-N,N'-ditolyl-1,10-phenanthroline-2,9-dicarboxamide, **L<sup>28</sup>:** N,N,N',N'-tertaethyl-4,7-(bis(pentoxy))-1,10-phenanthroline-2,9-dicarboxamide, **L<sup>29</sup>:** 4,7-dichloro-N,N'-diethyl-N,N'-bis(4-hexylphenyl)-1,10-phenanthroline-2,9-dicarboxamide, **L<sup>30</sup>:**

N,N'-dimethyl-N,N'-bis(2'-pyridinecarboxamide)-1,2ethane, **L<sup>31</sup>**: 7,16-bis(pyridine-4-carbamoyl)-1,4,10,13-tetraoxa-7,16-diazacyclo-octadecane, **L<sup>32</sup>**: 13,18-Dihexyl1,2,3,4,4a,8b,9,10,11,12,12a,13,18,18a-tetradecahydro-1,4:9,12-dimethanodiquinolino[3,4-b:4',3'-j][1,10]phenanthroline-14,17-dione, **L<sup>33</sup>**: 2,11-Dihexyl-3,4,9,10-tetraphenyl-2,11-dihydrodipyrido[3,4-b:4',3'-j][1,10]phenanthroline-1,12-dione.

### Abbreviations for Ancillary ligands/anions

**NCS**: Isothiocyanate, **SCN**: Thiocyanate, **Pmb**: 4-methylbenzoate, **Benzo**: Benzoate, **N<sub>2</sub>S<sub>2</sub>**: Diacetyl-bis-hydrazonato-S-methyl-carbodithioate, **Clof**: Clofibrate, **Deab**: 4-(diethylamino) benzoate, **Dmab**: Dimethylaminobenzoate, **Cl-Ac**: Chloroacetate, **Cbenz**: Chlorobenzoate, **NS**: S-methylisopropylidenehydrazinecarbodithioate, **Bpfp**: 4-pyridylformyl) piperazine, **Mal**: Malonic acid, **Hmph**: Homophthalate, **Mip**: 5-methylisophthalate, **MeOip**: 5-methoxyisophthalate, **SUL**: 5-sulphosalicylic acid, **PhthH**: Phthalate (singly protonated), **OAc**: Acetate, **NPOE**: o-nitrophenyloctyl ether, **2F2N**: 2-fluorophenyl 2-nitrophenyl ether, **KTFPB**: tetrakis[3,5-bis(trifluoromethyl)-phenyl borarate].

### Graphical Abstract



## 1. General Overview

In coordination chemistry the dimensionalities of coordination networks are determined explicitly by the position of the donor atoms with respect to each other in a ligand molecule, and the coordination requirements of metal ions. Consequently, the ligand molecules with convergent coordination sites lead to mononuclear chelating complexes of zero dimensionality while those with the divergent sites leads to binuclear to polymeric complexes. The key prerequisite is that the ligand molecule should bridge between metal ions, and this will be possible if it is multidentate i.e., with more than one coordination sites, which must be positioned distant from each other (divergent in nature). Among various organic linkers the rigid bridging linkers are important as they control certain steric effects in the self-assembly process. By varying the ligand linker molecules and/or associated functional groups, diversity in structural topology can be achieved [1, 2].

The polymeric complexes are often referred to as coordination polymers (CPs) primarily due the presence of adhesive force *viz.* coordination covalent bond. The term coordination polymer can be defined as a self-assembled infinite array comprising metal nodes connected by certain organic linkers [3]. Metal-coordination polymers show remarkable structures, properties, and reactivities that are not present in mononuclear complexes. They are functional materials with wide range of potential applications in catalysis, molecular adsorption, magnetism and nonlinear optics [4]. The term coordination polymer generally covers a broad range of architectures varying from simple 1D chain involving small ligands to large mesoporous networks [5].

As is well known that the self-assembly process, and the type and topology of final product depends on the nature of metal ion and associated counter anion. In this context, transition metal ions have been extensively used as versatile connecting nodes in the coordination polymers because these metal ions display different geometries ranging from low coordination linear, T-shapes, and tetrahedral to high coordination square-pyramidal, trigonal-bipyramidal, octahedral, trigonal-prismatic, and pentagonal-bipyramidal geometries [6]. This feature of metal ions introduces structure element not usually seen in organic ligands which helps in fabricating efficient materials with valuable properties and definite topologies [7-13]. Moreover, the use of labile metal ions such as  $\text{Cu}^{+2}$ ,  $\text{Ag}^{+}$ ,  $\text{Ni}^{+2}$ ,  $\text{Zn}^{+2}$ ,  $\text{Cd}^{+2}$  and  $\text{Hg}^{+2}$  favour the crystalline product/single crystal formation by facilitating reversible bond formation between metal ions and ligand molecules so that the initial kinetically controlled products can rearrange

themselves to more ordered, thermodynamically favoured crystalline product [14], which can be used for structure elucidation by diffraction studies.

Sometimes inorganic anions such as  $\text{CN}^-$ ,  $\text{-(R,H)O}^-$ ,  $\text{Cl}^-$ ,  $\text{N}_3^-$ ,  $\text{-(R,O)SO}_3^-$ ,  $\text{-(R,O)PO}_3^-$  etc. break infinite metal-ligand assembly via bridging among adjacent metal nodes. This way organic–inorganic hybrid materials are obtained [15]. In the view of the role of rigid organic ligands in the self-assembly of coordination networks, the coordination complexes of the ligands with fully substituted nitrogen atom (tertiary nitrogen) of amide moiety ( $\text{CONRR}'$ ) are quite appealing owing to their interesting architectures, which involves coordination networks and/or hydrogen bonding networks or both, and diversity of applications associated with them. The important advantage of this class of ligands over others is their solubility in almost all organic solvents, and thus negligible chance of the precipitation of the resulting complex on the addition of metal salt. This could be attributed to the absence of hydrogen atom on amide nitrogen in contrast to secondary amides ( $\text{CONHR}$ ) that precludes the possibility of hydrogen bonding between neighbouring ligand /solvent molecules (in the complex too) resulting in a clear solution. Thus, there is a high probability to crystalize these ligands and their associated complexes to be studied by single crystal x-ray diffraction (SCXRD) for structure elucidation. Among these ligands, pyridine-2-carboxamide and 2,2'-bipyridine-6,6'-dicarboxamide ligands form one [16-18], while pyridine-2,6- and phenanthroline-2,9-dicarboxamides forms two and three 5-membered stable chelate rings, respectively, in their metal complexes by utilizing bidentate NO and tridentate ONO systems [19-32] (Figure 1). The convergent coordination sites of these ligands lead to mononuclear chelating complexes.

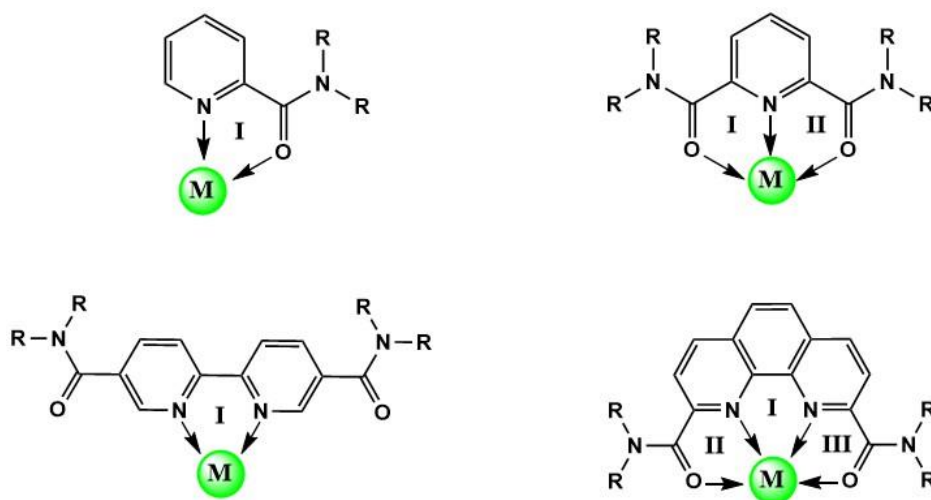


**Figure 1** Mononuclear complexes of different fully substituted dicarboxamide ligands due to convergent coordination sites.

On the contrary, pyridine-3- and 4-carboxamide ligands containing carboxamide side arm positioned at the *meta* and *para* position relative to the pyridine nitrogen [16, 33-61] and, imidazolidine-2-thione or/and piperazine anchored bis(3- or 4-pyridylformyl) ligands form coordination polymers of higher dimensionality owing to the disposition of donor sites far from each other (divergent coordination sites) [62-76] (Figure 2). These ligand molecules bridge between adjacent metal centres to form variety of structures ranging from dimeric complexes to 1D, 2D, and 3D polymers.

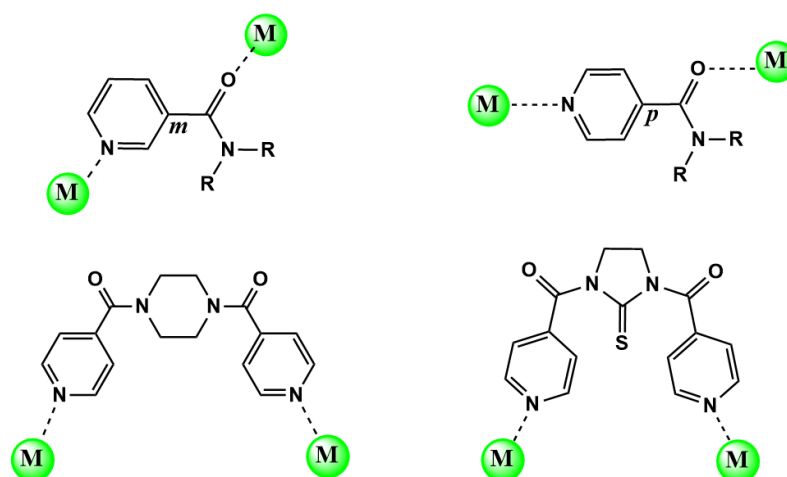
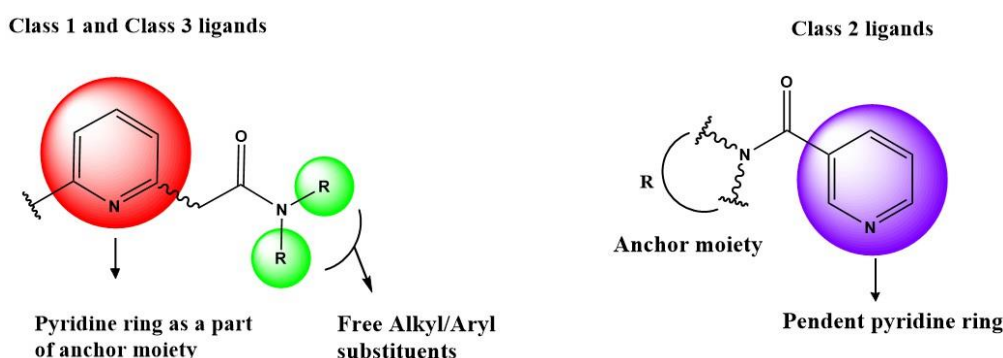


**Figure 2** Divergent coordination sites of different fully substituted dicarboxamide ligands that lead to coordination complexes of higher dimensionality.



This review focusses on the discussion of structural chemistry and applications of the coordination complexes synthesized using carboxamide/dicarboxamide ligands containing tertiary amide linkage (CONRR'), and pyridine ring, which can either be a central anchor moiety or part of it (bipyridyl or phenanthroline etc.), or as a free pendent moiety (**Scheme I**).

### Scheme I



So far, a few review articles on pyridine carboxamide ligands with secondary nitrogen atoms (-CONHR-) have been reported in literature. However, there have been no reports or reviews so far on carboxamide/dicarboxamide ligands with tertiary amide nitrogen atoms and their complexes, which makes the present review the first of its kind [77-78]. Also, we want to mention here that along with the discussion on structural chemistry and properties of complexes, we have tabulated the bond lengths of M-L, M-X<sub>anion</sub>, and M-S<sub>Solvent</sub> bonds of the complexes in Table 1, which could be helpful for the researchers interested in crystallographic parameters. Furthermore, to make the crystal data search easy for the researchers on CSD database we have included the CSD codes in Table 1. Finally, the applications of the complexes, and the notable results obtained are tabulated in Table 2.

## 2. Classification of Ligands

The ligands are chiefly classified into three classes (Chart 1) based upon the type of anchor moiety and the position of pyridine ring with respect to it. The classification of the ligands is as follows:

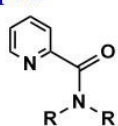
- a. **Class 1:** This class comprises mono- and dicarboxamide ligands containing pyridine ring as an anchor moiety with fully substituted amide nitrogen atom

having free aliphatic or/and aromatic groups (Scheme I). This class is further divided into following types-

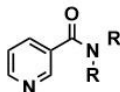
- i. **Type 1** - Pyridine mono-carboxamide ligands containing an amide side arm with free aliphatic groups such as methyl, ethyl, isopropyl, and isobutyl on nitrogen atom of amide group. (**L<sup>1</sup>- L<sup>5</sup>**, Chart 1).
- ii. **Type 2** - Pyridine dicarboxamide ligands (two side arms) with free substituents such as aliphatic, benzyl, or both aliphatic and aromatic groups. (**L<sup>6</sup>- L<sup>18</sup>**, Chart 1).
- b. **Class 2:** Ligand molecules containing pyridine rings as a pendent moiety (Scheme I). This class contains two types-
  - i. **Type 3** - Ligand molecules having pendant pyridine rings connected to imidazolidine-2-thione anchor moiety (**L<sup>19</sup> and L<sup>20</sup>**, Chart 1).
  - ii. **Type 4** - Ligand molecules containing pendant pyridine rings connected to piperazine anchor moiety (**L<sup>21</sup> and L<sup>22</sup>**, Chart 1).
- c. **Class 3:** These ligand molecules contain pyridine ring as a part of fused ring system or/and bipyridine system (Scheme I). This class again contains two types-
  - i. **Type 5** - Ligands with 2,2'-bipyridine anchor moieties connected to free aliphatic, or both aliphatic and aromatic substituents together (**L<sup>23</sup> - L<sup>25</sup>**, Chart 1).
  - ii. **Type 6** - Ligands containing phenanthroline anchor moieties connected to free aliphatic, or both aliphatic and aromatic substituents together (**L<sup>26</sup>- L<sup>29</sup>**, Chart 1).
- d. **Miscellaneous** - This class contains complex ligand molecules such as crown ether, bis-lactam based ligands etc. (**L<sup>30</sup>- L<sup>34</sup>**, Chart 1).

The coordination modes shown by these ligand molecules in the metal complexes are depicted in the scheme II.

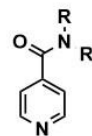
## Type 1



R = <sup>i</sup>Pr; L<sup>1</sup>  
R = <sup>i</sup>Bu; L<sup>2</sup>

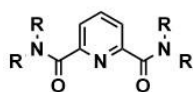


R = Et; L<sup>3</sup>

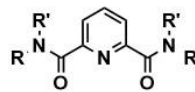


R = <sup>i</sup>Pr; L<sup>4</sup>  
R = <sup>i</sup>Bu; L<sup>5</sup>

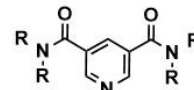
## Type 2



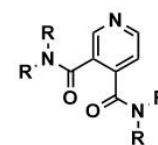
R = Me; L<sup>6</sup>  
R = Et; L<sup>7</sup>  
R = Bu; L<sup>8</sup>  
R = <sup>i</sup>Pr; L<sup>9</sup>  
R = <sup>i</sup>Bu; L<sup>10</sup>



R, R' = Benz; L<sup>11</sup>  
R, R' = Me, Phen; L<sup>12</sup>  
R, R' = Et, Phen; L<sup>13</sup>  
R, R' = Et, *p*-tolyl; L<sup>14</sup>

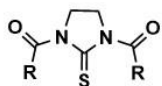


R = <sup>i</sup>Pr; L<sup>15</sup>  
R = <sup>i</sup>Bu; L<sup>16</sup>



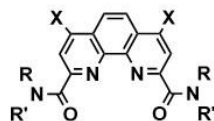
R = <sup>i</sup>Pr; L<sup>17</sup>  
R = <sup>i</sup>Bu; L<sup>18</sup>

## Type 3



R = ; L<sup>19</sup>  
R = ; L<sup>20</sup>

## Type 6



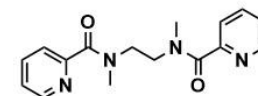
R, R' = Et, ; L<sup>26</sup>  
X = H; L<sup>26</sup>

R, R' = Et, ; L<sup>27</sup>  
X = H; L<sup>27</sup>

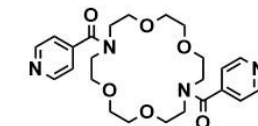
R, R' = Et,  
X = pentoxy; L<sup>28</sup>

R, R' = Et, ; L<sup>29</sup>  
X = Cl; L<sup>29</sup>

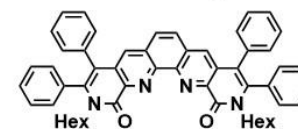
## Miscellaneous



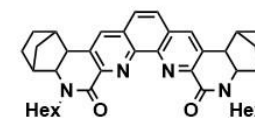
L<sup>30</sup>



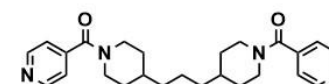
L<sup>31</sup>



L<sup>32</sup>

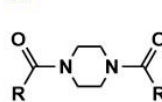


L<sup>33</sup>



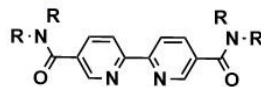
L<sup>34</sup>

## Type 4



R = ; L<sup>21</sup>  
R = ; L<sup>22</sup>

## Type 5



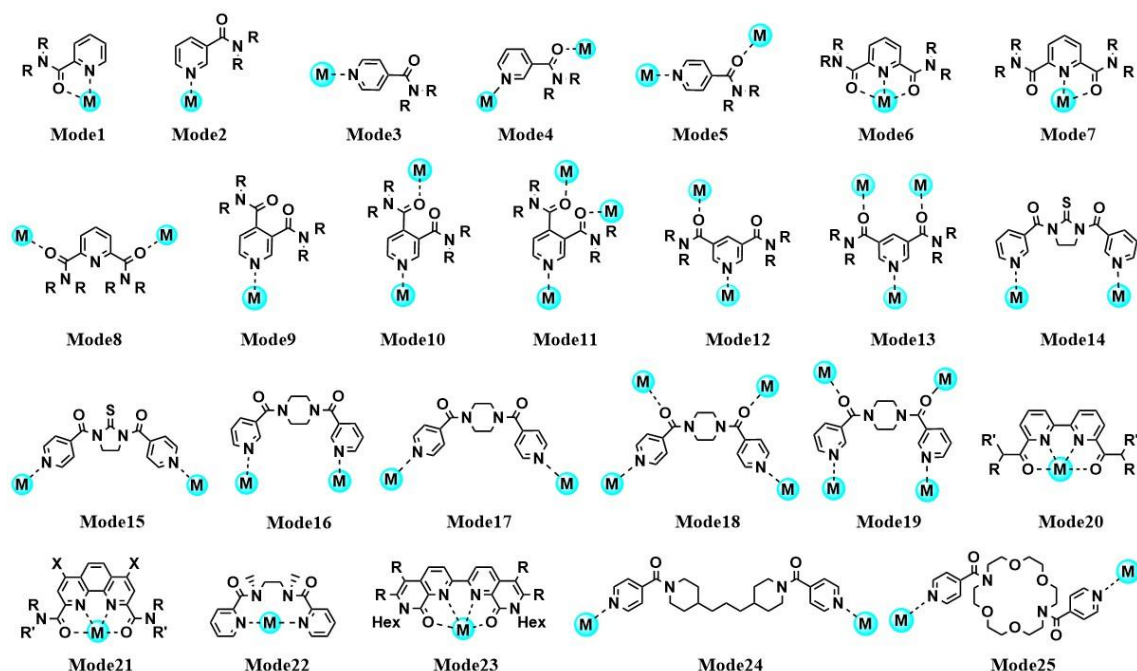
R, R' = Et, Phen; L<sup>23</sup>

R, R' = Et, ; L<sup>24</sup>

R, R' = Et, ; L<sup>25</sup>

Chart 1 Structure of Ligand L<sup>1</sup>-L<sup>34</sup>

**Scheme II-** Coordination modes of ligands.



## 2.1 Coordination complexes of Class I ligands

### 2.1.1 Type 1 Ligands

#### 2.1.1.1 Monomeric complexes

In these complexes, the ligand molecules display coordination modes 1-4 (Scheme II). Mononuclear complexes  $[\text{Co}(\text{L}^1)_2\text{Cl}_2]$  (**1**) and  $[\text{Ag}(\text{L}^1)_2\text{NO}_3]$  (**2**) were synthesized using  $\text{L}^1$  molecule with Co(II) and Ag(I) ions, respectively. The complex **1** contains Co(II) ion in a distorted octahedral environment shaped by two chelating  $\text{L}^1$  molecules, and two chloride anions (Figure 3a). Conversely, complex **2** has Ag(I) ion in a square planar geometry ( $\tau$  (Geometry index)  $\approx 0.2$ ) provided by two chelating  $\text{L}^1$  molecules, and a nitrate ion (Figure 3c). The 2D hydrogen bonded network in **1** was produced by  $\text{C-H}\cdots\text{Cl}$  interactions involving terminal methyl and methine groups, and the coordinated chloride ions (Figure 3b), while weak  $\text{C-H}\cdots\text{O}$  and  $\text{C-H}\cdots\pi$  interactions in **2** weaves a 2D hydrogen bonded network in *ac* plane (Figure 3d). In both these complexes,  $\text{L}^1$  molecules display coordination mode1. The complexes  $[\text{Zn}(\text{L}^1)_2(\text{ClO}_4)_2]$  (**3**) and  $[\text{Cu}(\text{L}^2)_2(\text{ClO}_4)_2]$  (**4**) were isostructural to **1**, differing in the type of metal ion and ligand molecules present [16].

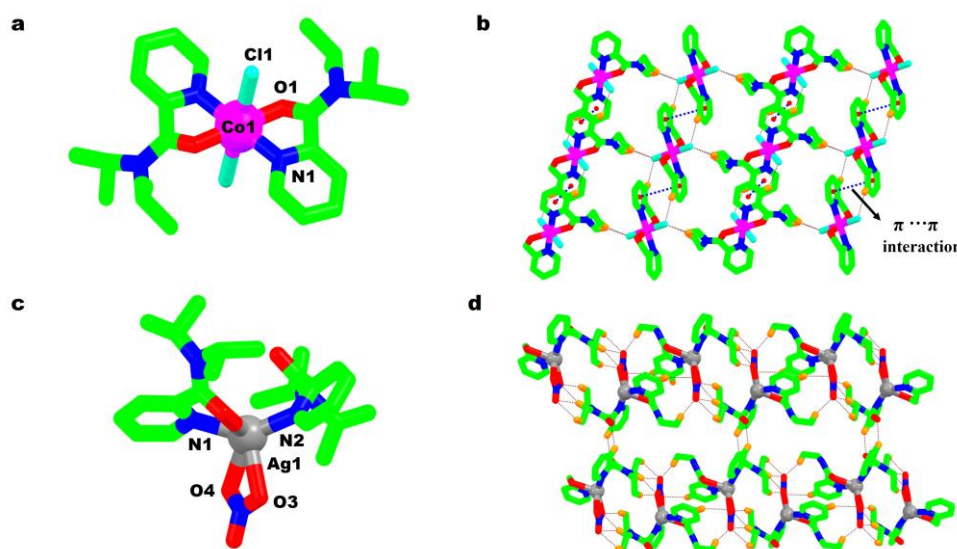


Figure 3 a) Unique crystallographic unit of the complex **1** showing coordination environment around Co(II) ion, b) 2D hydrogen bonded network of **1** supported by C-H $\cdots$ Cl and  $\pi\cdots\pi$  interactions, c) coordination environment around Ag(I) ion in complex **2**, and d) hydrogen bonded 2D sheet of the complex **2**.

The octahedral complex  $[\text{Cu}(\text{L}^1)_2(\text{Cl})_2]$  (**5**) has two crystallographically independent molecules, rotated through an angle of *ca.*  $45^\circ$  relative to each other (Figure 4a). These coordination units form 1D hydrogen bonded chains along *a* axis, which were connected through C-H $\cdots$ O, C-H $\cdots$ Cl and C-H $\cdots\pi$  interactions to yield a 2D hydrogen bonded network (Figure 4b). Isostructural complex  $[\text{Cu}(\text{L}^1)_2(\text{ClO}_4)_2]$  (**6**) differs in the axial coordination with perchlorate ions positioned at axial sites instead of chloride ions in **5** [17]. An octahedral Zn(II) complex  $[\text{Zn}(\text{L}^3)_2(\text{NCS})_2(\text{H}_2\text{O})_2]$  (**7**), reported by Bigoli *et al.* has a square planar arrangement of two water molecules and two isothiocyanate ions. Whereas monodentate  $\text{L}^3$  molecules (in mode2) were located at axial sites (Figure 4c). The  $\text{O}_w\text{-H}\cdots\text{O}$  and  $\text{O}_w\text{-H}\cdots\text{S}$  interactions between isothiocyanate ions and water molecules connect these units into a 2D hydrogen bonding sheet (Figure 4d) [34].

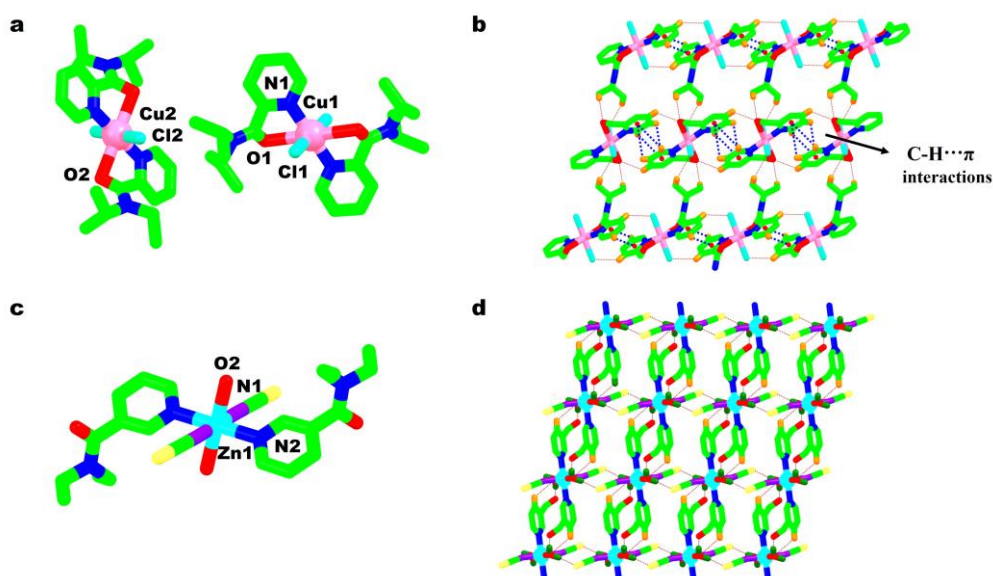


Figure 4 a) Crystallographic independent units of the complex **5** and coordination environment around Cu(II) ions, b) 2D hydrogen bonded network of **5** supported by C-H...Cl and C-H... $\pi$  interactions, c) coordination environment around Zn(II) ion in the complex **7**, and d) 2D hydrogen bonded sheet of the complex **7** involving coordinated water molecules and isothiocyanate ions.

Mononuclear complex  $[\text{Co}(\text{L}^3)_2(\text{pmb})_2(\text{H}_2\text{O})_2]$  (**8**) has an inversion centre located on Co(II) ion (Figure 5a).

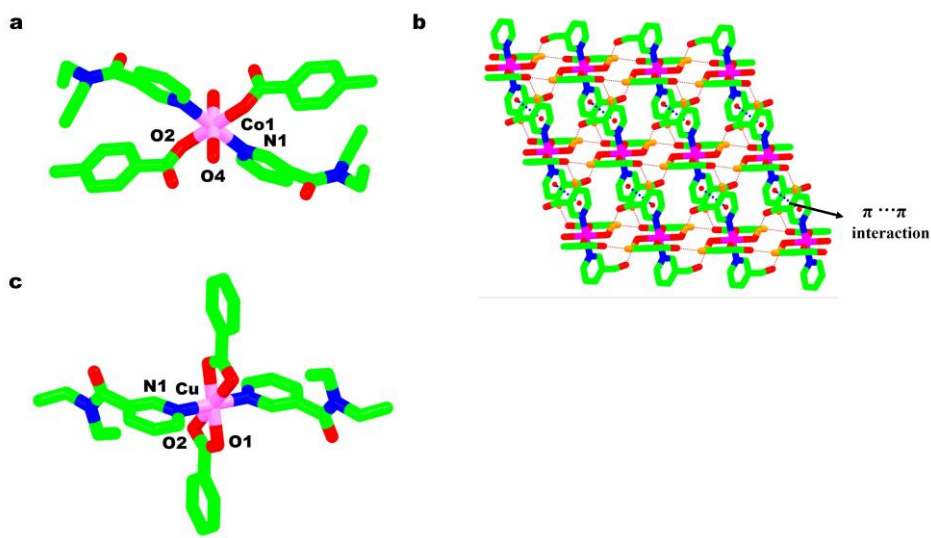


Figure 5 a) Unique crystallographic unit of the complex **8**, b) perspective view of 2D hydrogen bonded sheet containing mononuclear units connected by O-H...O, C-H...O, and  $\pi$ ... $\pi$  interactions in the complex **8**, and c) view of coordination unit of the complex **9**.



The adjacent octahedral Co(II) units were linked into a two-dimensional sheet parallel to *ab* plane by O-H $\cdots$ O and C-H $\cdots$ O hydrogen bonding interactions, endorsed by  $\pi\cdots\pi$  interactions  $\sim 3.5441$  Å between pyridine rings (Figure 5b) [35]. Working on the series of complexes containing benzoate salt, transition metal ions and  $L^3$  molecules, T. Hökelek *et al.* have synthesized a centrosymmetric monomeric complex  $[Cu(\text{Benzo})_2(L^3)_2]$  (**9**) containing Cu(II) ion coordinated to two monodentate  $L^3$  molecules in mode2, and two bidentate chelating benzoate ions (Figure 5c). Based on the weak interaction between Cu(II) ion and benzoate oxygen atoms, extremely tetragonally distorted octahedron coordination geometry was suggested around the Cu(II) ions [36].

Pannu *et al.* have reported two mononuclear complexes  $[Cu(L^4)_2(H_2O)_4][CuL^4Cl_3]_2$  (**10**), and  $[Cu(L^4)_4(C_3H_8O)_2] \cdot (ClO_4)_2$  (**11**) [37]. The cationic structural unit  $[Cu(L^4)_2(H_2O)_4]^{2+}$  of **10** has octahedral Cu(II) ion whereas it was tetrahedral in the anionic unit  $[Cu(L^4)(Cl)_3]^-$  (Figure 6a). In both complexes,  $L^4$  molecules have shown coordination mode3. The overall charge neutrality of the complex was maintained by electrostatic interaction between octahedral  $[Cu(L^4)_2(H_2O)_4]^{2+}$  unit surrounded by two anionic units  $[Cu(L^4)(Cl)_3]^-$  units (Figure 6b).

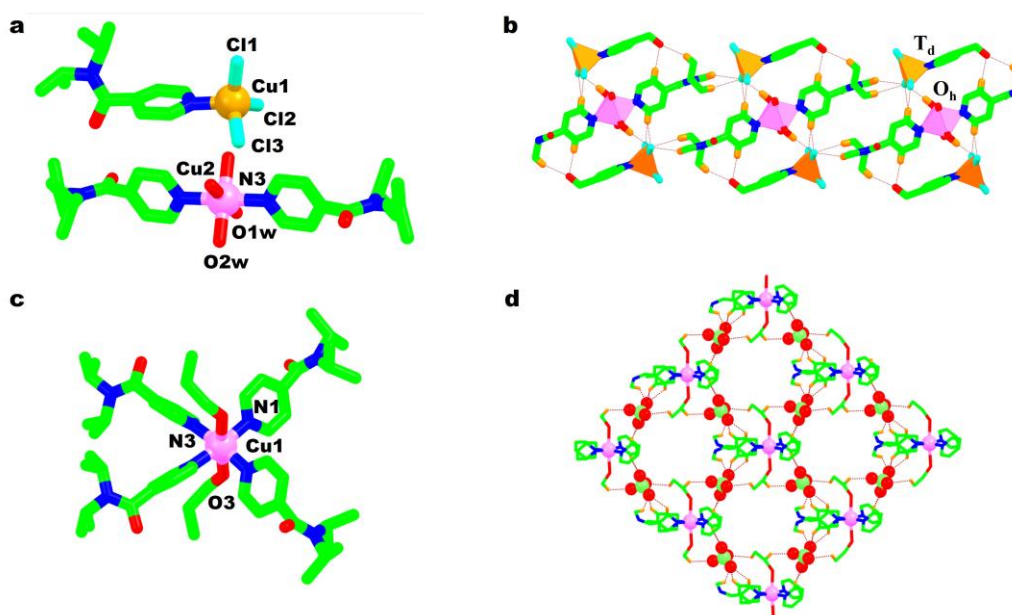


Figure 6 a) View of crystallographic unit of the complex **10** with Cu(II) ions in different chemical environments, b) pictorial view of hydrogen bonded trinuclear units of the complex **10**, c) coordination environment around Cu(II) ion in the complex **11**, and d) perspective view of 2D hydrogen bonded sheet comprising metallic units and perchlorate anions.



These three ionic entities were held together by hydrogen bonding interactions to form a 1D chain containing  $\text{Cu(II)}(T_d) \cdots \text{Cu(II)}(\text{O}_h) \cdots \text{Cu(II)}(T_d)$  hydrogen bonded tri-nuclear units (Figure 6b). The octahedral Cu(II) ion in the complex **11** lies on the two fold axis of rotation (Figure 6c). A highly disordered perchlorate ion outside the coordination sphere interconnects neighbouring octahedral units by intermolecular hydrogen bonding interactions to form a 2D hydrogen bonded sheet (Figure 6d) [37]. The complex  $[\text{Cu}(\text{L}^4)_2(\text{NO}_3)_2(\text{H}_2\text{O})_{1.5}]$  (**12**) has two crystallographic independent units crystallized in the crystal lattice, comprising octahedral Cu(II) ions surrounded by two  $\text{L}^4$  molecules coordinated in mode3, two nitrate anions, and two water molecules (Figure 7a).

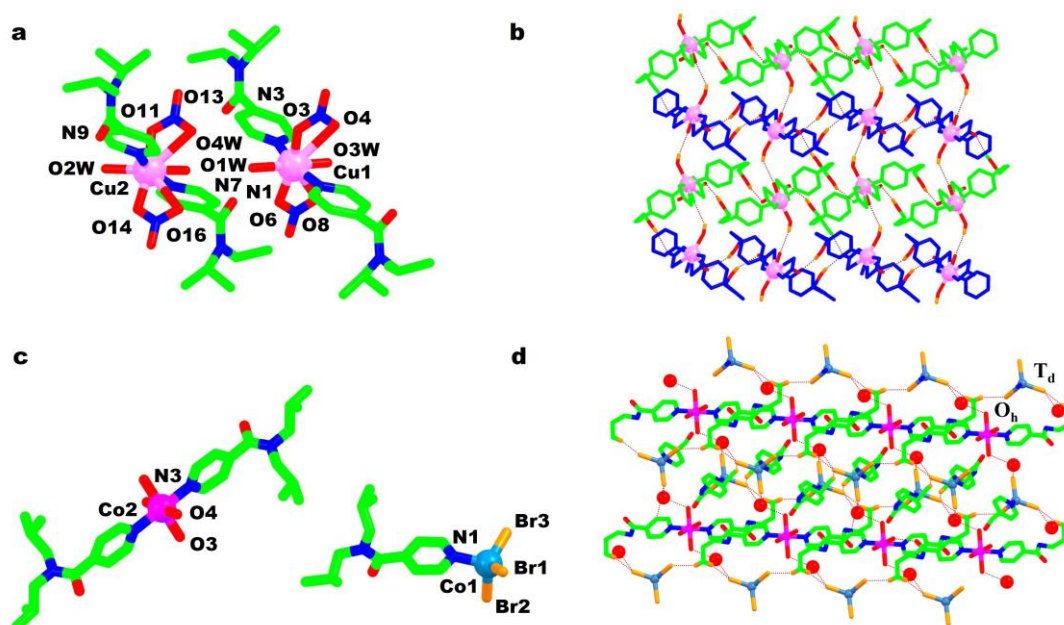


Figure 7 a) View of a) crystallographic independent units of the complex **12** containing Cu(II) ions in octahedral geometry, b) hydrogen bonded between adjacent units of the complex **12**, c) crystallographic independent units of complex **13** with Co(II) ions in different chemical environments, and d) 2D hydrogen bonded sheet comprising trimeric units and water molecules (in red spheres). (Note- In the Figure 7b, the ligand molecules of crystallographic units are shown in blue and green colours for better visualization of 2D network).

Moreover, extensive hydrogen bonding involving coordinated nitrate ions, water molecules, and carbonyl groups of neighbouring mononuclear units form a 2D hydrogen bonded network [16] (Figure 7b).

Similar to complex **10**, a new complex  $[\text{Co}(\text{L}^5)_2(\text{H}_2\text{O})_4][\text{Co}(\text{L}^5)\text{Br}_3]_2 \cdot 2\text{H}_2\text{O}$  (**13**) has ionic product containing an octahedral cationic  $[\text{Co}(\text{L}^5)_2(\text{H}_2\text{O})_4]^{2+}$  and a tetrahedral anionic  $[\text{Co}(\text{L}^5)(\text{Br})_3]^-$  unit crystallized in the unit cell (Figure 7c). In both units,  $\text{L}^5$  molecules were coordinated to  $\text{Co}(\text{II})$  ions in mode3. A 1D hydrogen bonded chain running diagonally to  $ab$  plane containing both ionic structural units and lattice water molecules was constructed via  $\text{O} \cdots \text{Br}$  and  $\text{O} \cdots \text{O}$  interactions (Figure 7d). This chain was comprised of hydrogen bonded trinuclear  $\text{Co}^{\text{II}}_{\text{Td}} \cdots \text{Co}^{\text{II}}_{\text{Oh}} \cdots \text{Co}^{\text{II}}_{\text{Td}}$  units involving octahedral cationic unit surrounded by two tetrahedral  $[\text{Co}(\text{L}^5)(\text{Br})_3]^-$  anionic units to maintain overall charge neutrality. The adjacent parallel chains were further held together by  $\text{C}-\text{H} \cdots \text{Br}$  interaction to form a 2D hydrogen bonded sheet along  $ab$  plane (Figure 7d) [38].

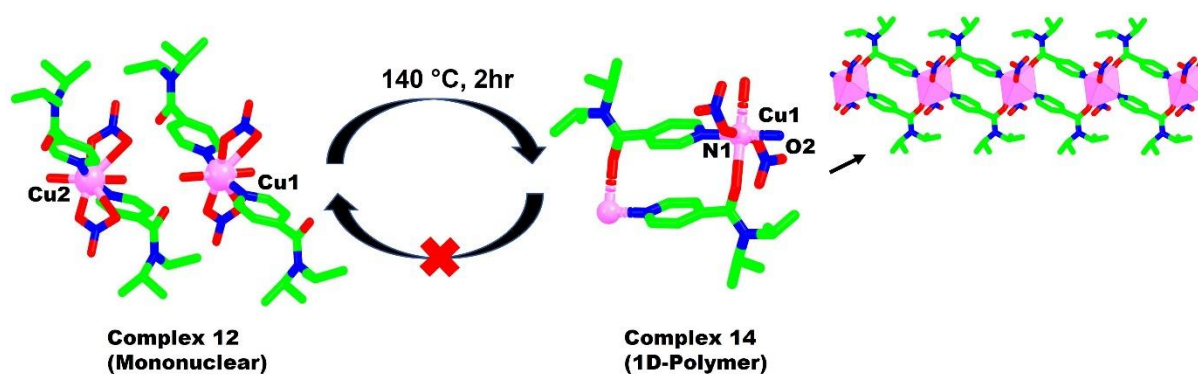


Figure 8 Single crystal to single crystal transformation (SCSC) of the complex **12** to complex **14** on heating.

Singh *et al.* have studied single crystal to single crystal transformation between the complexes induced thermally and/or by anion exchange. The mononuclear complex  $[\text{Cu}(\text{L}^4)_2(\text{NO}_3)_2(\text{H}_2\text{O})_{1.5}]$  (**12**) synthesised using  $\text{Cu}(\text{NO}_3)_2$  and  $\text{L}^4$  in 1:1 molar ratio at room temperature underwent irreversible thermal single crystal to single crystal (SCSC) transformation to a 1D coordination polymer  $[\text{Cu}(\text{L}^4)_2(\text{NO}_3)_2]_n$  (**14**) by the loss of water molecule upon heating (Figure 8) [39]. Although both complexes were synthesized using  $\text{L}^4$  molecules, different coordination modes of  $\text{L}^4$  molecules *viz.* mode3 (monodentate) in complex **12**, and mode4 in complex **14** have resulted in different structures.

### 2.1.1.2 Dimeric complexes

Coordination modes shown by the ligand molecules in here are mode 2-5. A metal exchange reaction involving replacement of Cu(II) ion in  $[(L^3)CuCl]_4O_2$  with Zn(II) ions using  $[Zn(N_2S_2)]_2$  complex was reported by Davies *et al.*. In this pursuit, the complex  $[L^3CuCl]_4O_2$  was reacted with 2 moles of  $[Zn(N_2S_2)]_2$  to give an intermediate product  $[Zn(N_2S_2)L^3]$  on stirring the mixture for 10 minutes, and a stable dimeric complex  $[Zn_2Cl_4(L^3)_2]$  (**15**) while stirring it for three hours at room temperature.

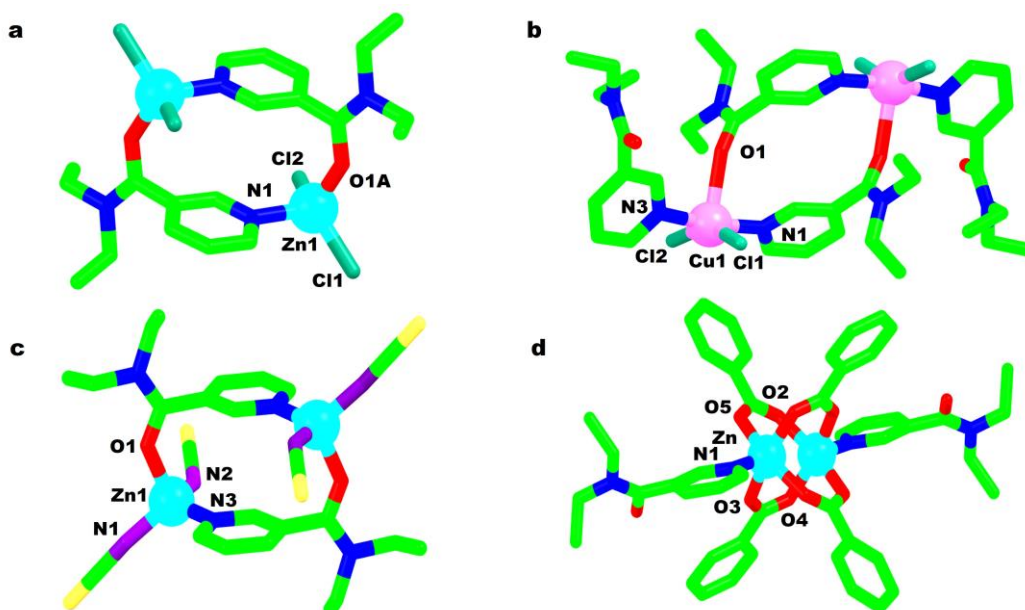


Figure 9 View of the unique crystallographic unit of a) complex **15** containing Zn(II) ions in tetrahedral geometry, b) complex **16** with Cu(II) ions in trigonal-bipyramidal geometry, c) complex **17** with Zn(II) ions in tetrahedral geometry and d) complex **18** with Zn(II) ions in square pyramidal geometry.

In the crystal structure of centrosymmetric dimeric unit  $[ZnCl_2(L^3)]_2$ , tetrahedral Zn(II) ion was coordinated to two terminal chloride ions, and two bridged  $L^3$  ligands in mode4 (Figure 9a). Besides crystallographic analysis, the kinetics of transmetallation reaction has also been well demonstrated [40]. In the dimeric complex  $[(L^3)_2CuCl_2]_2$  (**16**), the Cu(II) ions in a trigonal-bipyramidal geometry were bridged by  $L^3$  molecule in mode 4 (Figure 9b). While symmetry related  $L^3$  molecules were coordinated axially in mode2 [41]. Bigoli *et al.* have reported a dimeric complex  $[Zn(L^3)_2(NCS)_2]$  (**17**) containing tetrahedral Zn(II) ion, obtained as a stable transformed product when the crystals of complex **7** were kept undisturbed in the mother liquor

(Figure 9c) [42]. Necefoglu *et al.* have synthesized the dimeric complex  $[\text{Zn}(\text{L}^3)_2(\text{Benzo})_2]_2$  (**18**) to study the coordination behaviour of  $\text{L}^3$  molecule with Zn(II) metal. The complex has  $D_{4h}$  symmetry of the  $\text{Zn}_2(\text{N})_2(\text{O}_2\text{C})_4$  core owing to square pyramidal arrangement of symmetrically bridged benzoate ions (no variation in C-O bond length), and a terminal  $\text{L}^3$  molecule in mode2 (Figure 9d) around Zn(II) ions. The bridging of benzoate anions has also resulted in weak  $\text{Zn}\cdots\text{Zn}$  interaction of the order of 2.886(4) Å [43].

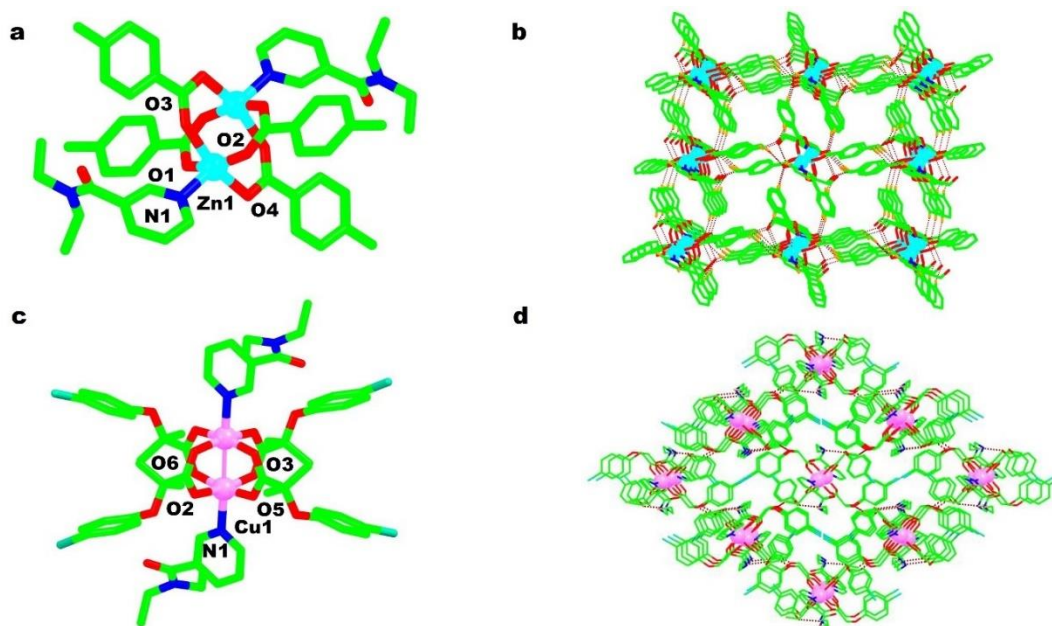


Figure 10 View of a) crystallographic unit of the complex **19**, b) 3D hydrogen bonded framework of **19**, c) octahedral Cu(II) ions connected to each other ( $\text{Cu}\cdots\text{Cu}^i = 2.6481(9)$  Å) in a binuclear paddle-wheel of complex **20**, and d) interlinked binuclear paddle-wheel units in a 3D hydrogen bonded network of the complex **20**.

The complex  $[\text{Zn}(\text{L}^3)_2(\text{pmb})_2]_2$  (**19**) has isostructural  $\text{Zn}_2(\text{N})_2(\text{O}_2\text{C})_4$  core as complex **18** (Figure 10a and 11), differing in the counter anion present [44]. In the crystal lattice of **19**, a three-dimensional hydrogen bonded framework was constructed through  $\text{C-H}\cdots\text{O}$  interactions between adjacent dimeric units, stabilized by  $\pi\cdots\pi$  interactions (Figure 10b).

J. Moncol *et al.* have prepared and characterized a binuclear paddle-wheel Cu(II) complex  $[\text{Cu}(\text{Clf})_2(\text{L}^3)]_2$  (**20**) with a centrosymmetric tetracarboxylic dimeric core (Figure 10c). The symmetrical *syn-syn* bridging of clofibrate anions results in short  $\text{Cu}\cdots\text{Cu}^i$  (2.6481(9) Å) contacts. The paddle-wheel Cu(II) units were linked by weak  $\text{C-H}\cdots\text{O}$  interactions to form a three-dimensional hydrogen bonded framework (Figure 10d) [45].

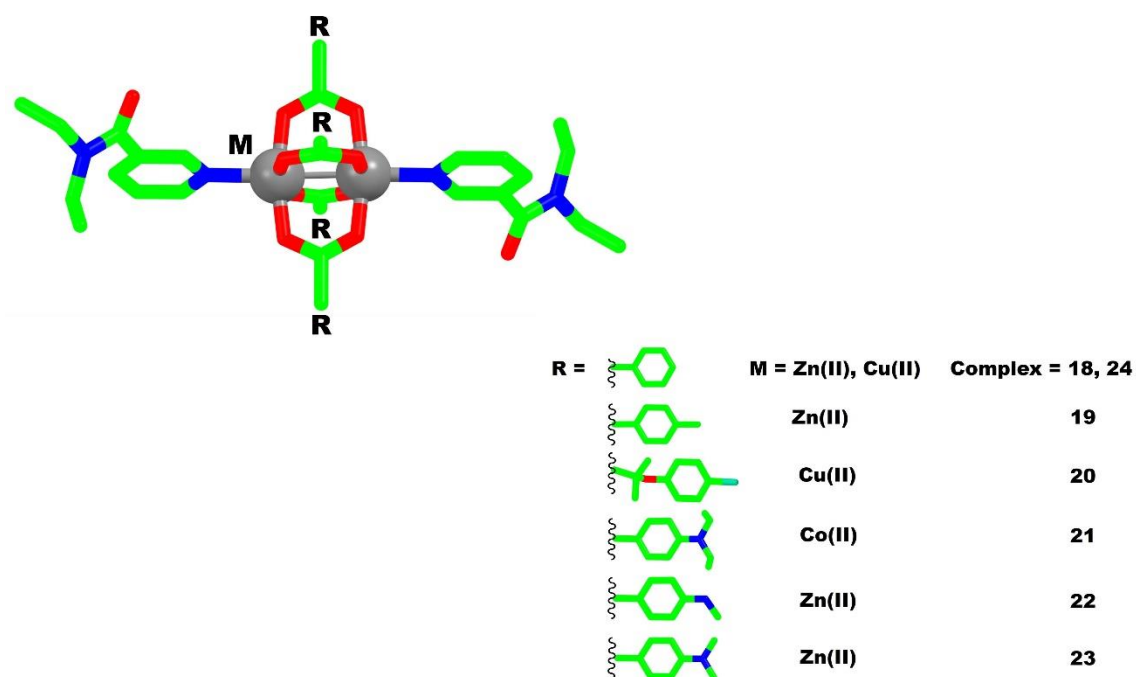


Figure 11 View of the combination of metal ions and carboxylate ions used in dimeric paddle wheel complexes **18-24**.

The complex  $[\text{Co}(\text{Deab})_2(\text{L}^3)]_2$  (**21**) has a paddle-wheel structural unit (Figure 11) as complexes **19** and **20**, respectively, with each Co(II) ion in distorted square-pyramidal geometry. The dihedral angles between carboxylate groups and benzene rings of Deab anions were  $7.06(11)^\circ$  and  $4.42(9)^\circ$ , respectively [46]. In the dimeric complex  $[\text{Zn}(\text{Mab})_2(\text{L}^3)]_2 \cdot \text{H}_2\text{O}$  (**22**) with square pyramidal Zn(II) ions (Figure 11), the dihedral angles between coordinated carboxylate anions and benzene rings in **22** were  $10.57(10)^\circ$  and  $16.63(12)^\circ$  while between pyridine and benzene rings the angles were  $40.49(6)^\circ$  and  $51.25(6)^\circ$  [47]. Likewise in complex  $[\text{Zn}(\text{Dmab})_2(\text{L}^3)]_2$  (**23**), the carboxylate anions were slightly tilted with respect to adjacent benzene rings as illustrated by dihedral angles of  $5.31(8)^\circ$  and  $11(9)^\circ$ . Similarly, pyridine rings of  $\text{L}^3$  ligands were oriented at an angle of  $66.26(6)^\circ$  and  $37.88(7)^\circ$  relative to benzene rings [48]. Holelek *et al.* have reported a centrosymmetric complex  $[\text{Cu}(\text{Benzo})_2(\text{L}^3)]_2$  (**24**) (Figure 10) [49]. The benzoate bridges led to smallest  $\text{Cu} \cdots \text{Cu}$  ( $2.613 \text{ \AA}$ ) interaction between square-pyramidal centres due to weak orbital overlap between Cu(II) ions. The dimeric structure of complex **24** synthesized using same molar ratio of reactants might be due the change of the solvent i.e. ethanol in **24** and methanol in monomeric complex **9** [36].



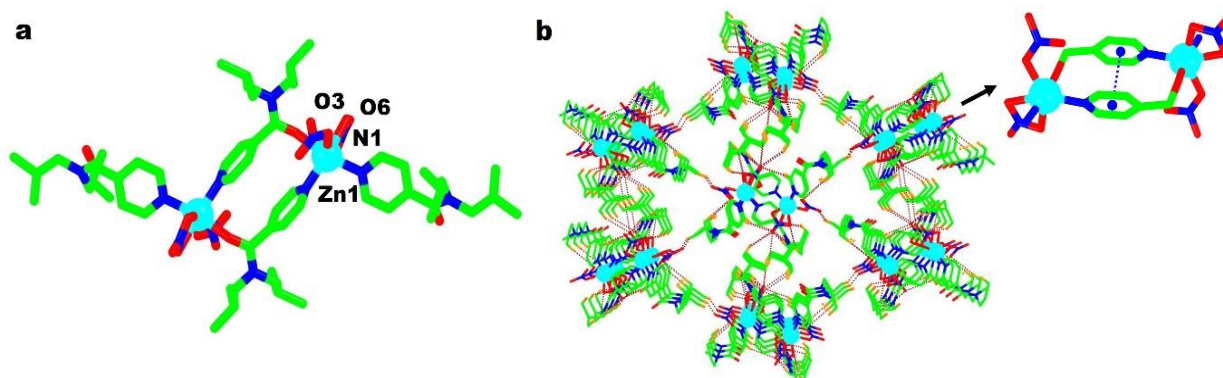


Figure 12 View of a) centrosymmetric dimeric unit of the complex **25**, and b) 3D hydrogen bonded framework involving C-H $\cdots$ O and  $\pi\cdots\pi$  (inset) interactions.

The dimeric complex  $[\text{Zn}(\text{L}^5)_2(\text{NO}_3)_2]_2$  (**25**) has Zn(II) ions coordinated to three  $\text{L}^5$  molecules displaying different coordination modes; mode3 and mode5 (Figure 12a). The remaining coordination sites were occupied by two nitrate anions, with one nitrate group coordinated as a bidentate chelating ligand while other remained monodentate. The dihedral angles of  $54.1(2)^\circ$  and  $85.5(3)^\circ$  between pyridine rings and amide groups display *gauche* and perpendicular orientation of pyridine rings with respect to amide groups. Furthermore, the C-H $\cdots$ O interactions between nitrate anions and ligand molecules has led to a 3D hydrogen bonded network, supported by strong  $\pi\cdots\pi$  between pyridine rings (Figure 12b) [16].

### 2.1.1.3 Trinuclear complexes

A trinuclear  $\text{CaZn}_2$  complex  $[\text{CaZn}_2(\text{L}^3)_2(\text{Benzo})_6]$  (**26**) was obtained as a side product in the reaction mixture of  $[\text{Zn}(\text{L}^3)_2(\text{Benzo})_2]_2$  (**18**) due to the calcium containing impurity in the reactants. The metal ion trio Zn-Ca-Zn was unsymmetrically bridged by benzoate ions to form a linear array. Two types of coordination geometries were observed: octahedral for Ca(II) ion provided by six benzoate ions, and tetrahedral for Zn(II) ions provided by three benzoate ions and a monodentate  $\text{L}^3$  molecule coordinated in mode2 (Figure 13) [43, 50].

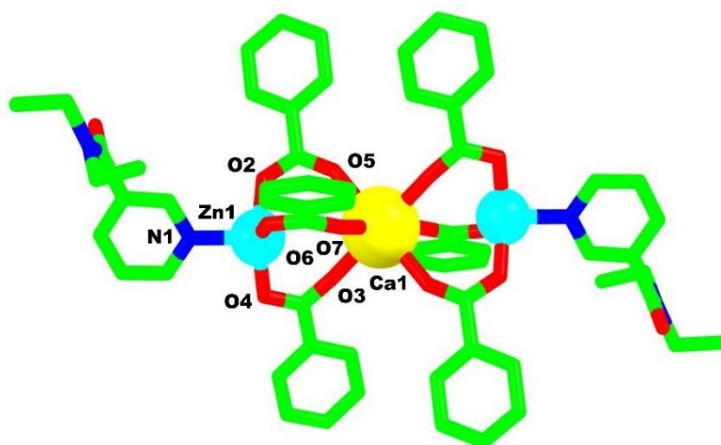


Figure 13 Pictorial presentation of centrosymmetric  $\text{CaZn}_2$  trinuclear unit of the complex **26**.

#### 2.1.1.4 1D-Polymeric complexes

In 1D polymeric complexes, the coordination modes shown by the ligands are mode 4 and mode 5. Reversible phase transition on cooling the complex  $[\text{Fe}(\text{NCS})_2(\text{L}^3)]_n$  (**27**) from 230K to 150K was reported by Ondrejčková *et al.* This transition has affected the Z value (no. of molecules in the unit cell) from one unit of the complex at high temperature phase (HT) to two units at low temperature (LT) phase. The phase transition has also resulted in the loss of centrosymmetry (about Fe(II) ion) due to the rotation of one of the ethyl groups around N-C(ethyl) bond, causing changes in the ligand molecule. In both phases, the complex has ligand driven 1D coordination chain comprising  $\text{L}^3$  molecules bridged (in mode 4) between octahedral Fe(II) centres, supported by weak  $\text{C-H}\cdots\pi$  interactions between the chains (Figure 14a and 14b) [51]. Mautner *et al.* have reported an anion driven 1D polymer  $[\text{Cd}(\text{L}^3)(\text{Cl})_2(\text{H}_2\text{O})]_n$  (**28**) (Figure 14c and 14d) containing edge sharing planar  $\text{Cd}_2\text{Cl}_2$ -rings sharing. These chains were linked into a 2D-supramolecular sheet in *bc*-plane by strong  $\text{O-H}\cdots\text{O}$  hydrogen bonds, supported by  $\pi$ - $\pi$  stacking interaction of the order  $3.601(2) \text{ \AA}$  between pyridine rings (Figure 14d) [52].



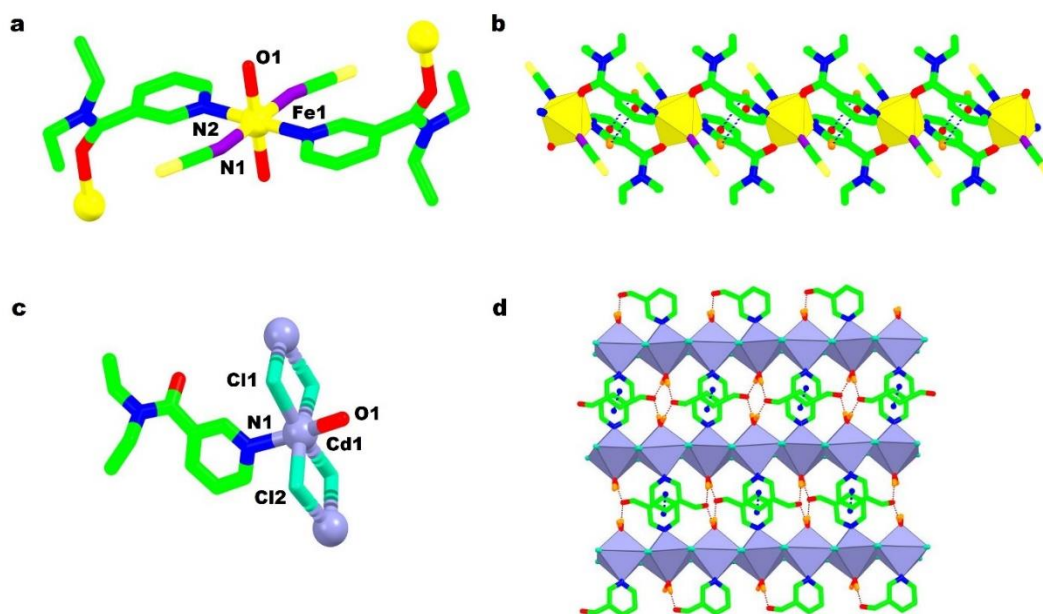


Figure 14 View of a) octahedral environment of Fe(II) in the complex **27**, b) 1D coordination chain reinforced by C-H $\cdots$  $\pi$  interactions in the complex **27**, c) unique crystallographic unit of the complex **28**, and d) 2D hydrogen bonded sheet of the complex **28** constructed by O<sub>w</sub>-H $\cdots$ O and supported by  $\pi\cdots\pi$  interactions.

The complex  $[\text{Mn}(\text{L}^3)_2(\text{NCS})_2]_n$  (**29**) has octahedral Mn(II) nodes (Figure 15a) coordinated to bridged  $\text{L}^3$  molecules (Figure 15a and 15b), and free isothiocyanate ions displaying linear coordination as depicted by N(1)-C(1)-S(1) angle of  $178.4(3)^\circ$  [53].

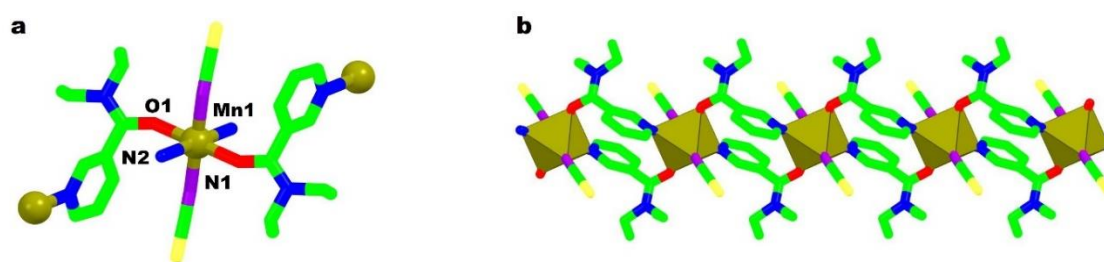


Figure 15 View of a) octahedral environment of Mn(II) ion in the centrosymmetric unit of the complex **29**, and b) 1D coordination chain of the complex **29**.

The polymeric *catena* complex  $[\text{Mn}_2(\text{Pmb})_4(\text{L}^3)_2(\text{H}_2\text{O})]_n$  (**30**) has two crystallographically independent dimeric units containing Mn(II) ions in the crystal lattice (Figure 16a). In each unit, the octahedral coordination around Mn(II) ions (Mn1/Mn2 in first and Mn3/Mn4 in second unit) was provided by O atom of monodentate  $\text{Pmb}^-$  ion, O:O atoms of two bridged

Pmb<sup>-</sup> ions, O:N atoms of two unique **L**<sup>3</sup> molecules, and a O atom of bridged water molecule. In each unit, the **L**<sup>3</sup> molecule (coordinated *via* N atom) was in *trans*-position relative to the water molecule while the monodentate Pmb<sup>-</sup> anion, and **L**<sup>3</sup> molecule (coordinated using O atom) were in *trans* position to bridged Pmb<sup>-</sup> anions (Figure 16a). These dimeric units were connected by **L**<sup>3</sup> molecules bridged in mode4 to form a 1D coordination chain (Figure 16b) [54]. The extended 1D zig-zag chain of the complex [Cu<sub>2</sub>(Cl-Ac)<sub>4</sub>(**L**<sup>3</sup>)<sub>n</sub>] (**31**) has paddle-wheel Cu<sub>2</sub>(Cl-Ac)<sub>4</sub> units of square pyramidal Cu(II) ions (Figure 16c). In each paddle-wheel unit, short Cu...Cu distances of the order of 2.741(1) and 2.6751 were observed due to bridged chloroacetate anions. Due to the different orientations of bridged **L**<sup>3</sup> molecules, a pattern – [Cu<sub>2</sub>(Cl-Ac)<sub>4</sub>-(**L**<sup>3</sup>-O,N)-Cu<sub>2</sub>(Cl-Ac)<sub>4</sub>-(**L**<sup>3</sup>-N,O)]– (Figure 16c) was observed along the 1D chain. The adjacent parallel chains were linked into a 2-D hydrogen bonded network by weak hydrogen bonding C-H...O interactions (Figure 16d) [55].

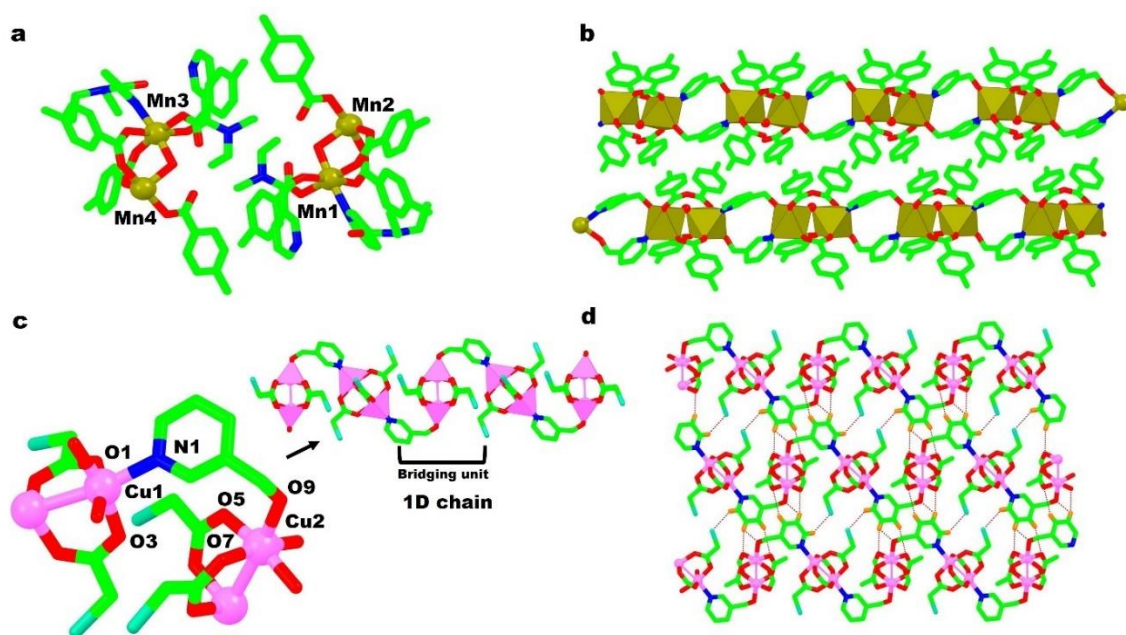


Figure 16 Perspective view of a) crystallographic independent dimeric units of the complex **30**, b) 1D coordination chain formed by bridged Pmb anions and water molecules in the complex **30**, c) unique crystallographic unit of complex **31** along with the 1D chain (inset), and d) 2D hydrogen bonded sheet of the complex **31**. (Note- side groups on amide nitrogen atom have been deleted for structural clarity).

The complex  $[\{\text{Co}(\text{L}^4)_2(\text{H}_2\text{O})_2\}(\text{ClO}_4)_2(\text{CH}_3\text{COCH}_3)_2(\text{H}_2\text{O})_2]_n$  (**32**) has octahedral Co(II) ions in the cationic  $[\text{Co}(\text{L}^4)_2(\text{H}_2\text{O})_2]_n^{+2}$  double chain containing bridged  $\text{L}^4$  molecules in mode 5. Along the chain, antiparallel orientation of pyridine ring facilitates  $\pi$ - $\pi$  interactions to support the 1D chain (Figure 17a, inset). In the hydrogen bonded framework, the hydrogen bonding between cationic chains, and anionic chains involving hydrogen bonding amid perchlorate anion, acetone and lattice water molecules (Figure 15b) generates a 2D sheet structure with ABABAB.... type arrangement of these chains in *ab* plane (Figure 17b) [56].

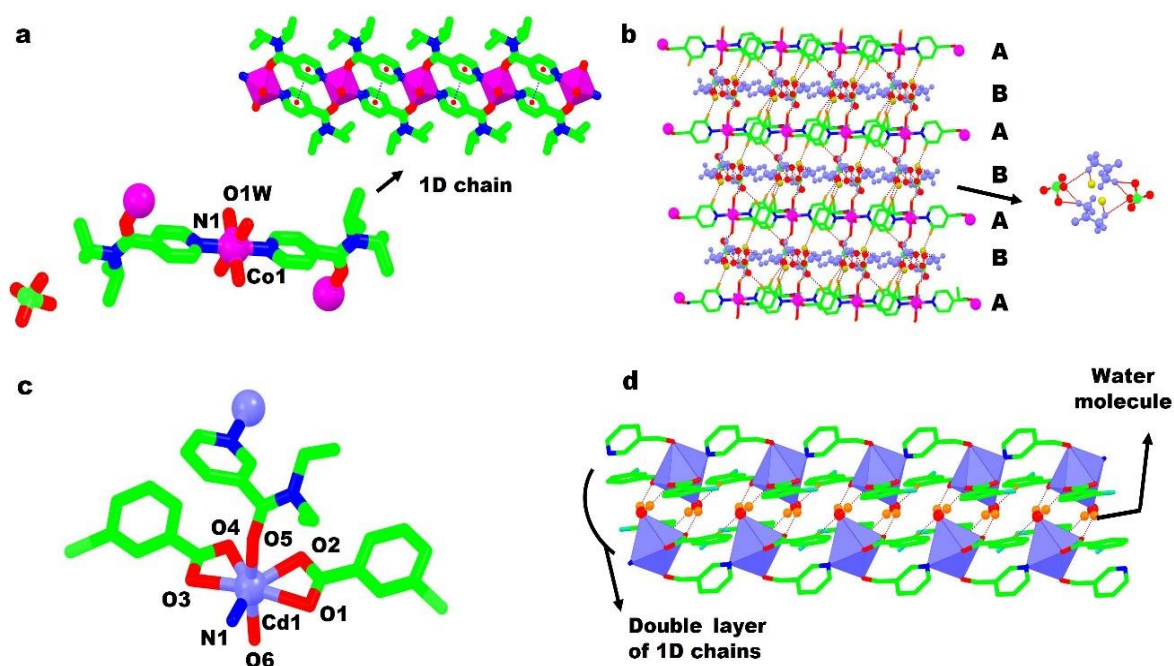


Figure 17 Pictorial presentation of a) centrosymmetric unit and the 1D chain of complex **32**, b) 2D hydrogen bonded sheets with ABAB.... pattern involving 1D coordination chain (A) and a hydrogen bonded chain formed by perchlorate, acetone and water molecules (B) of the complex **32**, c) unique crystallographic unit of **33** comprising distorted pentagonal-bipyramidal geometry around Cd(II) ion, and d) 1D tape formed by hydrogen bonding between coordinated carboxylate groups and water molecules of adjacent coordination chains in the complex **33**.

Bozkurt *et al.* have reported a 1D *catena*- $[\text{Cd}(\text{Cbenz})_2(\text{L}^3)(\text{H}_2\text{O})_n]_n$  (**33**) complex containing Cd(II) ions in pentagonal-bipyramidal geometry (Figure 17 c). The benzyl rings in the adjacent chains were slightly oriented relative to each other as depicted by dihedral angle of  $1.89(13)^\circ$  (Figure 17d). In the crystal lattice,  $\text{O}_w\text{--H}\cdots\text{O}$  interactions between water molecules and carboxylate groups connect the adjacent chains into a double layer parallel to *bc*-plane (Figure

17d). The  $\pi\cdots\pi$  interactions between benzyl rings (3.912 (2) Å) and weak C–H $\cdots$ O interactions between **L**<sup>3</sup> molecules and carboxylate groups further reinforce the hydrogen bonded double chain [57].

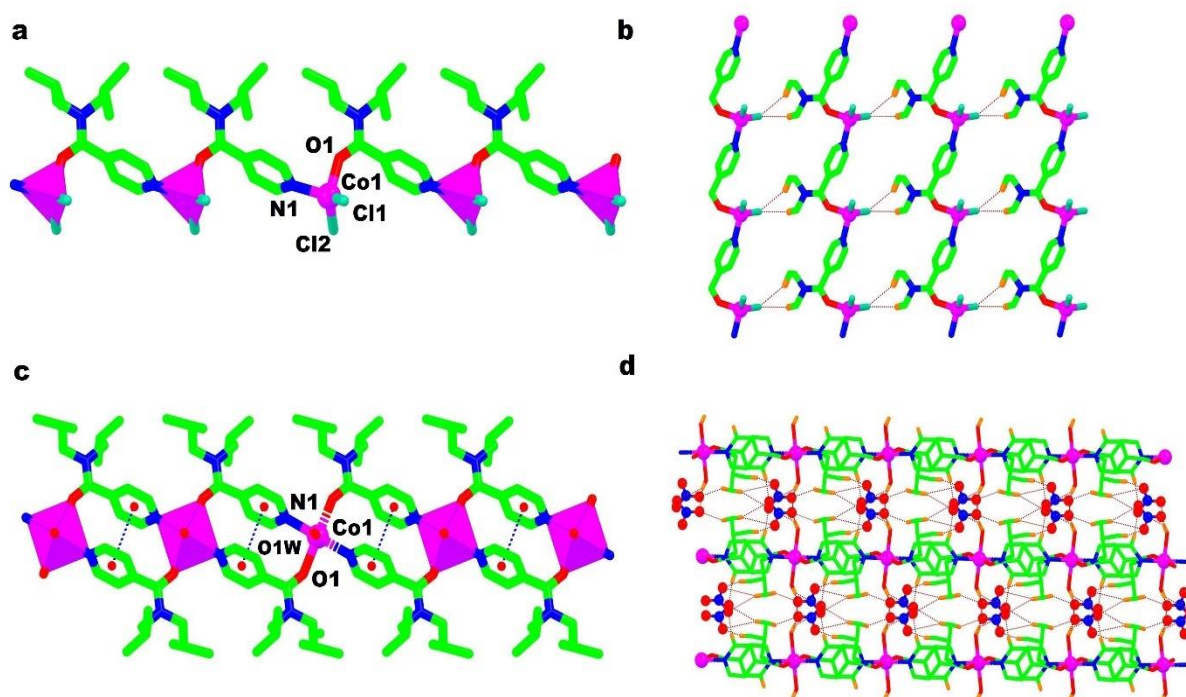


Figure 18 View of a) 1D coordination chain of tetrahedral Co(II) ions of the complex **34**, b) hydrogen bonded 2D sheet involving C–H $\cdots$ Cl interactions between 1D coordination chains in the complex **34**, c) 1D tape of the complex **35** supported by  $\pi\cdots\pi$  interactions, and d) 2D hydrogen bonded corrugated sheet of the complex **35**. (Note- Nitrate ions have not been shown in the Figure 18c and atoms not participating in hydrogen bonding have been deleted for clarity in the figure 18d).

The complex  $[\text{Co}(\text{L}^5)(\text{Cl})_2]_n$  (**34**) has 1D chains of tetrahedral cobalt (II) ions (Figure 18a), which were connected into a 2D sheet in *ab* plane by intermolecular C–H $\cdots$ Cl hydrogen bonding interactions between terminal chloride ions and **L**<sup>5</sup> molecules (Figure 18b) [38]. The 1D polymeric tape of complex  $[\text{Co}(\text{L}^5)_2(\text{H}_2\text{O})_2]_n \cdot 2\text{NO}_3$  (**35**) has octahedral Co(II) ions linked together by bridged **L**<sup>5</sup> molecules (mode5) [16]. The 1D tape was stabilized by  $\pi\cdots\pi$  interactions between adjacent pyridine rings ( $\text{Cg}\cdots\text{Cg} = 3.468$  Å, Figure 18c). The amide moiety of **L**<sup>5</sup> molecule was twisted out relative to the plane of pyridine ring as illustrated by dihedral angle of 74.39 (23)°. Furthermore, a 2D corrugated hydrogen bonded chain in *ac* plane



was constructed by the hydrogen bonding interactions between adjacent chains involving lattice nitrate ions,  $L^5$  and coordinated water molecules (Figure 18d) [16].

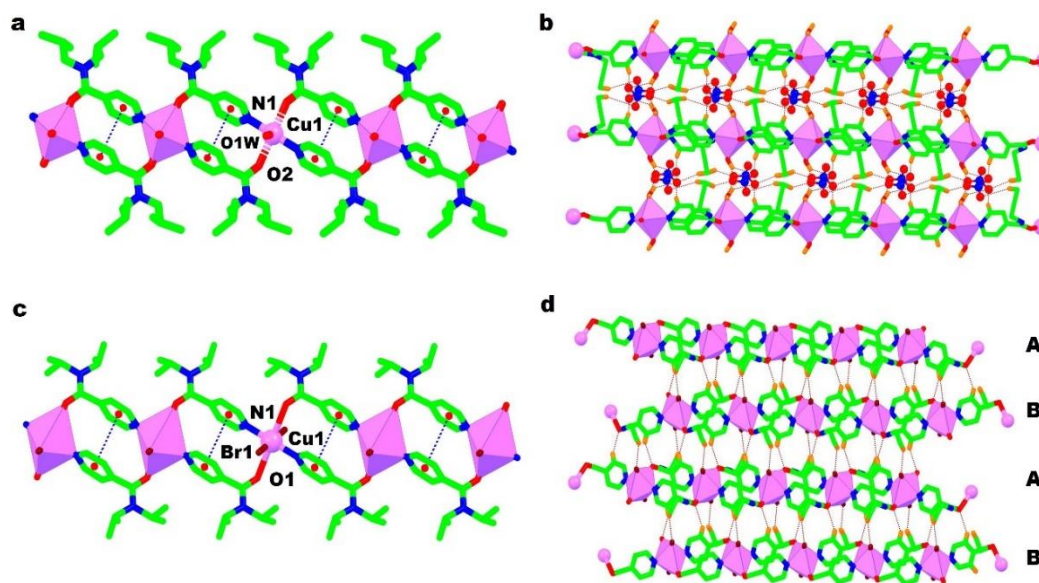


Figure 19 Pictorial view of a) 1D coordination chain of the complex **36** supported by  $\pi\cdots\pi$  interactions, b) corrugated hydrogen bonded 2D sheet of the complex **36**, c) 1D chain of the complex **37** supported by  $\pi\cdots\pi$  interactions, and d) 2D hydrogen bonded network of the complex **37** with ABAB.... pattern of coordination chains (Note- Nitrate ions have deleted in the Figure 19a for the sake of clarity).

The 1D tapes of octahedrally coordinated Cu(II) ions in the complexes  $[\{Cu(L^5)_2(H_2O)_2\}(NO_3)_2]_n$  (**36**) and  $[Cu(L^4)_2Br_2]_n$  (**37**), respectively, were supported by  $\pi\cdots\pi$  interaction between anti-parallelly oriented pyridine rings (Figure 19a and 19c). Extensive intermolecular hydrogen bonding interactions involving nitrate ions and coordinated water molecules in complex **36** connects parallel adjacent 1D linear tapes to generate 2D sheets parallel to the  $bc$  plane (Figure 19b). While in complex **37**, C–H $\cdots$ Br interactions involving terminal bromide ions and  $L^5$  molecules of neighbouring chains weaves a 2D sheet parallel in  $bc$  plane (Figure 19d). This 2D sheet contains ABABA.... type arrangement of 1D tapes due to different orientation of neighbouring chains relative to each other (Figure 19d) [37]. Complex  $[(Co)_3(L^4)_4Cl_6]_n$  (**38**) has linear Co( $T_d$ )–Co( $O_h$ )–Co( $T_d$ ) tri-nuclear units bridged by  $L^4$  molecules along the 1D chain (Figure 20a). The central Co(II) ion has octahedral geometry with the inversion centre passing through it, whereas the terminal Co(II) ions has tetrahedral geometry (Figure 20a).

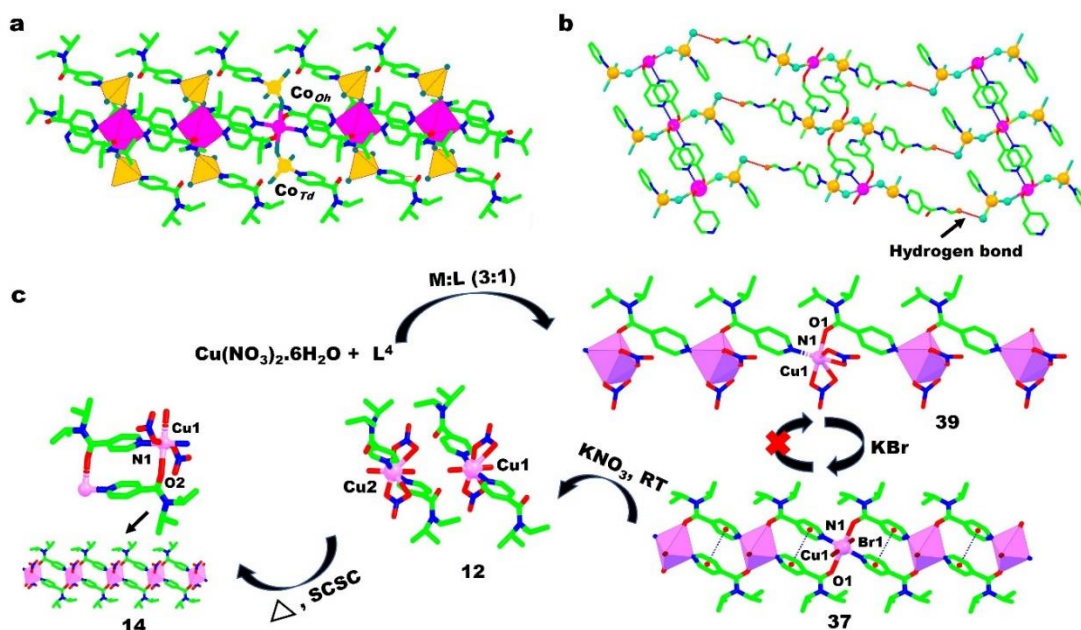


Figure 20 a) View of a) mixed  $\text{Co}(\text{T}_d)\text{--Co}(\text{O}_h)\text{--Co}(\text{T}_d)$  assembly in the 1D chain of complex **38**, b) 2D sheet formed by  $\text{C--H}\cdots\text{Cl}$  hydrogen bonding interactions between adjacent chains in the complex **38**, and c) transformation of the complexes on varying counter anions or/and reaction conditions (Note- Some atoms have been deleted from Figure 20b for the sake of clarity).

The unsymmetrical bridging of the chloride ions b/w the successive  $\text{Co}(\text{O}_h)\text{--Co}(\text{T}_d)$  ions has led to the formation of linear trinuclear unit  $\text{T}_d\text{--O}_h\text{--T}_d$  with corner sharing polyhedron [58]. The neighbouring 1D chains were held together into a 2D sheet structure in *ac* plane by  $\text{C--H}\cdots\text{Cl}$  hydrogen bonding interactions (Figure 20b). The complex  $[\text{Cu}(\text{L}^4)(\text{NO}_3)_2]_n$  (**39**) obtained using 3:1 M:L ratio [39] has shown irreversible transformation to a 1D complex  $[\text{Cu}(\text{L}^4)_2(\text{Br})_2]_n$  (**37**) when mixed with KBr (Figure 20c) [37, 39]. In both complexes the  $\text{L}^4$  molecules were bridged in mode5. Furthermore, the room temperature change of 1D complex **37** to a mononuclear complex  $[\text{Cu}(\text{L}^4)_2(\text{NO}_3)_2(\text{H}_2\text{O})_{1.5}]_2$  (**12**) (ligand coordinated in mode3) was observed on reacting with  $\text{KNO}_3$  (Figure 20c) [16, 39]. On further heating, the complex **12** underwent thermal SCSC (single crystal to single crystal) transformation to a 1D coordination polymer  $[\text{Cu}(\text{L}^4)_2(\text{NO}_3)_2]_n$  (**14**) (Figure 20c) [39].

### 2.1.1.5 2D-Polymeric complexes

A 2D polymeric system  $trans-[Mn(L^3)_2(N_3)_2]_n$  (**40**) has octahedral Mn(II) ions coordinated to two  $L^3$  molecules in mode2, and four azide ions in *trans*-arrangement (Figure 21a).

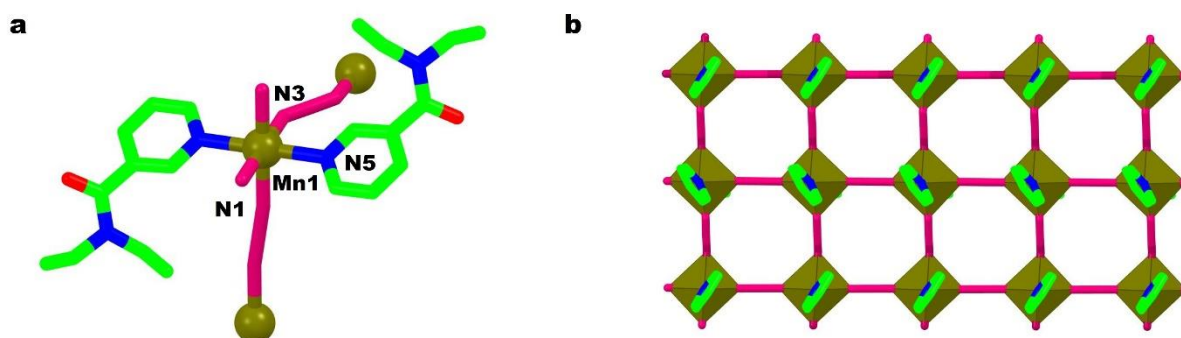


Figure 21 Pictorial representation of a) centrosymmetric unit of the complex **40**, and b) 2D coordination sheet of the complex **40** formed by  $\mu_{1,3}$ -azido bridges. (Note- Amide chains have been deleted for better visualization of the structure.)

The  $\mu_{1,3}$ -azido bridges between successive Mn(II) ions constructs a two-dimensional polymeric sheet in the *bc* plane (Figure 21b). Two types of azido bridges have been observed in the complex; one with Mn-N-N bond angle of  $148.4(2)^\circ$ , while the other with the  $171.7(2)^\circ$  [59].

### 2.1.1.6 3D-Polymeric complexes

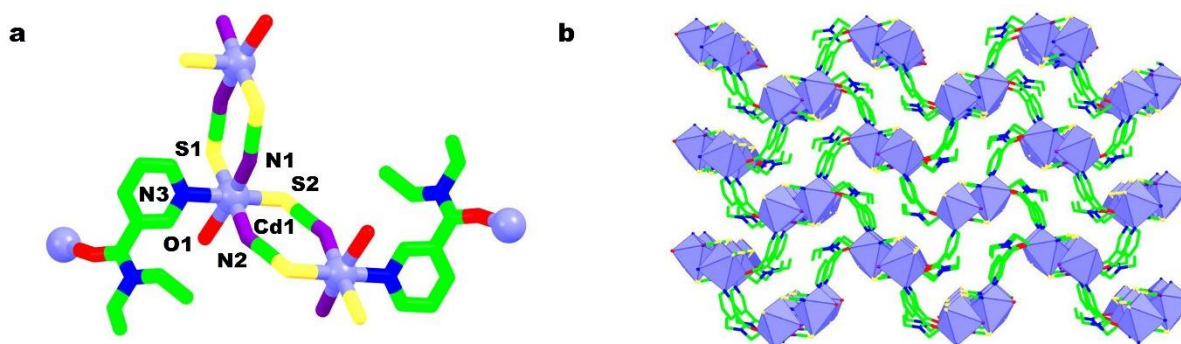


Figure 22 View of a) unique crystallographic unit of the complex **41** with N,N and S,S pairs of thiocyanato ions in *cis*-position, and b) 3D coordination framework of the complex **41**.

The complex  $[Cd(L^3)(NCS)_2]_n$  (**41**) has a three-dimensional network of octahedral Cd(II) ions, each coordinated to bridged  $L^3$  molecules (in mode4) and thiocyanate ions (Figure 22a and 22b). The thiocyanate anions were coordinated in linear fashion, displaying torsion angles of  $178.5(4)^\circ$  (N(1)-C(1)-S(1)) and  $177.1(4)^\circ$  (N(2)-C(2)-S(2)), respectively [60]. The complex **41**



has three-dimensional structure in contrast to **29** (1D chain) [53] due to the bridging of thiocyanate anions between octahedral Cd(II) centres (Figure 22b).

### 2.1.1.7 Metal cluster

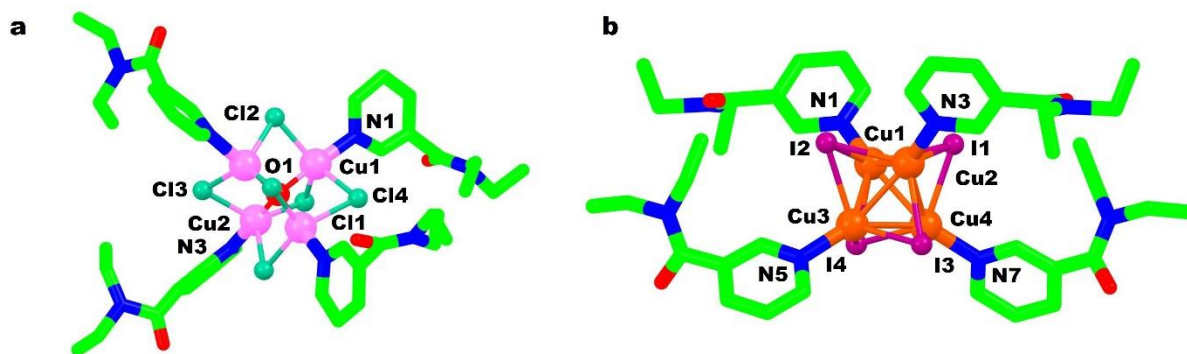


Figure 23 Pictorial presentation of a) tetra-nuclear cluster of trigonal bipyramidal Cu(II) ions of the complex **42** with two-fold axis passing through oxo and one of the chloride ligands, and b) tetrahedrally distorted cubane core Cu<sub>4</sub>I<sub>4</sub> of tetrahedrally coordinated Cu(I) ions of the complex **43**.

Toukhy *et al.* analytically (spectrophotometric titrations) studied the transmetallation of a tetranuclear complex [(L<sup>3</sup>)<sub>4</sub>Cu<sub>4</sub>Cl<sub>6</sub>O] (**42**) using Ni(NS)<sub>2</sub> in methylene chloride. The complex **42** was obtained as a side product of the crystallisation of some Cu(II) tetrameric complexes *viz.* [(L<sup>3</sup>)CuCl]<sub>4</sub>O<sub>2</sub>, [(L<sup>3</sup>)CuCl]<sub>4</sub>(CO)<sub>3</sub> and [(L<sup>3</sup>)CuCl]<sub>4</sub>Cl<sub>4</sub> of L<sup>3</sup>. In the complex, Cu(II) ions with trigonal bipyramidal geometry were lying at the corners of the tetrahedron, connected to each other by μ-chloro bridges (Figure 23a). At the centre of tetra-nuclear metal cluster, a μ<sub>4</sub>-oxo ion was tetrahedrally coordinated to four Cu(II) ions [61]. Air stable Cu(I) cluster [CuI(L<sup>3</sup>)]<sub>4</sub> (**43**) has tetrahedrally distorted Cu<sub>4</sub>I<sub>4</sub> cubane core with alternating Cu(I) and iodide ions (Figure 23b). Each Cu(I) ions was tetrahedrally coordinated to the three triply bridged iodide ions and a N atom of the pyridyl ring of L<sup>3</sup> molecule. The Cu⋯Cu nonbonding distances observed in the Cu<sub>4</sub>I<sub>4</sub> cubane core were in the range 2.6301(21) - 2.6964 (20) Å [62]. In both these complexes, the L<sup>3</sup> molecules were coordinated in mode2.

## 2.1.2 Type 2 Ligands

### 2.1.2.1 Monomeric complexes

Coordination modes shown by the ligands are mode 6 and 7. The complexes [Cu(L<sup>7</sup>)Cl<sub>2</sub>] (**44**) and [Cu(L<sup>7</sup>)Cl(ClO<sub>4</sub>)] (**45**) have five coordinated Cu(II) ion with trigonally distorted

rectangular bipyramidal arrangement ( $\tau = 0.18$  (7) and  $0.41$  (8)) of  $L^7$  molecule and the counter anions around the metal ion (Figure 24a and 24b).

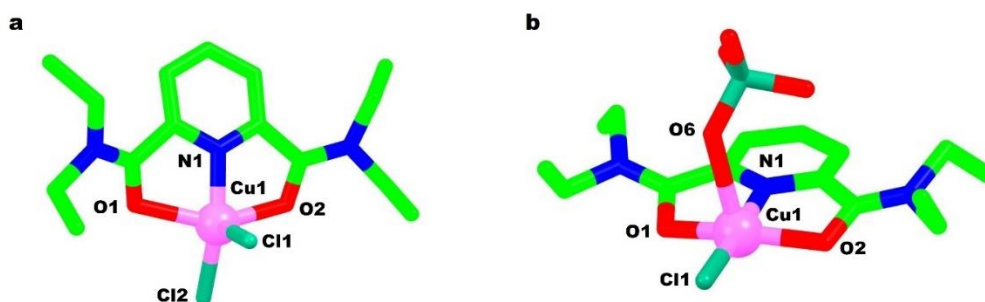


Figure 24 Pictorial view of the trigonally distorted rectangular bipyramidal environment of Cu(II) ions in a) complex **44**, and b) complex **45**.

In both the complexes, chelating  $L^7$  molecule was coordinated in mode6 using ONO donor set. Molar conductance measurements in ethanol and nitrobenzene have illustrated that complex **44** was a non-electrolyte while the complex **45** was a uni-univalent electrolyte, ionized as  $[CuClL^7]^+$ :  $ClO_4^-$  pair in nitrobenzene and acetonitrile [20]. Three octahedral complexes viz.  $[Co(L^7)_2(H_2O)_2](ClO_4)_2 \cdot H_2O$  (**46**),  $[Co(L^7)_2(H_2O)_2](PF_6)_2 \cdot H_2O$  (**47**) and  $[Co(L^7)_2(CH_3CN)](PF_6)_2$  (**48**) were reported by Kapoor *et al.* Among these, complexes **46** (Figure 25a) and **47** contains isostructural  $[Co(L^7)_2(H_2O)_2]^{2+}$  cationic units with twofold axis of symmetry passing through Co(II) ion. Both complexes have  $L^7$  molecules coordinated in a bidentate chelating mode7. These cationic units were hydrogen bonded to the lattice water molecules to form a 1D chain running perpendicular to the *ac* plane. These 1D chains were linked to a 2D hydrogen bonded network via perchlorate anions entrapped in the flexible linear columns generated by these chains (Figure 25b). The complex **48** differs from **46** in the coordination modes shown by  $L^7$  molecules; mode6 and mode7 using ON and ONO sets, respectively, in the cationic unit  $[Co(L^7)_2CH_3CN]^{2+}$  (Figure 25c) [21].

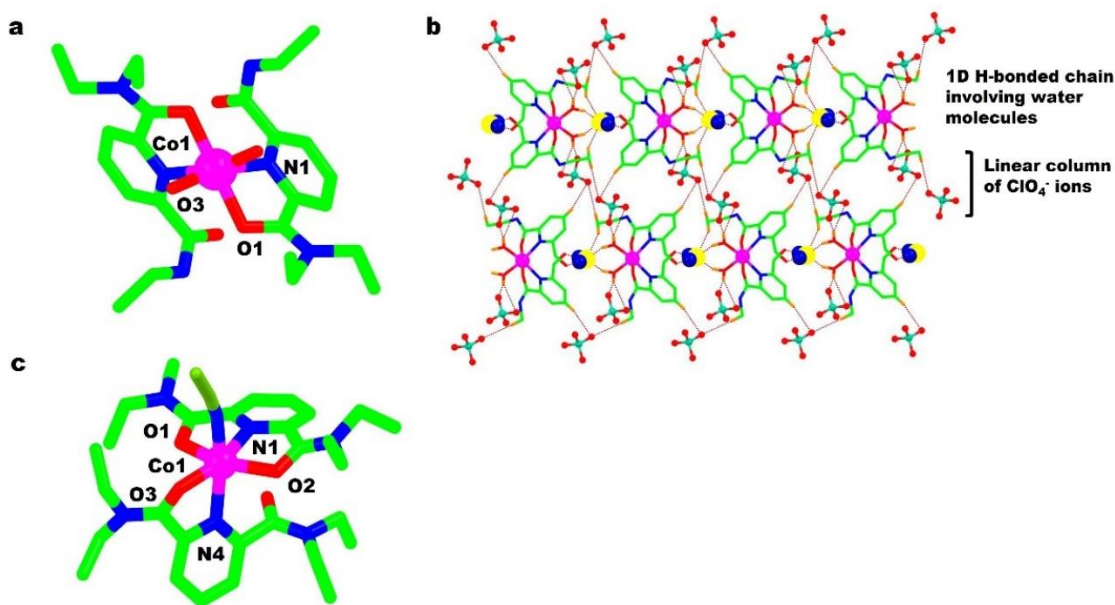


Figure 25 Pictorial view of a) octahedral coordination of Co(II) ion in the complex **46**, b) 2D hydrogen bonded sheet involving lattice water molecules and perchlorate ions of the complex **46**, and c) unique coordination unit of the complex **48**. (Note – Counter anions are not shown in the coordination units of complexes **46** and **48**. Oxygen atoms of water molecules in the Figure 25b are shown in yellow, while hydrogen atoms are shown in blue.)

Five new complexes  $[\text{Ni}(\text{L}^6)(\text{H}_2\text{O})_3](\text{NO}_3)_2$  (**49**),  $[\text{Ni}(\text{L}^7)(\text{H}_2\text{O})_2(\text{NO}_3)](\text{NO}_3)$  (**50**),  $[\text{Co}(\text{L}^6)(\text{NO}_3)_2]$  (**51**),  $[\text{Co}(\text{L}^7)(\text{NO}_3)_2]$  (**52**) and  $[\text{Cu}(\text{L}^9)(\text{NO}_3)_2]$  (**53**) were synthesized using  $\text{L}^6$ ,  $\text{L}^7$ , and  $\text{L}^9$  molecules (Figure 26a – 26d) [22]. Different coordination geometries were observed in all complexes ranging from distorted pentagonal-bipyramidal in Co(II) complexes (**51** and **52**), octahedral in Ni(II) complexes (**49** and **50**) to distorted square pyramidal in Cu(II) complex (**53**). These discrepancies were due to the diverse coordination modes shown by nitrate ions with bidentate chelating mode in Co(II) complexes (Figure 26c), and mono- and bidentate modes in Cu(II) complex (**53**) (Figure 26d). Whereas in Ni(II) complexes, the nitrate ions were ionic (uncoordinated) in **49** (Figure 26a), and both monodentate and ionic in **50** (Figure 26b). Though complexes **49** and **50** were isostructural, they differ in the composition of first coordination sphere with coordinated water molecule in complex **49** was replaced by nitrate ion in **50**.

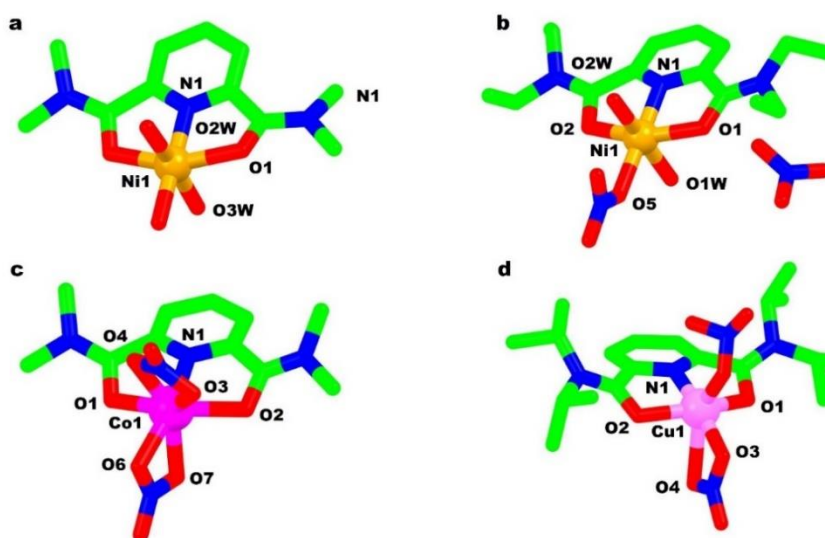


Figure 26 Pictorial presentation of a) coordination environment of Ni(II) ion in the complex **49**, b) nitrate ions showing monodentate coordination and ionic mode in the complex **50**, c) bidentate chelating mode of nitrate ions in the complex **51**, and d) mono- and bidentate modes of nitrate ions in the complex **53**. (Note – Uncoordinated nitrate ions have been deleted for clarity in the complex **49**)

Four Cu(II) complexes  $[\text{Cu}(\text{L}^7)\text{Cl}(\text{CF}_3\text{SO}_3)]$  (**54**),  $[\text{Cu}(\text{L}^9)(\text{Cl})(\text{ClO}_4)]$  (**55**),  $[\text{Cu}(\text{L}^{10})(\text{Cl})(\text{ClO}_4)]$  (**56**), and  $[\text{Cu}(\text{L}^9)(\text{CF}_3\text{SO}_3)_2(\text{H}_2\text{O})]$  (**57**) were reported by Kapoor *et al.*. Among them, complexes **54** (Figure 27a), **55**, and **56** have five coordinated Cu(II) ion with distorted square-pyramidal geometry ( $\tau = 0.057, 0.134$  and  $0.344$ ) whereas it was octahedral in **57** (Figure 27c). In all complexes, ligand molecules were coordinated to Cu(II) ions in chelating mode<sup>6</sup>. In addition, lowering of local site symmetry of  $\text{CF}_3\text{SO}_3$  from  $\text{C}_{3v}$  to  $\text{C}_s$ , and from  $\text{T}_d$  to  $\text{C}_{3v}$  for  $\text{ClO}_4^-$  ions was also observed in the I.R spectra of these complexes. Interestingly, complexes of the type  $[\text{CuCl}(\text{X})(\text{L})_2]$  with square pyramidal Cu(II) ion was formed when 1 mole of counter ion was consumed while 2 mole of it has resulted in an octahedral complex  $[\text{CuX}_2(\text{L})_2(\text{H}_2\text{O})]$  [23]. In the crystal lattice of complex **54**, adjacent dimeric units were held together by  $\text{C}-\text{H}\cdots\text{O}$  interactions to form 1D chains stacked in a parallel fashion, which were further interconnected by  $\text{C}-\text{H}\cdots\text{F}$  hydrogen bonding interactions to form a 2D sheet in *ab* plane (Figure 27b).

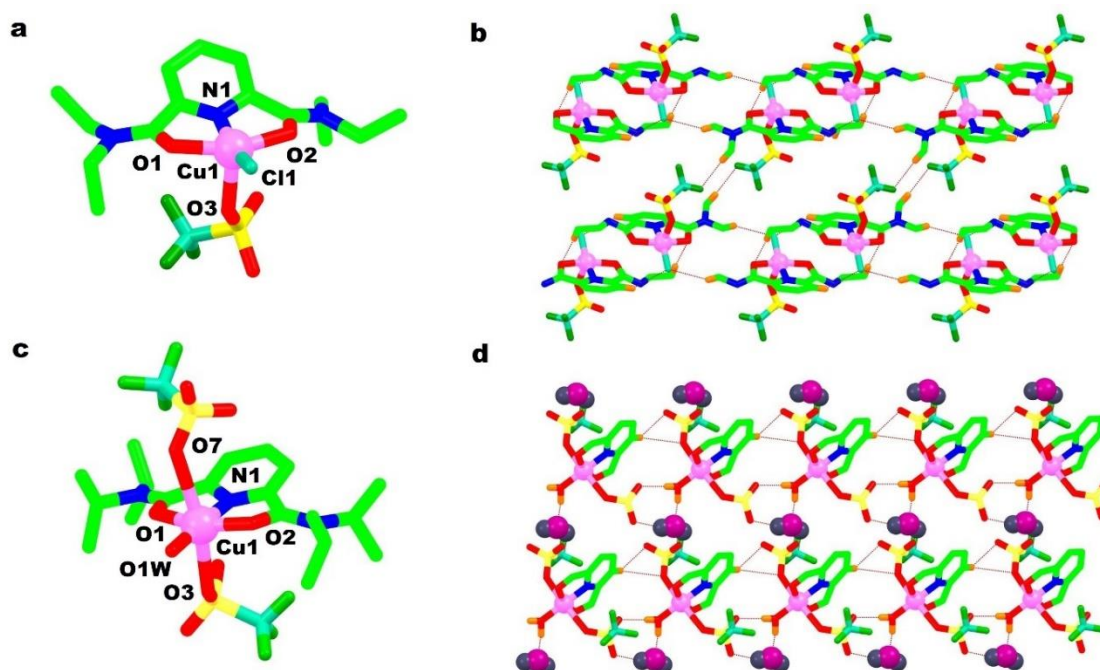


Figure 27 View of a) distorted square-pyramidal geometry of Cu(II) ion in the complex **54**, b) 2D hydrogen bonded network of **54** constructed by C–H $\cdots$ O and C–H $\cdots$ F interactions involving triflate ions and methylene groups, c) octahedral coordination of Cu(II) ion in the complex **57**, and d) 2D hydrogen bonded network of the complex **57** involving triflate ions, and lattice and coordinated water molecules. (Note – In all figures, chlorine atoms are shown in cyan and fluorine atoms are shown in dark green colour. Lattice water molecules are shown in maroon/violet colour in the Figure 27d).

However, in complex **57** a 2D hydrogen bonded network parallel to *ac* plane was generated due to extensive hydrogen bonding between lattice and coordinate water molecules, and triflate ions as well (Figure 27d).



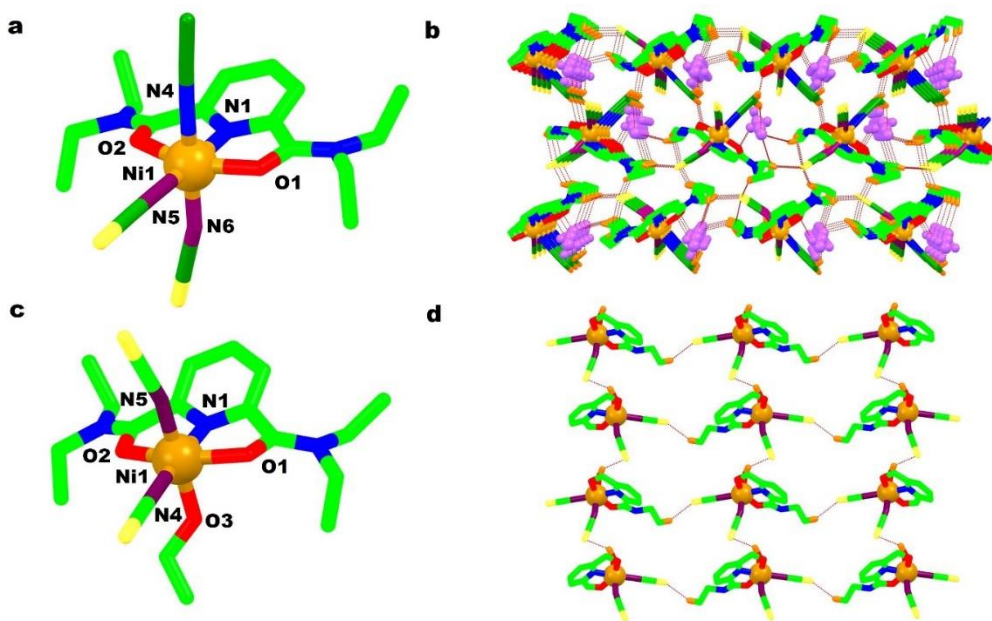


Figure 28 View of a) octahedral environment of Cu(II) ion in the complex **58**, b) 3D hydrogen bonded framework of **58** constructed by hydrogen bonding between the octahedral units and the lattice acetonitrile molecules (violet colour), c) octahedral coordination of Cu(II) ion in the complex **59**, and d) 2D hydrogen bonded network of **59** involving coordinated thiocyanate ions and ethanol molecules.

Variations in the coordination geometries of Ni(II) ions in different solvents were investigated for two complexes of the composition  $[\text{Ni}(\text{NCS})_2(\text{L}^7)(\text{CH}_3\text{CN})]\cdot\text{CH}_3\text{CN}$  (**58**) and  $[\text{Ni}(\text{NCS})_2(\text{L}^7)(\text{C}_2\text{H}_5\text{OH})]$  (**59**) [24]. Both complexes were isostructural containing octahedral Ni(II) ions and  $\text{L}^7$  molecules coordinated in mode6, and differs with respect to the coordinated solvent molecules (Figure 28a and 28c). Weak hydrogen bonding interactions involving  $\text{C}-\text{H}\cdots\text{S}$  interactions among octahedral units, and  $\text{C}-\text{H}\cdots\text{N}$  interactions with acetonitrile molecules construct a 3D framework in complex **58** (Figure 28b) [24]. Likewise, a 2D hydrogen bonded network was constructed in the complex **59** via  $\text{O}-\text{H}\cdots\text{S}$ ,  $\text{C}-\text{H}\cdots\text{S}$ , and  $\text{C}-\text{H}\cdots\text{O}$  interactions between the octahedral units and ethanol molecules (Figure 28d). The use of the tridentate ligand  $\text{L}^9$  for the enforced synthesis of uranyl(VI) cis-dihalide complexes of the type  $\text{UO}_2\text{X}_2\text{L}$  ( $\text{X} = \text{Cl}, \text{Br}$ ) was demonstrated by Duval *et al.* [25]. Complexes  $[\text{U}(\text{O}_2)(\text{Cl}_2)(\text{L}^9)]$  (**60**) and  $[\text{U}(\text{O}_2)(\text{Br}_2)(\text{L}^9)]$  (**61**) were isostructural, with each of them containing U(VI) centre in a distorted pentagonal bipyramidal geometry provided by oxide and halide ions, and tridentate (mode6) ligand  $\text{L}^9$  molecules (Figure 29a). The halide ions in both complexes were showing *cis*-equatorial coordination to U(VI) ions [25].

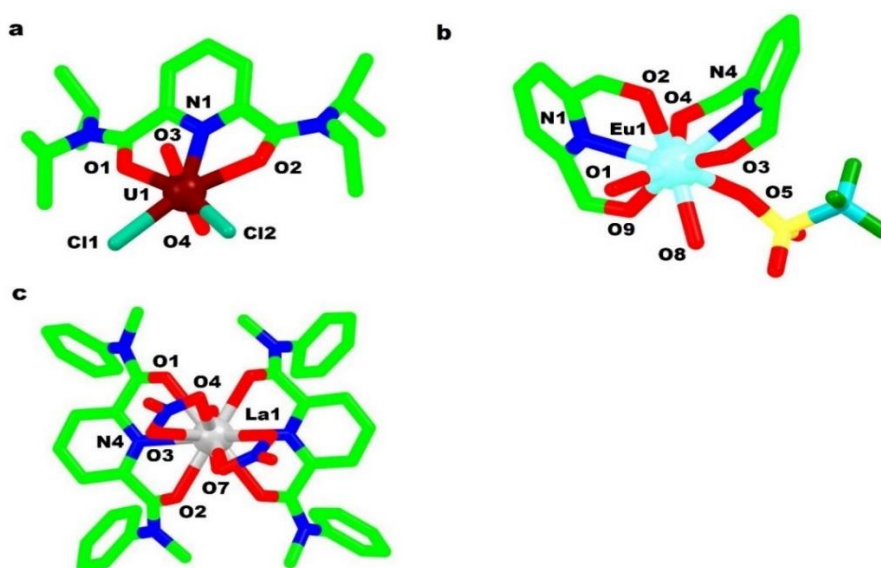


Figure 29 View of a) distorted pentagonal bipyramidal geometry of  $\text{UO}_2(\text{IV})$  ion of the complex **60**, b) distorted mono-capped square antiprism environment of  $\text{Eu}(\text{III})$  ion of the complex **62**, and c) centrosymmetric unit  $[\text{La}(\text{NO}_3)_3(\text{L}^{12})_2]$  containing 12-coordinated  $\text{La}(\text{III})$  ion in the complex **64**. (Note- Amide nitrogen atoms and substituted groups on it have been deleted in the Figure 29b).

A new 1:2 (M:L) complex  $[\text{Eu}(\text{L}^9)_2(\text{H}_2\text{O})_2(\text{CF}_3\text{SO}_3)](\text{CF}_3\text{SO}_3)_2(\text{THF})_{1.5}$  (**62**) containing a nine coordinated  $\text{Eu}(\text{III})$  centre was synthesized by Borgne *et al.* [26]. The coordination sphere around  $\text{Eu}(\text{III})$  ion was a distorted mono-capped square antiprism (MSA) with one of the tetragonal faces capped by water molecule (Figure 29b). Isostructural complex  $[\text{Gd}(\text{L}^{11})_2(\text{H}_2\text{O})_2(\text{CF}_3\text{SO}_3)](\text{CF}_3\text{SO}_3)_2(\text{tBuOMe})_2$  (**63**) has analogous coordination environment around  $\text{Gd}(\text{III})$  ion, differing in relation to the coordinated ligand molecule, and solvent of crystallization. The lanthanum complex  $[\text{La}(\text{NO}_3)_3(\text{L}^{12})_2]$  (**64**) has a 12-coordinated  $\text{La}(\text{III})$  ion, surrounded by two  $\text{L}^{12}$  molecules (in mode6) and three bidentate nitrate ions (Figure 29c). The complex was symmetric about a  $C_2$  axis of symmetry passing through the  $\text{La}(\text{III})$  ion and a nitrate ion. The other symmetry related nitrate ions ( $C_2$  symmetry) were positioned on the hemisphere opposite to axial nitrate ion lying on  $C_2$  axis [27].



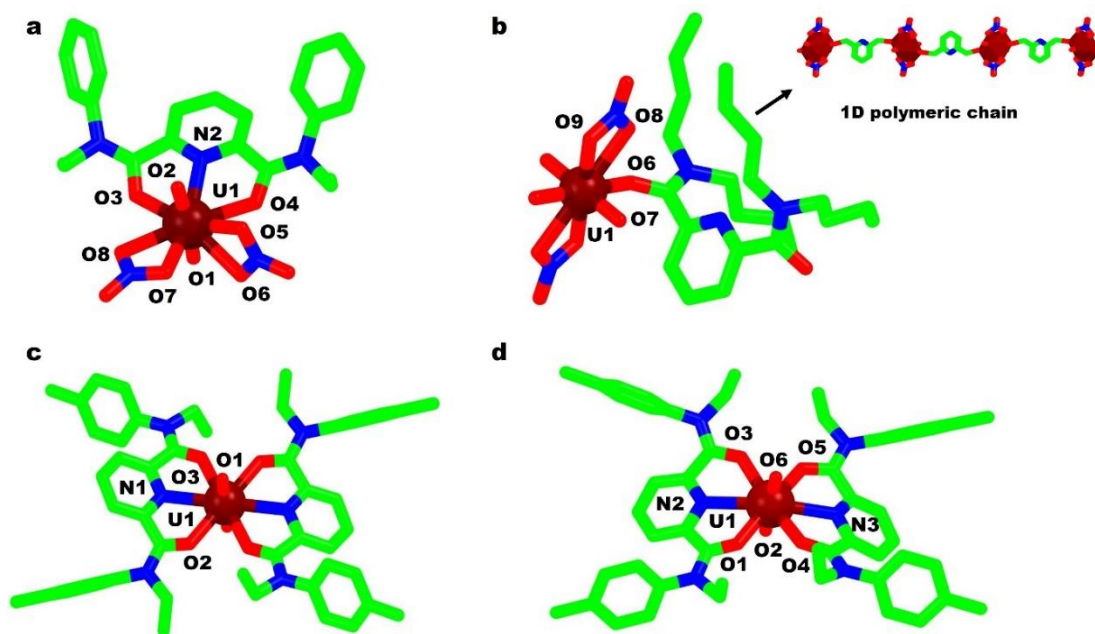


Figure 30 Pictorial view of a) mononuclear unit of the complex **65** and b) 1D polymeric chain (inset) of the complex **66**, c) coordination environment of  $\text{UO}_2(\text{IV})$  ion in the complex **67**, and d) coordination environment of  $\text{UO}_2(\text{IV})$  ion in the complex **68**. (Note- The counter-anions have not been shown in the Figure 30c and 30d.)

The effect of the substituents on the coordination behaviour of ligand molecules  $\text{L}^{13}$  and  $\text{L}^8$  in  $\text{UO}_2(\text{IV})$  complexes was investigated by Alyyapyshev *et al.* The complex  $[(\text{L}^{13})\text{UO}_2(\text{NO}_3)_2] \cdot \text{CH}_2\text{Cl}_2$  (**65**) containing ethyl and phenyl groups as substituents on amide nitrogen atoms was a mononuclear complex with  $\text{UO}_2^{+2}$  cation surrounded by two nitrate ions and a chelating  $\text{L}^{13}$  molecule (mode6) in the equatorial plane (Figure 30a). Whereas bulky butyl groups on  $\text{L}^8$  in the complex  $[(\text{L}^8)\text{UO}_2(\text{NO}_3)_2]_n$  (**66**) hinders the formation of simple mononuclear complex, resulting in a 1D polymeric chain. Each  $\text{UO}_2^{+2}$  cation in **66** was surrounded by symmetry related nitrate ions and bridged  $\text{L}^8$  molecules in mode8 (Figure 30b). The SCXRD analysis illustrated a 1:1 M:L complex for both ligands, which was also supported by DFT calculations and extraction experiments [28].

Yong *et al.* studied the coordination and extraction mechanism of  $\text{U}(\text{VI})$  ion with  $\text{L}^{14}$  molecule using room temperature ionic liquids (RTIL, see the application section). In this pursuit, they have synthesized complexes  $[\text{U}_{0.5}(\text{O})_2(\text{L}^{14})]_2(\text{NTf}_2)$  (**67**) and  $[\text{U}(\text{O})_2(\text{L}^{14})_2](\text{PF}_6)$  (**68**) in  $\text{LiNTf}_2$  and  $\text{KPF}_6$  ionic liquids, respectively. Both these complexes contain eight coordinated  $\text{UO}_2(\text{IV})$

ion bounded to two  $L^{14}$  molecules in mode6, and two oxide ions (Figures 30c and 30d). The complex **67** differs from **68** in the presence of inversion centre on the  $UO_2(IV)$  ion, which was absent in complex **68** [29].

### 2.1.2.2 Dimeric complexes

Coordination modes shown by the ligand molecules are mode 7 and mode 9. The binuclear complex  $[Cu_2(Cl)_4(L^9)_2] \cdot 2CH_3CN$  (**69**) containing bridged  $Cl^-$  ions and chelating  $L^9$  molecules has a weak anti-ferromagnetic coupled  $Cu(II)$  pair with nonbonding  $Cu \cdots Cu$  distance of 3.424 Å. The local geometry around each  $Cu(II)$  ion was distorted square-pyramidal ( $\tau = 0.36$ , Figure 31a) with the ligand molecules coordinated in mode7 using NO set [79]. Akin to **69**, complex  $[ \{ CuCl(L^1) \}_2 (\mu-Cl)_2 ]$  (**70**) was a centrosymmetric dimer comprising square-pyramidal  $Cu(II)$  ions surrounded by bridged chloride ions and terminal chloride ions, and a  $L^1$  molecule (mode1) [17].

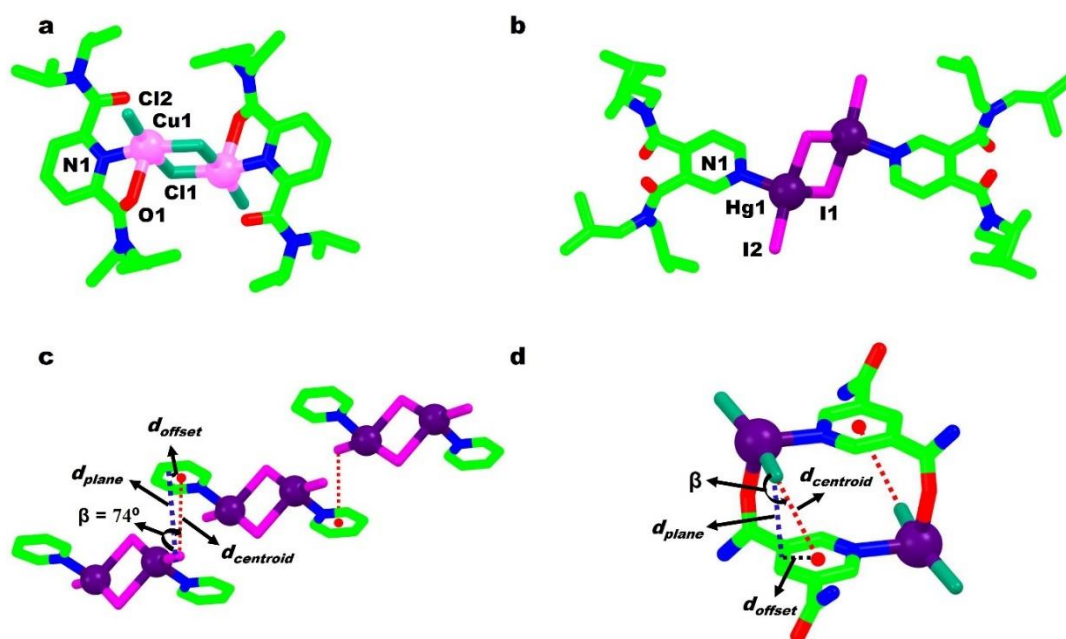


Figure 31 View of a) distorted square-pyramidal geometry of  $Cu(II)$  ions in the centrosymmetric dimeric unit of the complex **69**, b) tetrahedral geometry of  $Hg(II)$  ions in the complex **71**, c) semi-localized type  $Lp \cdots \pi$  interactions among adjacent dimeric units of the complex **71**, and d) representative dimeric unit of the complexes **72-74** supported by semi-localized type  $Lp \cdots \pi$  interactions.

Rana *et al.* studied the effect of bulky groups of the ligand, counter anions and various non-covalent interactions on the final structure of Hg(II) complexes. In the series of six complexes synthesized using **L**<sup>17</sup> and **L**<sup>18</sup>, the only dimeric complex obtained was [Hg(**L**<sup>18</sup>)I<sub>2</sub>]<sub>2</sub> (**71**) (Figure 31b) while rest of the complexes (discussed in 2D polymer section) were 2D coordination polymers [80]. The rationale of the formation of dimeric complex was attributed to the control of primary structure by large size and soft nature of bridged and terminal iodides together with the steric congestion of isobutyl groups that resulted in the formation of Hg<sub>2</sub>I<sub>2</sub> bridge and monodentate coordination of ligand molecule in mode9. The dimeric unit was further supported by Lp $\cdots\pi$  ( $\beta \sim 74^\circ$ , Semi-localized type i.e the electronegative atom lies above one of the bond of aromatic ring) interactions between coordinated iodide ions and pyridine rings of adjacent dimeric units (Figure 31c). In a similar work, different interactions, and their effect on final structure of self-assembly process was discussed using the notion of “Crystal engineering”. For this, six new complexes of Hg(II) were synthesized using **L**<sup>15</sup> and **L**<sup>16</sup> molecules. Among them, complexes **72-74** were dimers comprising bridged **L**<sup>15</sup> molecules (mode11) in the centrosymmetric [Hg(**L**<sup>15</sup>)X<sub>2</sub>]<sub>2</sub> (X= Cl<sup>-</sup>, Br<sup>-</sup>, and I<sup>-</sup>) unit. These dimeric units were supported by Lp $\cdots\pi$  interactions between halide anions and pyridine rings ( $\beta \sim 61-74^\circ$ , Semi-localized type) (Figure 31d) [81].

### 2.1.2.3 1D coordination polymers

Coordination modes shown by the ligand molecules are mode12 and mode13. Rana *et al.* discussed the factors governing the bridging of ligand molecules and/or halide ions or both between Hg(II) ions in the 1D chain [81]. The complex [Hg(**L**<sup>16</sup>)Cl<sub>2</sub>]<sub>n</sub> (**75**) (Figure 32a) containing tetrahedral Hg(II) ions was a ligand driven coordination polymer owing to steric congestion imposed by isobutyl groups, which results in the bridging of **L**<sup>16</sup> molecules (3-c linker) in mode13 between adjacent metal centres, and thus compensates for the halide bridging (Figure 32b). Conversely, the complexes **76** and **77** involve the bridging of both ligand molecules and halide ions in the 1D coordination chain. In both complexes, centrosymmetric [Hg<sub>2</sub>( $\mu_2$ -**L**<sup>16</sup>)<sub>2</sub>X<sub>2</sub>]<sub>n</sub> units (X = Br<sup>-</sup> in (**76**), and I<sup>-</sup> in (**77**)) containing square-pyramidal Hg(II) ions (Figure 32c) bridged by **L**<sup>16</sup> molecules in mode12 (2-c linker) were connected by halide ions to form a 1D zig-zag chain (Figure 32d). Additionally, role of anions, solvent molecules, and various non-covalent interactions in the self-assembly process were well demonstrated [81].

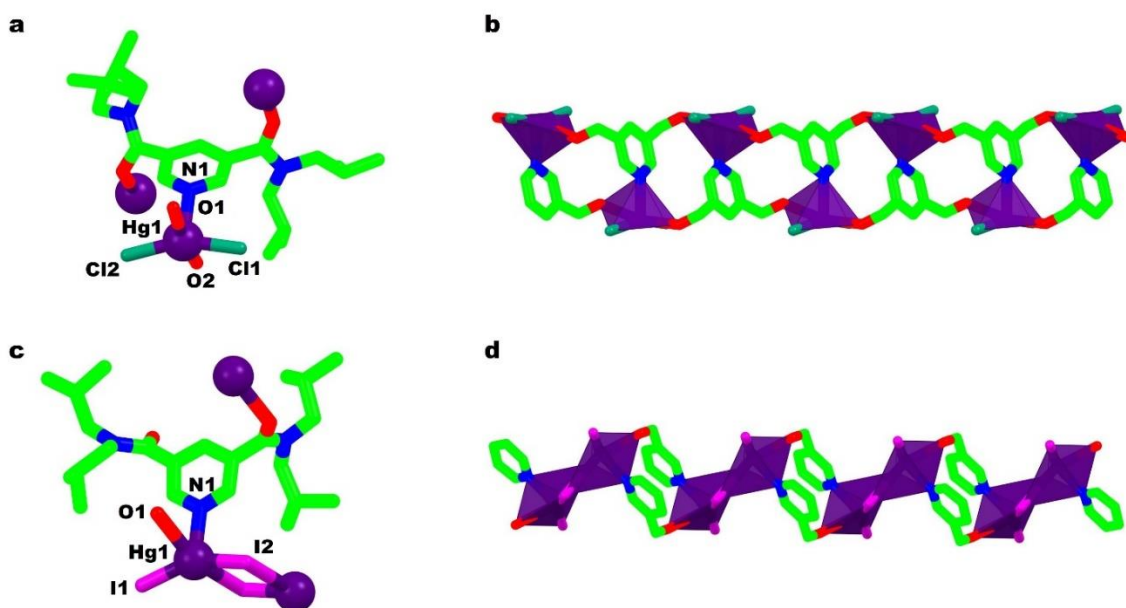


Figure 32 View of a) tetrahedrally coordinated Hg(II) ion in the complex **75**, b) ligand driven 1D coordination chain of the complex **75**, c) square-pyramidal coordination environment of Hg(II) ion in the complex **76**, and d) 1D coordination chain involving bridged halide ions and  $L^{16}$  molecules of the complex **76**.

#### 2.1.2.4 2D coordination polymers

Coordination modes shown by the ligand molecules are mode10 and mode11. The effect of coordination mode of counter anions, divergent nature of ligands, steric factors, and various non-covalent interactions on the self-assembly of  $HgX_2$  ( $X = Cl^-$ ,  $Br^-$ , and  $I^-$ ) units with  $L^{17}$  and  $L^{18}$  molecules have been reported [80]. It was observed that the five complexes containing  $L^{17}$  molecules were 2D coordination polymers (CPs, Figure 33 a-d) with the ubiquitous  $Hg_2X_2$  bridges and bridged ligand molecules (mode10, 2-c linker) were present in a double salt  $[[Hg(L^{17})Cl_2][HgCl_2]]_n$  (**78**), and isostructural complexes **79** and **80** containing  $[Hg(L^{17})X_2]_n$  ( $X = Br$  in **79** and  $I$  in **80**) units. The complex **78** has two different 1D chains comprising  $[HgCl_2]$  and  $[Hg(L^{17})Cl_2]$  moieties, respectively, which were linked together in a 2D network by  $\mu_2$ - and  $\mu_3$ -bridged chloride bridges.

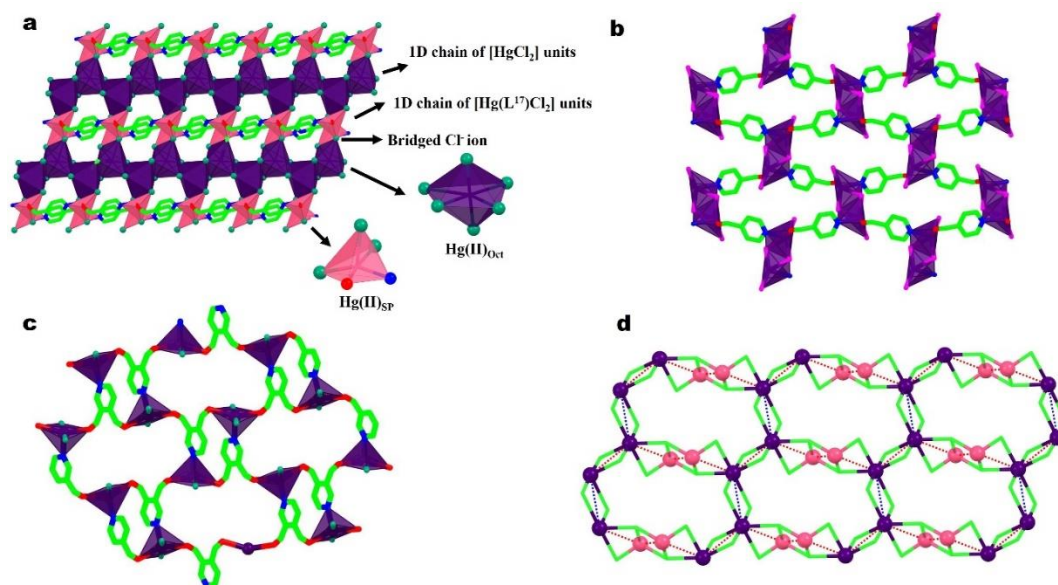


Figure 33 View of a) 2D sheet involving  $[\text{HgCl}_2]_n$  and  $[\text{Hg}(\text{L}^{17})\text{Cl}_2]_n$  chains connected by  $\text{Cl}^-$  bridges in the complex **78**, b) 2D network containing edge sharing  $[\text{Hg}(\text{L}^{17})\text{X}_2]_2$  units connected by  $\mu_2$ -bridged  $\text{L}^{17}$  molecules in the complexes **79** and **80**, c) ligand driven 2D network of the complexes **81** and **82** containing  $\mu_3$ -bridged  $\text{L}^{18}$  molecules with no halide bridges, and d) 2D framework of the complex **78** endorsed by mercurophilic interactions.

(Figure 33a). Two types of coordination geometries were observed for  $\text{Hg}(\text{II})$  ions, a distorted octahedral geometry in the 1D chain of  $[\text{HgCl}_2]_n$  units and a distorted square pyramidal environment in the chain of  $[\text{Hg}(\text{L}^{17})\text{Cl}_2]_n$  units. Conversely, the complexes **79** and **80** have edge sharing  $[\text{Hg}(\text{L}^{17})\text{X}_2]_2$  units ( $\text{X} = \text{Br}^-$  in **79**,  $\text{I}^-$  in **80**) of square pyramidal  $\text{Hg}(\text{II})$  ions, connected by bridged  $\text{L}^{17}$  molecules (mode10, 2-c linker) in the 2D framework (Figure 33b). The complexes of  $\text{L}^{18}$  molecules with the structural formula  $[\text{Hg}(\text{L}^{18})\text{X}_2]_n$  ( $\text{X} = \text{Cl}^-$  in **81** and  $\text{Br}^-$  in **82**) were ligand driven polymer owing to the steric congestion offered by isobutyl groups that results in bridging of  $\text{L}^{18}$  molecules in mode11 (3-c linker) thereby avoiding halide bridges (Figure 33c). Additionally, various non-covalent interactions *viz.*  $\text{C-H}\cdots\text{X}$ ,  $\text{Lp}\cdots\pi$  ( $\beta \sim 74^\circ$ , Semi-localized type) in complex **78**,  $\pi\cdots\pi$  in complexes **81** and **82** and  $\text{C-H}\cdots\pi$  interactions in complexes **79**, **81** and **82** further reinforce the 2D sheets. Mercurophilic interactions (3.81, 3.96 and 4.01 Å) were also found to strengthen 2D framework in the double salt **78** (Figure 33d) [80].



## 2.2 Coordination complexes of Class II Ligands

### 2.2.1 Type 3 Ligands

#### 2.2.1.1 Dimeric complexes

Coordination modes shown by the ligand molecules are mode14 and mode17. Li *et al.* reported a centrosymmetric complex  $[\text{Hg}(\text{I})_2(\text{L}^{19})]_2 \cdot 3\text{H}_2\text{O}$  (**83**) containing cisoid  $\text{L}^{19}$  molecules, bridged (in mode14) between symmetry related tetrahedral  $\text{Hg}(\text{II})$  ions to form a metallamacrocycle (Figure 34a). The adjacent metallacycles were parallelly stacked into 1D columns and then to a two-dimensional supramolecular architecture with the help of short contacts between uncoordinated water molecules and terminal  $\text{I}^-$  ions (Figure 34b) [63].

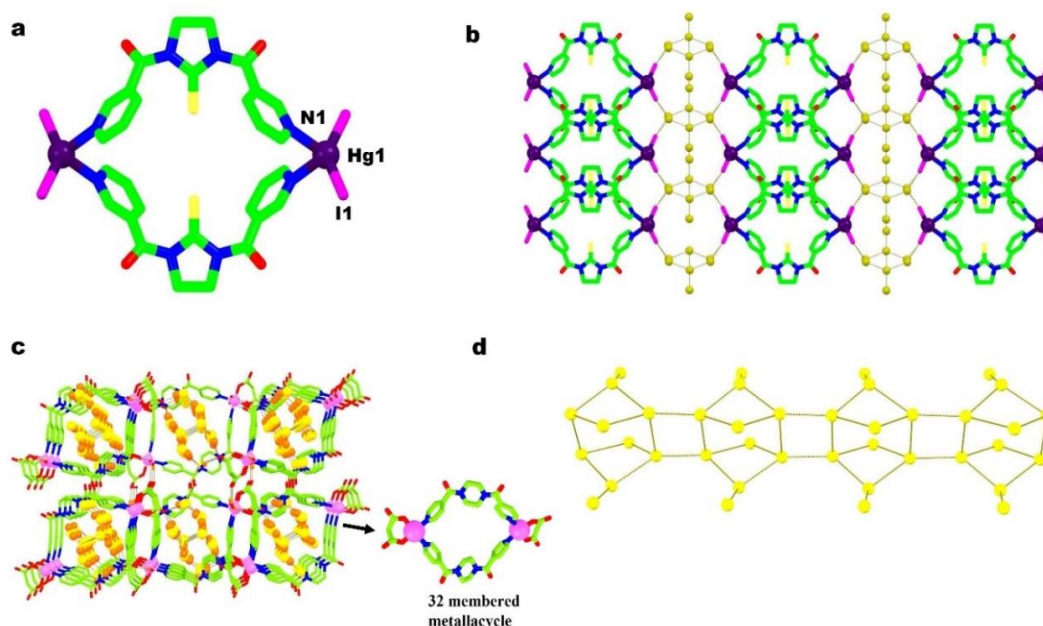


Figure 34 View of a) metallacycle of the complex **83** containing tetrahedrally coordinated  $\text{Hg}(\text{II})$  ions, b) 2D sheet of stacked metalocyclic units in the complex **83**, c) 3D hydrogen bonding framework of **84** involving hydrogen bonding between water molecules and  $\text{Cu}(\text{II})$  metallacycles, and d) hydrogen bonded tape motif with T6(6)4(4)4(3)4(3) type aggregation of lattice water molecules of the complex **84**. (Note- The oxygen atoms of water molecules are shown in mustard colour in the Figure 34b, while it is yellow colour in the Figures 34c and 34d. Hydrogen atoms of water molecules are shown in orange colour).

The complex  $\{[\text{Cu}_2(\text{mal})_2(\text{L}^{22})_2(\text{H}_2\text{O})_2] \cdot 10\text{H}_2\text{O}\}_n$  (**84**) has a 32 membered metallacycle containing square pyramidal  $\text{Cu}(\text{II})$  ions. Around each  $\text{Cu}(\text{II})$  ion, symmetry related  $\text{L}^{22}$



molecules, and *cis* basal mal ions were positioned in a square planar arrangement (Figure 34 c) [64]. While the water molecule located at the axial sites completes the coordination geometry. The entrapped water molecules, mal ions, and  $L^{22}$  molecules participate in extensive hydrogen bonding to allow neighbouring  $[Cu_2(mal)_2(L^{22})_2(H_2O)_2]$  units to interact in a ‘head to tail’ fashion (Figure 34 c). Moreover, hydrogen bonding among water molecules generates an infinite tape of repeating T6(6)4(4)4(3)4(3) type aggregation comprising alternating six-membered chair and four membered rings (Figure 34d). This hydrogen bonded pattern further generates nanotubular channels occupying 22.8% (SOV) of the total unit cell volume.

### 2.2.1.2 1D-Polymeric complexes

Coordination modes shown by the ligand molecules are mode14-17. The complex  $\{[Cd(SCN)_2(L^{19})_2] \cdot 2(CH_3OH)\}_n$  (**85**) has a 1D helical chain of octahedrally coordinated Cd(II) ions (Figure 35a and 35b) connected by  $L^{19}$  molecules bridged in mode15 [65]. Along the chain, 24-membered metallocyclic rings were generated in which  $L^{19}$  molecules display GG-conformation (Figure 35b). Conversely, the complex  $[CdI_2(L^{20})]_n$  (**86**) contains 1D zig-zag chains of tetrahedral Cd(II) ions (Figure 35c and 35d), which were held together into a 2D framework by weak C–H $\cdots$ S (2.658Å) interactions (Figure 35d). Isostructural to **85**, the complex  $\{[Cd(NO_3)_2(L^{19})_2] \cdot 2(CH_3OH)\}_n$  (**87**) differs in the composition of the octahedral environment of Cd(II) ion at axial sites (nitrate ions in **87**, and thiocyanate ions in **85**) [65]. Complexes  $[Co(NCS)_2(CH_3OH)_2(L^{21})]_n$  (**88**) and  $\{[Co(H_2O)_2(CH_3OH)_2(L^{22})](NO_3)_2\}_n$  (**89**) were synthesized using pyridyl/piperazine based  $L^{21}$  and  $L^{22}$  ligands by Xu *et al.* [66].

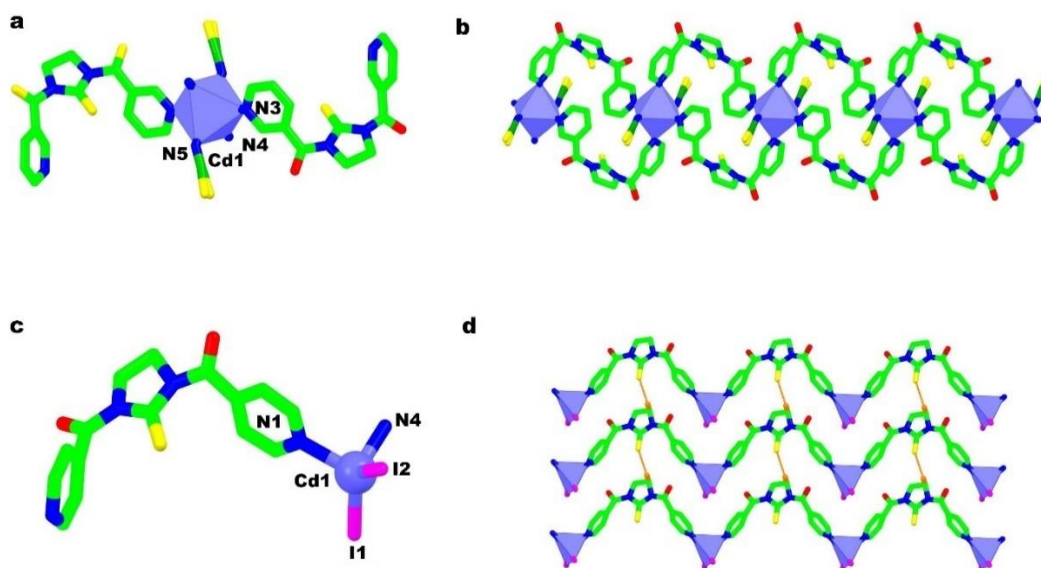


Figure 35 View of a) centrosymmetric unit containing octahedral Cd(II) ion in the complex **85**, b) 1D coordination chain of the complex **85** containing GG-conformation of ligand molecules, c) coordination unit containing tetrahedral Cd(II) ion in the complex **86**, and d) 2D hydrogen bonding framework of **86** involving C–H $\cdots$ S interactions.

These compounds have 1D polymeric chains differing in the construction of octahedral coordination sphere around the Co(II) ions. In the complex **88**, the octahedron was shaped by two methanol molecules, and two nitrogen atoms of the isothiocyanate ions in square planar fashion (Figure 36a) while the square plane in **89** involves two water and two methanol molecules (Figure 36c). The axial coordination in both complexes was provided by  $L^{21}$  molecules coordinated in mode16. The 1D chains in **88** were linked into a 2D network in *ac* plane by  $SNCS\cdots O_{\text{methanol}}$  contacts ( $S\cdots O$  3.243 Å, 130.4°) (Figure 36b). Whereas in complex **89**, the 2D hydrogen bonded network was constructed through  $O_W-H\cdots O$  hydrogen bonds involving water and ligand molecules, and nitrate ions (Figure 36d) [66].

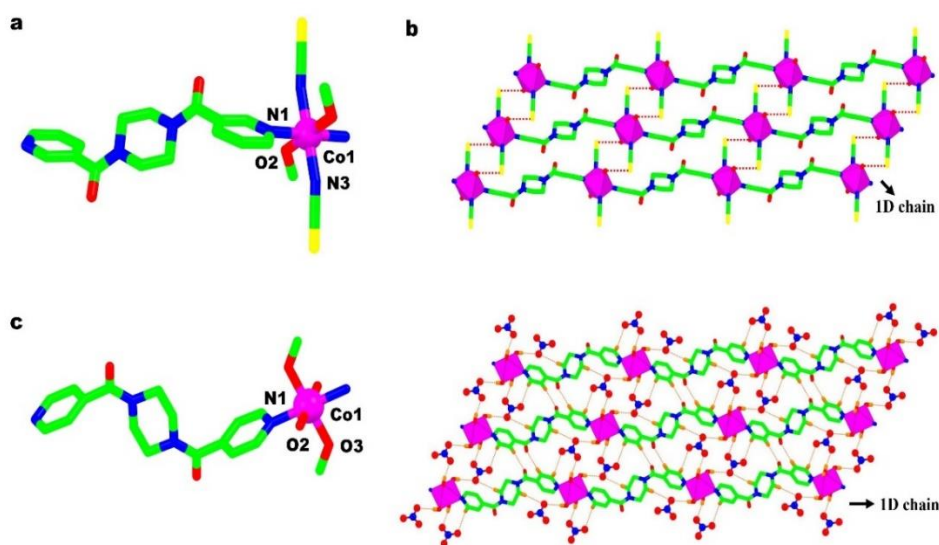


Figure 36 View of a) octahedral coordination environment around Co(II) ion in the complex **88**, b) 1D coordination chains connected by short  $S_{NCS} \cdots O_{\text{methanol}}$  contacts in the complex **88**, c) octahedral geometry of Co(II) ion in the complex **89**, and d) 2D hydrogen bonded network involving 1D coordination chains, nitrate ions and water molecules in **89**.

The complex  $[ZnCl_2(L^{21})]_n$  (**90**) has 1D wave like infinite chains (Figure 37a) of tetrahedral Zn(II) ions linked to each other into a 2D layered structure via weak  $C-H \cdots Cl$  (3.850 Å) interactions (Figure 37a) [67]. Isostructural to **90**, the complex  $[HgI_2(L^{21})]_n$  (**91**) was comprised of 1D zig-zag chains of tetrahedral Hg(II) ions [68]. The Co(II) ions of the alternating 1D chains of anionic  $[Co(hmph)_2(L^{22})]_n^{2n-}$  and cationic  $[Co(H_2O)_4(L^{22})]_n^{2n+}$  units of the complex  $\{[Co(H_2O)_4(L^{22})][Co(hmph)_2(L^{22})] \cdot 6H_2O\}_n$  (**92**) have octahedral geometry in the respective chains (Figure 37b and Figure 37c). Each Co(II) ion of anionic unit was coordinated to *cis*-hmp<sup>h</sup> anions, and *trans*  $L^{22}$  molecules (model 17) whereas the Co(II) ions in cationic unit were coordinated to four water molecules, and two *trans*  $L^{22}$  molecules. Hydrogen bonding between coordinated water molecules in cationic chain and oxygen atoms of hmp<sup>h</sup> ions in the anionic chain connects these alternate coordination chains into a 1D tape (Figure 37c) [69]. The  $[NiO_4N_2]$  core of the complex  $\{Ni(Hmip)_2(L^{22})(H_2O)_2\} \cdot 2H_2mip\}_n$  (**93**) has octahedral Ni(II) ion, coordinated to *trans*-Hmip ions, *trans*- $L^{22}$  ligands, and two water molecules. The singly protonated Hmip ions displayed monodentate coordination to Ni(II) ion whereas  $L^{22}$  molecules were bridged among Ni(II) ions in model 17 [70].

Wilseck *et al.* reported a coordination polymer  $\{[\text{Cu}(\text{H}_2\text{MeOip})(\text{HMeOip})_2(\text{L}^{22})].3\text{H}_2\text{O}\}_n$  (**94**) containing 1D polymeric ladder motifs [71] containing Cu(II) ions in a distorted square pyramidal environment. Besides, hydrogen bonding between hydroxyl groups of ligated HMeOip ions and unligated HMeOip carboxylate groups of the adjacent chains construct a twofold interpenetrated binodal supramolecular **hms** net with rare  $(6^3)(6^98)$  topology (Figure 37d).

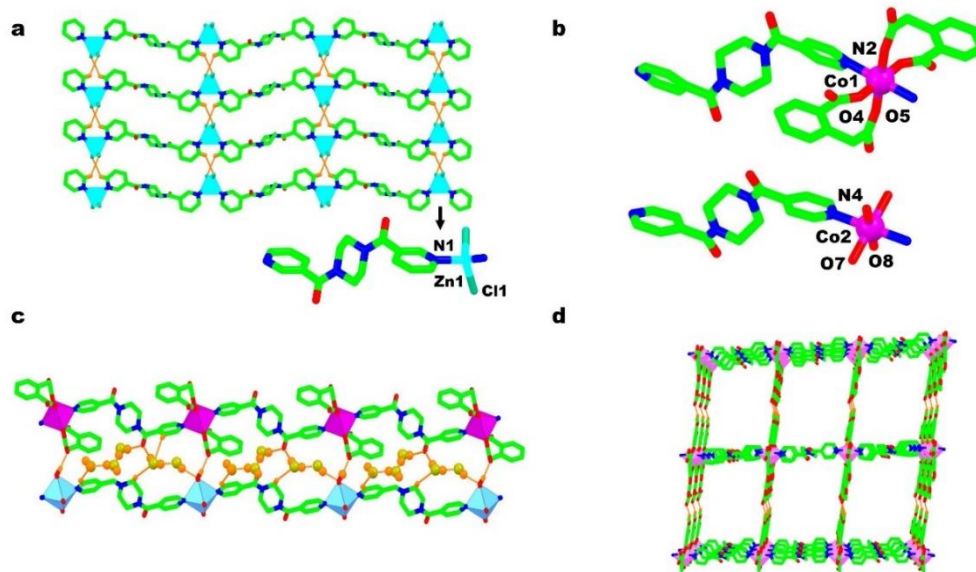


Figure 37 View of a) 2D layered structured comprising zig-zag 1D chains of the complex **90**, b) octahedrally coordinated Co(II) ions in the cationic and anionic units of the complex **92**, c) hydrogen bonded 1D tape of anionic  $[\text{Co}(\text{hmph})_2(\text{L}^{22})]_n^{2n-}$  and cationic  $[\text{Co}(\text{H}_2\text{O})_4(\text{L}^{22})]_n^{2n+}$  of the complex **92**, and d) 3D hydrogen bonded network of the complex **94** with a rare topology  $(6^3)(6^98)$ .

### 2.2.1.3 2D-polymeric complexes

Coordination modes shown by the ligand molecules are mode15, mode18, and mode19. The 2D grid of the complex  $[\text{CuBr}_2(\text{L}^{22})]_n$  (**95**) has 14- and 24-membered circuits comprising octahedral Cu(II) ions and exotetradentate  $\text{L}^{22}$  molecules (mode18). The 14-membered circuits were stabilized by supramolecular  $\pi$ - $\pi$  stacking interactions between pyridyl rings of  $\text{L}^{22}$  molecules, while no such interactions were observed in 24-membered circuits (Figure 38a) [72]. L. Liu *et al.* have hydrothermally prepared a 2D coordination polymer  $\{[\text{Cd}(\text{L}^{22})(\text{H}_2\text{O})_2](\text{SUL})(\text{H}_2\text{O})_{0.5}\}_n$  (**96**) with (4,4) rhomboid grid structure akin to complex **95**. Furthermore, the free SUL anions sandwiched between adjacent 2D layers in a head-to-end arrangement interconnects adjacent 2D

layers into a 3D hydrogen bonded network through sulfo and carboxyl groups (Figure 38b) [73]. A 2D complex  $[\text{CdCl}_2(\text{L}^{20})_4]_n$  (**97**) has a zig-zag arrangement of bridged  $\text{L}^{20}$  molecules (mode15) around the octahedral  $\text{Cd}(\text{II})$  ions. The pyridine rings of  $\text{L}^{20}$  molecules were twisted relative to each other as depicted by the dihedral angle of  $61.8^\circ$

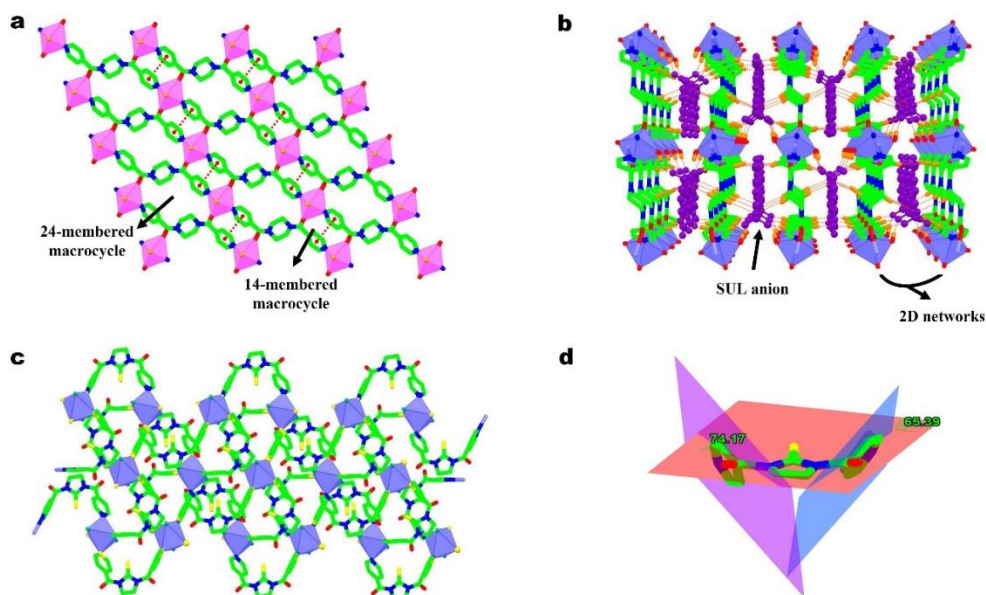


Figure 38 View of a) 2D grid containing 14- and 24-membered macrocycles of the complex **95**, b) 3D hydrogen bonded network comprising sandwiched SUL anions between 2D coordination sheets in the complex **96**, c) 2D coordination network with zig-zag arrangement of bridged ligand molecules in the complex **97** and d) pyridine rings oriented out of plane relative to mercaptoimidazoline moiety in the complex **97**. while the dihedral angles amid 2-mercaptoimidazoline moiety and pyridine rings were  $65.2^\circ$  and  $74.2^\circ$ , respectively (Figure 38d) [65]. The complexes  $\{[\text{Zn}(\text{NCS})_2(\text{L}^{21})_2] \cdot 2\text{H}_2\text{O}\}_n$  (**98**) and  $\{[\text{Mn}(\text{H}_2\text{O})_2(\text{SO}_4)(\text{L}^{21})](\text{H}_2\text{O})_3(\text{CH}_3\text{OH})\}_n$  (**99**) have a 2D layered rhombohedral grid structure [68]. The rhombohedral grids of **98** were composed of 60-membered  $\text{Zn}_4(\text{L}^{21})_4$  rings with the dimension  $14.231 \times 15.586 \text{ \AA}$  along the 2D coordination network in *ac*-plane (Figure 39a). Conversely, the 2D structure of the complex **99** contains two types of chains *viz.*  $-\text{Mn1}-\text{L}^{21}-\text{Mn1}-\text{L}^{21}-$  and  $-\text{Mn2}-\text{L}^{21}-\text{Mn2}-\text{L}^{21}-$  along the *c* direction. These alternating parallel chains were linked by sulphate anions into a 2D corrugated rhombohedral grid structure [68].



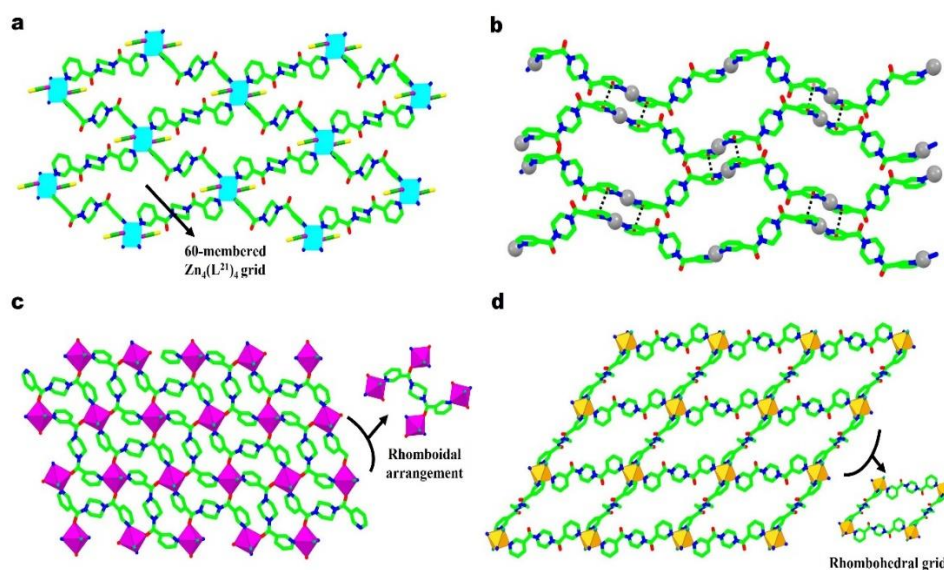


Figure 39 View of a) 2D framework of the complex **98** containing 60-membered  $\text{Zn}_4(\text{L}^{21})_4$  rings, b) 2D coordination network supported by argentophilic and  $\pi \cdots \pi$  interactions in the complex **100**, c) 2D framework of the complex **101** and d) 2D framework of the complex **102**.

The linear 1D coordination chains  $\cdots \text{L}^{21} \cdots \text{Ag} \cdots \text{L}^{21} \cdots \text{Ag}$  of the complex  $\{[\text{Ag}(\text{L}^{21})] \cdot \text{NO}_3 \cdot \text{H}_2\text{O}\}_n$  (**100**) comprising 2-coordinated Ag(I) ions were linked into a 2D double-crossed corrugated structure by strong  $\text{Ag} \cdots \text{Ag}$  interaction of the order of 3.29 Å (Figure 39b). These axial  $\text{Ag} \cdots \text{Ag}$  separations were shorter than the sum of the van der Waals radius for silver (3.44 Å). The argentophilic interactions were further enforced by these strong  $\pi$ - $\pi$  stacking interactions of the order of 3.553 Å between pyridine rings of the adjacent chains [74]. Two dimensional coordination polymers *viz.*  $[\text{Co}(\text{Cl})(\text{L}^{21})_{0.5}]_n$  (**101**) and  $\{[\text{NiCl}_2(\text{L}^{21})_{0.5}(\text{L}^{21})_{0.5}](\text{H}_2\text{O})_2\}_n$  (**102**) differs in the final topology of the framework with the 2D coordination network in complex **101** has rhomboidal distribution of four neighbouring Co(II) ions ( $\text{Co} \cdots \text{Co}$  distance, 8.369 Å) bridged by exotetradentate  $\text{L}^{21}$  molecules (Figure 39c). Whereas the complex **102** has rhombohedral grids  $\text{Ni}_4(\text{L}^{21})_4$  with the Ni(II) ions located at the vertices (Figure 39d). In addition, two slightly different kinds of  $\text{L}^{21}$  molecules differing in the orientation of pyridine rings with respect to piperazine unit were observed. In  $\text{L}^{21}$  (1) molecule, two parallel pyridine rings were reclined at an angle of  $121.3^\circ$  relative to  $\text{NC}_2$  trigonal planes of the piperazine unit, whereas the dihedral angle with the  $\text{C}_4$  plane of the piperazine



unit was  $138.8^\circ$ . In  $L^{21}$  (2) molecule, the corresponding angles were  $54.7$  and  $38.7^\circ$ , respectively [67].

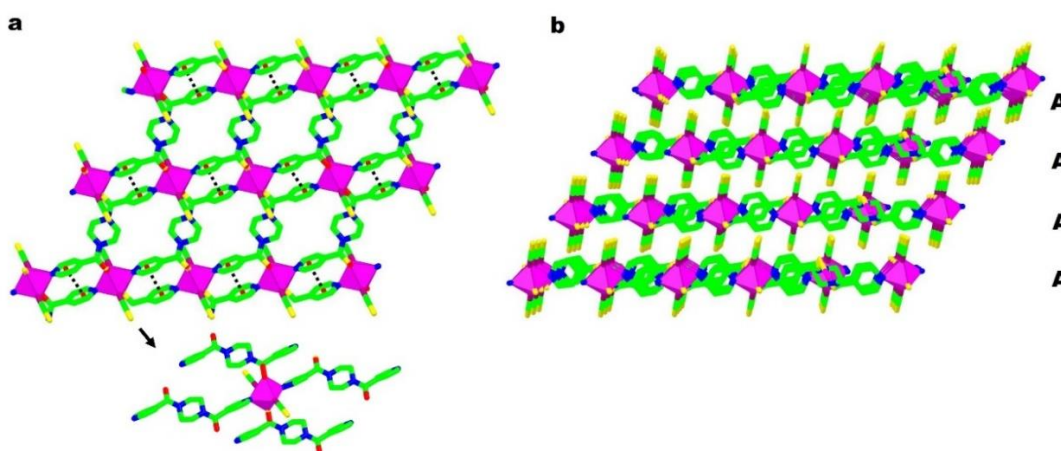


Figure 40 View of a) 2D framework of the complex **103** containing 14- and 24-membered metallo-cyclic rings, and b) stacked 2D sheets showing AAAA type pattern. The octahedral Co(II) ion of the complex  $[Co(NCS)_2(L^{22})]_n$  (**103**) was surrounded by *trans*-isothiocyanate anions, and four symmetry related *trans*-L<sup>22</sup> molecules (Figure 40a). Besides, the exotetradentate L<sup>22</sup> molecules (mode 18) connect four Co(II) ions related to each other by inversion symmetry. Along the 2D sheet, alternating 14- and 24-membered metallo-cyclic rings viz.  $\{CoOC_4N\}_2$  and  $\{CoOCN(C)_2N(C)_4N\}_2$  display through space Co $\cdots$ Co distances of  $7.805 \text{ \AA}$  (in first ring) and  $12.030 \text{ \AA}$  (in second ring), respectively, across the circuits (Figure 40a). Among metallo-cyclic rings, the small ring circuits (14 membered) were also supported by  $\pi\cdots\pi$  stacking interactions ( $3.699(3) \text{ \AA}$ ) between pyridyl rings. The adjacent 2D layers were stacked over one another with the isothiocyanate ions projecting above and below the layer planes to give AAA type pattern (Figure 40b) [75]. The complexes  $[CdCl_2(L^{22})]_n$  (**104**) and  $[Cd(NO_3)_2(L^{22})]_n$  (**105**) differing in the metal and counter ions present were topologically similar to complex **103** [76].

#### 2.2.1.4 3D-polymeric complexes

Coordination mode shown by the ligand molecule is mode19. A three dimensional layered coordination polymer  $[Cd(N_3)_2(L^{21})_2]_n$  (**106**) with tetragonal prism channels was reported by Hou *et al.*. In the crystal lattice, four  $\mu$ -1,3-azide ions in the square planar arrangement, and the two pyridine nitrogen atoms from symmetry related L<sup>21</sup> molecules at the axial positions provide the octahedral environment around each Cd(II)

ion, which sits on the inversion centre (Figure 41a). The adjacent Cd(II) ions were bridged by azide ions to form 2D layers (Figure 41b), which were further linked to each other into a 3D framework by 2C (2-connecting, mode16) *trans*-**L**<sup>21</sup> molecules (Figure 40c). In the 3D framework, **L**<sup>21</sup> molecules were present at the four edges of tetragonal prism channel, which was cut off by 2D layers of Cd(II) ions comprising rhombohedral grids Cd<sub>4</sub>(N<sub>3</sub>)<sub>4</sub> (Figure 41d) [68].

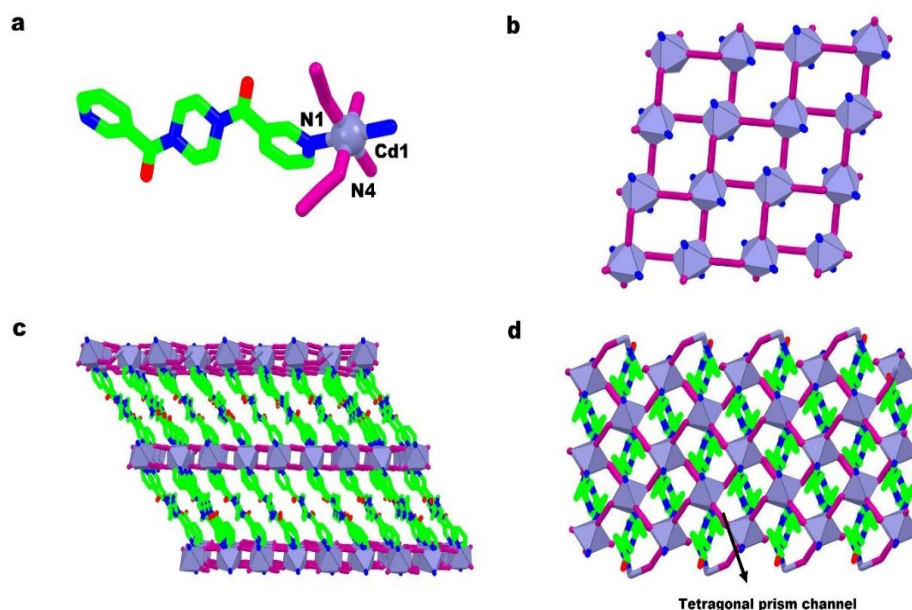


Figure 41 View of a) centrosymmetric unit of the complex **106**, b) 2D network comprising Cd(II) ions bridged by μ-1,3-azide ions, c) 3D framework involving 2D sheets of Cd(II) ions connected by bridged *trans*-**L**<sup>21</sup> molecules, and d) tetragonal prism channels cut off by Cd<sub>4</sub>(N<sub>3</sub>)<sub>4</sub> grids in the complex **106**.

## 2.3 Coordination complexes of Class III Ligands

### 2.3.1 Type 5 and Type 6 ligands

#### 2.3.1.1 Monomeric complexes

Coordination modes shown by the ligand molecule are mode20 and mode 21. A series of isostructural mononuclear complexes [Ln(**L**<sup>23</sup>)(NO<sub>3</sub>)<sub>3</sub>] (Ln = Pr (**107**), Nd (**108**), Gd (**109**), and Tb (**110**)) of **L**<sup>23</sup> were synthesized to compare and comprehend the differences between Am<sup>III</sup>/ Eu<sup>III</sup> extraction by its congeners, differing in the type of substituents on amide nitrogen atom. Crystal structure of the complexes show that the chelating (mode20) **L**<sup>23</sup> molecule, and three nitrate ions displaying bidentate coordination mode grant bi-capped square antiprism geometry to Ln(III) ions (Figure

42a). In all complexes, the M-N bonds of bipyridine unit and M-O bonds of carboxamide groups have different bond lengths owing to the steric hinderance between nitrate ions and carboxamide groups of **L**<sup>23</sup>. Thus, inequivalent bond lengths were independent of the nature of metal ion and lanthanide contraction as well. The variation in the torsion angle N2-C1-C1'-N2' of 5° and 4.6° for Nd and Pr complexes, and 12.8 and 11° for Gd and Tb complexes, respectively, was the probable reason for such discrepancies. Moreover, DFT calculations have shown that *s-s-s* conformer of **L**<sup>23</sup> molecule was most prone to metal ion binding with minimum potential energy surface (PES) value of 3.64 kcal/mol. Formation of 1:1 Metal:Ligand complexes were further supported by UV-Vis spectrophotometric titrations [18].

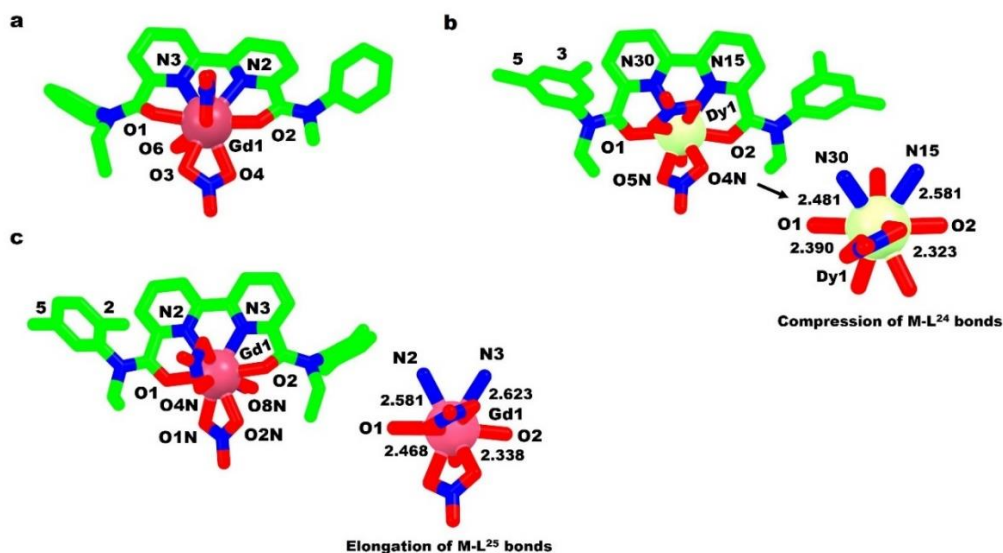


Figure 42 Pictorial presentation of a) bi-capped square antiprism coordination geometry around Gd(III) ion in the complex **109** b) compression of M-L<sup>24</sup> bonds due to the substitution of phenyl rings at 3, 5-position in the complex **111**, c) elongation of M-L<sup>25</sup> bonds due to substitution of methyl groups at 2,5- position of phenyl rings of **L**<sup>25</sup> in the complex **112**. (Note- The mononuclear complex in Figure 42a is the representative unit of isostructural complexes of Pr(III) (**107**), Nd(III) (**108**), and Tb(III) (**110**))

Borisova *et al.* studied the impact of secondary coordination sphere of 2,2'-bipyridyl-6,6'-dicarboxylic dimethylanilides on the structure and stability of its lanthanide complexes and compared the results with unmethylated ligand derivative. In this pursuit, some lanthanide complexes have been synthesized. In the complex

$\text{Dy}(\text{NO}_3)_3(\text{L}^{24})]$  (**111**), substitution of methyl groups at 3,5- position of the phenyl rings led to significant compression of the Ln–O and Ln–N bonds (Figure 42b), which facilitates metal ions to enter deeper into the cavity of the ligand whereas substitution at 2,5- position of phenyl rings (Figure 42c) has caused steric hinderance in complex  $[\text{Gd}(\text{NO}_3)_3(\text{L}^{25})]$  (**112**), which led to the elongation of Ln–O and Ln–N bonds compared to unmethylated complexes of  $\text{L}^{23}$  molecule. In both complexes, the flexibility of the ligand molecules and the disposition of carboxamide oxygen atoms in or out of the mean plane of bipyridyl moiety has led the ligands to adopt lariat crown ether [19].

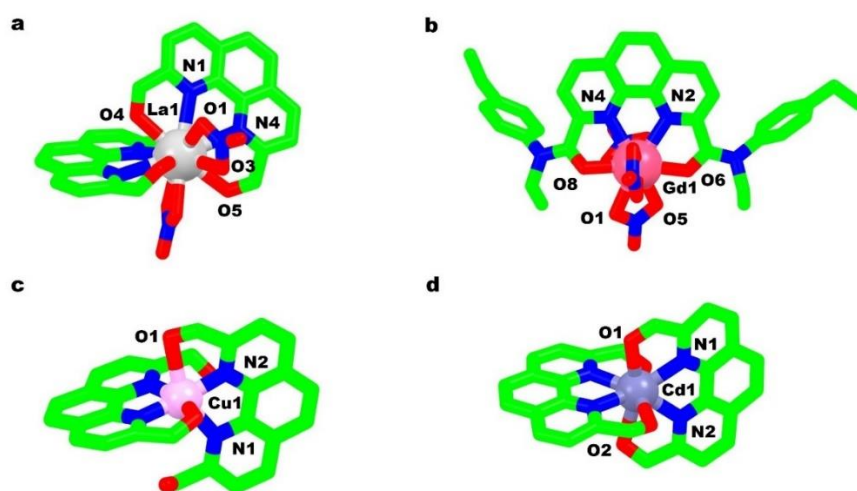


Figure 43 View of a) 12-coordination geometry of La(III) ion in the complex **113**, b) 10-coordination geometry of Gd(III) ion in the complex **115**, c) tetragonal pyramid geometry around Cu(II) ion in the complex **117**, and d) 7-coordinated Cd(II) ion in the complex **118**. (Note- Tertiary nitrogen atoms of amide group and the respective substituents appended to it have been deleted for clarity in the complexes **113**, **116**, and **118**. Both the solvent molecules, and the counter anions crystallized in the lattice have also been deleted.)

In another work, Alyapyshev *et al.* synthesized few lanthanide (La(III), Nd(III) and Gd(III)) and transition metal complexes (Cu(II) and Cd(II)) using  $\text{L}^{26}$  molecule to understand the M–L complex formation [30]. In the centrosymmetric complex  $[\text{La}(\text{L}^{26})_2(\text{NO}_3)_2]\text{NO}_3 \cdot 2\text{DCM}$  (**113**), the 12-coordination geometry around La(III) was granted by two  $\text{L}^{26}$  molecules (mode21), and two nitrate ions, while an uncoordinated nitrate ion was crystallized outside the coordination sphere to balance the charge (Figure 43a). Moreover, carbonyl groups of carboxamide moieties were not coplanar

with respect to phenanthroline plane. In contrast, isostructural Nd(III) (**114**) and Gd(III) (**115**) complexes  $[\text{Ln}(\text{L}^{26})(\text{NO}_3)_3] \cdot 2\text{DCM}$  have 10-coordination geometry around Ln(III) ions, provided by chelating  $\text{L}^{26}$  molecule (mode21), and three nitrate ions (Figure 43b). From diffraction studies it was observed that the small lanthanide ions (Nd(III) ions and Gd(III)) complex with one  $\text{L}^{26}$  molecule while bigger ion (La(III)) prefer to complex with two  $\text{L}^{26}$  molecules. Apart from the lanthanide complexes, some transition metal complexes of  $\text{L}^{26}$  with Cu(II), Cd(II), and Zn(II) have also been studied. Among them,  $[\text{Cu}(\text{L}^{26})_2] \cdot 2\text{NO}_3$  (**116**) and  $[\text{Zn}(\text{L}^{26})_2] \cdot 2\text{NO}_3$  (**117**) complexes were isostructural containing metal ions in tetragonal pyramid environment (6-coordinated) (Figure 43c). Whereas the complex  $[\text{Cd}(\text{L}^{26})_2] \cdot 2\text{NO}_3$  (**118**) has pentagonal-bipyramidal coordination environment (7-coordinated) around Cd(II) ion (Figure 43d). This trend in the change of coordination number further supports the higher extraction ability towards Cd(II) over Cu(II) and Zn(II) ions [30].

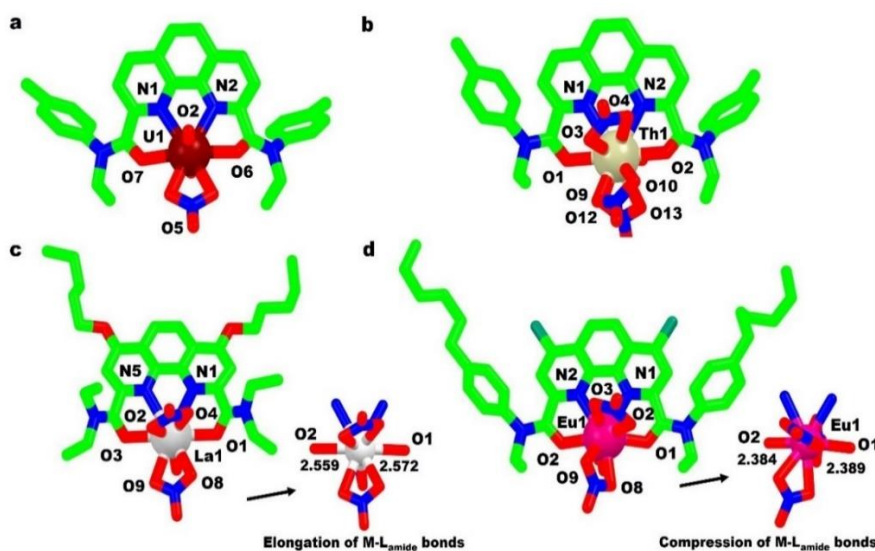


Figure 44 View of a) 8-coordination geometry of U(VI) ion in the complex **119**, b) 12-coordination geometry of Th(IV) ion in the complex **120**, c) coordination environment around La(III) ion and the elongation of M- $\text{L}_{\text{amide}}$  bonds in the complex **121**, and d) coordination environment of Eu(III) ion and the compression of M- $\text{L}_{\text{amide}}$  bonds in the complex **122**. (Note- The solvent molecules and counter anions crystallized in the lattice have been deleted for complexes **119** and **120**.)

Xiao *et al.* studied the solvent extraction and complexation behaviour of phenanthroline based  $\text{L}^{27}$  ligand towards actinides and lanthanides [31]. The complexation mechanism

of  $L^{27}$  towards Th(IV) and U(VI) was studied by single crystal analysis. The complex  $[UO_2(NO_3)(L^{27})] \cdot (CH_3)_2N^+ \cdot (H_2O)_2$  (**119**) has eight coordination geometry around U(VI) granted by two oxide ions, a chelating  $L^{27}$  (mode21), and a nitrate ion (Figure 44a). Whereas Th(IV) ion of the complex  $[Th(NO_3)_4(L^{27})] \cdot H_2O$  (**120**) has 12-coordination geometry, provided by four nitrate anions, and a  $L^{27}$  molecule in mode 21 (Figure 44b). Both complexes have shown 1:1 (M:L) stoichiometry. Furthermore, the extraction studies in acidic medium illustrate high selectivity of  $L^{27}$  molecule towards actinides compared to the lanthanides due to the covalent nature of An-N bonds as illustrated by DFT calculations.

In another study, Borisova *et al.* studied the effect of substituents on the complexation behaviour of phenanthroline ring and amide moieties of the ligands  $L^{28}$  and  $L^{29}$ , respectively, towards the lanthanides. In this quest, monometallic complexes  $[La(L^{28})(NO_3)_3]$  (**121**) and  $[Eu(L^{29})(NO_3)_3]$  (**122**) were synthesized (Figure 44c and 44d). Both the complexes have their metal ions in distorted bicapped square antiprism geometry. The elongation of La-O<sub>amide</sub> ( $\sim 2.560 \text{ \AA}$ , Figure 44c) in the complex **121** compared to Ln-O<sub>amide</sub> bond in the complexes with aryl-alky substituents illustrate the lower affinity of amidic-ethyl substituents towards the Ln(III) ions. Conversely, shorter Eu-O<sub>amide</sub> ( $\sim 2.400 \text{ \AA}$ , Figure 44d) bond distances in complex **122** with aryl-alky substituents on  $L^{29}$  molecule indicates the higher affinity towards Ln(III) ions that enhances the effectiveness and selectivity of Ln(III) extraction [32].



## 2.4 Coordination complexes of Ligands with complex structure (Miscellaneous)

### 2.4.1 Monomeric complexes

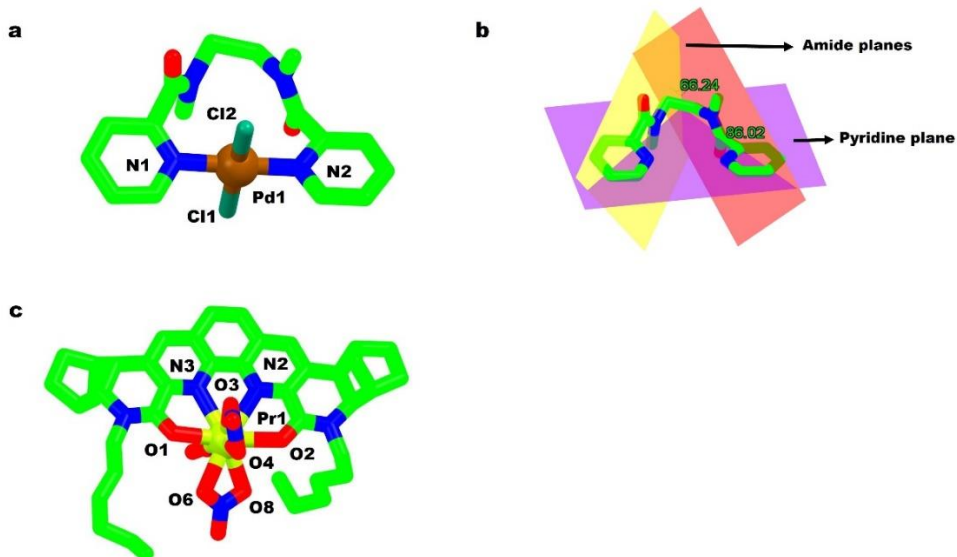


Figure 45 View of a) centrosymmetric unit of the complex **123**, b) dihedral angles between amide planes, and between amide and pyridine planes in the complex **123**, and c) representative mononuclear unit of the complexes **124-128**.

Coordination modes shown by the ligand molecule are mode22 and mode 23. A rare  $N_2$ -*trans*-bidentate coordination mode was observed for  $L^{30}$  molecule in the square planar complex  $[Pd(L^{30})Cl_2]$  (**123**) (Figure 45a). The picolinamide moieties were non-planar relative to each other as illustrated by dihedral angles of 66.2 and 86.1° between amide group planes and pyridine ring planes (Figure 45b). In addition, the ethane link was in staggered conformation with N-C-C-N torsion angle of 58.8° [82]. Popova *et al.* reported some lanthanide complexes of rigid 2,9-bis-lactam-1,10-phenanthroline based ligands, and studied the selectivity of  $L^{32}$  (with saturated  $\delta$ -lactam rings) and  $L^{33}$  (with unsaturated  $\delta$ -lactam rings) molecules towards Am (III)/Eu (III) ions. The mononuclear complexes of  $L^{32}$ , synthesized with the structural formula  $[Ln(L^{32})(NO_3)_3]$  (Figure 45c) ( $Ln = Pr(III)$  (**124**),  $Nd(III)$  (**125**),  $Eu(III)$  (**126**),  $Gd(III)$  (**127**) and  $Tb(III)$  (**128**)) were isomorphous. The 10-coordinated  $Ln(III)$  ion in each complex was surrounded by three nitrate anions and a chelating  $L^{32}$  molecule (mode23) to give a 1:1 (M:L) stoichiometry. In all complexes, shorter M-O<sub>amide</sub> distances than M-N<sub>phenanthroline</sub> illustrated the stronger

binding affinity of the oxygen atoms. Besides, it was observed that  $L^{33}$  with unsaturated  $\delta$ -lactam rings was the most selective extractant of Am(III) over Eu(III) than  $L^{32}$  with saturated  $\delta$ -lactam rings. The selectivity of the ligands for Am(III) was also studied by DFT calculations [33].

#### 2.4.2 Dimeric complexes

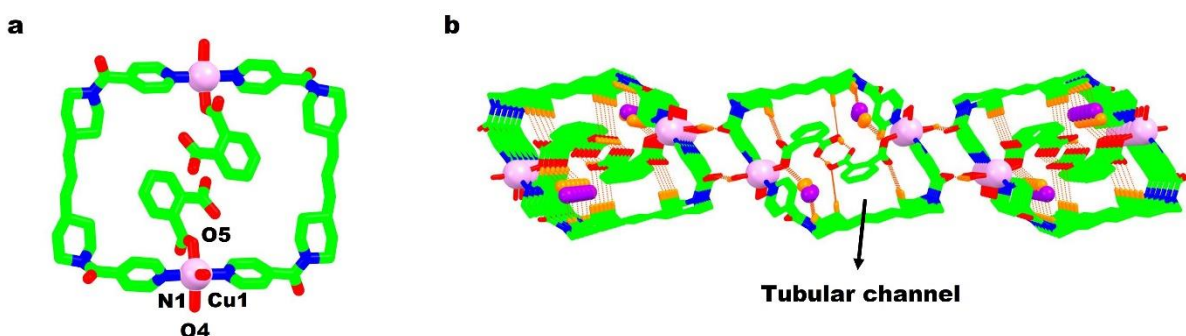


Figure 46 View of a) cationic unit  $[Cu_2(phtH)_2(L^{34})_2(H_2O)_4]^{+2}$  containing  $L^{34}$  molecules oriented in U-conformation, and b) 2D network of tubular channels formed by hydrogen bonding between neighbouring cationic units in the complex **129**.

Coordination mode shown by the ligand molecule is mode24. Murray *et al.* reported a cyclic complex  $\{[Cu_2(phtH)_2(L^{34})_2(H_2O)_4](NO_3)_2 \cdot H_2O$  (**129**) containing square pyramidal Cu(II) ion coordinated to singly protonated phtH molecule, two *trans*- $L^{34}$  (mode24) and two *cis*-aqua molecules (Figure 46a). In the cationic unit  $[Cu_2(phtH)_2(L^{34})_2(H_2O)_4]^{+2}$ , the  $L^{34}$  molecules were oriented in U-conformation with  $\Psi$  angle of  $9.9^\circ$ . In the ring motif  $[Cu_2(L^{34})_2]$ , phtH anions were projected towards the ring and the  $Cu \cdots Cu$  non-bonding distance observed was 12.34 Å. The neighbouring cationic units were associated to each other by the hydrogen bonding between the carboxylate anions of adjacent units to form a supramolecular tube motif along the *a*-axis. The adjacent tubular channels were aggregated via the hydrogen bonding between aqua ligands and carbonyl groups of  $L^{34}$  molecules to form a 2D framework (Figure 46b) [83].

#### 2.4.3 1D polymer

Coordination mode shown by the ligand molecule is mode25. The 1D chain of  $[Cu_2(OAc)_4(L^{31})_2]_n$  (**130**) has alternating diazatetraoxa macrocyclic backbone and  $Cu_2(OAc)_4$  units (Figure 47a and b) [84]. The pyridine rings of  $L^{31}$  were slightly tilted

relative to amide junctions with NCCC torsion angle of  $-82^\circ$  and  $82^\circ$ . Each paddlewheel  $\text{Cu}_2(\text{OAc})_4$  unit has square pyramidal  $\text{Cu}(\text{II})$  ions coordinated to four bridged  $\text{OAc}^-$  anions, and neutral  $\text{L}^{31}$  molecule (mode25). In addition, the bridging of acetate ions in the paddlewheel also resulted in shorter  $\text{Cu}\cdots\text{Cu}$  distance of the order 2.611 Å.

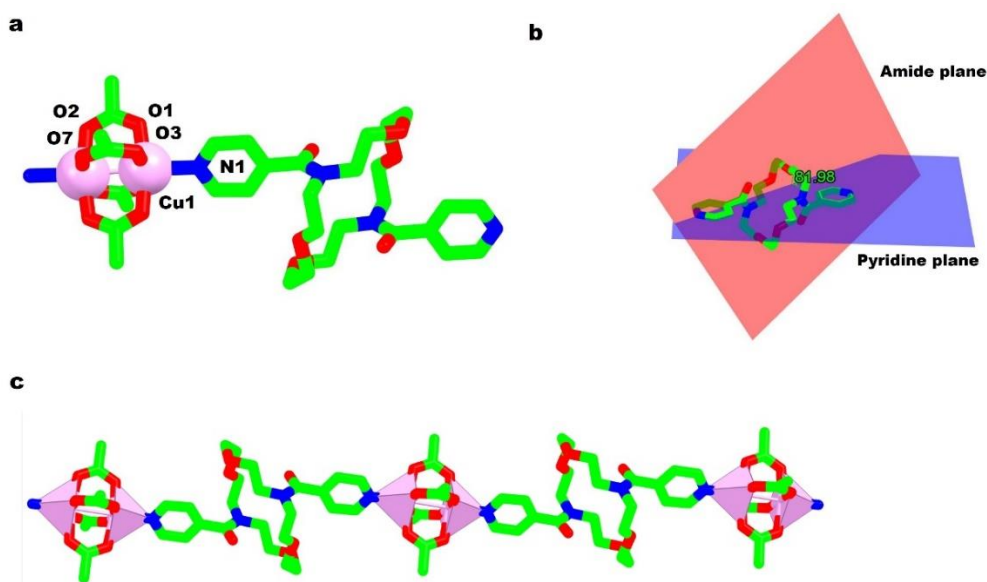


Figure 47 View of a) repeating centrosymmetric unit of complex the **130**, b) orientation of pyridine ring w.r.t amide plane, and c) 1D coordination polymer containing bridged  $\text{L}^{31}$  molecules between  $\text{Cu}(\text{II})$  paddlewheel units.

### 3. Applications

#### 3.1 Solvato- and Thermochromism

Mononuclear complex  $[\text{Cu}(\text{L}^1)_2(\text{Cl})_2]$  (**5**), and a dimeric complex  $[\{\text{CuCl}(\text{L}^1)\}_2(\mu\text{-Cl})_2]$  (**71**) were obtained from the same reaction mixture exhibited solvatochromism in various solvents [17]. The UV-Vis spectra of blue coloured solution of the dimeric complex **71** in methanol was same as that of monomeric complex **5**, which illustrates a six coordinated tetragonal structure involving the breaking  $\text{Cu-Cl}$  bridges followed by the coordination of solvent molecules. Whereas the yellow-green solution in acetonitrile involving LMCT ( $\text{Cl}_{\text{Bridged}} \rightarrow \text{Cu}$ ) and d-d bands have dimeric structure of the complexes **5** and **71**. Similarly, the green coloured solution of these complexes in chloroform and dichloromethane involving charge transfer transition was due to the presence of dimeric structure. The colourless solution of these complexes in the polar solvents viz. DMF and DMSO has a monomeric six coordinated structure due to strong

coordination of the solvent molecules at the axial position, causing the red shift of d-d bands due to the destabilisation of d-electrons. In addition, the complex **5** has also shown irreversible thermo-chromism upon heating, which involves colour change from blue to green on heating at 160° C with the transformation from octahedral to dimeric square pyramidal complex with bridged chloride ions [17].

### 3.2 Magnetism and Magnetic properties

#### 3.2.1 Room Temperature Magnetism

Paramagnetic behaviour of the complexes  $[\text{Cu}(\text{L}^7)\text{Cl}_2]$  (**44**) and  $[\text{Cu}(\text{L}^7)\text{Cl}(\text{ClO}_4)]$  (**45**) was assessed by magnetic moment studies that illustrate the magnetic moment of 1.95 B.M and 1.88 B.M, respectively, after diamagnetic correction. The observed paramagnetic behaviour involves no spin-spin interactions [20]. In the complexes  $[\text{Co}(\text{L}^7)_2(\text{H}_2\text{O})_2](\text{ClO}_4)_2 \cdot \text{H}_2\text{O}$  (**46**),  $[\text{Co}(\text{L}^7)_2(\text{H}_2\text{O})_2](\text{PF}_6)_2 \cdot \text{H}_2\text{O}$  (**47**), and  $[\text{Co}(\text{L}^7)_2(\text{CH}_3\text{CN})](\text{PF}_6)_2$  (**48**) a high spin octahedral structure was established through room temperature magnetic moment studies that give the values in the range 4.75-5.01  $\mu_B$ , consistent with the presence of three unpaired electrons [21]. Magnetic measurements performed at 300 K on the complexes  $[\text{Ni}(\text{NCS})_2(\text{L}^7)(\text{CH}_3\text{CN})] \cdot \text{CH}_3\text{CN}$  (**58**) and  $[\text{Ni}(\text{NCS})_2(\text{L}^7)(\text{C}_2\text{H}_5\text{OH})]$  (**59**) display magnetic moment values of 2.82 and 2.88  $\mu_B$ , respectively [24].

#### 3.2.2 Variable Temperature Magnetism

Variable temperature magnetic susceptibility measurement was done on a dimeric complex  $[\{\text{CuCl}(\text{L}^1)\}_2(\mu\text{-Cl})_2]$  (**70**) to investigate the type of coupling between the Cu(II) ions, and to determine magneto-structural correlation. The high  $\chi_M T$  values of 0.92  $\text{cm}^3 \text{mol}^{-1} \text{K}$  and 1.12  $\text{cm}^3 \text{mol}^{-1} \text{K}$ , at 300 K and 15 K (in the plot  $\chi_M T$  vs,  $T$ ), respectively, along with magnetic exchange coupling parameter ' $J$ ' with the value of 43.1  $\text{cm}^{-1}$  illustrates the presence of ferromagnetically coupled Cu(II) ions. In addition, the molecular structure of **70** display a distortion from a SP geometry with coplanar bases to TBP (Cu-Cl-Cu angle ' $\alpha$ ' = 93.6° and bifold angle ' $\sigma$ ' = 34.9°) [17]. The solid state, variable temperature magnetic susceptibility data was collected for the complex  $[\text{Cu}_2(\text{Cl})_4(\text{L}^9)_2] \cdot 2\text{CH}_3\text{CN}$  (**69**) using 1.0 T field. In the temperature range of 5-300 K, the observed  $\chi_M T$  value of 0.88  $\text{cm}^3 \text{mol}^{-1} \text{K}$  at 300 K was higher than that expected for two uncoupled spins  $S = 1/2$ , which upon cooling decreases slowly upto 50 K followed by a steep drop off in the value up to

0.56 cm<sup>3</sup> mol<sup>-1</sup> K at 5K. The single electron on each Cu(II) ion involved in the coupling belongs to the d-orbital ( $x^2-y^2$ ), and the interaction between these magnetic orbitals occurred through bridged Cl<sup>-</sup> ions. The anti-ferromagnetic exchange interactions were observed owing to the large Cu-Cl-Cu angle (95.3°) and a rather small bifold angle ( $\sigma = 13.84^\circ$ ), which increases the energy difference between magnetic orbitals [79]. Magnetic properties of the complex [Co(L<sup>5</sup>)(Cl)<sub>2</sub>]<sub>n</sub> (**34**) was analysed in the temperature range 2 K to 300 K by considering each Co(*T<sub>d</sub>*) ion in the chain as an isolated system, and taking into account a considerable zero-field splitting contribution due to tetrahedral distortions. The magnetic interactions through the bridging ligands were ruled out [37]. In the plot of  $\chi_M T$  vs. *T*, gradual decrease in  $\chi_M T$  values was observed from 2.62 cm<sup>3</sup> mol<sup>-1</sup> K at 300 K to 2.27 cm<sup>3</sup> K mol<sup>-1</sup> at 50 K. Below this a steep drop to 1.15 cm<sup>3</sup> K mol<sup>-1</sup> was observed. The  $M/N\mu_B$  vs. *H/T* plot showed the zero-field splitting (ZFS) of the ground state as there was no overlap of isofield lines [38]. Important parameters obtained by the fitting of experimental data is tabulated in Table 2.

A high spin Co(*T<sub>d</sub>*)–Co(*O<sub>h</sub>*)–Co(*T<sub>d</sub>*) trinuclear system was considered to explain the magnetism of [Co(L<sup>5</sup>)<sub>2</sub>(H<sub>2</sub>O)<sub>4</sub>][Co(L<sup>5</sup>)(Br)<sub>3</sub>]<sub>2</sub>·2H<sub>2</sub>O (**13**). The magnetic behaviour was illustrated as a plot of  $\chi_M T$  vs. *T* in which a plateau was observed on cooling the sample from 9.32 cm<sup>3</sup> K mol<sup>-1</sup> at 300 K up to 75 K followed by a sharp drop to 4.74 cm<sup>3</sup> K mol<sup>-1</sup> at 1.99 K, which was attributed to zero-field splitting (ZFS) of ground states due to intermolecular interactions. Owing to the complexity of the system, the interpretation of data was done in two parts using: MAGPACK-fit programme (below 80 K) and VPMAG programme (above 80K) [38]. The results (Table 2) illustrate weak antiferromagnetic interactions between Co(*O<sub>h</sub>*) and Co(*T<sub>d</sub>*) centres. Akin to complex **13**, a trinuclear system Co(*T<sub>d</sub>*)–Co(*O<sub>h</sub>*)–Co(*T<sub>d</sub>*) was found in the complex [Co<sub>3</sub>(L<sup>4</sup>)<sub>4</sub>(Cl)<sub>6</sub>]<sub>n</sub> (**38**) with Co(II) bridged by chloride ions [58]. The magnetic behaviour of the complex in the temperature range 2 to 300 K displays  $\chi_M T$  value of 8.95 cm<sup>3</sup> K mol<sup>-1</sup> at RT, followed by abrupt drop to a value of 5.39 cm<sup>3</sup> K mol<sup>-1</sup> at 1.99 K on cooling the sample. The data illustrates that Co(*T<sub>d</sub>*) and Co(*O<sub>h</sub>*) centres were interacting ferromagnetically with the central position of the trinuclear unit occupied by high spin Co(II) ion (*S* = 3/2) at high temperature. Herein too, magnetic data was analysed using the programs MAGPACK-fit and

VPMAG FORTRAN to obtain the best fit. The most significant effects examined at each interval of the temperature shows spin–orbit coupling of  $\text{Co}(\text{O}_h)$  dominating at high temperatures, while the zero-field splitting parameters of the  $\text{Co}(T_d)$  becomes significant at the low temperature. The spin–spin magnetic interaction was however detected for the whole range of temperature [58].

A drop in  $\chi_{\text{MT}}$  values from  $3.54 \text{ cm}^3 \text{ mol}^{-1} \text{ K}$  at RT to  $2.36 \text{ cm}^3 \text{ mol}^{-1} \text{ K}$  at 1.8 K on cooling the complex  $[\text{Fe}(\text{NCS})_2(\text{L}^3)_2]_n$  (**27**) was observed. This trend was attributed to the presence of zero-field splitting effect and weak anti-ferromagnetic coupling at low temperature range between Fe(II) centres (Table 2). These results demonstrated the presence of high-spin octahedral Fe(II) with  $^5\text{T}_{2g}$  as ground state [51]. Magnetic susceptibility measurements on *trans*- $[\text{Mn}(\text{L}^3)_2(\text{N}_3)_2]_n$  (**40**) in the range 300 K - 2 K have illustrated anti-ferromagnetic interactions between the metal centres. Two super exchange pathways (exchange coupling constants ' $J$ ') based on azido bridges were proposed that showed an exchange through the bridge N(11)-N(12)-N(11C) involving overlap of  $d_{xz}$  and  $d_{yz}$  orbitals of Mn(II) with the nonbonding  $\pi$ -orbitals of the azido ligand, whereas the other bridge N(21)-N(22)-(N21A) with the lower bond angle enhances the overlap of  $d_{z^2}$  and  $\pi$ -molecular orbitals of the ligand [59]. Likewise, lower Mn-N-N bond angle ( $148.4^\circ$ ) promotes overlap of  $d_{z^2}$  of the Mn(II) ion and  $\pi$ -molecular orbitals of azido group. Whereas higher Mn-N-N bond angle ( $171.7^\circ$ ) enhances overlap of  $d_{xz}$  and  $d_{yz}$  of Mn(II) and  $\pi$ -molecular orbitals of azido group.

### 3.3 Non-linear optical properties

The third order NLO studies on the complex  $[\text{Hg}(\text{I})_2(\text{L}^{19})]_2 \cdot 3\text{H}_2\text{O}$  (**83**) in the DMF solution using 532 nm laser pulse showed the strong NLO self-focussing effect with third order susceptibility ' $\chi^{(3)}$ ' and hyperpolarizability ( $\gamma$ ) of the order  $2.23 \times 10^{-11} \text{ esu}$  and  $3.24 \times 10^{-29} \text{ esu}$ , respectively [63]. Nonlinear optical properties of  $[\text{Co}(\text{NCS})_2(\text{CH}_3\text{OH})_2(\text{L}^{21})]_n$  (**88**) were studied in DMF using Z-scan technique. The NLO refractive index ' $n_2$ ' value of  $3.05 \times 10^{-16} \text{ esu}$  and the non-linear absorption coefficient value ' $\alpha_2$ ' =  $1.41 \times 10^{-10} \text{ mW}^{-1}$  illustrate third order non-linear optical property of the polymer [66]. Non-linear absorption coefficient ' $\alpha_2$ ' =  $9.00 \times 10^{-11} \text{ mW}^{-1}$  obtained from normalized transmittance vs Z mm plot, and the NLO refractive index ' $n_2$ ' of the order  $3.24 \times 10^{-16} \text{ esu}$  illustrates the self-focusing performance of the polymer



$\{[\text{Co}(\text{H}_2\text{O})_2(\text{CH}_3\text{OH})_2(\text{L}^{22})](\text{NO}_3)_2\}_n$  (**89**) with a third order nonlinear optical behaviour [66]. Similarly, complexes  $[\text{ZnCl}_2(\text{L}^{21})]_n$  (**90**),  $[\text{CoCl}(\text{L}^{21})_{0.5}]_n$  (**101**) and  $\{[\text{NiCl}_2(\text{L}^{121})_{0.5}(\text{L}^{121})_{0.5}](\text{H}_2\text{O})_2\}_n$  (**102**) exhibited third order NLO effects with the  $n_2$  (third order refractive index) value calculated as  $1.73 \times 10^{-11}$ ,  $1.65 \times 10^{-11}$  and  $1.47 \times 10^{-11}$  esu, respectively [67]. Among these the complex **101** exhibited strong non-linear absorptive properties with the non-linear absorption coefficient ' $\alpha$ ' value of  $3.31 \times 10^{-11}$  m W<sup>-1</sup>. The presence of extensive  $\pi$ -delocalisation and increased conjugation in the chains of **101** compared to **102** was responsible for large strong NLO effects. The complexes  $\{[\text{Zn}(\text{NCS})_2(\text{L}^{21})_2] \cdot 2\text{H}_2\text{O}\}_n$  (**98**),  $\{[\text{Mn}(\text{H}_2\text{O})_2(\text{SO}_4)(\text{L}^{21})](\text{H}_2\text{O})_3(\text{CH}_3\text{OH})\}_n$  (**99**), and  $[\text{Cd}(\text{N}_3)_2(\text{L}^{21})_2]_n$  (**106**) exhibit third order NLO properties as depicted by  $\alpha_2$  (non-linear absorption coefficient) values of the order of  $6.9 \times 10^{-9}$  mW<sup>-1</sup>,  $9.2 \times 10^{-9}$  mW<sup>-1</sup>, and  $7.1 \times 10^{-9}$  mW<sup>-1</sup> for **98**, **100**, and **106**, respectively. The hyper-polarizability ( $\gamma$ ) values for these polymers showed them to be good NLO materials (Table 2) [68]. Third order NLO effect ( $\alpha_2 = 2.24 \times 10^{-10}$ ) for the complex  $\{[\text{Ag}(\text{L}^{21})] \cdot \text{NO}_3(\text{H}_2\text{O})\}_n$  (**100**) was observed due to the incorporation of photoactive Ag(I) ions, which enhances nonlinear absorptions by introducing more sublevels in the energy hierarchy to allow spin-orbit couplings and ISC (intersystem conversion) in the excited states. The contributions of the Ag(I) ion and the  $\text{L}^{21}$  molecule towards the optical non-linearity of the complex was confirmed from the theoretical calculations, which illustrates that the LUMO orbital was primarily silver based (68.46% contribution) whereas the LUMO-1 (30.77% contribution) and the HOMO orbitals were ligand based [74].

### 3.4 Biological applications

To test the biological activity of the complex  $[\text{Cu}(\text{Clop})_2(\text{L}^3)_2]_2$  (**20**) various strains of bacteria (*S. aureus* and *E. Coli.*) and fungi (*A. alternate*, *B. cinerea* and *M. gypseum*) have been cultured. The antimicrobial activity was measured by IC<sub>50</sub> and MIC values. The complex **20** has shown antibacterial inhibition activity towards G<sup>+</sup> *S. aureus* with the IC<sub>50</sub> and MIC (Minimum inhibitory concentration) values of 3.05 mmol L<sup>-1</sup> and  $\sim >5$  mmol L<sup>-1</sup>, respectively. Whereas it remains inactive towards G<sup>-</sup> *E. Coli* bacteria. Among various strains of fungi, the complex has shown excellent activity towards *M. gypseum* with IC<sub>50</sub> and MIC values of 2.5 mmol L<sup>-1</sup> and 5<sup>a</sup> mmol L<sup>-1</sup>, respectively ('a' stands for the concentration inducing microbicidal effect (MMC) [45].

In other study, complexes  $[\text{Co}(\text{L}^1)_2\text{Cl}_2]$  (**1**),  $[\text{Ag}(\text{L}^1)_2\text{NO}_3]$  (**2**),  $[\text{Zn}(\text{L}^1)_2(\text{ClO}_4)_2]$  (**3**),  $[\text{Cu}(\text{L}^2)_2(\text{ClO}_4)_2]$  (**4**),  $[\text{Cu}(\text{L}^4)_2(\text{NO}_3)_2(\text{H}_2\text{O})_{1.5}]$  (**12**),  $[\text{Zn}(\text{L}^5)_2(\text{NO}_3)_2]_2$  (**25**), and  $[\text{Co}(\text{L}^5)_2(\text{H}_2\text{O})_2]_n \cdot 2\text{NO}_3$  (**35**) were explored for their antibacterial and antifungal activities [16]. They were tested against  $G^+$  *S. aureus*,  $G^-$  *E. coli*, *K. pneumoniae* and *P. aeruginosa* bacterial stains. Although most of them have shown inhibitory response towards different bacterial strains but the MIC values were high as shown in Table 2. The best response was observed for the complexes **2** and **4** towards *K. pneumoniae* bacteria with MIC values 0.01 and 0.025 mg/ml, respectively. In addition, complexes **1**, **3**, **12**, **25**, and **35** have shown excellent inhibitory response towards the fungus *C. albicans* with MIC values in the range 0.007-0.008 mg/ml.

### 3.5 Sensing Studies

#### 3.5.1 Metal complex as sensor

A 2D coordination polymer  $\{[\text{Cd}(\text{L}^{22})(\text{H}_2\text{O})_2](\text{SUL})(\text{H}_2\text{O})_{0.5}\}_n$  (**97**) was explored as a metal sensing probe in the aqueous solution containing various cations. The cations  $\text{Co}^{+2}$ ,  $\text{Cd}^{+2}$ ,  $\text{Ba}^{+2}$ ,  $\text{Ag}^{+2}$ ,  $\text{Ca}^{+2}$ ,  $\text{Zn}^{+2}$ ,  $\text{Sr}^{+2}$ ,  $\text{Pb}^{+2}$ ,  $\text{Mn}^{+2}$ ,  $\text{Ni}^{+2}$ ,  $\text{Hg}^{+2}$ ,  $\text{Fe}^{+2}$  and  $\text{Cu}^{+2}$  ions tested were at  $10^{-4}$  M concentration using fluorescence titrations. Among these cations the complex **97** was selective for  $\text{Cu}^{+2}$  ions [73].

#### 3.5.2 Ligand as sensor

Ligand  $\text{L}^{26}$  was used as an ionophore material in the potentiometric sensor fabricated by incorporating  $\text{L}^{26}$  molecule into the polymeric membrane using two solvent plasticizers viz. o-nitrophenyloctyl ether (NPOE) and 2-fluorophenyl 2-nitrophenyl ether (2F2N), along with an ion-exchanger tetrakis[3,5-bis(trifluoromethyl)-phenyl borate (KTFPB). The potentiometric measurements with respect to standard Ag/AgCl electrode shows good Nernstian response for Zn(II), Cu(II), Cd(II), and Pb(II) illustrating good sensitivity towards these ions (Table 2), while no response was observed for Co(II) and Ni(II). The  $\text{L}^{26}$  molecule have shown high sensitivity over selectivity towards these metal ions [30].

### 3.6 Extraction applications

#### 3.6.1 Extraction of lanthanides by ligand molecules

The selectivity of  $\text{L}^{24}$  and  $\text{L}^{25}$  towards lanthanide series was studied using  $1 \times 10^{-4}$  M solution of lanthanides in nitric acid (except 3 M solution for promethium), and 0.05 M solution of ligands in nitrobenzene. For  $\text{L}^{25}$  molecule with *ortho* substituted

methyl group, there was a decrease in extraction of heavier Ln(III) ions and increase in extraction of lighter ions. Conversely, a nonlinear increase in the metal extraction (maximum for Nd ions) was observed using  $L^{24}$  molecule with *meta* substituted methyl groups on the phenyl ring. The rationale for the selectivity of *ortho* derivative ( $L^{25}$ ) towards small ions was attributed to the repulsion between the nitrate ions and *ortho*-methyl groups or the steric hindrance for larger Ln(III) ions. However, higher selectivity of  $L^{25}$  molecules towards Nd(III) and Sm(III) ions was due to the lariat crown ether like conformation of ligand in the complexes. Akin to selectivity factor, the stability constants were also affected by the electronic effects of methyl groups. Good correlations between distribution ratios and stability constants were observed in “dry” acetonitrile for light lanthanide region (La-Gd) with the values 0.85 for  $L^{24}$  and 0.96 for  $L^{25}$ , showing that the extraction is dependent upon stability of the complexes (Table 2). Moderate correlation was observed for heavy lanthanide region (Tb-Lu) with the values 0.54 for  $L^{25}$  (in wet acetonitrile) and 0.96 for  $L^{25}$  in “dry” acetonitrile, illustrating that the extraction experiments for the former are governed by hydration effects [19].

Extraction ability of  $L^{26}$  towards lanthanides displayed a drop from La(III) to Lu(III) ions. On the contrary, its tetraalkyl-diamide derivative displays no selectivity towards lanthanides [30].

### 3.6.1.1 Extraction of Am(III) and Eu(III)

Ligand  $L^{26}$  was studied for the extraction of Am(III) and Eu(III) in the nitric acid solution. It was observed that, the extraction ability of the ligand was increasing with the increase in nitric acid concentration from 0.5 to 3M. In addition, metal extraction or distribution ratios were increasing with the increase in ligand concentration in the organic phase. Solvation number of Am(III) and Eu(III) obtained from distribution ratios data was 1.8 and 1.6, respectively. The dialkyl-diaryl-diamide  $L^{26}$  has shown almost double extraction ability towards actinides (Ac) than its tetraalkyl-diamide counterpart, owing to the low pre-organization energy required to form a chelating complex with the metal ions (Table2) [30].

### 3.6.1.2 Extraction of Am(III) and other lanthanide ions

The  $L^{26}$  molecule at 0.05 M concentration has shown a decrease in the extraction of lanthanide ions with the decrease in the ionic radii (La to Lu) in low concentration

nitric acid solutions (Table 2). The rationale for this trend was given with the aid of DFT calculations that illustrate decrease in metal-to-ligand binding energies with increase in the atomic number of Ln(III) ions in the complex with the formula  $[(L^{26})Ln(NO_3)]$ . Also the distribution ratios for Am(III) and lighter lanthanides (Table 2) were similar for  $L^{26}$  at the different acid concentrations (1M, 3M, and 5M), thus it was impossible to separate them. The increase in Am/Ln separation factor values for the selective recovery of Am(III) was observed with the increase in nitric acid concentrations (5M and 6M). The solvation number values (Table 2) obtained from the experimental data demonstrate a predominant complex  $Ln(L^{26})_2(NO_3)_3$  in the organic phase [30].

### 3.6.1.3 Extraction of transition metal ions and lead

Ligand  $L^{26}$  and its tetraalkyl-diamide derivative have shown high distribution ratios ( $>100$ , Table 2) for Cu(II) and Cd(II) ions in 3M nitric acid solution, even at concentration as low as 0.01 M. The distribution ratio values were much lower for Zn(II) and Pb(II) ions with the observed order of extraction as  $Cd > Cu > Pb > Zn$  for  $L^{26}$  molecule, while the order  $Cu > Cd > Zn > Pb$  was observed for its tetraalkyl-diamide counterpart [30].

Yong *et al.* have studied the extraction of U(VI) ion using  $L^{27}$  molecule as an extractant in the room temperature ionic liquids (RTILs) viz.  $[C_4mim][PF_6]$  and  $[C_4mim][NTf_2]$  (nonaqueous phase), under acidic conditions. Besides, the extraction experiments were also conducted in organic solvents such as chloroform for comparison purpose. It was observed that, with the increase in nitric concentration the extraction efficiency (Table 2) was increased slightly from 93% to 96% for  $L^{27}/[C_4mim][PF_6]$  system, and 94% to 98% for  $L^{27}/[C_4mim][NTf_2]$  system illustrating negligible role of nitrate anions in extraction process. However, for  $L^{27}$ /chloroform system, the extraction efficiency was too low ( $\sim 10$  to 56 with increase in acid concentration, Table 2). Even in the absence of nitric acid, these ionic liquid-based extraction systems have shown higher extraction values than the organic solvent-based system (phenyltrifluoromethyl sulfone, F-13). The UV-vis measurements have illustrated a cation exchange mechanism involved in the extraction process due to the linear increase in concentration of  $C_4mim^+$  ions in the aqueous phase with the increase in extraction percentage of U(VI) ions. Also, the

FTIR and EXAFS studies demonstrate that the weakly coordinating anions  $\text{NTf}_2^-$  and  $\text{PF}_6^-$  of RTILs promotes the formation of 1:2 complex  $[\text{UO}_2 (\text{L}^{27})_2]^{-2}$  by crystallizing as counter-anions in addition to cation exchange mechanism [31].

Furthermore, the  $\text{L}^{27}$  molecule has exhibited high selectivity towards MA(III) ions (minor actinides) and light actinides *viz.* Th, U, Np and Pu over lanthanides in the acidic medium because of the presence of soft nitrogen and hard oxygen atoms of the amide moieties. In the extraction system with 1M  $\text{HNO}_3$ /cyclohexane, high values of distribution ratios (Table 2) for Th(IV), U(VI) and Am(III) ions *viz.* 205, 25 and 6, respectively, along with the high values of separation factors ( $SF$ ) (Table 2) relative to Eu(III) ions display selective nature of  $\text{L}^{27}$  towards actinides. The stability constant ' $\log \beta$ ' value of  $\sim 4$  for Th(IV) and U(VI) complexes calculated from UV-Vis titrations further supports the higher selectivity of  $\text{L}^{27}$  molecule [31]. The unprecedented affinity of  $\text{L}^{32}$  and  $\text{L}^{33}$  molecules towards Am(III) was revealed in the liquid-liquid distribution experiments performed in nitric acid/1,2-dichloroethane mixture. It was observed that the rigid  $\text{L}^{32}$  and  $\text{L}^{33}$  ligand molecules have shown remarkable extraction of Am(III) and Eu(III) ions with the distribution ratio values (Table 2) six times more than less preorganized ligand with free tetraoctyl side chains. While the  $\text{L}^{32}$  molecule surpassed the limits of reported radioanalytical method, the  $\text{L}^{33}$  ligand with unsaturated lactam rings displayed unprecedented selectivity for Am(III) in preference to Eu(III) ion even at the low acid concentration (0.3 M nitric acid) as depicted from  $SF_{\text{Am/Eu}}$  value of the order of  $\sim 500$ , and high distribution ratios (Table 2). The low  $SF_{\text{Am/Eu}}$  value ( $\sim 200$ ) at the high acid concentration (3M nitric acid) was due to the competitive acid extraction that affects the selectivity of the ligand [33].

#### 4. Conclusions

In this review, we have presented different molecular designs of the ligands comprising pyridine moieties and carboxamide linkages with tertiary amide nitrogen atoms (OCNRR'), which were used to synthesize coordination complexes with variety of applications. We have gathered the literature pertaining to this very class of the ligands and associated complexes to illustrate the progress made till date. To simplify the things, we made classification of the ligands based on the position of pyridine ring with respect to the anchor moiety and subsequently

relevant coordination complexes were systematically grouped under the categories *viz* mononuclear complexes, 1D, 2D, and 3D coordination polymers, metal clusters etc, based on the dimensionality of coordination networks. Careful analysis of the complexes illustrates that the dimensionality of the coordination networks is primarily dictated by the nature of coordination sites where convergent sites have resulted in chelating mononuclear complexes while divergent sites resulted in coordination polymers of higher dimensionality. But in few cases, counter anions among adjacent metal centres and non-covalent interactions have played vital role in extending the dimensionality of coordination network. In addition, lattice anions and solvent of crystallization also participate in extending the dimensionality of coordination frameworks through hydrogen bonding. Variety of applications displayed by the coordination complexes such as sensor, chromic, magnetic, optical materials etc. could be related to chemical/electronic structure of the ligand, coordination requirements of metal ions, and framework structures. For instance, magnetic properties were observed in complexes containing transition metal ions with partially filled d-orbitals; chromism was observed in complexes with coordinatively unsaturated metal ion; fluorescence property was introduced owing to fluorophores in organic ligand; antimicrobial activities due the presence of metal ions etc. In general, the coordination complexes/polymers can be tailored to fabricate efficient materials with wide variety of applications by the meticulous selection of metal-ligand combination. Besides, some ligand molecules with phenanthroline core moiety in which pyridine rings are fused to benzene ring have successfully been explored for the separation/extraction of Am(III)/Ln(III), with high affinity achieved towards Am(III) over lanthanides owing to the presence of bulky groups on amide nitrogen atom. We believe that there could be more possible ways to design ligands with the combination of fully substituted amide group and pyridine ring to fabricate promising materials for various emerging applications.

**Acknowledgements.** We are grateful to the Natural Sciences and Engineering Research Council of Canada (DDG-2022-00002), the Canadian Queen Elizabeth II Diamond Jubilee Scholarships, The Canadian Foundation for Innovation (37843), Mitacs and the Université du Québec à Trois-Rivières.



## 5. References

1. B. Moulton, M. J. Zaworotko, From Molecules to Crystal Engineering: Supramolecular Isomerism and Polymorphism in Network Solids, *Chem. Rev.*, 101 (2001), 1629-1658. <https://doi.org/10.1021/cr9900432>.
2. M. J. Zaworotko, Superstructural diversity in two dimensions: Crystal engineering of laminated solids, *Chem. Commun.*, 1 (2001), 1-9. <https://doi.org/10.1039/B007127G>.
3. J. C. Bailar, Coordination Polymers, in: W. L. Jolly (Eds.), *Preparative Inorganic Reactions*, Vol. 1, Interscience, New York, 1964, pp. 1-25.
4. S. R. Batten, R. Robson, Interpenetrating Nets: Ordered, Periodic Entanglement, *Angew. Chem. Int. Ed.*, 37 (1998), 1460-1494. [https://doi.org/10.1002/\(SICI\)1521-3773\(19980619\)37:11<1460::AID-ANIE1460>3.0.CO;2-Z](https://doi.org/10.1002/(SICI)1521-3773(19980619)37:11<1460::AID-ANIE1460>3.0.CO;2-Z).
5. a) S. L. James, Metal-organic frameworks, *Chem. Soc. Rev.*, 32 (2003), 276-288. <https://doi.org/10.1039/B200393G>.
6. S. Kitagawa, S. Noro, Coordination polymers: Infinite systems, in: J. A. McCleverty, T. J. Meyer (Eds), *Comprehensive Coordination Chemistry II*, Elsevier: Oxford, 2004, pp. 231-261.
7. B. Moulton, M.J. Zaworotko, From Molecules to Crystal Engineering: Supramolecular Isomerism and Polymorphism in Network Solids, *Chem. Rev.*, 101 (2001), 1629-1658. <https://doi.org/10.1021/cr9900432>.
8. C. Janiak, Engineering coordination polymers towards applications, *Dalton Trans.*, 14 (2003), 2781- 2804. <https://doi.org/10.1039/B305705B>.
9. R. Robson, A net-based approach to coordination polymers, *J. Chem. Soc., Dalton Trans.*, 21 (2000), 3735-3744. <https://doi.org/10.1039/B003591M>.
10. A.J. Blake, N. R. Champness, P. Hubberstey, W. S. Li, M. A. Withersby, M. Schröder, Inorganic crystal engineering using self-assembly of tailored building-blocks, *Coord. Chem. Rev.*, 183 (1999), 117-138. [https://doi.org/10.1016/S0010-8545\(98\)00173-8](https://doi.org/10.1016/S0010-8545(98)00173-8).
11. D. Braga, F. Grepioni, G. R. Desiraju. Crystal Engineering and Organometallic Architectures, *Chem. Rev.*, 98 (1998), 1375-1406. <https://doi.org/10.1021/cr960091b>.
12. D. Braga, F. Grepioni. Organometallic crystal engineering: prospects for a systematic design, *Coord. Chem. Rev.*, 183 (1999), 19-41. [https://doi.org/10.1016/S0010-8545\(98\)90172-2](https://doi.org/10.1016/S0010-8545(98)90172-2).

13. M. Kurmoo, Magnetic Metal-organic frameworks, *Chem. Soc. Rev.*, 38 (2009), 1353-1379. <https://doi.org/10.1039/B804757J>.
14. B. F. Hoskins and R. Robson, Design and construction of a new class of scaffolding-like materials comprising infinite polymeric frameworks of 3D-linked molecular rods. A reappraisal of the zinc cyanide and cadmium cyanide structures and the synthesis and structure of the diamond-related frameworks  $[\text{N}(\text{CH}_3)_4][\text{CuI}(\text{ZnII}(\text{CN})_4)]$  and  $\text{CuI}[4,4',4'',4''']\text{-tetracyanotetraphenylmethane}]\text{BF}_4 \cdot \text{x} \text{C}_6\text{H}_5\text{NO}_2$ , *J. Am. Chem. Soc.*, 1990, 112, 1546-1554. <https://doi.org/10.1021/ja00160a038>.
15. P. J. Hagrman, D. Hagrman and J. Zubieta, *Angew. Chem. Int. Ed. Engl.*, 38 (1999), 2638-2684. [https://doi.org/10.1002/\(sici\)1521-3773\(19990917\)38:18<2638::aid-anie2638>3.0.co;2-4](https://doi.org/10.1002/(sici)1521-3773(19990917)38:18<2638::aid-anie2638>3.0.co;2-4).
16. I. Lumb, B. S. Sran, H. Sood, D. S. Arora and G. Hundal, Coordination chemistry of Cu (II), Co (II), Zn (II) and Ag (I) complexes of isomeric pyridine 2-and 4-carboxamides and their biological activity evaluation, *Polyhedron*, 127 (2017), 153-166. <https://doi.org/10.1016/j.poly.2017.01.063>.
17. I. Lumb, M. S. Hundal, M. Corbella, V. Gómez, and G. Hundal, Copper(II) complexes of N,N-diisopropylpicolinamide – Solvatochromic and thermochromic phase change of a monomeric complex to a ferromagnetically coupled dimeric complex, *Eur. J. Inorg. Chem.*, 27 (2013), 4799. <https://doi.org/10.1002/ejic.201300548>
18. N. E. Borisova, A. A. Kostin, E. A. Eroshkina, M. D. Reshetova, K. A. Lyssenko, E. N. Spodine, L. N. Puntus, Lanthanide Complexes with Tetradentate  $N,N',O,O'$ -Dipyridyl-Based Ligands: Structure, Stability, and Photophysical Properties, *Eur. J. Inorg. Chem.*, 13 (2014), 2219-2229. <https://doi.org/10.1002/ejic.201301271>.
19. N. E. Borisova, T. B. Sumyanova, A. V. Kharcheva, P. I. Matveev, A. V. Ivanov, E. A. Razumova, S. V. Patsaeva, The lanthanide complexes of 2,2'-bipyridyl-6,6'-dicarboxylic dimethylanilides: The influence of a secondary coordination sphere on the stability, structure, luminescence and f-element extraction, *Dalton Trans.*, 47 (2018), 16755-16765. <https://doi.org/10.1039/C8DT03734E>.
20. P. Kapoor, A. Kumar, J. Nistandra, P. Venugopalan, Five coordinate complexes of N,N,N',N'-tetraethylpyridine-2,6-dicarboxamide with copper Crystal and molecular structures of dichloro(N,N,N',N'-tetraethylpyridine-2,6-dicarboxamido)copper(II) and chloro(perchlorato)(N,N,N',N'-tetraethylpyridine-2,6-dicarboxamido)copper(II),

- Transition Metal Chemistry*, **25** (2000), 465-469.  
<https://doi.org/10.1023/A:1007022431374>.
21. R. Kapoor, A. Pathak, P. Kapoor, and P. Venugopalan, Studies on cobalt(II) complexes with *N,N,N',N'*-tetraethylpyridine-2,6-dicarboxamide(L1) containing  $\text{PF}_6^-$ ,  $\text{BF}_4^-$ ,  $\text{ClO}_4^-$  and  $\text{NO}_3^-$  anions: X-ray crystal structures of  $[\text{Co}(\text{L}_1)_2(\text{CH}_3\text{CN})](\text{PF}_6)_2$  and  $[\text{Co}(\text{L}_1)_2(\text{H}_2\text{O})_2](\text{X})_2 \cdot \text{H}_2\text{O}$  ( $\text{X}=\text{PF}_6^-, \text{ClO}_4^-$ ), *Polyhedron*, **25** (2006), 31-38.  
<https://doi.org/10.1016/j.poly.2005.06.060>.
22. P. Kapoor, A. P. S. Pannu, M. Sharma, G. Hundal, R. Kapoor, M. S. Hundal, Syntheses and structures of cobalt(II), nickel(II), and copper(II) complexes with *N,N,N',N'*-tetraalkylpyridine-2,6-dicarboxamides (O-daap) containing nitrate as the counter ion, *J. Coord. Chem.*, **64** (2011), 256-271. <https://doi.org/10.1080/00958972.2010.542237>.
23. P. Kapoor, A. P. S. Pannu, M. Sharma, M. S. Hundal, R. Kapoor, Syntheses and X-ray crystal structures of five- and six-coordinate copper(II) complexes of *N,N,N',N'*-tetraalkylpyridine-2,6-dicarboxamides containing  $-\text{OClO}_3$  and  $-\text{OSO}_2\text{CF}_3$  counter ions, *J. Coord. Chem.*, **63** (2010), 3635-3647.  
<https://doi.org/10.1080/00958972.2010.517267>.
24. R. Kapoor, A. Kataria, A. Pathak, P. Venugopalan, G. Hundal, P. Kapoor, X-ray diffraction, spectral and magnetic studies of the nickel(II) thiocyanate complexes with tridentate 2,6-dithiocarboxamidopyridine *SNS* and 2,6-dicarboxamidopyridine *ONO* ligands: Influence of donor atoms on the coordination geometry of nickel, *Polyhedron*, **24** (2005), 1221-1231.  
<https://doi.org/10.1016/j.poly.2005.04.006>.
25. P. B. Duval, S. Kannan, C. L. Barnes, Convenient syntheses of uranyl(VI) *cis*-dihalide complexes as anhydrous starting materials, *Inorg. Chem. Commun.*, **9** (2006), 426-428.  
<https://doi.org/10.1016/j.inoche.2006.01.023>.
26. T. L. Borgne, J.-M. Bénech, S. Floquet, G. Bernardinelli, C. Aliprandini, P. Bettens and C. Piguet, Monometallic lanthanide complexes with tridentate 2,6-dicarboxamidopyridine ligands. Influence of peripheral substitutions on steric congestion and antenna effect, *Dalton Trans.*, **20** (2003), 3856-3868.  
<https://doi.org/10.1039/B307413G>.

27. A. Fujiwara, Y. Nakano, T. Yaita, K. Okuno, Structural studies of lanthanide nitrate–*N,N'*-dimethyl-*N,N'*-diphenylpyridine-2,6-dicarboxamide complexes, *J. Alloys Comds.*, 456 (2008), 429-435. <https://doi.org/10.1016/j.jallcom.2007.02.056>.
28. M. Alyapyshev, V. Babain, L. Tkachenko, V. Gurzhiy, A. Zolotarev, Y. Ustynyuk, I. Gloriov, A. Lumpov, D. Dar'in, A. Paulenova, Complexes of Uranyl Nitrate with 2,6-Pyridinedicarboxamides: Synthesis, Crystal Structure, and DFT Study, *Z. Anorg. Allg. Chem.* 643 (2017), 585-592. <https://doi.org/10.1002/zaac.201700063>.
29. L. Yuan, M. Sun, L. Mei, L. Wang, L. Zheng, Z. Gao, J. Zhang, Y. Zhao, Z. Chai, W. Shi, New Insight of Coordination and Extraction of Uranium(VI) with N-Donating Ligands in Room Temperature Ionic Liquids: *N,N'*-Diethyl-*N,N'*-ditolyldipicolinamide as a Case Study, *Inorganic Chemistry*, 54 (2015), 1992-1999. <https://doi.org/10.1021/ic502890w>.
30. M. Alyapyshev, J. Ashina, D. Dar'in, E. Kenf, D. Kirsanov, L. Tkachenko, A. Legin, G. Starova, V. Babain, 1,10-Phenanthroline-2,9-dicarboxamides as ligands for separation and sensing of hazardous metals, *RSC Advances*, 2016, 6, 68642-68652. <https://doi.org/10.1039/C6RA08946A>.
31. C. Xiao, C. Wang, L. Yuan, B. Li, H. He, S. Wang, Y. Zhao, Z. Chai, W. Shi, Excellent Selectivity for Actinides with a Tetradentate 2,9-Diamide-1,10-Phenanthroline Ligand in Highly Acidic Solution: A Hard–Soft Donor Combined Strategy, *Inorganic Chemistry*, 53 (2014), 1712-1720. <https://doi.org/10.1021/ic402784c>.
32. N. E. Borisova, A. A. Kostin, M. D. Reshetova, K. A. Lyssenko, E. V. Belova, B. F. Myasoedov, The structurally rigid tetradentate *N,N',O,O'*-ligands based on phenanthroline for binding of f-elements: The substituents vs. structures of the complexes, *Inorg.Chim.Acta*, 478 (2018), 148-154. <https://doi.org/10.1016/j.ica.2018.03.042>.
33. S. J. Popova, A. S. Ivanov, V. S. Bryantsev, F. V. S. Junior, R. Custelcean, I. Popovs, M. M. Dekarske, B. A. Moyer, Bis-lactam-1,10-phenanthroline (BLPhen), a New Type of Preorganized Mixed N,O-Donor Ligand That Separates Am(III) over Eu(III) with Exceptionally High Efficiency, *Inorganic Chemistry*, 56 (2017), 5911-5917. <https://doi.org/10.1021/acs.inorgchem.7b00555>.

34. F. Bigoli, A. Braibanti, M. A. Pellinghelli, A. Tiripicchio, The crystal and molecular structure of diaquobis(*N,N*-diethylnicotinamide)diisothiocyanatozinc, *Acta Cryst.*, B29 (1973), 2344-2348. <https://doi.org/10.1107/S0567740873006679>.
35. H. Necefoglu, E. Cimen, B. Tercan, E. Ermis, T. Hökelek, Diaquabis(*N,N*-diethylnicotinamide-*N*<sup>1</sup>)bis(4-methylbenzoato-*O*)cobalt(II), *Acta Cryst.*, E66 (2010), m556-m557. <https://doi.org/10.1107/S1600536810013954>.
36. T. Hökelek, H. Gündüz, H. Necefoglu, trans-Bis(benzoato-*O,O'*)bis(*N,N*-diethylnicotinamide-κ*N*<sup>1</sup>)copper(II), *Acta Cryst.*, C52 (1996), 2470-2473. <https://doi.org/10.1107/S0108270196006312>
37. A. P. S. Pannu, P. Kapoor, G. Hundal, R. Kapoor, M. Martinez-Ripoll, R. J. Butcher, M. S. Hundal, Coordination driven or/and H-bonded Cu(II)–*N,N*-dialkylisonicotinamide frameworks, *Polyhedron*, **30** (2011), 1691-1702. <https://doi.org/10.1016/j.poly.2011.03.047>.
38. A. P. S. Pannu, P. Kapoor, G. Hundal, R. Kapoor, M. Corbella, N. Aliaga-Alcalde, M. S. Hundal, Magneto-structural studies of two new cobalt-*N,N*-diisobutylisonicotinamide compounds: [CoLCl<sub>2</sub>]<sub>n</sub> and [Co(L)<sub>2</sub>(H<sub>2</sub>O)<sub>4</sub>][CoLBr<sub>3</sub>]<sub>2</sub>·2H<sub>2</sub>O, *Dalton Trans.*, 40 (2011), 12560-12569. <https://doi.org/10.1039/C1DT10991J>.
39. B. S. Sran, S. Sharma, G. Hundal, Self-assembly and supramolecular isomerism in copper (II) coordination compounds of pyridine-4-carboxamide based ligand, *Inorg.Chim.Acta*, 486 (2019), 74-82. <https://doi.org/10.1016/j.ica.2018.10.042>.
40. G. Davies, A. El-Toukhy, K. D. Onan, M. Veidis, Transmetallation reactions of tetranuclear copper(II) complexes. I. Crystal and molecular structures of an intermediate and a final product of reaction of di-μ-oxo-tetra[chloro(DENC)copper(II)], (DENC = *N,N*-diethylnicotinamide) with [Zn(N<sub>2</sub>S<sub>2</sub>), (N<sub>2</sub>S<sub>2</sub> = diacetyl-bis-hydrazonato-S-methyl-carboditithioate) in aprotic solvents, *Inorg.Chim.Acta*, 84 (1984), 41-50. [https://doi.org/10.1016/S0020-1693\(00\)87667-7](https://doi.org/10.1016/S0020-1693(00)87667-7).
41. G. Davies, A. El-Toukhy, K. D. Onan, M. Veidis, Synthesis, structure and properties of the isomeric dinuclear complexes [(DENC)<sub>2</sub>CuX<sub>2</sub>]<sub>2</sub> (DENC = *N,N*-diethylnicotinamide; X = Cl or Br) and the kinetics of their reactions with DENC in methylene chloride, *Inorg. Chim. Acta*, 98 (1985), 85-94. [https://doi.org/10.1016/S0020-1693\(00\)84916-6](https://doi.org/10.1016/S0020-1693(00)84916-6).

42. F. Bigoli, A. Braibanti, M. A. Pellinghelli, A. Tiripicchio, The crystal and molecular structure of di- $\mu$ -( $N,N$ -diethylnicotinamide- $O,N$ )-tetrakisothiocyanatodizinc, *Acta Cryst.*, B29 (1973), 2708-2712. <https://doi.org/10.1107/S0567740873007417>.
43. H. Necefoglu, W. Clegg, A. J. Scott, Tetrakis( $\mu$ -benzoato)bis[( $N,N$ -diethylnicotinamide)zinc(II)], *Acta Cryst.*, E58 (2002), m121-m122. <https://doi.org/10.1107/S1600536802002088>.
44. H. Necefoglu, E. Cimen, B. Tercan, H. Dal, T. Hokelek, Tetrakis( $\mu$ -4-methylbenzoato- $\kappa^2 O:O'$ )bis[( $N,N$ -diethylnicotinamide- $\kappa N^1$ )zinc(II)], *Acta Cryst.*, E66 (2010), m485-m486. <https://doi.org/10.1107/S1600536810011517>.
45. J. Moncol, B. Kalinakova, J. Svorec, M. Kleinova, M. Koman, D. Hudecova, M. Melnik, M. Mazur, M. Valko, Spectral properties and bio-activity of copper(II) clofibrates, part III: crystal structure of  $Cu(clofibrate)_2(2\text{-pyridylmethanol})_2$ ,  $Cu(clofibrate)_2(4\text{-pyridylmethanol})_2(H_2O)$  dihydrate, and  $Cu_2(clofibrate)_4(N,N\text{-diethylnicotinamide})_2$ , *Inorg. Chim. Acta*, 357 (2004), 3211-3222. <https://doi.org/10.1016/j.ica.2004.03.043>.
46. T. Hökelek, E. G. Saglam, B. Tercan, O. Aybirdi, H. Necefoglu, Tetrakis[ $\mu$ -4-(diethylamino)benzoato- $\kappa^2 O:O'$ ]bis[( $N,N$ -diethylnicotinamide- $\kappa N^1$ )cobalt(II)], *Acta Cryst.*, E67(2011), m28-m29. <https://doi.org/10.1107/S160053681005004X>.
47. T. Hökelek, F. Yilmaz, B. Tercan, Ö. Aybirdi, H. Necefoglu, Tetrakis[ $\mu$ -4-(methylamino)benzoato- $\kappa^2 O:O'$ ]bis[( $N,N$ -diethylnicotinamide- $N^1$ )zinc(II)] dihydrate, *Acta Cryst.*, E65 (2009), m1328-m1329. <https://doi.org/10.1107/S1600536809040409>.
48. T. Hökelek, H. Dal, B. Tercan, Ö. Aybirdi, H. Necefoglu, Tetrakis[ $\mu$ -4-(dimethylamino)benzoato- $\kappa^2 O:O'$ ]bis[( $N,N$ -diethylnicotinamide- $\kappa N^1$ )zinc(II)], E65 (2009), *Acta Cryst.*, m1582-m1583. <https://doi.org/10.1107/S1600536809047473>.
49. T. Hökelek, H. Necefoglu, M. Balci, Tetrakis( $\mu$ -benzoato- $O:O'$ )bis( $N,N$ -diethylnicotinamide- $N'$ )dicopper(II), *Acta Cryst.* C51 (1995), 2020-2023. <https://doi.org/10.1107/S0108270195000618>.
50. H. Necefoglu, W. Clegg, A. J. Scott, A linear trinuclear  $CaZn_2$  complex with bridging benzoate ligands, *Acta Cryst.*, E58 (2002), m123-m124. <https://doi.org/10.1107/S160053680200209X>.
51. I. Ondrejčovičová, S. Galková, J. Mroziński, Julia Kłak, T. Lis and Z. Olejnik, New polymeric thiocyanatoiron(II) complex with  $N,N'$ -diethylnicotinamide– Synthesis,



- structure, magnetic and spectral properties, *Inorg. Chim. Acta*, 361 (2008), 2483-2490. <https://doi.org/10.1016/j.ica.2008.01.009>.
52. F. A. Mautner, M. A. S. Goher, H. E. Moustafa, M. A. M. Abu-Youssef, L. Öhrström, 1D and 3D coordination polymers with the  $M(\mu_1, \mu_1-X)_2M$  motif ( $M = Na, Zn, Cd$ ): Observation of a linear  $[Na(H_2O)_4]^+$  cation and a five-connected **sqp**-net, *Polyhedron*, 26 (2007), 2703-2712. <https://doi.org/10.1016/j.poly.2007.01.009>.
53. F. Bigoli, A. Braibanti, M. A. Pellinghelli, A. Tiripicchio, The crystal and molecular structure of di- $\mu$ -(*N,N*-diethylnicotinamide-*O,N*)-diisothiocyanatomanganese(II), *Acta Cryst. B* 29 (1973), 39-43. <https://doi.org/10.1107/S0567740873001949>.
54. T. Hokelek, H. Dal, B. Tercan, E. Cimen, H. Necefoglu, catena-Poly[[ $(4\text{-methylbenzoato-}\kappa O)$ manganese(II)]- $\mu$ -aqua-bis( $\mu$ -4-methylbenzoato- $\kappa^2 O:O'$ )] $[(4\text{-methylbenzoato-}\kappa O)$ manganese(II)]-bis( $\mu$ -*N,N*-diethylnicotinamide)- $\kappa^2 N^3:O_2:O:N^3]$ , *Acta Cryst.*, E66 (2010), m734-m735. <https://doi.org/10.1107/S1600536810020076>.
55. J. Moncol, M. Mudra, P. Lonneck, M. Hewitt, M. Valko, H. Morris, J. Svorec, M. Melnik, M. Mazur, M. Koman, Crystal structures and spectroscopic behavior of monomeric, dimeric and polymeric copper(II) chloroacetate adducts with isonicotinamide, *N*-methylnicotinamide and *N,N*-diethylnicotinamide, *Inorg.Chim.Acta*, 360 (2007), 3213-3225. <https://doi.org/10.1016/j.ica.2007.03.027>.
56. A. P. S. Pannu, P. Kapoor, G. Hundal, R. Kapoor, M. Martinez-Ripoll, M. S. Hundal, A self-assembled 3-D network propagated by coordination polymerization and H-bonding: synthesis and X-ray crystal structure of  $[\{Co(L)_2(H_2O)_2\}(ClO_4)_2(CH_3COCH_3)_2(H_2O)_2]_n$ , where  $L = N,N$ -diisopropylisonicotinamide, *J. Coord. Chem.*, 64 (2011), 1566-1577. <https://doi.org/10.1080/00958972.2011.574286>.
57. N. Bozkurt, T. Tunc, N. Caylak Delibas, H. Necefoglu, T. Hokelek, catena-Poly[[aqua-bis(3-chlorobenzoato- $\kappa^2 O_2O'$ )cadmium]- $\mu$ -*N,N*-diethylnicotinamide- $\kappa^2 N^1:O$ ], *Acta Cryst.*, E 69 (2013), m466-m467. <https://doi.org/10.1107/S160053681301965X>.
58. P. Kapoor, A. P. S. Pannu, G. Hundal, R. Kapoor, M. Corbella, N. Aliaga-Alcalde, M. S. Hundal, First report on *N,N'*-diisoalkylisonicotinamide 1D coordination networks containing linear trinuclear  $[Co_3L_4Cl_6]$  units with mixed  $Co^{II}(T_d)$ - $Co^{II}(O_h)$ - $Co^{II}(T_d)$  geometries; structure and magnetic properties, *Dalton Trans.*, 39 (2010), 7951-7959. <https://doi.org/10.1039/C0DT00245C>.

59. M. A. S. Goher, M. A. M. Abu-Youssef, F. A. Mautner, R. Vicente, A. Escuer, Superechange Interactions through Quasi-Linear End-to-End Azido Bridges: Structural and Magnetic Characterisation of a New Two-Dimensional Manganese–Azido System  $[\text{Mn}(\text{DENA})_2(\text{N}_3)_2]_n$  (DENA = diethylnicotinamide), *Eur. J. Inorg. Chem.*, 2000 (2000), 1819-1823. [https://doi.org/10.1002/1099-0682\(200008\)2000:8<1819::AID-EJIC1819>3.0.CO;2-K](https://doi.org/10.1002/1099-0682(200008)2000:8<1819::AID-EJIC1819>3.0.CO;2-K).
60. F. Bigoli, A. Braibanti, M. A. Pellinghelli, A. Tiripicchio, The crystal and molecular structure of mono-(*N,N*-diethylnicotinamide)cadmium dithiocyanate, *Acta Cryst.*, **B28** (1972), 962-966. <https://doi.org/10.1107/S0567740872003474>.
61. A. El-Toukhy, Guang-Zuan Cai, G. Davies, T. R. Gilbert, K. D. Onan, M. Veidis, Transmetalation reactions of tetranuclear copper(II) complexes. 2. Stoichiometry and products of reaction of  $[(\text{DENC})\text{CuCl}]_4\text{O}_2$ ,  $[(\text{DENC})\text{CuCl}]_4(\text{CO}_3)_2$ ,  $[(\text{DENC})\text{CuCl}]_4\text{Cl}_4$ , and  $(\text{DENC})_4\text{Cu}_4\text{Cl}_6\text{O}$  (DENC = *N,N*-diethylnicotinamide) with  $\text{Ni}(\text{NS})_2$ , the kinetics of product isomerization in aprotic solvents, and inhibition of copper-catalyzed phenolic oxidative coupling by dioxygen through transmetalation, *J. Am. Chem. Soc.*, 106 (1984), 4596-4605. <https://doi.org/10.1021/ja00328a050>.
62. M. R. Churchill, G. Davies, M. A. El-Sayed, J. P. Hutchinson, M. W. Rupich, Synthesis, structure and properties of the tetranuclear complexes  $[(\text{DENC})\text{CuX}]_4$  (DENC = *N,N*-diethylnicotinamide; X = Cl, Br, I) and the kinetics of oxidation of the chloride and bromide by dioxygen in aprotic solvents, *Inorg. Chem.*, 21 (1982), 995-1001. <https://doi.org/10.1021/ic00133a025>.
63. L. Li, Y. Song, H. Hou, Z. Liu, Y. Fan, Y. Zhu, Self-assembly and third-order optical properties of  $\text{HgI}_2$  with linear and angular bipyridine ligands, *Inorg. Chim. Acta*, 358 (2005), 3259-3266. <https://doi.org/10.1016/j.ica.2005.03.051>.
64. B. S. Stone, R. L. LaDuca, Stacked ring-like coordination complex molecules threaded by infinite water tapes, *Inorg. Chem. Commun.*, 43 (2014), 56-59. <https://doi.org/10.1016/j.inoche.2014.02.011>.
65. L. Li, J. Zhao, C. Wang, S. Yang, H. Hou, Four 1D and 2D Cadmium(II) complexes cased on different anions and two modified bipyridyl ligands: Syntheses, Structures, Thermogravimetric, and Fluorescent Properties, *Z. Anorg. Allg. Chem.*, 638 (2012), 187-194. <https://doi.org/10.1002/zaac.201100324>.

66. H. Xu, Y. Song, H. Hou, Crystal structures and third-order NLO properties in DMF solution of Co(II)-bpfp coordination polymers (bpfp= $N,N'$ -bis(pyridylformyl)piperazine), *Inorg. Chim. Acta*, 357 (2004), 3541-3548. <https://doi.org/10.1016/j.ica.2004.05.007>.
67. H. Xu, Y. Song, L. Mi, H. Hou, M. Tang, Y. Sang, Y. Fan and Y. Pan, Coordination frameworks constructed from bipyridyl piperazine and  $MCl_2$  ( $M = Co, Ni, Zn$ ): structural characterization and optical properties, *Dalton Trans.*, 62 (2006), 838-845. <https://doi.org/10.1039/B508177G>.
68. H. Hou, Y. Song, H. Xu, Y. Wei, Y. Fan, Y. Zhu, L. Li, C. Du, Polymeric Complexes with “Piperazine–Pyridine” Building Blocks: Synthesis, Network Structures, and Third-Order Nonlinear Optical Properties, *Macromolecules*, 36 (2003), 999-1008. <https://doi.org/10.1021/ma025787n>.
69. C. M. Rogers, C. Y. Wang, G. A. Farnum, R. L. LaDuca, Divalent metal homophthalate coordination polymers with long-spanning dipyrityl ligands containing piperazine moieties, *Inorg. Chim. Acta*, 403 (2013), 78-84. <https://doi.org/10.1016/j.ica.2013.01.005>.
70. E. J. Glatz, C. M. Rogers, L. D. Bell, R. L. LaDuca, Metal- and Substituent-Dependent Structural Diversity in Cobalt and Nickel Isophthalate Coordination Polymers with Bis(4-pyridylformyl)piperazine Tethers, *Z. Anorg. Allg. Chem.*, 641 (2015), 1357-1365. <http://dx.doi.org/10.1002/zaac.201500127>.
71. Z. M. Wilseck, C. M. Gandolfo, R. L. LaDuca, Topological diversity in copper aromatic *meta*-dicarboxylate coordination polymers with bis(pyridylformyl)piperazine coligands, *Inorg. Chim. Acta*, 363 (2010), 3865-3873. <https://doi.org/10.1016/j.ica.2010.07.045>.
72. A. Banisafar, R. L. LaDuca, Layered copper bromide coordination polymers from bis(pyridyl)piperazine-type precursors: Ligand dependent valence tuning and *in situ* hydrothermal reaction chemistry, *Inorg. Chim. Acta*, 373 (2011), 295-300. <https://doi.org/10.1016/j.ica.2011.03.068>.
73. L. Liu, C. Lian, Y. Long, X. Guo, L. Yang, Two cadmium coordination polymers containing piperazine-1,4-diylbis(pyridine-4-ylmethanone): Highly selective luminescent recognition of  $Cu^{2+}$ , *Inorg. Chim. Acta*, 453 (2016), 186-192. <https://doi.org/10.1016/j.ica.2016.07.049>.

74. H. Xu, Y. L. Song, X. R. Meng, H. W. Hou, M. S. Tang, Y. T. Fan, Strong optical limiting effects of two Ag(I)-bridged metal-organic polymers, *Chem. Phys.*, 359 (2009), 101-110. <https://doi.org/10.1016/j.chemphys.2009.03.011>.
75. Z. M. Wilseck, R. L. LaDuca, Poly[[ $\mu_4$ -bis(4-pyridylcarbonyl)piperazine- $\kappa^4 N:N':O:O'$ ]bis(thiocyanato- $\kappa N$ )cobalt(II)], *Acta Cryst.* E66 (2010), m713. <https://doi.org/10.1107/S160053681001915X>.
76. J. S. Lucas, A. L. Pochodylo, R. L. LaDuca, Cadmium bis(4-pyridylformyl)piperazine coordination polymers: layered nets and a novel 3,5-connected binodal lattice, *CrystEngComm*, 12 (2010), 3310-3317. <https://doi.org/10.1039/C0CE00117A>.
77. A. Rajput, R. Mukherjee, Coordination chemistry with pyridine/pyrazine amide ligands. Some noteworthy results, *Coordination chem. Rev.*, 257 (2013), 350-368. <https://doi.org/10.1016/j.ccr.2012.03.024>.
78. S. Pachisia, R. Gupta, Architectural and catalytic aspects of designer materials built using metalloligands of pyridine-2,6-dicarboxamide based ligands, *Dalton Trans.*, 49 (2020), 14731-14748. <https://doi.org/10.1039/D0DT03058A>.
79. P. Kapoor, A. P. S. Pannu, M. Sharma, M. S. Hundal, R. Kapoor, M. Corbella, N. Aliaga-Alcalde, Syntheses, X-ray crystal structure and magnetic studies of a new dinuclear  $Cu^{II}$  complex,  $[Cu_2(\mu-Cl)_2L_2Cl_2] \cdot 2CH_3CN$ , L: N,N,N',N'-tetraisopropylpyridine-2,6-dicarboxamide, *J. Mol. Struct.*, 981 (2010), 40-45. <https://doi.org/10.1016/j.molstruc.2010.07.021>.
80. L. K. Rana, S. Sharma, and G. Hundal, First Report on Crystal Engineering of Hg(II) Halides with Fully Substituted 3,4-Pyridinedicarboxamides: Generation of Two-Dimensional Coordination Polymers and Linear Zig-Zag Chains of Mercury Metal Ions, *Cryst. Growth & Des.*, 16 (2016), 92-107. <https://doi.org/10.1021/acs.cgd.5b00989>.
81. L. K. Rana, S. Sharma, G. Hundal, Crystal engineering of versatile Hg(II) halides complexes of N,N,N',N'-tetraalkyl substituted 3,5- pyridinedicarboxamides, *J. Mol. Str.*, 1153 (2017), 324-332. <https://doi.org/10.1016/j.molstruc.2017.10.015>.
82. M. W. Mulqi, F. S. Stephens, R. S. Vagg, Studies on the metal-amide bond. XVI. the coordination chemistry of the di-tertiary amide ligand N,N'-dimethyl-N,N'-bis (2'-pyridinecarboxamide)-1,2-ethane, [bpenMe<sub>2</sub>], including the crystal structure of trans-

- [Pd (bpenMe<sub>2</sub>)Cl<sub>2</sub>], *Inorg.Chim.Acta*, 63 (1982), 197-207.  
[https://doi.org/10.1016/S0020-1693\(00\)81913-1](https://doi.org/10.1016/S0020-1693(00)81913-1).
83. N. H. Murray, E. M. Low, A. L. Pochodylo, R. L. LaDuca, Copper aromatic dicarboxylate complexes with a very long conformationally flexible dipyridyl ligand: Coordination polymers and a supramolecular nanotube, *Inorg.Chim.Acta*, 428 (2015), 73-82. <https://doi.org/10.1016/j.ica.2014.12.026>.
84. E. Graf, M. W. Hosseini, J.-M. Planeix, and N. Kyritsakas, Molecular tectonics: design of coordinating tectons based on diazamacrocycles bearing pyridine units and formation of 1D copper coordination networks, *New J. Chem.*, 29 (2005), 343-346. <https://doi.org/10.1039/B416145A>.

**Table 1- Relevant crystallographic parameters of the complexes.**

Complex	Binding mode of ligand	Binding mode of anion	M-N <sub>Pridine</sub>	M-O <sub>Amide</sub>	M-X <sub>Anion</sub>	M-S <sub>Solvent</sub>	Geometry	Structure type	CSD code	Ref
[Co(L <sup>1</sup> ) <sub>2</sub> Cl <sub>2</sub> ] ( <b>1</b> )	Bidentate chelating	IP	2.094 (13)	2.131 (1)	2.421 (3)	-	Octahedral	Monomer	FAQSAU	16
[Ag(L <sup>1</sup> ) <sub>2</sub> NO <sub>3</sub> ] ( <b>2</b> )	Bidentate chelating, monodentate	IP	2.273 (2) 2.223 (2)	2.667 (3)	2.571 (3) 2.500 (3)	-	Square pyramidal	Monomer	FAQSEY	
[Zn(L <sup>1</sup> ) <sub>2</sub> (ClO <sub>4</sub> ) <sub>2</sub> ] ( <b>3</b> )	Bidentate Chelating	IP	2.067 (3)	2.277 (3)	2.037 (3)	-	Octahedral	Monomer	FAQSIC	
[Cu(L <sup>2</sup> ) <sub>2</sub> (ClO <sub>4</sub> ) <sub>2</sub> ] ( <b>4</b> )	Bidentate chelating	IP	1.973 (2)	1.92 (2)	2.612 (2)	-	Octahedral	Monomer	FAQSOI	
[Cu(L <sup>4</sup> ) <sub>2</sub> (NO <sub>3</sub> ) <sub>2</sub> (H <sub>2</sub> O) <sub>1.5</sub> ] ( <b>12</b> )	Monodentate	IP	2.017(5) 2.007 (4)	-	2.012 (4) 2.008 (5)	1.764 (5) 2.234 (5)	Octahedral	Monomer	FAQFIP	(16, 39)
[Zn(L <sup>5</sup> ) <sub>2</sub> (NO <sub>3</sub> ) <sub>2</sub> ] <sub>2</sub> ( <b>25</b> )	Bridging bidentate, Monodentate	IP	2.144 (3) 2.078 (3)	2.195 (3)	2.031 (4) 2.144 (3) 2.377 (3)	-	Octahedral	Dimer	FAQFEL	



$[\text{Co}(\text{L}^5)_2(\text{H}_2\text{O})_2]_n \cdot 2\text{NO}_3$ ( <b>35</b> )	Bridging bidentate	CS	2.144 (3)	2.160 (3)	-	2.062 (3)	Octahedral	1D-Polymer	FAQSUO	
$[\text{Cu}(\text{L}^1)_2(\text{Cl})_2]$ ( <b>5</b> )	Bidentate chelating	IP	2.002 (1) 1.971 (1)	2.661 (1) 2.543 (1)	2.279 (5) 2.313 (5)	-	Octahedral	Monomer	PIHFIX	
$[\text{Cu}(\text{L}^1)_2(\text{ClO}_4)_2]$ ( <b>6</b> )	Bidentate chelating	IP	1.971 (1)	1.948 (1)	2.458 (1)	-	Octahedral	Monomer	PIHFAP	
$[\{\text{CuCl}(\text{L}^1)\}_2(\mu\text{-Cl})_2]$ ( <b>70</b> )	Bidentate chelating	IP	2.003 (2)	2.249 (2)	2.270 (8) 2.419 (8)	-	Distorted square pyramidal	Dimer	PIHFET	<b>17</b>
$[\text{Zn}(\text{L}^3)_2(\text{NCS})_2(\text{H}_2\text{O})_2]$ ( <b>7</b> )	Monodentate	IP	2.171(4)	-	2.107 (5)	2.129 (3)	Octahedral	Monomer	AENAZN 10	<b>34</b>
$[\text{Co}(\text{L}^3)_2(\text{pmb})_2(\text{H}_2\text{O})_2]$ ( <b>8</b> )	Monodentate	IP	2.1439 (14)	-	2.0885 (12)	2.1209 (12)	Octahedral	Monomer	NUPBOQ	<b>35</b>
$[\text{Cu}(\text{Benzo})_2(\text{L}^3)_2]$ ( <b>9</b> )	Monodentate	IP	2.004 (3)	-	1.995 (2) 2.451 (4)	-	Octahedral	Monomer	TEKDOC	<b>36</b>
$[\text{Cu}(\text{L}^4)_2(\text{H}_2\text{O})_4] \cdot [\text{CuL}^4\text{Cl}_3]_2$ ( <b>10</b> )	Monodentate	IP, CS	2.062 (2) 2.031 (2)	-	2.213 (3) 2.252 (2) 2.273 (5)	2.002 (3) 2.113 (2)	Octahedral, Tetrahedral	Monomer	ORITUF	
$[\text{Cu}(\text{L}^4)_4(\text{C}_3\text{H}_8\text{O})_2] \cdot \text{ClO}_4)_2]$ ( <b>11</b> )	Monodentate	CS	2.030 (3) 2.033(3)	-	-	2.490 (3)	Octahedral	Monomer	ORIVAN	<b>37</b>
$[\{\text{Cu}(\text{L}^5)_2(\text{H}_2\text{O})_2\}(\text{NO}_3)_2]_n$ ( <b>36</b> )	Bidentate bridging	IP	2.018 (3)	2.328 (2)	-	2.045 (3)	Octahedral	1D-polymer	ORIT0Z	

$[\text{Cu}(\text{L}^4)_2\text{Br}_2]_n$ ( <b>37</b> )	Bidentate bridging	IP	1.994 (4)	2.753 (3)	2.4456 (9)	-	Octahedral	1D-polymer	ORITIT	(37, 39)
$[\text{Co}(\text{L}^5)_2(\text{H}_2\text{O})_4][\text{Co}(\text{L}^5)(\text{Br})_3]_2 \cdot 2\text{H}_2\text{O}$ ( <b>13</b> )	Monodentate	IP, CS	2.061 (6) 2.134 (5)	-	2.294 (1) 2.318 (1) 2.370 (1)	2.08 2(5) 2.112 (5)	Octahedral, Tetrahedral	Monomer	RAJSOM	<b>38</b>
$[\text{Co}(\text{L}^5)(\text{Cl})_2]_n$ ( <b>34</b> )	Bidentate bridging	IP	2.052 (5)	1.989 (4)	2.217 (2) 2.222 (1)	-	Tetrahedral	1D-polymer	RAJSIG	
$[\text{Cu}(\text{L}^4)_2(\text{NO}_3)_2]_n$ ( <b>14</b> )	Bidentate bridging	IP	1.988 (2)	2.665 (15)	2.010 (15)	-	Octahedral	1D-polymer	WIPZIH	<b>39</b>
$[\text{Cu}(\text{L}^4)(\text{NO}_3)_2]_n$ ( <b>39</b> )	Bidentate bridging	IP	1.985 (2)	1.968 (2)	2.598 (5) 1.957 (5)	-	Octahedral	1D-polymer	WIPRIZ	
$[\text{ZnCl}_2(\text{L}^3)]_2$ ( <b>15</b> )	Bidentate bridging	IP	2.073 (6)	2.010 (5)	2.203 (2) 2.199 (2)	-	Tetrahedral	Dimer	CIKHAF	<b>40</b>
$[(\text{L}^3)_2\text{CuCl}_2]_2$ ( <b>16</b> )	Bidentate bridging	IP	2.007 (4) 2.012 (3)	2.475 (3)	2.254 (1) 2.282 (1)	-	Trigonal bipyramidal	Dimer	CURRUC	<b>41</b>
$[\text{Zn}(\text{L}^3)_2(\text{NCS})_2]$ ( <b>17</b> )	Bridging bidentate	IP	2.006 (5)	2.014 (4)	1.921 (5) 1.929 (4)	-	Tetrahedral	Dimer	DENTZN10	<b>42</b>
$[\text{Zn}(\text{L}^3)_2(\text{Benzo})_2]_2$ ( <b>18</b> )	Monodentate	IP	2.0254 (14)	-	2.0130 (14) 2.0417 (14) 2.0471 (13) 2.0530 (13)	-	Square pyramidal	Dimer	FACQOQ	<b>43</b>

$[\text{Zn}(\text{L}^3)_2(\text{pmb})_2]_2$ ( <b>19</b> )	Monodentate	IP	2.0340 (10)	-	2.0235 (9) 2.0420 (9) 2.0264 (9) 2.1196 (9)	-	Square pyramidal	Dimer	KUSHIQ	<b>44</b>
$[\text{Cu}(\text{Clf})_2(\text{L}^3)_2]_2$ ( <b>20</b> )	Monodentate	IP	2.179 (3)	-	1.968 (2) 1.980 (2) 1.985(2) 1.987 (2)	-	Square pyramidal	Dimer	OBONJO	<b>45</b>
$[\text{Co}(\text{Deab})_2(\text{L}^3)]_2$ ( <b>21</b> )	Monodentate	IP	2.0702 (2)	-	2.029 (15) 2.0262 (2) 2.035 (15) 2.0223 (15)	-	Square pyramidal	Dimer	QAHNOE	<b>46</b>
$\text{Zn}(\text{Mab})_2(\text{L}^3)_2 \cdot \text{H}_2\text{O}$ ( <b>22</b> )	Monodentate	IP	2.052 (14)	-	2.0224 (13) 2.021 (13) 2.046 (13) 2.082 (14)	-	Square pyramidal	Dimer	RUDWUJ	<b>47</b>
$[\text{Zn}(\text{Dmab})_2(\text{L}^3)]_2$ ( <b>23</b> )	Monodentate	IP	2.045 (13)	-	2.0265 (12) 2.027 (12) 2.067 (12) 2.046 (12)	-	Square pyramidal	Dimer	RUGVOF	<b>48</b>
$[\text{Cu}(\text{Benzo})_2(\text{L}^3)]_2$ ( <b>24</b> )	Monodentate	IP	2.162 (6)	-	1.981 (6) 1.976 (6) 1.970 (5) 1.969 (5)	-	Square pyramidal	Dimer	ZENFAZ	<b>49</b>

$[\text{CaZn}_2(\text{L}^3)_2(\text{Benzo})_6]$ ( <b>26</b> )	Monodentate	IP	2.077(2)	-	1.942 (2) 1.959 (2) 1.943 (2) 2.273 (2) 2.311 (2)	-	Tetrahedral and Octahedral	Trinuclear Complex	FACQUW	<b>50</b>
$[\text{Fe}(\text{NCS})_2(\text{L}^3)_2]_n$ ( <b>27</b> )	Bridging bidentate	IP	2.261 (2) 2.260 (2) 2.265 (2)	2.119 (2) 2.124 (2) 2.133 (2)	2.118 (2) 2.107 (2)	-	Octahedral	1D-Polymer	OGAHUA	<b>51</b>
$[\text{Cd}(\text{L}^3)(\text{Cl})_2(\text{H}_2\text{O})]_n$ ( <b>28</b> )	Monodentate	IP	2.360 (3)	-	2.620 (8) 2.644 (8) 2.663 (9) 2.661 (8)	2.354 (2)	Octahedral	1D-Polymer	LIFXAA	<b>52</b>
$[\text{Mn}(\text{L}^3)(\text{NCS})]_n$ ( <b>29</b> )	Bridging bidentate	IP	2.167 (4)	2.177 (4)	1.149 (5) 1.626 (4)	-	Octahedral	1D-Polymer	ENCTMN	<b>53</b>
$[\text{Mn}_2(\text{Pmb})_4(\text{L}^3)_2(\text{H}_2\text{O})]_n$ ( <b>30</b> )	Bridging bidentate	IP	2.3152(2) 2.2854 (2) 2.282 (2) 2.2710 (2)	2.194 (14) 2.1755 (14)	2.153 (14) 2.143 (15) 2.1743 (15) 2.185 (15) 2.1482 (15) 2.111 (15) 2.1694(14) 2.203 (14) 2.172 (14) 2.161 (14) 2.181 (15)	2.2109 (13) 2.1990 (13)	Octahedral	1D-Polymer	QUXFOF	<b>54</b>

					2.1913 (14) 2.1071 (15) 2.142 (15) 2.154 (15) 2.207 (14)					
$[\text{Cu}_2(\text{Cl-Ac})_4(\text{L}^3)]_n$ ( <b>31</b> )	Bridging bidentate	IP	2.194 (2)	2.162 (2)	1.968 (2) 1.966 (2) 1.977 (2) 1.987 (2) 1.995 (2) 2.003 (2) 2.002 (2)		Square pyramidal	1D-Polymer	XEKXIV 01	<b>55</b>
$[\{\text{Co}(\text{L}^4)_2(\text{H}_2\text{O})_2\}(\text{ClO}_4)_2(\text{C}\text{H}_3\text{COCH}_3)_2(\text{H}_2\text{O})_2]_n$ ( <b>32</b> )	Bridging bidentate	IP	2.172 (4)	2.132 (3)	-	2.093 (3)	Octahedral	1D-Polymer	IQAGAJ	<b>56</b>
$[\text{Cd}(\text{Cbenz})_2(\text{L}^3)(\text{H}_2\text{O})_n]_n$ ( <b>33</b> )	Bridging bidentate	IP	2.305 (3)	2.410 (3) 2.323 (3) 2.421 (3) 2.360 (3)	2.504 (3)	2.314 (3)	Pentagonal- bipyramidal	1D-Polymer	AGACOC	<b>57</b>
$[\text{Co}_3(\text{L}^4)_4\text{Cl}_6]_n$ ( <b>38</b> )	Bridging bidentate	IP	2.064 (8) 2.528 (2)	2.278 (7)	2.732 (3) 2.282 (4) 2.204 (4) 2.217 (3)	-	Octahedral, Tetrahedral	1D-Polymer	LABQEM	<b>58</b>
<i>trans</i> - $[\text{Mn}(\text{L}^3)_2(\text{N}_3)_2]_n$ ( <b>40</b> )	Monodentate	IP	2.291 (3)	-	2.210(3)	-	Octahedral	2D-Polymer	WEYKEQ	<b>59</b>

$[\text{Cd}(\text{L}^3)(\text{NCS})_2]_n$ ( <b>41</b> )	Bridging bidentate	IP	2.355 (4)	2.373 (4)	2.292 (6) 2.295 (4) 2.621 (3) 2.704 (5)	-	Octahedral	3D-Polymer	ENICCD	<b>60</b>
$[(\text{L}^3)_4\text{Cu}_4\text{Cl}_6\text{O}]$ ( <b>42</b> )	Monodentate	IP	1.968 (2)	-	2.335 (2) 2.433 (2) 2.503 (2)	1.903 (2) (Oxo-group)	Trigonal bipyramidal	Tetranuclear Metal cluster	COBLOU	<b>61</b>
$[\text{CuI}(\text{L}^3)]_4$ ( <b>43</b> )	Monodentate	IP	2.042 (8) 2.032 (8) 2.028 (8)	-	2.656 (2) 2.736 (2) 2.6953(2) 2.743 (2) 2.6424 (17) 2.6921 (16) 2.728 (2) 2.649 (2) 2.7214 (17) 2.704 (2) 2.7493 (17) 2.621 (2)	-	Tetrahedral	Tetranuclear Metal cluster	BEPDAB	<b>62</b>
$[\text{Cu}(\text{L}^7)\text{Cl}_2]$ ( <b>44</b> )	Tridentate chelating	IP	1.973 (2)	2.177(2) 2.143(2)	2.321 (1) 2.187 (1)	-	tdp*	Monomer	WIYBOV	<b>20</b>
$[\text{Cu}(\text{L}^7)\text{Cl}(\text{ClO}_4)]$ ( <b>45</b> )	Tridentate Chelating	IP	1.933 (2)	1.990 (2) 2.021 (2)	2.1632 (9) 2.448 (3)	-	tdp*	Monomer	WIYBUB	



$[\text{Co}(\text{L}^7)_2(\text{H}_2\text{O})_2](\text{ClO}_4)_2 \cdot \text{H}_2\text{O}$ (46)	Bidentate chelating	CS	2.198 (2)	2.035 (2)	-	2.094 (2)	Octahedral	Monomer	JEDHEG	21
$[\text{Co}(\text{L}^7)_2(\text{H}_2\text{O})_2](\text{PF}_6)_2 \cdot \text{H}_2\text{O}$ (47)	Bidentate chelating	CS	2.189 (3)	2.041 (3)	-	2.101 (3)	Octahedral	Monomer	JEDHAC	
$[\text{Co}(\text{L}^7)_2(\text{CH}_3\text{CN})](\text{PF}_6)_2$ (48)	Bi-, tridentate chelating	CS	2.088 (4) 2.190 (4)	2.106 (3) 2.079 (3) 2.060 (3)	-	2.072 (9)	Octahedral	Monomer	JEDGUV	
$[\text{Ni}(\text{L}^6)(\text{H}_2\text{O})_3](\text{NO}_3)_2$ (49)	Tridentate chelating	IP, CS	1.989 (2)	2.109 (2)	-	2.047 (2) 2.008 (3)	Octahedral	Monomer	IKIBIO	22
$[\text{Ni}(\text{L}^7)(\text{H}_2\text{O})_2(\text{NO}_3)](\text{NO}_3)$ (50)	Tridentate chelating	IP, CS	1.999 (3)	2.067 (2) 2.078(2)	2.052 (2)	2.071 (2) 2.043 (2)	Octahedral	Monomer	IKIBOU	
$[\text{Co}(\text{L}^6)(\text{NO}_3)_2]$ (51)	Tridentate chelating	IP	2.066 (3)	2.175 (3) 2.179 (3)	2.258 (4) 2.188 (3) 2.148 (3) 2.177 (3)	-	Pentagonal bipyramidal	Monomer	IKIBAG	
$[\text{Co}(\text{L}^7)(\text{NO}_3)_2]$ (52)	Tridentate chelating	IP	2.071 (3)	2.152 (3) 2.185 (4)	2.284 (5) 2.208 (4) 2.087 (4) 2.162 (4)	-	Pentagonal bipyramidal	Monomer	IKIBEK	

[Cu(L <sup>9</sup> )(NO <sub>3</sub> ) <sub>2</sub> ] ( <b>53</b> )	Tridentate chelating	IP	1.934 (5)	2.061 (5) 2.063 (5)	1.972 (5) 2.122 (6)	-	Square pyramidal	Monomer	IKIBUA	
[Cu(L <sup>7</sup> )(Cl)(CF <sub>3</sub> SO <sub>3</sub> )] ( <b>54</b> )	Tridentate chelating	IP	1.948 (3)	2.026 (3)	2.188 (1) 2.212 (3)	-	Square pyramidal	Monomer	FADDOF	<b>23</b>
[Cu(L <sup>9</sup> )(Cl)(ClO <sub>4</sub> )] ( <b>55</b> )	Tridentate chelating	IP	1.956 (5)	1.986 (4) 2.007 (4)	2.175 (2) 2.350 (5)	-	Square pyramidal	Monomer	FADFEX	
[Cu(L <sup>10</sup> )(Cl)(ClO <sub>4</sub> )] ( <b>56</b> )	Tridentate chelating	IP	1.937 (4)	1.987 (3) 1.982 (3)	2.173 (2) 2.539 (4)	-	Square pyramidal	Monomer	FADDUL	
[Cu(L <sup>9</sup> )(CF <sub>3</sub> SO <sub>3</sub> ) <sub>2</sub> (H <sub>2</sub> O)] ( <b>57</b> )	Tridentate chelating	IP	1.900 (6)	1.966 (6) 1.952 (7)	2.584 (2)	2.172 (2)	Octahedral	Monomer	FADFAT	
[Ni(NCS) <sub>2</sub> (L <sup>7</sup> )(CH <sub>3</sub> CN)]. CH <sub>3</sub> CN ( <b>58</b> )	Tridentate chelating	IP	2.023 (3) 2.085 (3)	2.023 (3)	1.995 (3) 2.043 (4)	2.141 (4)	Octahedral	Monomer	HATXIK	<b>24</b>
[Ni(NCS) <sub>2</sub> (L <sup>7</sup> )(C <sub>2</sub> H <sub>5</sub> OH)] ( <b>59</b> )	Tridentate chelating	IP	2.030 (3)	2.123 (2) 2.137 (2)	1.980 (3) 2.045 (3)	2.078 (3)	Octahedral	Monomer	HATXOQ	
[U(O <sub>2</sub> )(Cl <sub>2</sub> )(L <sup>9</sup> )] ( <b>60</b> )	Tridentate chelating	IP	2.634 (2)	2.379 (2) 2.404 (2)	2.668 (8) 2.681 (8) 1.760 (2) 1.763 (2)	-	Pentagonal bi-pyramid	Monomer	NIXGAD	<b>25</b>
[U(O <sub>2</sub> )(Br <sub>2</sub> )(L <sup>9</sup> )] ( <b>61</b> )	Tridentate chelating	IP	2.648 (5)	2.405 (5) 2.383 (5)	2.847 (8) 2.864 (8) 1.756 (5)	-	Pentagonal bi-pyramid	Monomer	NIXGEH	

					1.757 (5)					
[Eu( <b>L</b> <sup>9</sup> ) <sub>2</sub> (H <sub>2</sub> O) <sub>2</sub> (CF <sub>3</sub> SO <sub>3</sub> )](C F <sub>3</sub> SO <sub>3</sub> ) <sub>2</sub> (THF) <sub>1.5</sub> ) ( <b>62</b> )	Tridentate chelating	IP, CS	2.594 (3) 2.600 (3)	2.386 (3) 2.419 (2) 2.403 (3) 2.463 (3)	2.459 (3)	2.438 (3) 2.444 (3)	Msa**	Monomer	ILOREG	<b>26</b>
[Gd( <b>L</b> <sup>11</sup> ) <sub>2</sub> (H <sub>2</sub> O) <sub>2</sub> (CF <sub>3</sub> SO <sub>3</sub> )]( CF <sub>3</sub> SO <sub>3</sub> ) <sub>2</sub> ( <sup>t</sup> BuOMe) <sub>2</sub> ( <b>63</b> )	Tridentate chelating	IP, CS	2.586 (3) 2.592 (3)	2.411 (2) 2.377 (3) 2.485 (3) 2.389 (3)	2.410 (3)	2.430 (3) 2.409 (3)	Msa**	Monomer	ILOROQ	
[La(NO <sub>3</sub> ) <sub>3</sub> ( <b>L</b> <sup>12</sup> ) <sub>2</sub> ] ( <b>64</b> )	Tridentate chelating	IP	2.781 (3)	2.745 (3) 2.606 (3)	2.636 (3) 2.644 (3) 2.755 (3)	-	12- coordinated	Monomer	YUMKIB	<b>27</b>
[( <b>L</b> <sup>13</sup> )UO <sub>2</sub> (NO <sub>3</sub> ) <sub>2</sub> ].CH <sub>2</sub> Cl <sub>2</sub> ( <b>65</b> )	Tridentate chelating	IP	2.640 (3)	2.396 (2) 2.431 (2)	1.758 (3) 1.759 (2) 2.504 (3) 2.515 (3) 2.615 (3) 2.835 (3)	-	9- coordinated	Monomer	DAPXEA	<b>28</b>
[( <b>L</b> <sup>8</sup> )UO <sub>2</sub> (NO <sub>3</sub> ) <sub>2</sub> ] <sub>n</sub> . ( <b>66</b> )	Bidentate bridging	IP	-	2.414 (2) 2.379 (2)	1.759 (2) 2.521 (2) 1.758 (3) 2.507 (3) 2.509 (3) 2.529 (2)	-	8- coordinated	1D-polymer	DAPXIE	

$[\text{U}_{1/2}(\text{O})_2(\text{L}^{14})]_2(\text{NTf}_2)$ ( <b>67</b> )	Tridentate chelating	IP, CS	2.716 (2)	2.411 (2) 2.413 (2)	1.749 (2)	-	8 coordinated	Monomer	SOSHUF	<b>29</b>
$[\text{U}(\text{O}_2)(\text{L}^{14})_2](\text{PF}_6)$ ( <b>68</b> )	Tridentate chelating	IP, CS	2.681 (2) 2.687 (2)	2.455 (2) 2.417 (2) 2.435 (2) 2.412 (2)	1.764 (2) 1.768 (2)	-	8 coordinated	Monomer	SOSJAN	
$[\text{Cu}_2(\text{Cl})_4(\text{L}^9)_2] \cdot 2\text{CH}_3\text{CN}$ ( <b>69</b> )	Bidentate chelating	IP	2.025 (4)	2.444 (2)	2..297 (2) 2.335 (2) 2.214 (2)	-	Square pyramidal	Dimer	OKOTOY	<b>79</b>
$[\text{Hg}(\text{L}^{18})(\text{I}_2)]_2$ ( <b>71</b> )	Monodentate	IP	2.443 (8)	-	2.986 (8) 2.712 (1)	-	Tetrahedral	Dimer	RUYWUF	<b>80</b>
$[\text{Hg}(\text{L}^{17})\text{Cl}_2][\text{HgCl}_2]$ ( <b>78</b> )	Bidentate bridging	CS	2.174 (6)	2.738 (6)	2.326 (2) 2.290 (4) 2.640 (2) 2.831 (2) 2.297 (3) 3.121 (2) 3.196 (3) 3.156 (3) 3.456 (5)	-	Square pyramidal	2D	RUYVUE	
$[\text{Hg}(\text{L}^{17})\text{Br}_2]_n$ ( <b>79</b> )	Bidentate bridging	IP	2.382 (4)	2.697 (4)	2.443 (1) 2.468 (1) 3.361 (2)	-	Square pyramidal	2D	RUYWAL	

$[\text{Hg}(\text{L}^{17})\text{I}_2]_n$ ( <b>80</b> )	Bidentate bridging	IP	2.391 (4)	2.948 (4)	2.613 (5) 2.638 (5) 3.446 (6)	-	Square pyramidal	2D	RUYWEP	
$[\text{Hg}(\text{L}^{18})\text{Cl}_2]_n$ ( <b>81</b> )	Tridentate Bridging	IP	2.628 (1)	2.757 (3) 2.641 (3)	2.3045 (1) 2.3080 (1)	-	Square pyramidal	2D	RUYWIT	
$[\text{Hg}(\text{L}^{18})\text{Br}_2]_n$ ( <b>82</b> )	Bidentate bridging	IP	2.611 (6)	2.748 (4) 2.616 (5)	2.452 (1) 2.447 (1)	-	Square pyramidal	2D	RUYWOZ	
$[\text{Hg}(\text{L}^{15})(\text{Cl})_2]_2 \cdot \text{CH}_3\text{CN}$ ( <b>72</b> )	Bidentate bridging	IP	2.412 (3)	2.545 (2)	2.322 (1) 2.317 (1)	-	Tetrahedral	Dimer	CEMVUO	<b>81</b>
$[\text{Hg}(\text{L}^{15})\text{Br}_2]_2 \cdot \text{C}_2\text{H}_5\text{OH}$ ( <b>73</b> )	Bidentate bridging	IP	2.426 (5)	2.538 (5)	2.441 (1) 2.446 (8)	-	Tetrahedral	Dimer	CEMWAV	
$[\text{Hg}(\text{L}^{15})\text{I}_2]_2 \cdot \text{C}_2\text{H}_5\text{OH}$ ( <b>74</b> )	Bidentate bridging	IP	2.437 (5)	2.549 (5)	2.616 (6) 2.618 (7)	-	Tetrahedral	Dimer	CEMWEZ	
$[\text{Hg}(\text{L}^{16})\text{Cl}_2]_n$ ( <b>75</b> )	Tridentate bridging	IP	2.444 (2)	2.592 (2) 2.864 (2)	2.327 (1) 2.313 (1)	-	Square pyramidal	1D	CEMVID	
$[\text{Hg}(\text{L}^{16})\text{Br}_2]_n$ ( <b>76</b> )	Bidentate bridging	IP	2.461 (3)	2.719 (2)	2.4519 (8) 2.498 (7) 3.346 (9)	-	Square pyramidal	1D	CEMWOJ	

$[\text{Hg}(\text{L}^{16})(\text{I}_2)]_n$ ( <b>77</b> )	Bidentate bridging	IP	2.455 (9)	2.676 (8)	2.611 (1) 2.615 (1) 3.661 (2)	-	Square pyramidal	1D	CEMWUP	
$[\text{Hg}(\text{I})_2(\text{L}^{19})]_2 \cdot 3\text{H}_2\text{O}$ ( <b>83</b> )	Bidentate bridging	IP	2.418 (7)	-	2.638 (1)	-	Tetrahedral	Dimer	JAPHEO	<b>63</b>
$\{[\text{Cu}_2(\text{mal})_2(\text{L}^{22})_2(\text{H}_2\text{O})_2] \cdot 10 \text{H}_2\text{O}\}_n$ ( <b>84</b> )	Monodentate	IP	2.005 (2) 2.018 (2)	-	1.9530 (2) 1.921 (2) 2.316 (2)	-	Square pyramidal	Dimer	FOKJEW	<b>64</b>
$\{[\text{Cd}(\text{SCN})_2(\text{L}^{19})_2] \cdot 2(\text{CH}_3\text{OH})\}_n$ ( <b>85</b> )	Bidentate bridging	IP	2.386 (4) 2.420 (4)	-	2.284 (4)	-	Octahedral	1D-polymer	TEBXAB	<b>65</b>
$[\text{CdI}_2(\text{L}^{20})]_n$ ( <b>86</b> )	Bidentate bridging	IP	2.292 (4) 2.325 (4)	-	2.697 (9) 2.712 (4)	-	Tetragonal	1D-polymer	TEBXIJ	
$\{[\text{Cd}(\text{NO}_3)_2(\text{L}^{19})_2] \cdot 2(\text{CH}_3\text{OH})\}_n$ ( <b>87</b> )	Bidentate bridging	IP	2.369 (3) 2.379 (3)	-	2.460 (3)	-	Octahedral	1D-polymer	TEBXEF	
$[\text{CdCl}_2(\text{L}^{20})_4]_n$ ( <b>97</b> )	Bidentate bridging	IP	2.464 (3) 2.484 (3)	-	2.535 (11)	-	Octahedral	2D-polymer	TEBXOP	
$[\text{Co}(\text{NCS})_2(\text{CH}_3\text{OH})_2(\text{L}^{21})]_n$ ( <b>88</b> )	Bidentate bridging	IP	2.157 (4)	2.148 (3)	2.089 (4)	-	Octahedral	1D-polymer	BICNIL	<b>66</b>
$\{[\text{Co}(\text{H}_2\text{O})_2(\text{CH}_3\text{OH})_2(\text{L}^{22})](\text{NO}_3)_2\}_n$ ( <b>89</b> )	Bidentate bridging	CS	2.176 (3)	2.090 (4)	-	2.093 (3)	Octahedral	1D-polymer	BICNEH	

$[\text{ZnCl}_2(\text{L}^{21})]_n$ ( <b>90</b> )	Bidentate bridging	IP	2.064 (2)	-	2.233 (1)	-	Octahedral	1D-polymer	SEDQAU	<b>67</b>
$[\text{CoCl}(\text{L}^{21})_{0.5}]_n$ ( <b>101</b> )	Tetradentate bridging	IP	2.153 (2)	2.149 (2)	2.453 (8)	-	Octahedral	2D-polymer	SEDPOH	
$\{[\text{NiCl}_2(\text{L}^{21})_{0.5}(\text{L}^{21})_{0.5}](\text{H}_2\text{O})_2\}_n$ ( <b>102</b> )	Bidentate bridging	IP	2.164 (4) 2.191 (4)	-	2.424 (1)	-	Octahedral	2D-polymer	SEDPUN	
$[\text{HgI}_2(\text{L}^{21})]_n$ ( <b>91</b> )	Bidentate bridging	IP	2.40 (1) 2.45 (1)	-	2.656 (2) 2.659 (2)	-	Tetrahedral	1D-polymer	SAQJUQ	<b>68</b>
$\{\text{Zn}(\text{NCS})_2(\text{L}^{21})_2\} \cdot 2\text{H}_2\text{O}\}_n$ ( <b>98</b> )	Bidentate bridging	IP	2.247 (2) 2.241 (2)	-	2.101 (2)	-	Octahedral	2D-polymer	SAQJIE	
$\{[\text{Mn}(\text{H}_2\text{O})_2(\text{SO}_4)(\text{L}^{21})](\text{H}_2\text{O})_3(\text{CH}_3\text{OH})\}_n$ ( <b>99</b> )	Bidentate bridging	IP	2.313 (2) 2.291 (2)	-	2.204 (2) 2.175 (2)	2.218 (2) 2.181 (2)	Octahedral	2D-polymer	SAQJEA	
$[\text{Cd}(\text{N}_3)_2(\text{L}^{21})_2]_n$ ( <b>106</b> )	Bidentate bridging	IP	2.362 (2)	-	2.330 (3) 2.326 (3)	-	Octahedral	3D-polymer	SAQJOK	
$\{[\text{Co}(\text{H}_2\text{O})_4(\text{L}^{22})][\text{Co}(\text{hmp})_2(\text{L}^{22})] \cdot 6\text{H}_2\text{O}\}_n$ ( <b>92</b> )	Bidentate	CS	2.1471 (12) 2.1622 (13)	-	2.0430 (10) 2.106 (11)	2.0512 (11) 2.1441 (10)	Octahedral	Dimer	CIDDUQ	<b>69</b>
$\{\text{Ni}(\text{Hmp})_2(\text{L}^{22})(\text{H}_2\text{O})_2\} \cdot 2\text{H}_2\text{O}\}_n$ ( <b>93</b> )	Bidentate	IP, CS	2.1092 (2)	-	2.011 (13)	2.092 (13)	Octahedral	1D-polymer	DUJQIK	<b>70</b>



$\{[\text{Cu}(\text{H}_2\text{MeOip})(\text{HMeOip})_2(\text{L}^{22})].3\text{H}_2\text{O}\}_n$ ( <b>94</b> )	Bidentate bridging	IP	1.910 (3) 2.01 (3)	-	1.934 (2) 1.96 (2) 2.31 (2)	-	Square pyramidal	1D-polymer	TAHQIE	<b>71</b>
$[\text{CuBr}_2(\text{L}^{22})]_n$ ( <b>95</b> )	Tetradentate bridging	IP	2.009 (3)	2.534 (2)	2.456 (4)	-	Octahedral	2D-polymer	AQUZUI	<b>72</b>
$\{[\text{Cd}(\text{L}^{22})(\text{H}_2\text{O})_2](\text{SUL})(\text{H}_2\text{O})_{0.5}\}_n$ ( <b>96</b> )	Monodentate	CS	2.318 (4)	2.315 (4)	-	2.248 (4)	Octahedral	1D-polymer	ATONEE	<b>73</b>
$\{[\text{Ag}(\text{L}^{21})].\text{NO}_3(\text{H}_2\text{O})\}_n$ ( <b>100</b> )	Bidentate bridging	CS	2.169 (4) 2.168 (5)	-	2.631(2)	-	Linear	2D-polymer	YULFAN	<b>74</b>
$[\text{Co}(\text{NCS})_2(\text{L}^{22})]_n$ ( <b>103</b> )	Tetradentate Bridging	IP	2.174 (2)	2.2034 (2)	-	2.03 (2)	Octahedral	2D-polymer	VUYTAL	<b>75</b>
$[\text{CdCl}_2(\text{L}^{22})]_n$ ( <b>104</b> )	Tetradentate Bridging	IP	2.363 (3)	2.38 (3)	2.5484 (10) 2.5485 (10)	-	Octahedral	2D-polymer	XUYN OV	<b>76</b>
$[\text{Cd}(\text{NO}_3)_2(\text{L}^{22})]_n$ ( <b>105</b> )	Tetradentate Bridging	IP	2.311 (3)	2.302 (2)	2.325 (3)	-	Octahedral	2D-polymer	XUYN UB	
$[\text{Pr}(\text{L}^{23})(\text{NO}_3)_3]$ ( <b>107</b> )	Tetradentate chelating	IP	2.623 (2) 2.694 (2)	2.4897 (18) 2.4142 (18)	2.5821 (18) 2.5893 (19) 2.5436 (19) 2.5418 (19) 2.5523 (19) 2.551 (2)	-	Bi-capped square antiprism	Monomer	QIZVOM	<b>18</b>
$[\text{Nd}(\text{L}^{23})(\text{NO}_3)_3]$ ( <b>108</b> )	Tetradentate chelating	IP	2.6054 (17) 2.6833 (17)	2.4807 (14) 2.4089 (15)	2.5703 (15) 2.5750 (16)	-	Bi-capped square antiprism	Monomer	QIZVIG	

[Gd(L <sup>23</sup> )(NO <sub>3</sub> ) <sub>3</sub> ] (109)	Tetradentate chelating	IP	2.6054 (17) 2.6833 (17)	2.4143 (17) 2.346 (2)	2.5251 (15) 2.525 (2) 2.5351 (16) 2.5345(16)	-	Bi-capped square antiprism	Monomer	QIZSEZ	
					2.513 (2) 2.5195 (19) 2.4923 (17) 2.4975 (18) 2.4735 (19) 2.4784 (18)					
[Tb(L <sup>23</sup> )(NO <sub>3</sub> ) <sub>3</sub> ] (110)	Tetradentate chelating	IP	2.5221 (19) 2.608 (2)	2.403 (2) 2.327 (2)	2.4952 (19) 2.472 (2) 2.478 (2) 2.456 (2) 2.481 (2)	-	Bi-capped square antiprism	Monomer	QIZVUS	
[Dy(NO <sub>3</sub> ) <sub>3</sub> (L <sup>24</sup> )] <sub>n</sub> (111)	Tetradentate chelating	IP	2.481 (2) 2.581 (2)	2.390 (2) 2.323 (2)	2.416 (2) 2.463 (2) 2.466 (2) 2.467 (2) 2.489 (2) 2.526 (2)	-	Bicapped square antiprism	Monomer	YINBIJ	19
[Gd(NO <sub>3</sub> ) <sub>3</sub> (L <sup>25</sup> )] <sub>n</sub> (112)	Tetradentate chelating	IP	2.5810 (11) 2.6229 (12)	2.4680 (11) 2.3383 (11)	2.4592 (12) 2.4827 (12)	-		Monomer	YIMZUS	

					2.4885 (11) 2.4932 (12) 2.4968 (12) 2.5239 (12)		Bicapped square antiprism			
[La(L <sup>26</sup> ) <sub>2</sub> (NO <sub>3</sub> ) <sub>3</sub> ].NO <sub>3</sub> .2DCM (113)	Tetradentate chelating	IP, CS	2.833 (3) 2.822 (3) 2.834 (3) 2.834 (3)	2.578 (2) 2.578 (2) 2.689 (2) 2.689 (2)	2.709 (2) 2.709 (2) 2.654 (2) 2.654 (2)	-	12- coordinated	Monomer	ORODAC	30
[Nd(L <sup>26</sup> ) (NO <sub>3</sub> ) <sub>3</sub> ]. 2DCM (114)	Tetradentate chelating	IP	2.599 (6) 2.636 (7)	2.510 (6) 2.389 (6)	2.533 (6) 2.517 (6) 2.553 (6) 2.565 (6) 2.555 (6) 2.600 (6)	-	12- coordinated	Monomer	ORODOQ	
[Gd(L <sup>26</sup> ) (NO <sub>3</sub> ) <sub>3</sub> ].DCM (115)	Tetradentate chelating	IP	2.542 (6) 2.572 (7)	2.486 (5) 2.373 (5)	2.507 (6) 2.461 (5) 2.505 (5) 2.527 (5) 2.486 (5)	-	10- coordinated	Monomer	OROCIJ	
[Cu(L <sup>26</sup> ) <sub>2</sub> ].2NO <sub>3</sub> (116)	Bi/Tridentate chelating	CS	1.919 (3) 1.971 (2) 2.156 (3) 2.245 (3)	2.068 (2)	-	-	Square pyramidal	Monomer	OROCUV	

$[\text{Zn}(\text{L}^{26})_2] \cdot 2\text{NO}_3$ ( <b>117</b> )	Bi/Tridentate chelating	CS	2.025 (4) 2.027 (4) 2.141 (4) 2.180 (4)	2.234 (3)	-	-	Trigonal bipyramidal	Monomer	OROCOP	
$[\text{Cd}(\text{L}^{26})_2] \cdot 2\text{NO}_3$ ( <b>118</b> )	Tri/Terdentate chelating	CS	2.3522 (2) 2.3389 (2) 2.3624 (2) 2.3712 (2)	2.4685 (2) 2.4692 (2) 2.4994 (2)	-	-	7- coordinated	Monomer	ORODEG	
$\text{UO}_2(\text{NO}_3)(\text{L}^{27}) \cdot ((\text{CH}_3)_2\text{NH}^+)(\text{H}_2\text{O})_2$ ( <b>119</b> )	Terdentate chelating	IP,CS	2.587 (2) 2.604 (2)	1.246 (2) 2.399 (2)	1.736 (2) 1.751 (2)	-	8- coordinated	Monomer	VIVWOO	<b>31</b>
$[\text{Th}(\text{NO}_3)_4(\text{L}^{27})] \cdot \text{H}_2\text{O}$ ( <b>120</b> )	Terdentate chelating	IP	2.690 (2) 2.697 (2)	2.447 (2) 2.465 (2)	2.559 (2) 2.623 (2) 2.634 (2) 2.575 (2) 2.576 (2) 2.578 (2) 2.569 (2) 2.587 (2)	-	12- coordinated	Monomer	VIVWII	
$[\text{La}(\text{L}^{28})(\text{NO}_3)_3]$ ( <b>121</b> )	Terdentate chelating	IP	2.712 (3) 2.716 (3)	2.559 (2) 2.572 (2)	2.583 (2) 2.598 (2) 2.605 (2) 2.627 (2)	-	10- coordinated	Monomer	XETKOZ	<b>32</b>
$[\text{Eu}(\text{L}^{29})(\text{NO}_3)_3]$ ( <b>122</b> )		IP	2.588 (4)	2.400 (3)	2.464 (13)	-		Monomer	XETKIT	

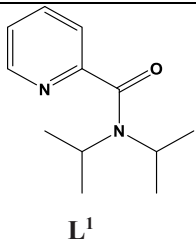
	Terdentate chelating		2.632 (3)	2.428 (4)	2.479 (4) 2.489 (3) 2.496 (10) 2.500 (4) 2.507 (4) 2.530 (9) 2.578 (11)		10- coordinated			
[Pd(L <sup>30</sup> )Cl <sub>2</sub> ] ( <b>123</b> )	Bidentate chelating	IP	2.001 (1) 1.99 (1)	-	2.325 (4) 2.297 (4)	-	Square planar	Monomer	BOKROU	<b>82</b>
[Pr(L <sup>32</sup> )(NO <sub>3</sub> ) <sub>3</sub> ] ( <b>124</b> )	Terdentate chelating	IP	2.696 (3) 2.678 (3)	2.455 (3) 2.482 (3)	2.534 (3) 2.542 (2) 2.551 (3) 2.552 (3) 2.559 (3) 2.578 (3)	-	10- coordinated	Monomer	QAMQUT	<b>33</b>
[Nd(L <sup>32</sup> )(NO <sub>3</sub> ) <sub>3</sub> ] ( <b>125</b> )	Terdentate chelating	IP	2.657 (4) 2.674 (4)	2.445 (3) 2.471 (3)	2.512 (4) 2.522 (4) 2.532 (4) 2.536 (5) 2.542 (4) 2.567 (4)	-	10- coordinated	Monomer	QAMQON	
[Eu(L <sup>32</sup> )(NO <sub>3</sub> ) <sub>3</sub> ] ( <b>126</b> )	Terdentate chelating	IP	2.628 (9)	2.439 (8) 2.414 (8)	2.452 (12) 2.454 (11)	-	10- coordinated	Monomer	QAMQED	

[Gd(L <sup>32</sup> )(NO <sub>3</sub> ) <sub>3</sub> ] ( <b>127</b> )	Terdentate chelating	IP	2.615 (10) 2.619 (9)	2.428 (9) 2.408 (9)	2.473 (12) 2.478 (8) 2.492 (11) 2.520 (8) 2.431 (13) 2.442 (15) 2.450 (13) 2.465 (9) 2.482 (13) 2.505 (10)	-	10 coordinated	Monomer	QAMQIH	
[Tb(L <sup>32</sup> )(NO <sub>3</sub> ) <sub>3</sub> ] ( <b>128</b> )	Terdentate chelating	IP	2.600 (4) 2.607 (4)	2.402 (4) 2.416 (4)	2.407 (5) 2.440 (5) 2.446 (5) 2.451 (4) 2.495 (4)	-	10 coordinated	Monomer	QAMRAA	
L <sup>33</sup>	-	-	-	-	-	-	-	-	QAMQAZ	
{[Cu <sub>2</sub> (phtH) <sub>2</sub> (L <sup>34</sup> ) <sub>2</sub> (H <sub>2</sub> O) <sub>4</sub> ]( NO <sub>3</sub> ) <sub>2</sub> ·H <sub>2</sub> O} ( <b>129</b> )	Bidentate Bridging	IP, CS	1.993 (3) 1.991 (3)	-	1.950 (3) 1.991 (3) 2.21 (3)	-	Square pyramidal	Macrocycle	VOTGES	<b>83</b>
[Cu <sub>2</sub> (OAc) <sub>4</sub> (L <sup>31</sup> ) <sub>2</sub> ] ( <b>130</b> )	Bidentate Bridging	IP	2.187 (2)	-	1.968 (2) 1.974 (2)	-	Square pyramidal	1D polymer	NAHKUJ	<b>84</b>

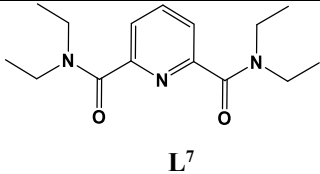
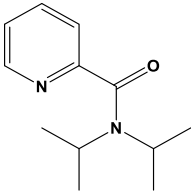
					1.967 (2)					
--	--	--	--	--	-----------	--	--	--	--	--

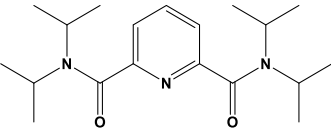
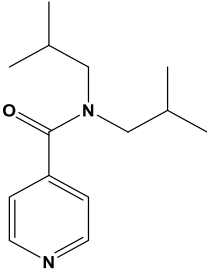
IP: Ion Pair, CS: Charge separated, \* Trigonally distorted rectangular pyramid, \*\* distorted monocapped square-antiprism.

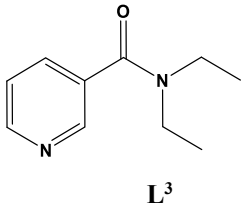
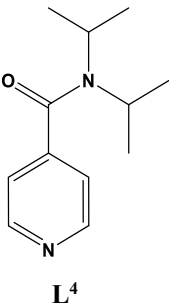
**Table 2- Summary of the applications of coordination complexes.**

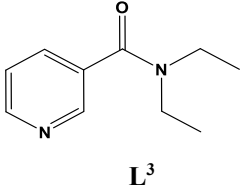
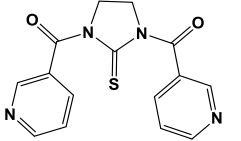
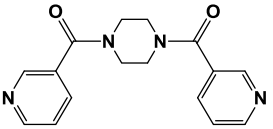
	Ligand used	Metal complex/ Ligand	Application	Noteworthy results	CCDC code	Reference
C H R O M I S M	 L <sup>1</sup>	[Cu(L <sup>1</sup> ) <sub>2</sub> (Cl) <sub>2</sub> ] ( <b>5</b> )	Solvato- and Thermochromism	<b>Thermochromism</b> Colour change from blue ( <b>5</b> ) to green ( <b>71</b> ) on heating at 160° C.	PIHFIX	17
		[{CuCl (L <sup>1</sup> )} <sub>2</sub> (μ-Cl) <sub>2</sub> ] ( <b>71</b> )		<b>Solvatochromism</b> -Blue coloured solution of octahedral complexes <b>5</b> and <b>71</b> in MeOH due to the d-d band at ca. 800 nm. -Yellow-green solution of complexes <b>5</b> and <b>71</b> in ACN due to LMCT (Cl <sub>Bridged</sub> → Cu(II) with shoulder bands at ca. 380 and 450 nm), and d-d bands (at ca. 800 nm).	PIHFET	

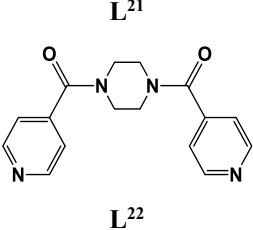


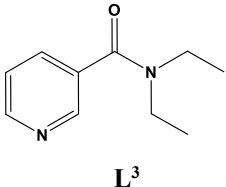
M A G N E T I S M	 <p style="text-align: center;"><b>L<sup>7</sup></b></p>	[Cu(L <sup>7</sup> )Cl <sub>2</sub> ] ( <b>44</b> )	Room Temperature Magnetism	1.95 BM (Paramagnetic behaviour)	WIYBOV	<b>20</b>
		[Cu(L <sup>7</sup> )Cl(ClO <sub>4</sub> )] ( <b>45</b> )	Room Temperature Magnetism	1.88 BM (Paramagnetic behaviour)	WIYBUB	<b>20</b>
		[Co(L <sup>7</sup> ) <sub>2</sub> (H <sub>2</sub> O) <sub>2</sub> ](ClO <sub>4</sub> ) <sub>2</sub> ·H <sub>2</sub> O ( <b>46</b> )	Room Temperature Magnetism	4.75 BM	JEDHEG	<b>21</b>
		[Co(L <sup>7</sup> ) <sub>2</sub> (H <sub>2</sub> O) <sub>2</sub> ](PF <sub>6</sub> ) <sub>2</sub> ·H <sub>2</sub> O ( <b>47</b> )	Room Temperature Magnetism	4.68 BM	JEDHAC	<b>21</b>
		[Co(L <sup>7</sup> ) <sub>2</sub> (CH <sub>3</sub> CN)](PF <sub>6</sub> ) <sub>2</sub> ( <b>48</b> )	Room Temperature Magnetism	5.01 BM	JEDGUV	<b>21</b>
		[Ni(NCS) <sub>2</sub> (L <sup>7</sup> )(CH <sub>3</sub> CN)]·CH <sub>3</sub> CN ( <b>58</b> )	Room Temperature Magnetism	2.82 BM	HATXIK	<b>24</b>
		[Ni(NCS) <sub>2</sub> (L <sup>7</sup> )(C <sub>2</sub> H <sub>5</sub> OH)] ( <b>59</b> )	Room Temperature Magnetism	2.88 BM	HATXOQ	<b>24</b>
		[{CuCl(L <sup>1</sup> )} <sub>2</sub> (μ-Cl) <sub>2</sub> ] ( <b>70</b> )	Variable Temperature Magnetism (from 300K to 2K)	Ferromagnetic coupling between Cu(II) ions involving a distortion from a SP geometry with coplanar bases to TBP.	PIHFET	<b>17</b>

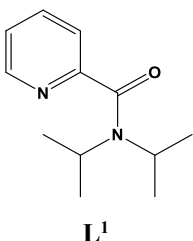
M A G N E T I S M	<b>L<sup>1</sup></b>			Magnetic parameters: $J^* = 43.1 \text{ cm}^{-1}$ ; $g^* = 2.14$ parameters.		
	 <b>L<sup>9</sup></b>	$[\text{Cu}_2(\text{Cl})_4(\text{L}^9)_2] \cdot 2\text{CH}_3\text{CN}$ ( <b>69</b> )	Variable Temperature Magnetism (from 300K to 5K)	Anti-ferromagnetic coupling between Cu(II) ions. Magnetic parameters: $J^* = -$ $3.72 \text{ cm}^{-1}$ ; $g^* = 2.09$ .	OKOTOY	<b>79</b>
	 <b>L<sup>5</sup></b>	$[\text{Co}(\text{L}^5)(\text{Cl})_2]_n$ ( <b>34</b> )	Variable Temperature Magnetism (from 300K to 2K)	The Co( <i>Td</i> ) ion was assumed as an isolated system without considering magnetic interactions via bridging ligands. Magnetic parameters: $ D ^* = 10.8 \text{ cm}^{-1}$ , $g_{\perp} = 1.92$ , $g_{\parallel} = 2.92$ .	RAJSIG	<b>38</b>
		$[\text{Co}(\text{L}^5)_2(\text{H}_2\text{O})_4][\text{Co}(\text{L}^5)(\text{Br})_3]_2 \cdot 2\text{H}_2\text{O}$ ( <b>13</b> )	Variable Temperature Magnetism (from 300K to 2K)	Low temperature data was fitted (below 80K) using MAGPACK program. Magnetic parameters: $g_{Co(Td)}^* = 2.89$ , $g_{Co(oh)}^* =$ $3.50$ , $ D_{Co(Td)} ^* = 10.62 \text{ cm}^{-1}$ ,	RAJSOM	<b>38</b>

MAGNETISM	 <p style="text-align: center;"><b>L<sup>3</sup></b></p>	$[\text{Fe}(\text{NCS})_2(\text{L}^3)_2]_n$ ( <b>27</b> )	Variable Temperature Magnetism (from 300 K to 1.8 K)	$ E_{\text{Co}} _{Td} = 2.95 \text{ cm}^{-1}$ , $J^* = -0.41 \text{ cm}^{-1}$ . High temperature data was fitted (above 80K) using VPMAG program. Magnetic parameters: $J_{L-S} = -107.1 \text{ cm}^{-1}$ , $\Delta^* = 240.9 \text{ cm}^{-1}$ , and $\lambda^* = 144.8 \text{ cm}^{-1}$ .  Zero-field splitting effect and weak anti-ferromagnetic coupling between high spin, octahedral Fe (II) centres. Magnetic parameters: $ D ^* = 2.97 \text{ cm}^{-1}$ , $g^* = 2.53$ , $J^* = -0.04 \text{ cm}^{-1}$ , $g^* = 2.26$ .	OGAHUA	<b>51</b>
	 <p style="text-align: center;"><b>L<sup>4</sup></b></p>	$[\text{Co}_3(\text{L}^4)_4(\text{Cl})_6]_n$ ( <b>38</b> )	Variable Temperature Magnetism (from 300 K to 2 K)	Weak ferromagnetic interactions between Co(II) centres. High temperature data (above 50K) was fitted using VPMAG program. Magnetic parameters: $J_{L-S} = -182 \text{ cm}^{-1}$ , $\Delta^* = 250 \text{ cm}^{-1}$ , and $\lambda^* = -138 \text{ cm}^{-1}$ .	LABQEM	<b>58</b>

MAGNETISM	 <p style="text-align: center;"><b>L<sup>3</sup></b></p>	<i>trans</i> -[Mn( <b>L<sup>3</sup></b> ) <sub>2</sub> (N <sub>3</sub> ) <sub>2</sub> ] <sub>n</sub> ( <b>40</b> )	Variable Temperature Magnetism (Data was taken from 300 K to 2 K at 100 G)	<p>Low temperature (below 50K) data was fitted using MAGPACK program.</p> <p>Magnetic parameters:</p> $J_{Co-Co}^* = 0.34 \text{ cm}^{-1}$ , $g_{Co}(Td)^* = 2.92$ , $g_{Co}(Oh) = 2.50$ $ D_{Co} _{Td}^* = 11.41 \text{ cm}^{-1}$ , $ E_{Co} _{Td} = 0.81 \text{ cm}^{-1}$ <p>Magnetic parameters:</p> $J_{Co-Co} = 3.42(1) \text{ cm}^{-1}$ ; $g = 2.01$ .	WEYKEQ	<b>59</b>
NONLINEAR	 <p style="text-align: center;"><b>L<sup>19</sup></b></p> 	[Hg(I) <sub>2</sub> ( <b>L<sup>19</sup></b> )] <sub>2</sub> ·3H <sub>2</sub> O ( <b>83</b> )	3 <sup>rd</sup> order NLO property	$n_2^* = 9.14 \times 10^{-18} \text{ m}^2 \text{ W}^{-1}$ , $\chi^{(3)} = 2.23 \times 10^{-11} \text{ esu}$ , and $\gamma^* = 3.24 \times 10^{-29} \text{ esu}$	JAPHEO	<b>63</b>
		[Co(NCS) <sub>2</sub> (CH <sub>3</sub> OH) <sub>2</sub> ( <b>L<sup>21</sup></b> )] <sub>n</sub> ( <b>88</b> )	3 <sup>rd</sup> order NLO property	$n_2^* = 3.24 \times 10^{-16} \text{ esu}$ , $\chi^{(3)} = 3.08 \times 10^{-12} \text{ esu}$ , and $\alpha_2^* = 9 \times 10^{-11} \text{ m W}^{-1}$	BICNIL	<b>66</b>

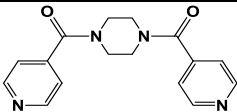
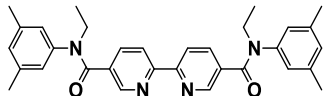
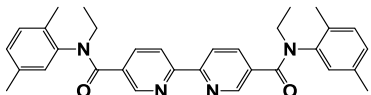
I N E A R  O P T I C S  N		$\{[\text{Co}(\text{H}_2\text{O})_2(\text{CH}_3\text{OH})_2(\text{L}^{22})](\text{NO}_3)_2\}_n$ ( <b>89</b> )	3 <sup>rd</sup> order NLO property	$n_2^* = 3.05 \times 10^{-16}$ esu, $\chi^{(3)*} = 4.70 \times 10^{-12}$ esu, and $\alpha_2'^* = 1.41 \times 10^{-10} \text{ m W}^{-1}$	BICNEH	<b>66</b>
		$[\text{ZnCl}_2(\text{L}^{21})]_n$ ( <b>90</b> )	3 <sup>rd</sup> order NLO property	$n_2^* = 1.73 \times 10^{-11}$ esu, $\chi^{(3)*} = 4.40 \times 10^{-13}$ esu, and $\gamma^* = 1.06 \times 10^{-30}$ esu	SEDQAU	<b>67</b>
		$[\text{CoCl}(\text{L}^{21})_{0.5}]_n$ ( <b>101</b> )	3 <sup>rd</sup> order NLO property	$n_2^* = 1.65 \times 10^{-11}$ esu, $\chi^{(3)*} = 11.7 \times 10^{-13}$ esu, and $\gamma^* = 2.70 \times 10^{-30}$ esu	SEDPOH	<b>67</b>
		$\{[\text{NiCl}_2(\text{L}^{21})_{0.5}(\text{L}^{21})_{0.5}](\text{H}_2\text{O})_2\}_n$ ( <b>102</b> )	3 <sup>rd</sup> order NLO property	$n_2^* = 1.47 \times 10^{-11}$ esu, $\chi^{(3)*} = 3.37 \times 10^{-13}$ esu, and $\gamma^* = 1.59 \times 10^{-30}$ esu	SEDPUN	<b>67</b>
		$\{[\text{Ag}(\text{L}^{21})].\text{NO}_3.(\text{H}_2\text{O})\}_n$ ( <b>100</b> )	3 <sup>rd</sup> order NLO property	$n_2^* = 1.35 \times 10^{-17}$ esu, $\chi^{(3)*} = 7.47 \times 10^{-12}$ esu, $\alpha_2'^* = 2.24 \times 10^{-10} \text{ m W}^{-1}$ , and $\gamma^* = 1.97 \times 10^{-28}$ esu	YULFAN	<b>74</b>
		$\{[\text{Zn}(\text{NCS})_2(\text{L}^{21})_2].2\text{H}_2\text{O}\}_n$ ( <b>98</b> )	3 <sup>rd</sup> order NLO property	$n_2^* = 1.93 \times 10^{-17}$ esu, $\chi^{(3)*} = 4.52 \times 10^{-11}$ esu, $\alpha_2'^* = 6.9$	SAQJIE	<b>68</b>

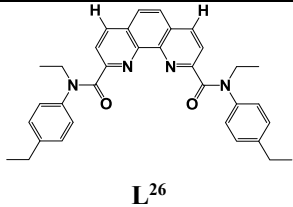
		$\{[\text{Mn}(\text{H}_2\text{O})_2(\text{SO}_4)(\text{L}^{21})](\text{H}_2\text{O})_3(\text{CH}_3\text{OH})\}_n$ ( <b>99</b> )  $[\text{Cd}(\text{N}_3)_2(\text{L}^{21})_2]_n$ ( <b>106</b> )	3 <sup>rd</sup> order NLO property  3 <sup>rd</sup> order NLO property	$\times 10^{-9} \text{ m W}^{-1}$ , and $\gamma^* = 9.1 \times 10^{-29} \text{ esu}$  $n_2^* = 2.73 \times 10^{-17} \text{ esu}$ , $\chi^{(3)*} = 6.39 \times 10^{-11} \text{ esu}$ , $\alpha_2'^* = 9.2 \times 10^{-9} \text{ m W}^{-1}$ , and $\gamma^* = 1.79 \times 10^{-28} \text{ esu}$  $n_2^* = 1.64 \times 10^{-17} \text{ esu}$ , $\chi^{(3)*} = 3.84 \times 10^{-11} \text{ esu}$ , $\alpha_2'^* = 7.1 \times 10^{-9} \text{ m W}^{-1}$ , and $\gamma^* = 9.66 \times 10^{-29} \text{ esu}$	SAQJEA  SAQJOK	<b>68</b>  <b>68</b>
B I O L O G I C A L	 <p style="text-align: center;"><b>L<sup>3</sup></b></p>	$[\text{Cu}(\text{Clop})_2(\text{L}^3)_2]_2$ ( <b>20</b> )	Antibacterial activity  Antifungal activity	$\text{G}^+$ <i>S. aureus</i> $\text{IC}_{50}^*$ : 3.05 mmol L <sup>-1</sup> $\text{MIC}^*$ : >5 mmol L <sup>-1</sup>  <i>A. Alternata</i> $\text{IC}_{50}^*$ : 3.35 mmol L <sup>-1</sup> $\text{MIC}^*$ : 5 <sup>a</sup> mmol L <sup>-1</sup> <i>B. Cinerea</i> $\text{IC}_{50}^*$ : 3.30 mmol L <sup>-1</sup> $\text{MIC}^*$ : >5 mmol L <sup>-1</sup>  <i>M. gypseum</i> $\text{IC}_{50}^*$ : 2.5 mmol L <sup>-1</sup>	OBONJOJ	<b>45</b>

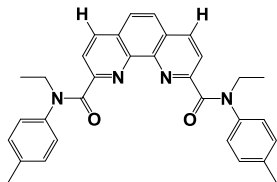
A C T I V I T Y  B I O L O G I C A	 <b>L<sup>1</sup></b>	<b>[Co(L<sup>1</sup>)<sub>2</sub>Cl<sub>2</sub>] (1)</b>	Antibacterial activity	MIC*: 5 <sup>a</sup> mmol L <sup>-1</sup> <i>S. aureus</i> MIC*: 0.5 mg/ml <i>K. pneumoniae</i> MIC*: 0.2 mg/ml	FAQSAU	<b>16</b>				
			Antifungal activity	<i>C. albicans</i> MIC*: 0.007 mg/ml						
			Antibacterial activity	<i>S. aureus</i> MIC*: 2 mg/ml <i>K. pneumoniae</i> MIC*: 0.01 mg/ml <i>G<sup>-</sup> E. coli</i> MIC*: 0.2 mg/ml			FAQSEY	<b>16</b>		
			Antifungal activity	<i>C. albicans</i> MIC*: 0.15 mg/ml						
			Antibacterial activity	<i>G<sup>-</sup> E. coli</i> MIC*: 2.5 mg/ml					FAQSIC	<b>16</b>
			Antibacterial activity	<i>S. aureus</i>						
	<b>[Ag(L<sup>1</sup>)<sub>2</sub>NO<sub>3</sub>] (2)</b>	Antibacterial activity	MIC*: 5 <sup>a</sup> mmol L <sup>-1</sup> <i>S. aureus</i> MIC*: 0.5 mg/ml <i>K. pneumoniae</i> MIC*: 0.2 mg/ml	FAQSOI	<b>16</b>					
		Antifungal activity	<i>C. albicans</i> MIC*: 0.007 mg/ml							
		Antibacterial activity	<i>S. aureus</i> MIC*: 2 mg/ml <i>K. pneumoniae</i> MIC*: 0.01 mg/ml <i>G<sup>-</sup> E. coli</i> MIC*: 0.2 mg/ml			FAQSIC	<b>16</b>			
		Antifungal activity	<i>C. albicans</i> MIC*: 0.15 mg/ml							
		Antibacterial activity	<i>G<sup>-</sup> E. coli</i> MIC*: 2.5 mg/ml					FAQSOI	<b>16</b>	
		Antibacterial activity	<i>S. aureus</i>							

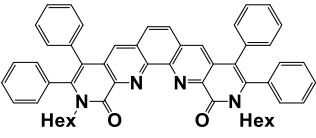
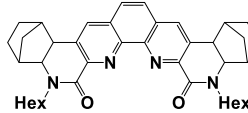




			Antifungal activity	MIC*: 0.5 mg/ml <i>K. pneumoniae</i> MIC*: 0.25 mg/ml <i>G<sup>-</sup> E. coli</i> MIC*: 2.5 mg/ml  <i>C. albicans</i> MIC*: 0.007 mg/ml		
S E N S I N G          S E	 <b>L<sup>22</sup></b>	$\{[\text{Cd}(\text{L}^{22})(\text{H}_2\text{O})_2](\text{SUL})(\text{H}_2\text{O})_{0.5}\}_n$ <b>(97)</b>	Molecular sensor	Selective for Cu <sup>+2</sup> ions	ATONEE	<b>73</b>
	 <b>L<sup>24</sup></b>		Lanthanide extraction (in acetonitrile)	log β* = 6 to 7.19 (La to Gd) log β* = 6.86 to 7.65 (Tb to Lu)	-	<b>19</b>
	 <b>L<sup>25</sup></b>		Lanthanide extraction (in acetonitrile)	log β* (in dry acetonitrile) log β = 6.11- 6.82 (La to Gd), and log β = 6.33 - 7.1 (Tb to Lu) log β* (in wet acetonitrile) log β = 4.5 - 4.87 (La to Gd) log β = 4.5 - 5.08 (Tb to Lu)	-	<b>19</b>
	<b>L<sup>26</sup></b>			<i>D</i> * values:	-	<b>30</b>

<p>N S I N G</p> <p>S E N S I N G</p>	 <p style="text-align: center;"><b>L<sup>26</sup></b></p>		<p>Extraction of f-elements (Am/Eu) in meta-nitrobenzotrifluoride / HNO<sub>3</sub></p> <p>Extraction of Am and other lanthanides in meta-nitrobenzotrifluoride / HNO<sub>3</sub></p> <p>Extraction of Transition metal ions and lead</p> <p>Ionophore material in potentiometric sensor</p>	<p>~ 500 (for Am in 3M HNO<sub>3</sub>); ~ 15 (for Eu in 3M HNO<sub>3</sub>).</p> <p><i>SF</i>*: 4.4 - 48 (from La-Gd); 69 - 277 (from Tb- Lu). <i>SN</i>*: 1.8 (for Am); 1.5 - 2 (from La-Lu).</p> <p>‘<i>D</i>’* for Cd ~ 2000 in 3M HNO<sub>3</sub>, Cu ~ 950 in 3M HNO<sub>3</sub>, Zn ~ 12 in 3M HNO<sub>3</sub>, and Pb ~ 55 in 3M HNO<sub>3</sub></p> <p>Nernst Response: For Zn(II) - 22 mV/dec; Cu(II) - 23 mV/dec; Cd(II) - 27 mV/dec; Pb(II) - 26 mV/dec using NPOE plasticizer. For Zn(II) - 23 mV/dec; Cu(II) - 26 mV/dec; Cd(II) - 20 mV/dec; Pb(II) - 34</p>	-	
---	--	--	--	---	---	--

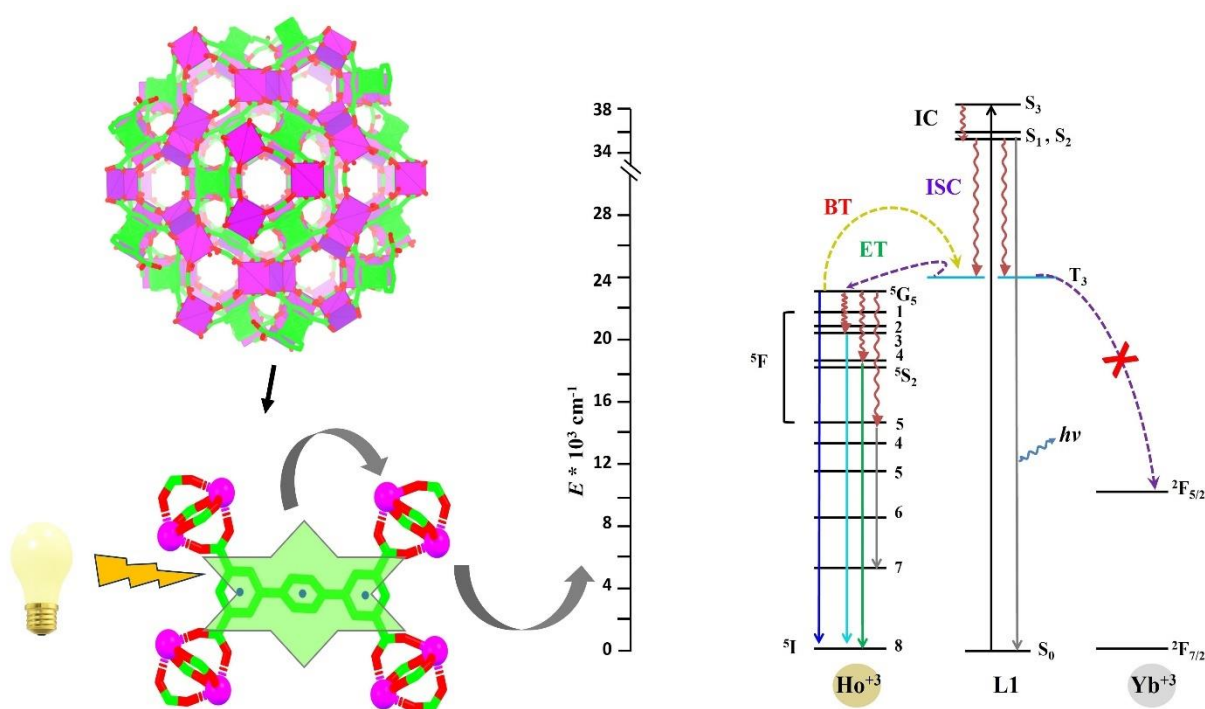
S E N S I N G	 <p style="text-align: center;"><b>L<sup>27</sup></b></p>	<b>L<sup>27</sup></b>	Extraction of U(VI) using ionic liquid-based extraction system	<p>mV/dec using 2F2N plasticizer.</p> <p>‘D’* and ‘E’* values:  <b>L<sup>27</sup></b>/[C<sub>4</sub>mim][NTf<sub>2</sub>] system (no acid), <math>D = 32</math> and <math>E = 94.1\%</math>.  <b>L<sup>27</sup></b>/[C<sub>4</sub>mim][NTf<sub>2</sub>] system in 3M HNO<sub>3</sub>, <math>D = 87</math> and <math>E = 97.8\%</math>  <b>L<sup>27</sup></b>/[C<sub>4</sub>mim][PF<sub>6</sub>] system (no acid), <math>D = 25</math> and <math>E = 92.6\%</math>.  <b>L<sup>27</sup></b>/[C<sub>4</sub>mim][PF<sub>6</sub>] system in 3M HNO<sub>3</sub>, <math>D = 44</math> and <math>E = 95.7\%</math>.</p>	-	<b>31</b>
			Extraction of Th(VI), U(VI) and Am(III) in the presence of Eu(III)	<p><math>D^*</math> values in 1M HNO<sub>3</sub>:  <math>D = 205</math> for Th (VI),  <math>D = 25</math> for U (IV),  <math>D = 6</math> for Am (III),  <math>D = 0.09</math> for Eu (III).  <math>SF^*</math> values values in 1M HNO<sub>3</sub> :  <math>SF = 2277</math> for Th (VI),  <math>SF = 277</math> for U (IV),  <math>SF = 67</math> for Am (III).</p>	-	<b>31</b>

S E N S I N G	 <p style="text-align: center;"><b>L<sup>32</sup></b></p>  <p style="text-align: center;"><b>L<sup>33</sup></b></p>	<b>L<sup>32</sup> and L<sup>33</sup></b>	Extraction of Am(III) in the presence of Eu(III)	<p>Stability constant values -  <math>\log \beta = 4.68</math> for U (IV)  <math>\log \beta = 4.39</math> for Th (VI)  <math>\log \beta = 3.81</math> for Eu (III)</p> <p><math>D^*</math> and <math>SF^*</math> values in 3 M HNO<sub>3</sub> for 1 mM <b>L<sup>32</sup></b>:  <math>D = &gt; 1000</math> for Am (III), and  <math>D = &gt; 1000</math> for Eu (III).  <math>SF_{Am/Eu}</math> - n.a.  For 1 mM <b>L<sup>33</sup></b> :  <math>D = 3525</math> for Am (III), and <math>D = 17.2</math> for Eu (III).  <math>SF_{Am/Eu}</math> - 211  <math>D^*</math> and <math>SF^*</math> values in 0.3 M HNO<sub>3</sub> using 1 mM <b>L<sup>33</sup></b> :  <math>D = 2132</math> for Am (III), and <math>D = 4.1</math> for Eu (III).  <math>SF_{Am/Eu}</math> - 516</p>	-	<b>33</b>
---------------------------------	---	--	--	--	---	-----------

\*  $g$  – Isotropic factor;  $J$  - Magnetic exchange coupling parameter;  $|D|$  – Zero field splitting;  $\Delta/\lambda$  - Spin-orbit coupling parameters;  $n_2$ - Refractive Index;  $\chi^{(3)}$  – Third order susceptibility;  $\gamma$  – Hyperpolarizability;  $\alpha_2$  - NLO absorption coefficient;  $\log \beta$  - Stability constant;  $D$  - Distribution ratio;  $SF$  - Separation factor;  $SN$  – Solvation number;  $E$  - Extraction efficiency; MIC – Minimum Inhibitory concentration;  $IC_{50}$  – Half-maximal inhibitory concentration.

## Chapter – 5

# Isomorphous Ln-MOFs with Terphenyl Tetracarboxylate Struts: Single Crystal, Photophysical and Theoretical Studies



## 5.1 Introduction

Trivalent lanthanide ions display sharp lines ( $\text{FWHM} < 10 \text{ nm}$ ) radiative emissions in the range  $0.2\text{-}5 \mu\text{m}$  in ultra-violet, visible, and near infrared regions of electromagnetic spectra owing to  $4f$ -emissions, which involves  $^{2S+1}L_J$  levels. Rationale for this is that  $4f$  electrons are efficiently screened from perturbing lattice effects by outermost  $5s$  and  $5p$  orbitals and thus they do not participate in the bonding. Hence the excited levels of  $\text{Ln(III)}$  ions are more electronic in nature that results in minimized non-radiative relaxation and sharp emissions. Another reason is that the electronic rearrangement of the  $4f$  orbitals and hence chemical bond lengths of  $\text{Ln(III)}$  ions in their complexes are not affected by electronic transitions following the absorption of light. Thus, the bond lengths remain the same in the excited state too, which according to Franck Condon principles leads to small Stokes shifts. These spectral features endow lanthanide containing materials/formations remarkable photo-physical properties to be used in bioimaging systems, lamp phosphors, sensing, biological assays, electro luminescent materials in LEDs and optical fibres. In reality,  $f$ - $f$  transitions of  $\text{Ln}^{+3}$  ions are forbidden (absorption coefficient  $0.1\text{-}10 \text{ M}^{-1}\text{cm}^{-1}$ ) due to the same parity of the excited states involved, thus direct excitation of these ions is insufficient, and according to Laporte's parity rule these transitions do not occur via ED (electric dipole) mechanism. On the contrary, sensitization of  $\text{Ln(III)}$  emissions (absorption coefficient  $10^4\text{-}10^5 \text{ M}^{-1}\text{cm}^{-1}$ ) could be triggered by organic ligand bearing light harvesting chromophores *via antenna effect* where energy absorbed by the ligand molecule is channeled onto the excited states of  $\text{Ln(III)}$  ion via intramolecular energy transfer. In literature, there are several reports on photoluminescence studies of discrete molecular edifices comprising different ligand designs and lanthanide ions, which illustrate high intrinsic quantum yields.

In the present work, we have synthesized four isomorphous  $\text{Ln-MOFs}$  comprising terphenyl tetracarboxylic acid and  $\text{Er(III)}$ ,  $\text{Ho(III)}$ ,  $\text{Tm(III)}$  and  $\text{Yr(III)}$  ions, respectively, and studied their photoluminescence in solid state suspension in DMF.



Emission spectra of these compounds was acquired in a solid-state suspension and the mechanism of the energy transfer from L1 to the resonating levels of Ln(III) ions using TDDFT calculations performed on L1 molecule. In addition, the effect of the solvent has also been discussed on the emission spectra. To the best of our knowledge such type of study using a solid-state suspension has never been done and reported before.

## 5.2 Objective

- Synthesis of isomorphous Ln-MOFs using terphenyltetracarboxylate struts.
- Structure elucidation of Ln-MOFs using single crystal X-ray diffraction.
- Photoluminescence studies.
- DFT studies on the ligand molecule to explain the L→M electron transfer mechanism.

## 5.3 Authors contribution

- Conceptualization – Love Karan Rana
- Data curation – Love Karan Rana, Alborz Bavandsavadkouhi, and Thierry Maris (SCXRD Data)
- Formal analysis – Love Karan Rana
- Investigation – Love Karan Rana
- Methodology – Love Karan Rana
- Supervision – Love Karan Rana
- Visualization – Love Karan Rana
- Writing - original draft – Love Karan Rana
- Writing – review and editing – Love Karan Rana and Prabhjot Kaur

## 5.4 Article

# Isomorphous Ln-MOFs with Terphenyl Tetracarboxylate Struts: Single Crystal, Photophysical and Theoretical Studies

Love Karan Rana<sup>1\*</sup>, Prabhjyot Kaur<sup>1</sup>, Alborz Bavandsavadkouhi<sup>1</sup>, and Thierry Maris<sup>2</sup>

<sup>1</sup>*Département de Chimie, Biochimie et physique, Institut de Recherche sur l'Hydrogène,  
Université du Québec à Trois-Rivières, Trois-Rivières, Québec, G9A 5H7, Canada*

<sup>2</sup>*Institut national de la recherche scientifique, Montréal, Québec, H2X 1E3, Canada*

\*To whom correspondence should be addressed. E-mail: [love.karan@uqtr.ca](mailto:love.karan@uqtr.ca)

## 1.1 Introduction

Trivalent lanthanide ions are fascinating in the context of their radiative emissions in ultra-violet, visible, and near infrared regions of electromagnetic spectra [1]. The  $4f$  emissions involving  $^{2S+1}L_J$  levels appear as sharp lines (FWHM < 10 nm) in the range 0.2-5  $\mu\text{m}$  [2] because the  $4f$ -electrons are efficiently screened from perturbing lattice effects by outermost  $5s$  and  $5p$  orbitals and thus they do not participate in the bonding. Hence the excited levels of Ln(III) ions are more electronic in nature that results in minimized non-radiative relaxation and sharp emissions. Another reason is that the electronic rearrangement of the  $4f$  orbitals and hence chemical bond lengths of Ln(III) ions in their complexes are not affected by electronic transitions following the absorption of light. Thus, the bond lengths remain the same in the excited state too, which according to Franck Condon principles leads to small Stokes shifts [3]. These spectral features endow lanthanide containing materials/formations remarkable photophysical properties to be used in bioimaging systems, lamp phosphors, sensing, biological assays, electro luminescent materials in LEDs and optical fibres [3]. In reality,  $f$ - $f$  transitions of  $\text{Ln}^{+3}$  ions are forbidden or have less probability to occur (absorption coefficient  $0.1$ - $10 \text{ M}^{-1}\text{cm}^{-1}$ ) because the excited states involved have the same parity thus direct excitation of these ions is insufficient, and according to Laporte's parity rule these transitions do not occur via ED (electric dipole) mechanism. On the contrary, sensitization of Ln(III) emissions (absorption coefficient  $10^4$ - $10^5 \text{ M}^{-1}\text{cm}^{-1}$ ) could be triggered by excitation of electronic levels of coordinated organic ligand bearing light harvesting chromophores. This phenomenon is called

*antenna effect* where energy absorbed by the ligand molecule is channeled onto the excited states of Ln(III) ion via intramolecular energy transfer [4]. It is indeed the electronic field generated by the ligand that weakly influences the electrons of 4f shell, resulting in the spectral fine structures due to the relaxation in the rules governing electronic transitions. In literature, there are several reports on photoluminescence studies of discrete molecular edifices comprising different ligand designs and lanthanide ions, which illustrate high intrinsic quantum yields [5a].

In the present work, we have synthesized four isomorphous Ln-MOFs comprising terphenyl tetracarboxylic acid and Er(III), Ho(III), Tm (III) and Yr(III) ions, respectively, and studied their photoluminescence in solid state suspension in DMF. The selection of the metal-ligand in the synthesis of metal-organic hybrid system (Ln-MOFs) containing Ln(III) ions with photoluminescent properties and the photosensitizer ligand molecule containing fluorophore moieties in the fabrication of photoluminescent materials was based merely on the implementation of the design principles of “crystal-engineering” [5b]. Although the total solvent accessible void volume in these MOFs represent 50% of the unit cell volume as calculated using PLATON [6], the irregular and partial coordination of the solvent molecules and formate ions to Ln(III) ions has led to impenetrable hybrid frameworks with small open channels. Moreover, except Er-MOF these compounds lose their framework integrity in other solvents upon solvent exchange. The Er-MOF is stable in ACN, and it has shown exchange of DMF molecules by ACN but this compound is decomposed on desolvation/activation. This behavior of MOFs has eliminated the option of their adsorption studies, thus restricting ourselves to study photoluminescence. In literature, majority of the photoluminescence studies concerning coordination complexes of lanthanides were done in solid state at low temperature, under nitrogen environment. Thus, the effect of air and the solvent molecules on the spectra have not been studied or reported. In the current study, we have analyzed the emission spectra of these compounds in a solid-state suspension using 1mg of the sample of Ln-MOF to avoid and/or minimize scattering. In addition, we have used TDDFT calculations performed on **L1** molecule to investigate the energy of its triplet state ( $T_1$  level) and used this information to propose the mechanism of energy transfer from **L1** to the resonating levels of Ln(III) ions. In addition, the effect of the solvent has also been discussed on the emission spectra. To the best

of our knowledge such type of study using a solid-state suspension has never been done and reported before.

## 1.2 Materials and methods

All chemicals *viz.* [1,1':4,1'']Terphenyl- 3,3'',5,5''-tetracarboxylic acid, and  $M(\text{NO}_3)_3 \cdot 5\text{H}_2\text{O}$  salts ( $M = \text{Ho(III)}, \text{Er(III)}, \text{Tm(III)}, \text{and Yb(III)}$ ) were procured from Sigma-Aldrich, and were used as received. Single crystal data for compounds **1-3** was collected on sealed tube Bruker APEX-II CCD equipped with graphite monochromator, while diffraction data for compound **4** was collected on Rigaku New Gemini, four- circle diffractometer equipped with fine-focus sealed X-ray tube and EosS2 detector with CCD plate. IR spectra were collected on Nicolet IS 10 Smart FT-IR spectrometer in the range  $600\text{--}4000\text{ cm}^{-1}$ . The solid-state UV-visible spectra were recorded on a Varian Cary 300 Bio UV-Vis spectrophotometer at 298 K using raised-angle transmittance apparatus. Photoluminescence studies were performed on a Cary spectrofluorometer using a UV-quartz cuvette with a 1 cm path length.

## 1.3 Single crystal structure solution

The structures of compounds **1-4** were solved using SHELXT [7] structure solution program and refined with the SHELXL [8] refinement package using least squares minimization in a graphical user interphase Olex2 [9]. All non-hydrogen atoms were refined anisotropically. The hydrogen atoms were refined isotropically on calculated positions using a riding model with their Uiso values constrained to 1.5 times the Ueq of their pivot atoms for terminal  $\text{sp}^3$  carbon atoms and 1.2 times for all other carbon atoms. Refinement of the crystal data of compounds **1-4** has shown two solvent accessible voids per unit cell, containing unresolved electron density corresponding to 1470 electrons in a volume of  $4716\text{ \AA}^3$ . The solvent mask routine of Olex 1.5 software is used to account for this electron density, which is consistent with the presence of  $5.5[\text{C}_3\text{H}_7\text{NO}]$  and  $1.833[\text{H}_2\text{O}]$  per unit cell. Crystallographic information for all compounds is shown in Table S1-S4.

## 1.4 DFT Calculations

The geometry of the ligand is optimized using a range-separated hybrid function  $\omega\text{B97X-D3}$  with atom-pairwise dispersion correction D30 [10]. In addition, def2-SVP function is used as a basis set [11]. The information about the excited states of the ligand is obtained from TD-DFT calculations performed using  $\omega\text{B97X-D3}$  method with a polarized triple-zeta basis set def2-TZVP [11]. Besides, an auxiliary basis set def2/J is used in DFT calculations for the

numerical precision [12]. The geometry optimization and the TD-DFT calculations are performed considering the effect of the DMF molecules using a CPCM model [13].

### 1.5 Synthesis of compounds 1-4

All the complexes were synthesized solvo-thermally using 5 mL dram glass vials. A mixture of **L1** (0.01 g, 0.025 mM) and  $\text{Ho}(\text{NO}_3)_3 \cdot 5\text{H}_2\text{O}$  salt (0.043 g, 0.099 mM) for **1**,  $\text{Er}(\text{NO}_3)_3 \cdot 6\text{H}_2\text{O}$  (0.044 g, 0.099 mM) for **2**,  $\text{Tm}(\text{NO}_3)_3 \cdot 6\text{H}_2\text{O}$  (0.044 g, 0.099 mM) for **3** and,  $\text{Yb}(\text{NO}_3)_3 \cdot 6\text{H}_2\text{O}$  (0.044 g, 0.099 mM) for **4** in four different 5 mL dram capped vials each containing 3 mL DMF was sonicated for 15 minutes at room temperature. Next, 800 equivalents of formic acid were added to each vial, which were then sealed and placed in a convection oven for 1 day at 110 °C. Next day, rhombus-shaped pale yellow and light pink crystals for compounds **1** and **2**, respectively, and colourless crystals for compounds **3** and **4**, respectively, were obtained. All the samples were washed with fresh DMF for at least four times before doing further analysis. Yield for **1**: 0.0072 g (72%). Anal. Calc. for **1**,  $\text{C}_{270}\text{H}_{234}\text{N}_{18}\text{O}_{126}\text{Ho}_{18}$  (%): C, 37.22; H, 2.71; N, 2.99. Found: C, 36.88; H, 2.89; N, 2.67. FT-IR ( $\text{cm}^{-1}$ ), (Figure S1, Table S5) 1650 (s), 1556 (m), 1450 (w).

Yield for **2**: 0.0079 g (79%). Anal. Calc. for **2**,  $\text{C}_{270}\text{H}_{234}\text{N}_{18}\text{O}_{126}\text{Er}_{18}$  (%): C, 37.13; H, 2.70; N, 2.90. Found: C, 36.93; H, 2.80; N, 2.76. FT-IR ( $\text{cm}^{-1}$ ), (Figure S1, Table S5) 1652 (s), 1726 (w), 1445 (w) 1545 (m).

Yield for **3**: 0.0079 g (79%). Anal. Calc. for **3**,  $\text{C}_{270}\text{H}_{234}\text{N}_{18}\text{O}_{126}\text{Tm}_{18}$  (%): C, 36.89; H, 2.49; N, 2.88. Found: C, 36.44; H, 2.58; N, 2.78. FT-IR ( $\text{cm}^{-1}$ ), (Figure S1, Table S5) 1449 (w), 1550 (m), 1651 (s).

Yield for **4**: 0.0079 g (79%). Anal. Calc. for **4**,  $\text{C}_{270}\text{H}_{234}\text{N}_{18}\text{O}_{126}\text{Yb}_{18}$  (%): C, 36.59; H, 2.67; N, 2.84. Found: C, 36.23; H, 2.82; N, 2.79. FT-IR ( $\text{cm}^{-1}$ ), (Figure S1, Table S5) 1619 (s), 1654 (s), 1450 (b).

### 1.6 Crystal structure of compound 1

The compounds **1-4** are isomorphous in nature thus only the molecular structure of compound **1** will be discussed here. The ORTEP representations of the rest of the complexes are shown in the supplementary information (Figure S2-S4). The compound **1** is crystallized in the space group  $\bar{R}32$  of a trigonal crystal system. The asymmetric unit of **1** shows a half  $\text{Ho}(\text{III})$  ion present on the  $c$ -glide, which is coordinated to a half **L1** ion, a half formate ion, and a DMF molecule (Figure 1a). The **L1** molecule contains an inversion centre present on the central

phenyl ring and a mirror/glide plane that divides it into two symmetrical halves. In addition, the glide plane passing through the carbon atom of formate ion cuts it into two equal halves. A unique binuclear paddlewheel unit  $[\text{Ho}_2(\text{COO})_4]$  containing two Ho(III) ions connected by four carboxylate ions is generated by the mirror plane around Ho(III) ions (Figure 1b), which is connected to adjacent binuclear units by bridging formate and  $\mu_8\text{-L1}$  ions in a three-dimensional framework (Figure 1c).

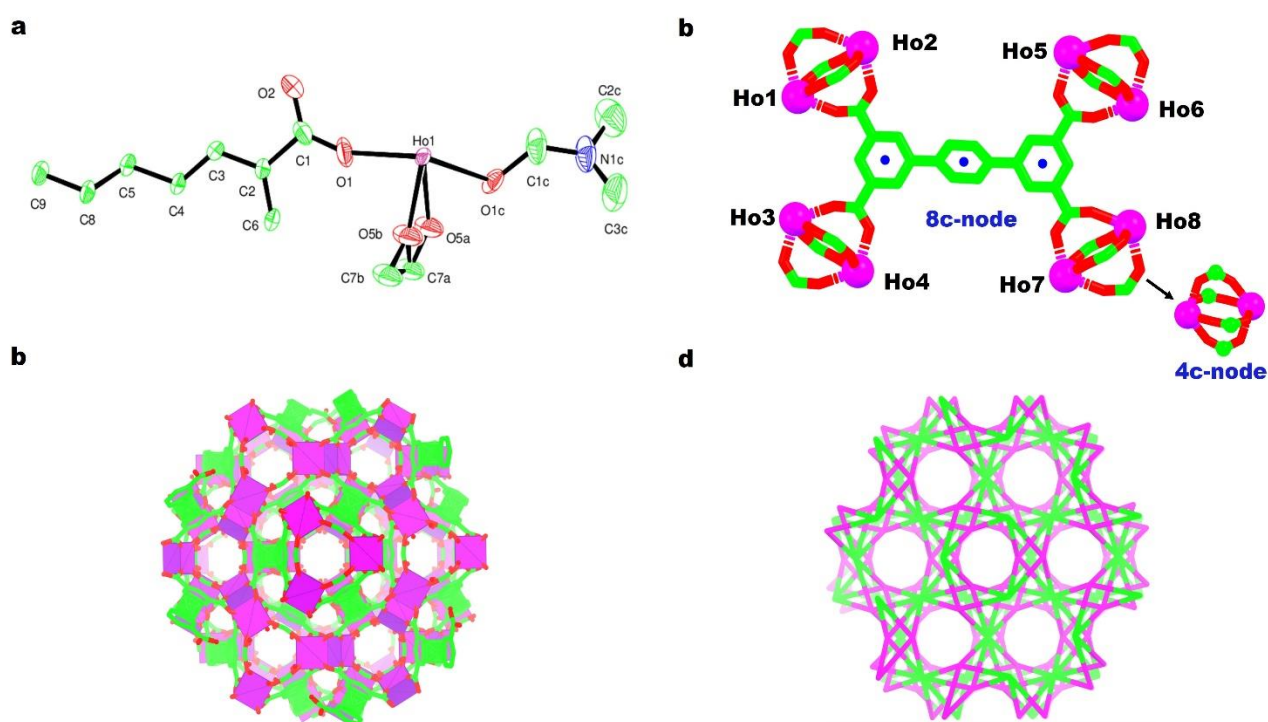


**Figure 1-** View of a) ORTEP representation of asymmetric unit of compound 1, b) Ho(III) paddlewheel units connected by bridged  $\mu_8\text{-L}$  ions to form 4- and 8c nodes, 3) polyhedral presentation of three dimensional framework down the *c*-axis, and d) 4,8-c bi-nodal net.

Topological analysis [14] on the framework illustrates a 4,8-c bi-nodal net of the type 4,8T24 with stoichiometry  $(4\text{-c})_2(8\text{-c})$  (Figure 1b-1d). The point symbol for the net is  $\{4^4.6^{16}.8^8\}\{4^6\}_2$ .

## 1.7 Coordination geometry of Ln(III) ions

In the compounds **1-4**, Ln(III) ions are 6-coordinated and there are five different coordination geometries possible for the same coordination number as shown in the Table 1. We have investigated the degree of distortion of the coordination polyhedra from the ideal polyhedron

geometry for Ho(III) complex only using SHAPE software [15]. The  $\text{LnO}_6$  coordination polyhedron of **1** shows a slight deviation from trigonal prism geometry (0.31, close to zero) than other possible polyhedral geometries (Table 1). Thus, the coordination geometry of Ho(III) ions can be best described as a trigonal prism. The continuous shape measures (CShM's) values illustrating the offset of atomic positions with respect to reference polyhedra are given in Table 1. Smaller the CShM's value, more the closeness of a given coordination geometry to an ideal polyhedra.

**Table 1**– Coordination geometries and CShM's values.

Label	Shape	CShM's value
HP-6	Hexagon	32.86
PPY-6	Pentagonal pyramid	16.28
OC-6	Octahedron	16.88
TPR-6	Trigonal prism	0.31
JPPY-5	Johnson pentagonal pyramid (J2)	20.14

## 1.8 FT-IR spectra

The vibrational spectra further confirm the presence of all functional groups as observed in the crystal structure. The vibrational frequencies at  $1430\text{ cm}^{-1}$  ( $\nu(\text{O-H})_{\text{Bending}}$ ),  $1726\text{ cm}^{-1}$  ( $\nu(\text{C=O})_{\text{Stretching}}$ ), and  $3330\text{ cm}^{-1}$  ( $\nu(\text{O-H})_{\text{Stretching}}$ ) could be assigned to the free carboxylic groups of **L1** molecule. In all lanthanide complexes, the  $\nu(\text{C=O})$  stretching frequency of the **L1** is shifted towards lower energy illustrating the deprotonation and the coordination of the carboxylic groups (carboxylate) to the lanthanide ions (Figure S1, Table S5). Furthermore, the  $\nu(\text{C=O})$  stretching frequencies at around  $1550\text{ cm}^{-1}$  for the complexes **1-4** show the presence of coordinated DMF molecules (Figure S1, Table S5).

## 1.9 Photophysical studies

Photophysical properties of the compounds are studied using a clear solution of **L1** and solid suspensions of compounds **1-4** in DMF. The electronic spectra of **L1** shows absorption in the range 250-330 nm with  $\lambda_{\text{max}}$  at 286 nm (Figure S5). Compounds **1** and **2** show absorption in the range 250-480 nm with the  $\lambda_{\text{max}}$  red shifted ( $\sim 18\text{ nm}$ ) relative to **L1** at 304 nm and 301 nm, respectively (Figure S5). While compound **3** shows maximum absorption at the same position



as **L1**, the  $\lambda_{\text{max}}$  is slightly red shifted ( $\sim 2$  nm) in compound **4** (Figure S5). The UV-Vis spectra clearly indicate that the absorption in the compounds **1-4** is dominated by the **L1** molecule. Thus, one can assume that the **L1** molecule could potentially sensitize the Ln(III) emissions in the compounds **1-4**.

The emission spectra of **L1** and compounds **1-4** were recorded using an excitation frequency ( $\lambda_{\text{ex}}$ ) of 260 nm for **L1** and all compounds. The **L1** molecule shows a broad emission band in the range 340-460 nm with the  $\lambda_{\text{max}}$  at around 375 nm assigned to intra-ligand ( $S_0 \leftarrow S_1$ ) transition (Figure 2). The photoluminescence spectra of the compounds **1-4** display characteristic 4f ion-based emissions in the ultraviolet and visible regions demonstrating that the **L1** molecule behaves as a photosensitizer (Figure 2). Moreover, the emission spectra of the compounds **1-4** also illustrate that the energy transfer from the ligand ( $T_1$ ) to the emitting levels of Ln(III) ion is not complete and is hampered by the ligand-based emissions as apparent from the weak ligand-centered emissions in the compounds **1** and **2**, and a broad emission spanning the range 330-475 nm in the compounds **3** and **4** (Figure 2). Such a phenomenon suggests that although **L1** can sensitize the Ln(III) emissions, it is not an ideal ligand to be considered as a perfect “antenna.”

It is worth noting that weak emission bands corresponding to the transitions *viz.*  $^5I_8 \leftarrow ^5G_5$  (430 nm) and  $^5I_8 \leftarrow ^5F_3$  (487 nm) of Ho(III) ion [16],  $^4I_{15/2} \leftarrow ^4G_{11/2}$  (392 nm),  $^4I_{15/2} \leftarrow ^4F_{3/2}$  (440 nm) and  $^4I_{15/2} \leftarrow ^4F_{7/2}$  (465 nm) of Er(III) ion [17a], and  $^3H_6 \leftarrow ^1G_4$  (470 nm) transition of Tm(III) fall in the emission range of the ligand [18] (Figure 2), suggesting a poor/partial sensitization of 4f emissions in the respective complexes.

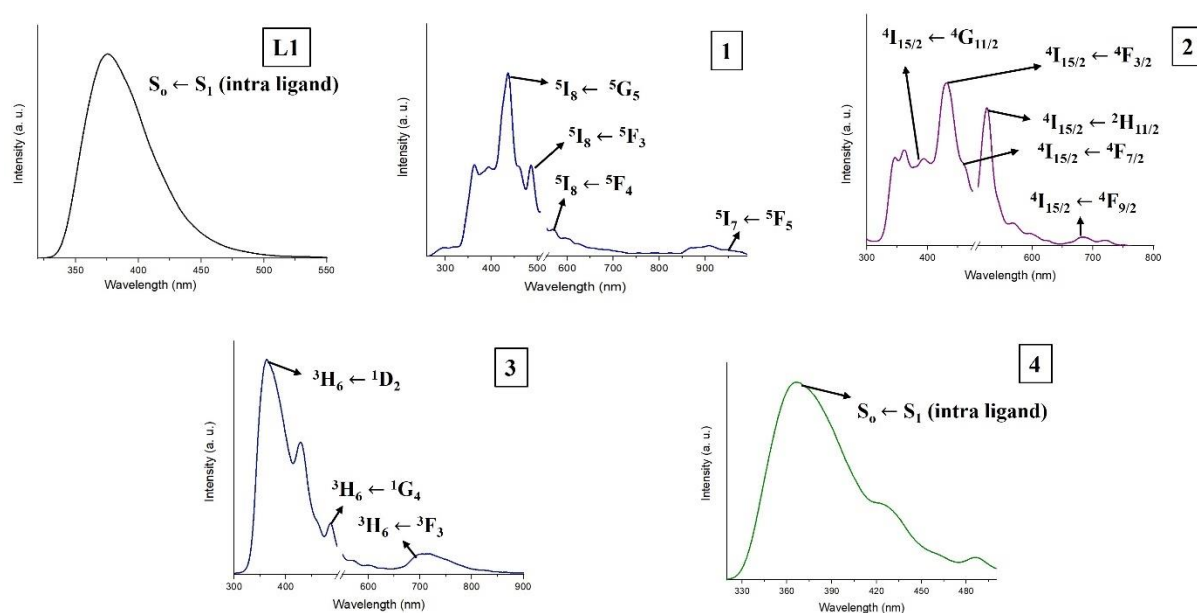


**Figure 2**– Showing characteristic emission bands of **L1** and Ln(III) ions in all complexes.

Note: The emission spectra were taken in solid-state suspension in DMF using excitation wavelength ( $\lambda_{\text{ex}}$ ) of 260 nm.

Besides, an emission band (compared to **L1**) in visible region corresponding to  $^4I_{15/2} \leftarrow ^2H_{11/2}$  (524 nm) transition and low intensity bands related to  $^4I_{15/2} \leftarrow ^4F_{9/2}$  (670 nm) transition of Er(III) ion [19],  $^5I_8 \leftarrow ^5F_4$  (552 nm) of Ho(III) and  $^3H_6 \leftarrow ^3F_3$  (690 nm) of Tm(III) ions are also observed [20] (Figure 2). In addition, the Ho(III) complex has also shown a weak NIR transition  $^5I_7 \leftarrow ^5F_5$  at 980 nm [21] (Figure 2). The low intensity of this bands can be attributed to the non-radiative vibrational deactivation by high energy C-H and C=O vibrations and/or overtones of DMF molecules, both coordinated as well as in the solution [4].

In general,  $f$ - $f$  transitions usually lead to sharp peaks but in the present study they are broad and obtuse, which can be attributed to two reasons – 1) hindered electron transfer from T<sub>1</sub> (**L1**) to  $4f$ -levels of Ln(III) [13] owing to back-transfer, and 2) the legible emission spectra for all compounds was obtained using emission monochromator slit-width at 10 mm, which might led to broadening of  $f$ - $f$  emissions as spiked nature of these transitions are more susceptible to bandwidth of spectrophotometer [22-23].

### 1.10 Excited states of the ligand (**L1**)

The information about the excited triplet and singlet states of **L1** is obtained from time-dependent density functional theory (TDDFT) (Table S6 and S7). The absorption spectra

obtained from TDDFT calculations illustrate that the  $S_0 \rightarrow S_3$  transition at 260 nm (theoretically ~259 nm) has the higher transition probability and hence higher oscillator strength (~1) as shown in Table 2, thus the excitation of the compounds **1-4** at this wavelength promotes the electron transfer to the emitting levels of respective lanthanide ions resulting in characteristic emission peaks.

**Table 2-** Excited singlet states and their oscillator strengths.

Singlet state	Wavelength	Oscillator Strength ( $f_{osc}$ )	Energy in $cm^{-1}$	Characteristic of the emission	$\pi \rightarrow \pi^*$ band character
Singlet 1	266.6	0.0409	37511.7	Non-radiative	Weak
Singlet 2	266.3	0.0013	37547.7	Non-radiative	Very Weak
Singlet 3	259.2	<b>0.9800</b>	<b>38992.8</b>	<b>Radiative</b>	<b>Strong</b>

For the optimal electron transfer according to Dexter and Sato [24] the energy gap between the lowest triplet state of the ligand and the emitting levels of the Ln(III) ion should lie in the range 2500-3500  $cm^{-1}$  [17]. On the contrary, the energy gap < 2500  $cm^{-1}$  weakens the lanthanide emission owing to back transfer of energy from Ln(III) ions to the ligand [25].

Inferences regarding the energy transfer process can be made by referring to the energy gap (' $\Delta$ ', in  $cm^{-1}$ ) between  $T_1$  state of the ligand (obtained theoretically) and the resonance energy levels of respective lanthanide ions (Table 3). In all compounds tabulated below (including complex **4**), the energy gap between  $T_1$  state and resonating levels of Ln(III) is less than 3500  $cm^{-1}$  which facilitates the forward energy transfer from the ligand to Ln(III) ions. Thus, back energy transfer is prevalent in these complexes resulting in weak and obtuse Ln(III) emissions, and broad ligand emissions. Once the ligand (L1) is excited to its higher excited states, relaxation to its lower energy singlet states ( $S_n \rightarrow S_1$ ) takes place by non-radiative decay pathways (internal conversion), and then to its lower energy triplet state ( $S_1 \rightarrow T_1$ ) by inter-system crossing [26]. This low energy triplet state is responsible for the photosensitization of Ln (III) ions, resulting in their characteristic emissions (Figure 3 and S6). In case of complex **4**, the dominant ligand emission could be attributed to the wide energy gap between the lower triplet state of the ligand and resonating level of yttrium ion.

**Table 3** – Energy difference ( $\Delta$ , in  $\text{cm}^{-1}$ ) of the emissive states of Ln(III) ions with respect to triplet state of **L1**.

Compound	Triplet state energy of ligand L1 (cm <sup>-1</sup> )	Excited states energies of Ln(III) ion (cm <sup>-1</sup> )	Energy difference ( Δ ) (cm <sup>-1</sup> )	Emitting level of Ln(III) ion
1	24661.6	23255.8	1405.8	<sup>5</sup> G <sub>5</sub>
		20533.9	4127.7	<sup>5</sup> F <sub>3</sub>
		18115.9	6545.7	<sup>5</sup> F <sub>4</sub>
2		25510.2	848.6	<sup>4</sup> G <sub>11/2</sub>
		22727.3	1934.3	<sup>4</sup> F <sub>3/2</sub>
		21505.4	3156.2	<sup>4</sup> F <sub>7/2</sub>
		19084.1	5577.5	<sup>2</sup> H <sub>11/2</sub>
3		27934	3272.4	<sup>1</sup> D <sub>2</sub>
		21277	3384.6	<sup>1</sup> G <sub>4</sub>
		14492.8	10169	<sup>3</sup> F <sub>3</sub>
4		10449.3	14212.3	<sup>2</sup> F <sub>5/2</sub>

Another reason for broad ligand emission in the compounds **1-4** could be ascribed to lower energy gap of  $1181 \text{ cm}^{-1}$  between singlet states i.e  $\text{S}_3$  (excited) and  $\text{S}_1$  (lower excited) (Table S8) than singlet-triplet state. Hence, there is a high probability of  $\text{S}_1 \rightarrow \text{S}_0$  transition to occur alongside the inter-system crossing (ISC,  $\text{S}_1 \rightarrow \text{T}_1$ ), which leads to the emission from the ligand. The tentative mechanism of the electron transfer and the photoluminescence is summarized in Figure 3 and Figure S6.

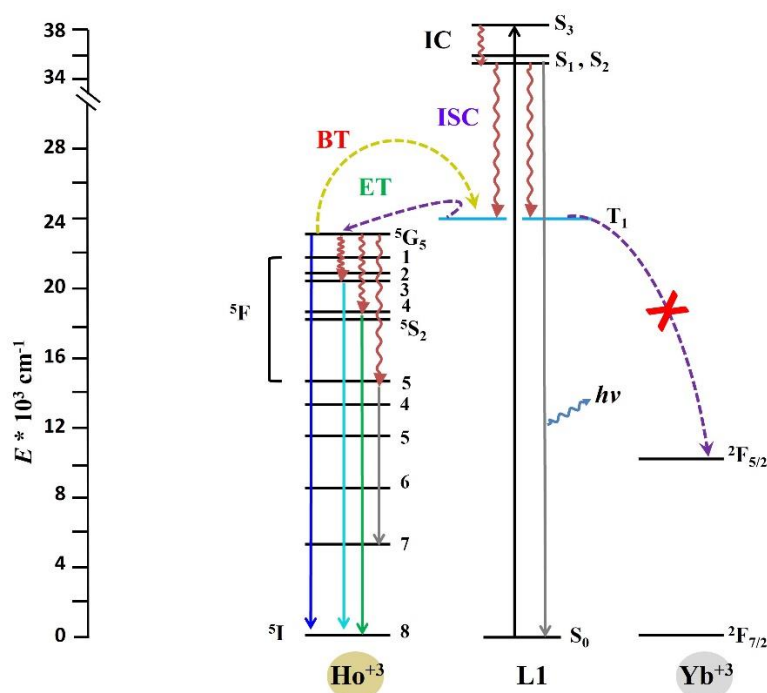


**Figure 3** – Simplified scheme showing the photosensitization of Ln(III) ions in the compounds **1** and **4** by **L1** molecule ( $T_1$  state), with associated photophysical phenomena. (IC – Internal conversion, ISC – Inter-system crossing, ET – Energy-transfer/Photosensitization, BT- Back transfer of energy)

### 1.11 Chromaticity coordinates and colour purity

The color coordinates of all compounds including the ligand are obtained using CIE 1931 color space as defined by the International Commission on Illumination (Figure 4) and are tabulated in the Table 3.

**Table 3** - Colour coordinates of compounds **1-4**.

Compound	CIE x	CIE y
L	0.1589	0.03482
1	0.19437	0.23463
2	0.19848	0.24618
3	0.18043	0.21768
4	0.15116	0.15385

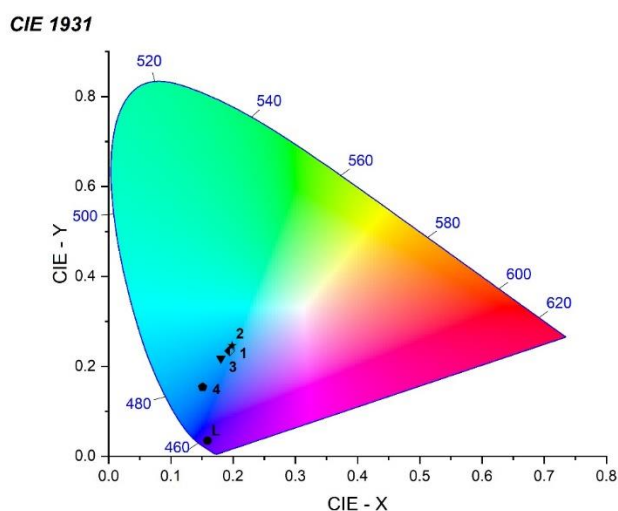


**Figure 4-** Colour coordinates of compounds **1-4** in the CIE 1931 color space.

Besides, the colour purity of the compounds **1-4** relative to 1931 CIE, standard illuminant C (0.3101, 0.3162) was computed using the following equation [27]:

$$\text{Colour purity} = \frac{\sqrt{(x_s - x_i)^2 + (y_s - y_i)^2}}{\sqrt{(x_d - x_i)^2 + (y_d - y_i)^2}} \times 100\%$$

where  $(x_s, y_s)$  represent the coordinates of the entire spectrum,  $(x_d, y_d)$  are the color coordinates of the dominant wavelength, and  $(x, y)$  are the coordinates of standard illuminant C of white light. The color purity of the complexes relative to  $\lambda_{\text{max}}$  (dominant wavelength) of characteristic emission bands are tabulated in the Table 4.

**Table 4** – Colour coordinates and colour purity of compounds **1-4**.

Compound	$x_d$ dominant	$y_d$ dominant	Purity (%)	$\lambda_{\text{max}}$ Dominant wavelength	$x_s$	$y_s$	Standard illuminant C (x,y)
<b>1</b>	0.169	0.007	45.27	431.6	0.180	0.234	(0.310, 0.316)
	0.114	0.826	28.16	525	0.180	0.234	
<b>2</b>	0.169	0.007	45.27	430	0.180	0.234	
<b>3</b>	0.175	0.005	52.22	360	0.169	0.209	
	0.064	0.217	66.78	486	0.169	0.209	
<b>4</b>	0.175	0.005	97.9	366	0.160	0.020	

## 1.12 Conclusion

In this research work, we have synthesized four isomorphous Ln-MOFs using a tethering ligand terphenyl tetra-carboxylic acid. These compounds are synthesized solvothermally and their molecular structures are elucidated by single crystal X-ray diffraction. Besides, different analytical techniques such as IR, UV-Vis and CHN elemental analysis are used to characterize these compounds. Although they are porous (void volume is 50% of the unit cell volume as calculated using PLATON), the loss of framework integrity upon activation precludes their use for adsorption studies. Thus, we have focused on the study of their room temperature photophysical properties. We have used solid state suspension of compounds **1-4** for the acquisition of the emission spectra in a nitrogen free environment. The results obtained illustrate that the **L1** molecule could potentially sensitize the characteristic Ln(III) emissions in all compounds except compound **4**, owing to large energy gap between  $T_1$  state of **L1** and emissive state of Yb(III) ( $^2F_{5/2}$ ). Furthermore, the back energy transfer from Ln(III) ions to **L1** hampers the efficiency of the sensitization process, which also suggests that **L1** it is not an ideal ligand to be considered as a perfect “antenna”.

## 1.13 References

1. B. Golesorkhi, L. Guénée, H. Nozary, A. Fürstenberg, Y. Suffren, S. V. Eliseeva, S. Petoud, A. Hauser, Claude Piguet, *Chem. Eur. J.*, 2018, **24**, 13158.
2. B. D. Bartolo, O. Forte (eds.), *Advances in Spectroscopy for Lasers and Sensing*, 403.
3. (a) J. C. G. Bünzli, C. Piguet, *Chem. Soc. Rev.*, 2005, **34**, 1048, (b) P. Sutar, V. M. Suresh, T. K. Maji, *Chem. Commun.*, 2015, **51**, 9876, (c) P. A. Tanner, *Chem. Soc. Rev.*, 2013, **42**, 5090. (d) M. C. Heffern, L. M. Matosziuk, T. J. Meade, *Chem. Rev.*, 2014, **114**, 4496; (e) J. C. G. Bünzli, *Chem. Rev.*, 2010, **110**, 2729, (f) S. V. Eliseeva, J. C. G. Bünzli, *New J. Chem.*, 2011, **35**, 1165. (g) C. Lincheneau, F. Stomeo, S. Comby, T. Gunnlaugsson, *Aust. J. Chem.*, 2011, **64**, 1315, (h) S. J. Bradberry, A. J. Savyasachi, M. Martinez-Calvo, T. Gunnlaugsson, *Coord. Chem. Rev.*, 2014, **273-274**, 226.
4. J. C. G. Bünzli, *Coord. Chem. Rev.*, 2015, **293-294**, 19.
5. S. Comby, J. C.G. Bünzli, *Handbook on the Physics and Chemistry of Rare Earths Vol. 37* edited by K.A. Gschneidner, Jr., J. C.G. Bünzli and V. K. Pecharsky, and b) G. R. Desiraju, *J. Am. Chem. Soc.* 2013, **135**, 9952.

6. A. L. Speck, *Acta Cryst.*, 2009, **D65**, 148.
7. G.M. Sheldrick, *Acta Cryst.*, 2015, **A71**, 3.
8. G.M. Sheldrick, *Acta Cryst.*, 2015, **C71**, 3.
9. O. V. Dolomanov, L. J. Bourhis, R. J. Gildea, J. A. K. Howard, H. Puschmann, *J. Appl. Cryst.* 2009, **42**, 339.
10. a) J. D, Chai, M. H. Gordon, *Phys. Chem. Chem. Phys.*, 2008, **10**, 6615, b) S. Grimme, J. Antony, S. Ehrlich, H. Krieg, *J. Chem. Phys.*, 2010, **132**, 154104.
11. F. Weigend and R. Ahlrichs, *Phys. Chem. Chem. Phys.*, 2005, **7**, 3297.
12. F. Weigend, *Phys. Chem. Chem. Phys.*, 2006, **8**, 1057.
13. A. V. Marenich, C. J. Cramer, D. G. Truhlar, *J. Phys. Chem. B*, 2009, **113**, 6378.
14. V. A. Blatov, A.P. Shevchenko, D.M. Proserpio, *Cryst. Growth Des.*, 2014, **14**, 3576.
15. M. Pinsky, D. Avnir. *Inorg. Chem.*, 1998, **37**, 5575.
16. V. Singh, P. Kumari, S. J. Dhoble, P. Holli, H. Jeong, V. Koteswararao, *Optik*, 2021, **242**, 167223.
17. a) W.T. Chen, *Journal of chemical research*, 2020, **44**, 727 b) B. Xu, B. Yan, *Spectrochim Acta A* 2007, **66**, 236.
18. E. W. Barrera, M. C. Pujol, J. J. Carvajal, X. Mateos, Rosa Solé, J. Massons, A. Speghini, M. Bettinelli, C. Cascales, M. Aguiló, F. Díaz, *Phys. Chem. Chem. Phys.*, 2014, **16**, 1679.
19. S. K. Taherunnisa, D. V. Krishna Reddy, T. S. Rao, K. S. Rudramamba, Y. A. Zhydashchevskyy, A. Suchocki, M. Piasecki, M. Rami Reddy, *Optical Materials*:X, 2019, **3**, 1000034.
20. R. Krishnan, J. Thirumalai, *New J. Chem.*, 2014, **38**, 3480.
21. F. A. Mautner, F. Bierbaumer, R. Vicente, S. Speed, A. Tubau, M. F. Bardia, R. C. Fischer, S. S. Massoud, *Molecules*, 2022, **27**, 1129.
22. Y. Hasegawa, Y. Kitagawa, T. Nakanish, *NPG Asia Materials*, 2018, **10**, 57.
23. J. Andres, and A. S. Chauvin, *Molecules*, **2020**, **25**, 4022;
24. a) S. Sato, M. Wada, *Bull. Chem. Soc. Jpn.*, 1970, **43**, 1955, b) D. L. Dexter, *J. Chem. Phys.* 1953, **21**, 836.
25. A) D. D. Morgan, D. Warshawsky, T. Atkinson, *Photochem. Photobiol.* 1977, **25**, 31, b) K. Palewska, H. Chojnacki, *Mol. Cryst. Liq. Cryst.* 1993, **229**, 31.
26. D. Frackowiak, *Journal of Photochemistry and Photobiology B: Biology*, 2, 1988, 399



27. H. L. Li, Z. L. Wang, S. J. Xu and J. H. Hao, *J. Electrochem. Soc.*, 2009, **156**, J112.

## **Chapter- 6**

### **Conclusion and Future work**

## 6. Conclusion and Future work

The research work described here involves the synthesis of transition and rare earth metal ions-based MOFs for metal-ion sensing and photoluminescence applications, respectively. We have applied the ideology of “Crystal engineering” right from the design of the ligand molecules to the selection of metal ions and synthesis of coordination compounds for desired applications. In this respect we have synthesized a mixed ligand Co-MOF to explore its metal ion sensing potential. While both ligands contribute to build a three-dimensional coordination network, the symmetrical dicarboxamide ligand was chosen to facilitate  $M^{+n} \cdots O_{amide}$  and  $M^{+n} \cdots \pi$  interactions with analyte ions from secondary amide group (-CONH-) and naphthalene ring in the sensing experiments. The amide oxygen has shown interactions with almost all metal ions chosen for fluorescence titrations owing to its borderline character due to the presence of double bond C=O (according to HSAB principles). Thus, we have discussed the sensing ability of Co-MOF in context of sensitive detection because it was impossible to obtain selectivity using this system. In addition, a Zn-MOF with interesting three-dimensional framework synthesized using mixed ligand strategy is not used in sensing studies due to the absence of a single/stable fluorescence emission.

In another research work, we tried to replace the dicarboxamide ligand as discussed above with its positional isomer differing in the position of pyridine ring relative to the amide moiety (third in the former and fourth in the later) to see any variation in the framework structure using Co(II), Ni(II), Cu(II) and Zn(II) metal ions. Only one-dimensional structures were obtained with Co(II), Cu(II) and Zn(II) ions. The SCXRD diffraction studies reveal that these compounds are isostructural. In addition, the chemical state identification of the metal ions and the information on the different chemical environments of the elements viz. C, N, O and Cl in the complexes are investigated by XPS analysis. Furthermore, DFT calculations are performed on the ligand and complexes to see the orbitals composition of ground and excited states. Also, the total energy ( $E_{Total}$ ) of metal ligand coordination bond in the complexes is calculated and its decomposition into different energies is done. These results are in good agreement with the crystallographic metal-ligand bond distances and also show that the metal-ligand bond is shorter in the copper complex than in the other compounds, as expected due to Jahn-Teller distortions.

Apart from the metal-ion sensing, we have synthesized isomorphous lanthanide MOFs (Ln-MOFs) using a symmetric terphenyl tetracarboxylic acid ligand to study their luminescence properties. The photoluminescence studies illustrate that although the ligand molecule can potentially sensitize the characteristic emissions of the respective Ln(III) ions, it cannot be used as an “antenna” molecule owing to ligand centered emissions and back transfer of energy. Furthermore, the mechanism of the electron transfer from the ligand to Ln(III) is explained with the aid of TDDFT calculations done on the ligand molecule. Apart from the luminescence studies, the colour coordinates and colour purity of the Ln-MOFs has also been discussed.

Finally, the review article included in the thesis discusses the coordination chemistry of the metal-complexes of tertiary carboxamide ligands with pendent pyridine rings. In this work, we have compiled the development made in this very class of the ligands right from the beginning until present by summarising only those coordination complexes and pertinent crystal structure parameters whose crystal structures have been reported in crystal structure database (CSD). To make the database search easy for the readers we have also included the CCDC codes of the complexes. Interesting molecular designs of the ligands have made them appealing in the synthesis of coordination compounds of diverse architectures. In addition, the applications of the coordination compounds of these ligands, and some ligand molecules have shown have been reviewed thoroughly in this article.

In future, we are more interested in selective than sensitive detection of toxic metal ions, and for this we will fabricate fluorescent sensors containing phenanthroline and imidazolidine-2-thione anchor moieties with thioamide linkages for the selective detection of As(III), Hg(II), Cd(II) and Pb(II) ions. Furthermore, the photophysical studies of Ln-MOFs discussed in this research work are done using solid-state suspension under nitrogen free environment and we want to analyze the photophysical properties of Ln-MOFs in the solid state under nitrogen environment to compare the differences (if any) in the Ln(III) emission spectra relative to that acquired in the solid-state suspension. Besides, our pursuit is to investigate the emission lifetimes, quantum yields, etc. associated with the Ln(III) emission. Also, TDDFT calculations will be done on the lanthanide compounds to gain deeper insight into the resonating states of **L1** and Ln(III) ions, which will then be used to explain the mechanism of energy transfer.

Along with the synthesis of the materials for sensing and photoluminescence applications, my research interest is to synthesize covalent organic frameworks (COFs) comprising triaminoheptazine (Melem) and crown-ether moieties, which will be explored as a potential electrode material and/or membrane material for battery applications. Besides, I am also interested in the synthesis of manganese based heteropoly anions for hydrogen production and/or fuel cell applications.

## 7. List of Publications

1. Facile Synthesis of isomeric Hexacyanopyridine Triphenylene Derivatives, Alborz Bavandsavadkouhi, **Love Karan Rana**, Heriniaina Randriamiharisoa, Mihela Cibian, and Benoit Daust, *ChemistrySelect*, 2025, 10, e02031.
2. Investigation of structural, optical, dielectric, and electrical properties of  $\text{NaMn}_4(\text{PO}_4)_3$  (NMP) with fillowite-type structure, Erman Eloge Nzaba Madila, Amina Lahrichi, Youness El Issmaeli, Malak Slaoui, **Love Karan Rana**, Taj-dine Lamcharfi, Adam Duong, *Journal of Molecular Structure*, 1322, 2025, 140418.
3. Fascinating Tertiary Carboxamide Ligands and Their Coordination Complexes: An account on Structural Chemistry and Practical Applications, **Love Karan Rana** and Prabhjyot Kaur (**Submitted in Coord. Chem. Rev.**)
4. Isostructural coordination polymers of tethering naphthalene anchored bis(2-methylpyridinecarboxamide) ligand, Single crystal, XPS, EDS, and Theoretical studies. **Love karan Rana**, Prabhjyot Kaur, Alborz Bavandsavadkouhi, Gurpreet Singh Selopal, and Adam Duong, *New Journal of Chemistry*, 2023, 47, 5477-5487.
5. An insight into sensitive detection of metal ions using a novel cobalt MOF: Single crystal, Photoluminescence and theoretical studies, **Love Karan Rana**, Prabhjyot Kaur, Thierry Maris, and Adam Duong, *CrystEngComm*, 2022, 24, 5460-5473.
6. A Rational Design of Microporous Nitrogen-Rich Lanthanide Metal–Organic Frameworks for  $\text{CO}_2/\text{CH}_4$  Separation, Midhun Mohan, Mohamed Essalhi, David Durette, **Love Karan rana**, Follivi kloutse Ayevide, Thierry Maris, Adam Duong, *ACS Appl. Mater. Interfaces*, 2020,12, 50619-50627.
7. Amidine/Amidinate Cobalt Complexes: One-Pot Synthesis, Mechanism, and Photocatalytic Application for Hydrogen Production, Sanil Rajak, Khaula Chair, **Love Karan Rana**, Prabhjyot kaur, Thierry Maris and Adam Duong, *Inorg. Chem.* 2020, 59, 14910-14919.
8. Intercalated 2D+2D hydrogen-bonded sheets in co-crystals of cobalt salt with 1H,1'H-[3,3']bipyridinyl-6,6'-dione, Midhun Mohan, **Love Karan Rana**, Thierry Maris, Adam Duong, *Can. J. Chem.*, 2020, 98, 5-6.

## **Annex/Appendix**

### **Supplementary Information**

## Annex 1: Supplementary Information of Article 1

### An Insight into Sensitive Detection of Metal Ions Using a Novel Cobalt MOF: Single Crystal, Photoluminescence, and Theoretical Studies

Love Karan Rana<sup>1</sup>, Prabhjyot Kaur<sup>1</sup>, Thierry Maris<sup>2</sup>, and Adam Duong<sup>1\*</sup>

<sup>1</sup>*Département de Chimie, Biochimie et physique and Institut de Recherche sur l'Hydrogène (DuongLab), Université du Québec à Trois-Rivières, Trois-Rivières, Québec, G9A 5H7, Canada*

<sup>2</sup>*Département de Chimie, Université de Montréal, Montréal, Québec, H3C 3J7, Canada*

#### Table of contents

Figure 1	Caption	Page No.
1	Comparison of PXRD pattern of asynthesized <b>1</b> and patterns recorded after exposing the MOF ( <b>1</b> ) to different metal ions solutions with the simulated pattern.	205
2	Comparison of PXRD pattern of asynthesized <b>2</b> and its simulated pattern.	206
3	Comparison of PXRD pattern of asynthesized <b>3</b> and its simulated pattern.	206
4	BFDH morphologies of <b>L1</b> , compound <b>1</b> and <b>2</b> .	207
5	<sup>1</sup> H-NMR of <b>L1</b> .	207
6	<sup>13</sup> C-NMR of <b>L1</b> .	208
7	IR spectra comparison of <b>L1</b> , <b>H2BDC</b> , <b>1</b> and <b>3</b> .	209
8	IR spectra comparison of <b>L1</b> , <b>L3</b> , and compound <b>2</b> .	210



<b>9</b>	<b>a)</b> ORTEP diagram of <b>L1</b> at 30% probability, <b>b)</b> showing dihedral angle between naphthalene and amide plane.	211
<b>10</b>	ORTEP diagram of compound <b>1</b> at 30% probability.	212
<b>11</b>	ORTEP diagram of compound <b>2</b> at 30% probability.	212
<b>12</b>	ORTEP diagram of compound <b>3</b> at 30% probability.	213
<b>13</b>	Thermal stability curve of compound <b>1</b> , <b>2</b> and <b>3</b> .	213
<b>14</b>	Electrostatic potentials mapped on electron iso-density surface at 0.01 au. MEP plot <b>a)</b> for <b>L1</b> , and <b>b)</b> compound <b>1</b> .	214
<b>15</b>	Quenching of fluorescence intensity of <b>1</b> by $\text{Cu}^{+2}$ , $\text{Fe}^{+2}$ , $\text{Pb}^{+2}$ , $\text{Cd}^{+2}$ , $\text{Co}^{+2}$ , and $\text{Cu}^{+}$ ions.	214
<b>16</b>	Emission spectra and the corresponding Stern-Volmer plots of <b>1</b> in different <b>a)</b> $\text{Ru}^{+3}$ , <b>b)</b> $\text{Fe}^{+3}$ and <b>c)</b> $\text{Hg}^{+2}$ concentrations in DMF.	215
<b>17</b>	Quenching of fluorescence of <b>1</b> by $\text{Ni}^{+2}$ , $\text{Be}^{+2}$ , $\text{Mn}^{+2}$ , and $\text{Zn}^{+2}$ ions.	216
<b>18</b>	Showing the comparison of fluorescence quenching of <b>1</b> with <b>a)</b> different Fe(III) and <b>b)</b> Cu(II) salts.	216
<b>19</b>	Illustrates negligible change in fluorescence intensity upon the addition of $\text{ClO}_4^-$ , $\text{SCN}^-$ , and $\text{Br}^-$ ions.	217
<b>Table</b>	<b>Caption</b>	
<b>1</b>	IR table	211
<b>2</b>	Pertinent atomic parameters for compound <b>1</b> , <b>2</b> , and	218

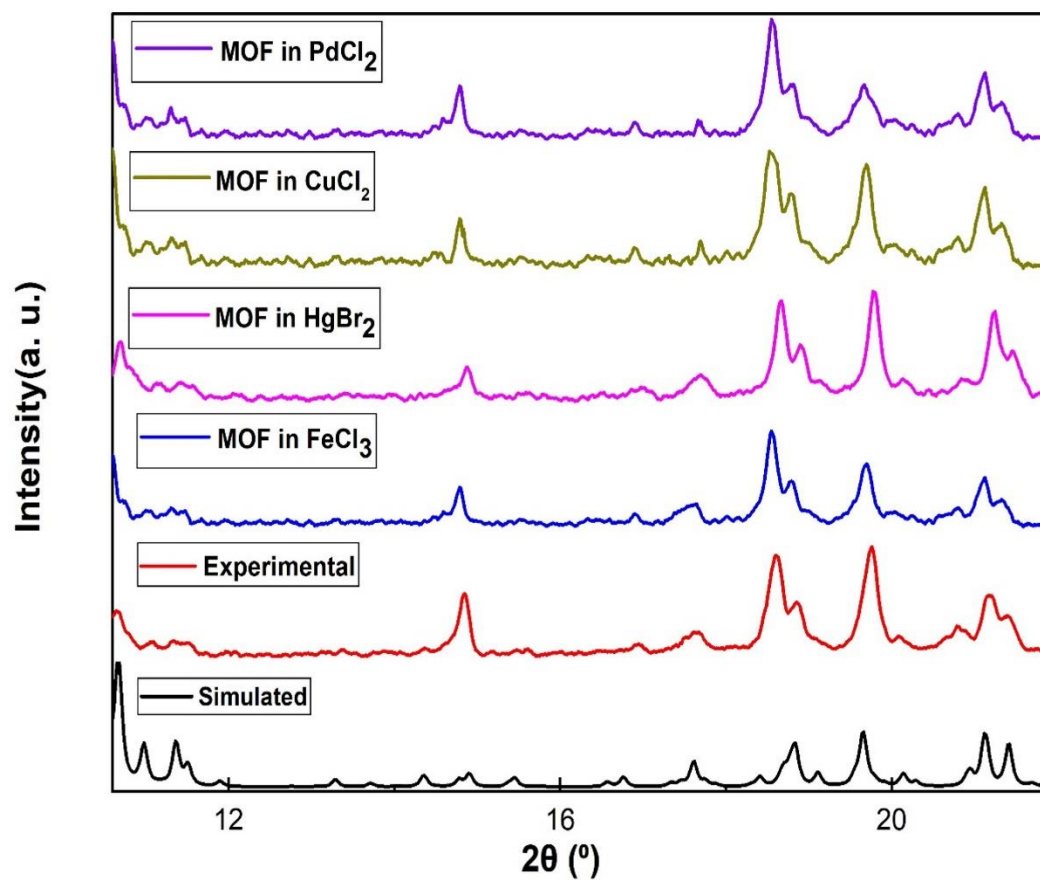


**Fig. S1-** Comparison of PXRD pattern of asynthesized compound **1** and patterns recorded after exposing **1** to different metal ions solutions with the simulated pattern.(Here compound **1** has been denoted as MOF for the illustration to be meaningful).

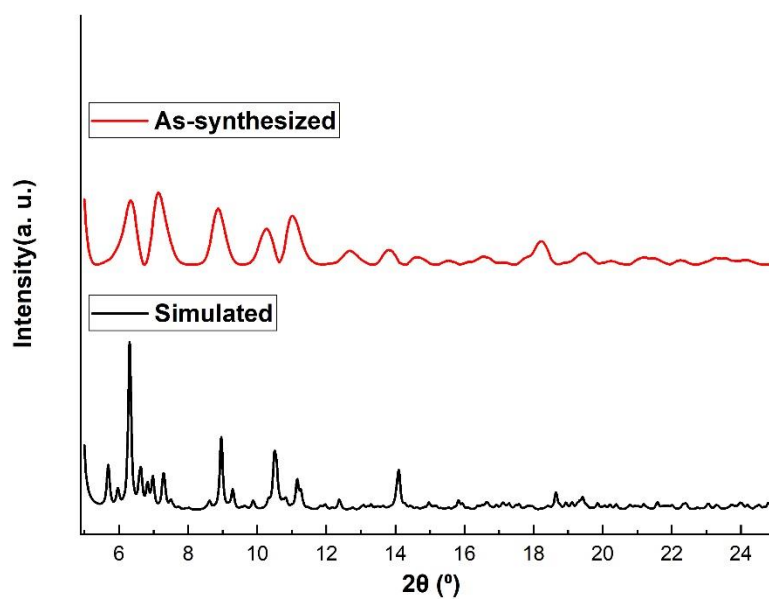


**Fig. S2-** Comparison of PXRD pattern of asynthesized compound **2** and its simulated pattern.

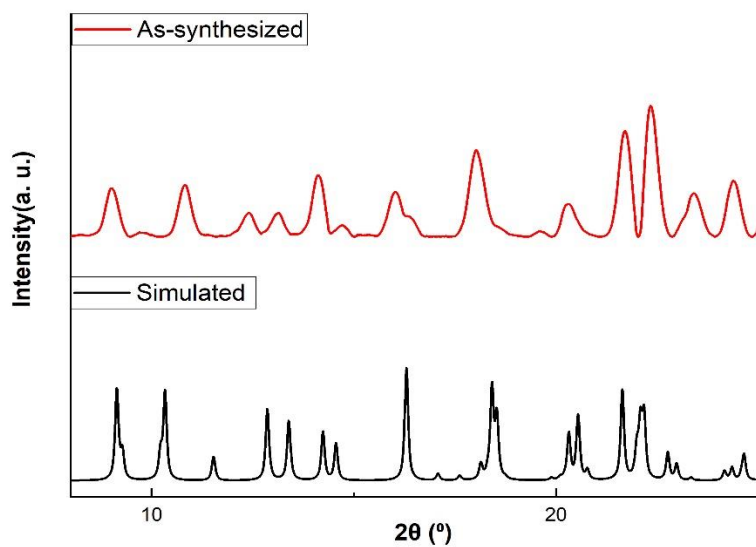


**Fig. S3-** Comparison of PXRD pattern of asynthesized compound **3** and its simulated pattern.

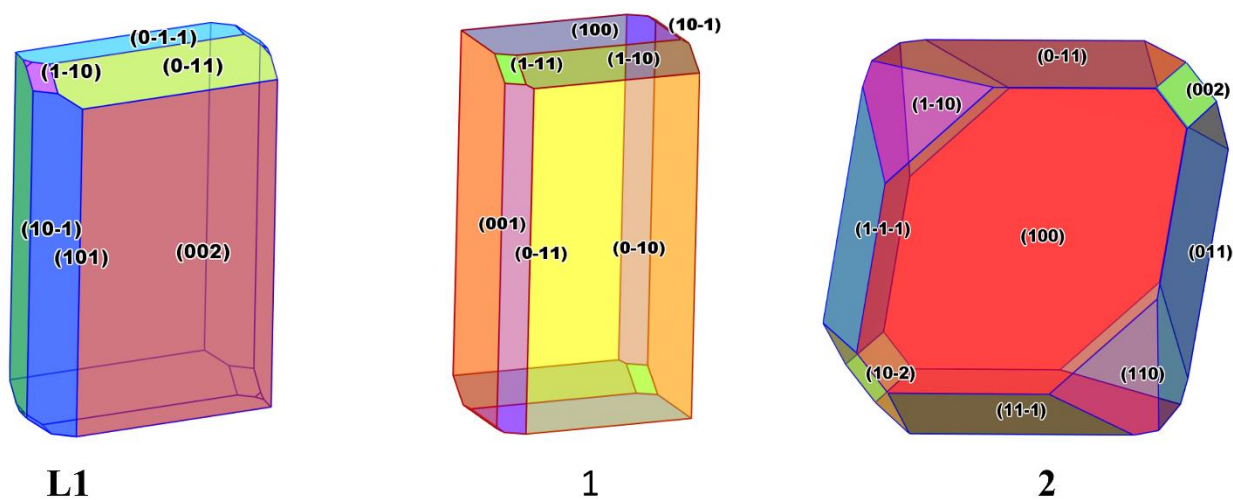


**Fig. S4-** BFDH morphologies of **L1**, compound **1** and **2**.

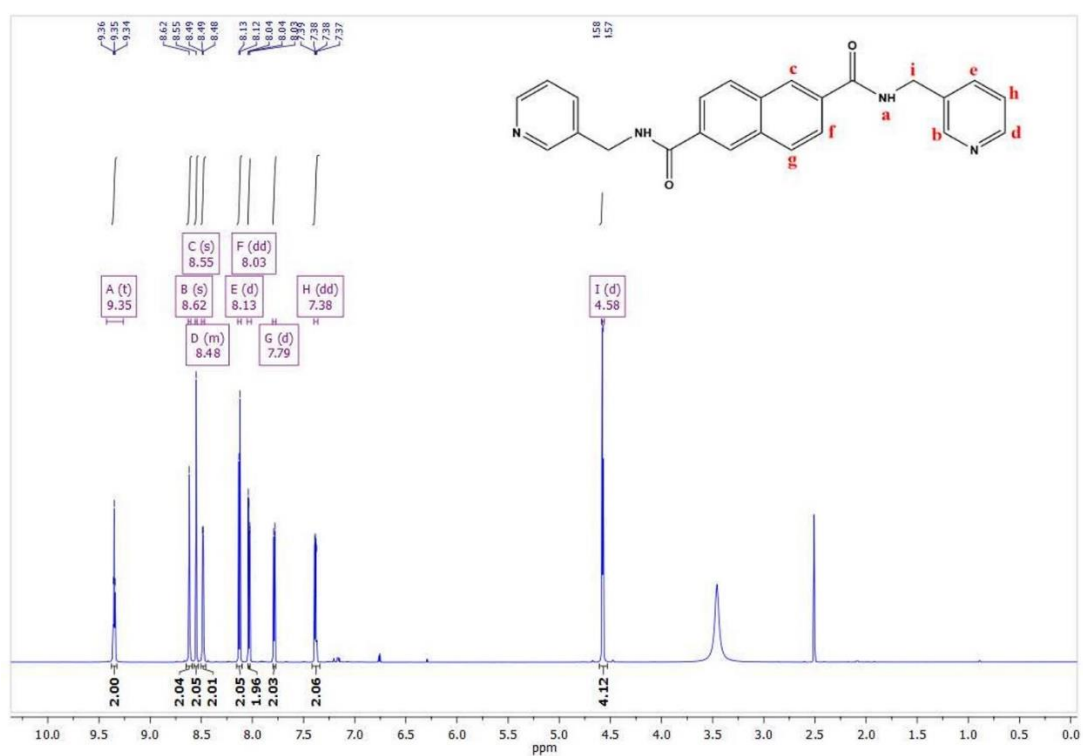


**Fig. S5**  $^1\text{H}$ -NMR of **L1**

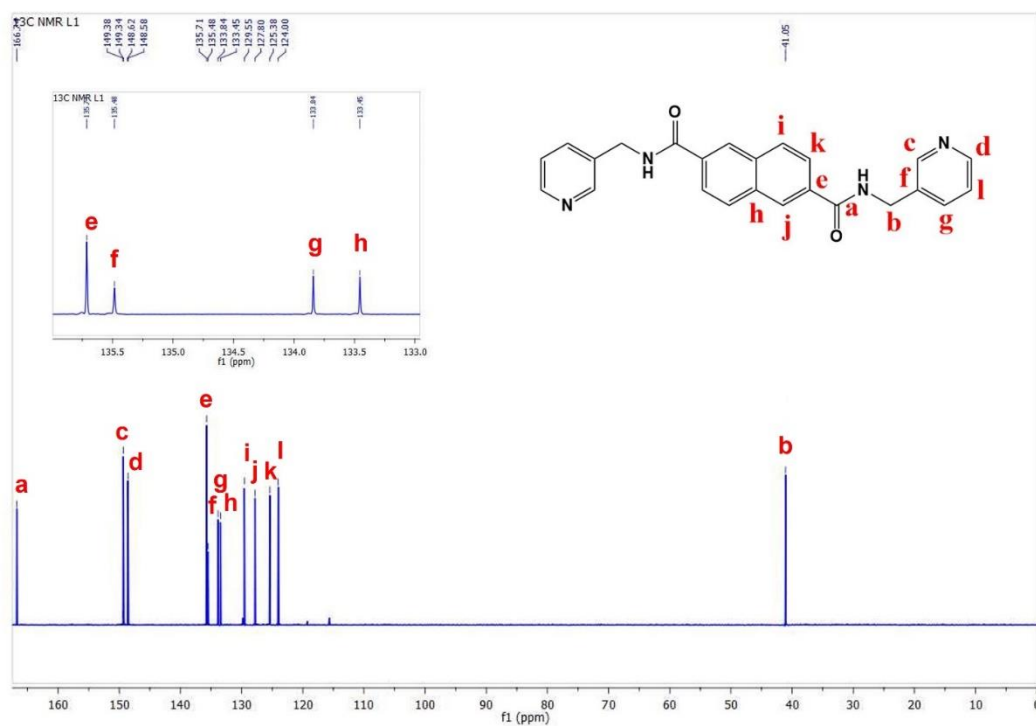


**Fig. S6**  $^{13}\text{C}$ -NMR of L1

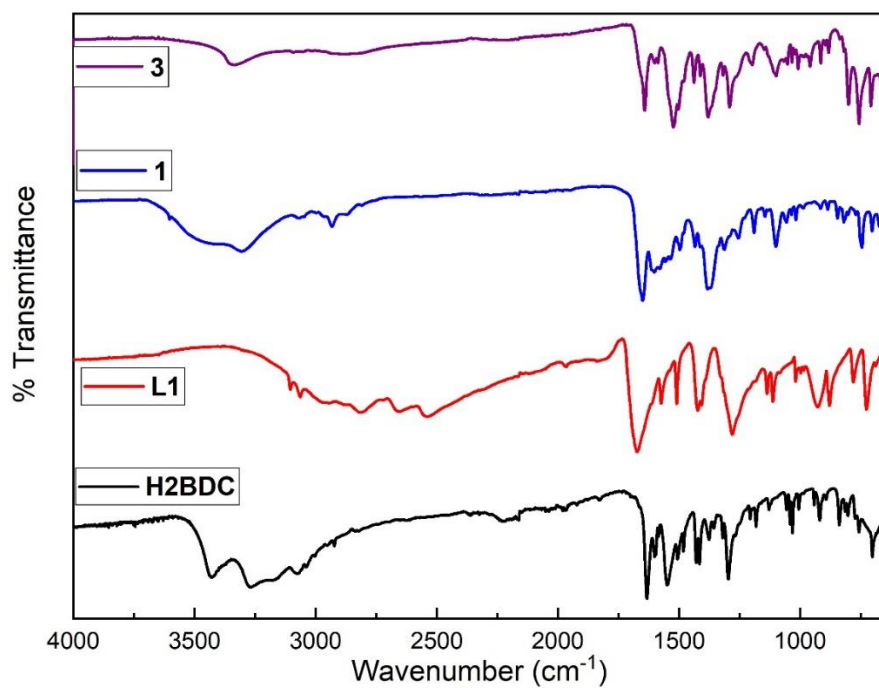


**Fig. S7** – IR spectra comparison of L1, H2BDC, and compound 1 and 3.

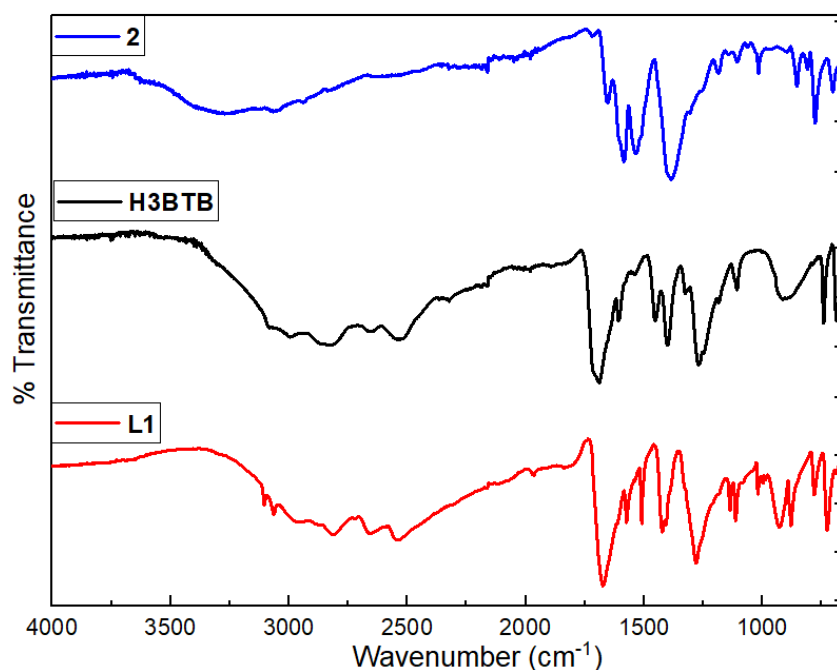
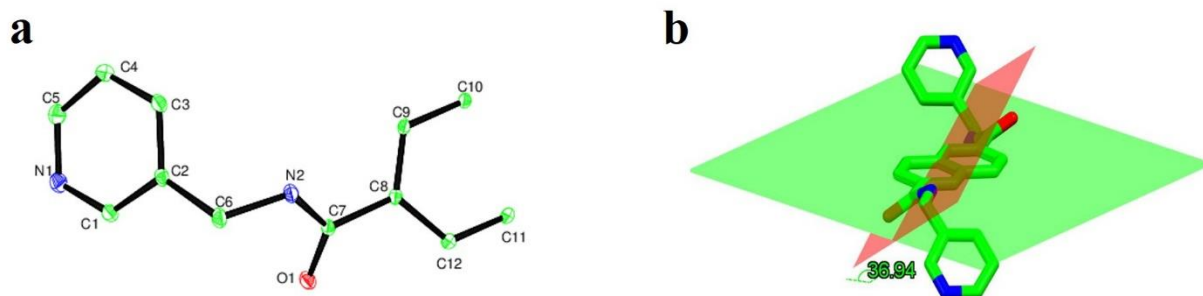


**Fig. S8** – IR spectra comparison of **L1**, **H3BTB**, and compound **2**.

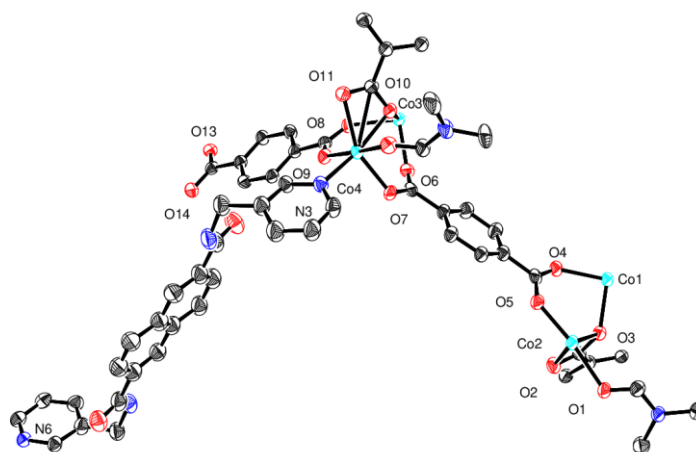
From the IR spectra (Fig. S7) it is apparent that the peak at 1509 and 1574  $\text{cm}^{-1}$  (C=N stretching, pyridine ring) in **L1** (Red graph) slightly shifted in the spectra of compound **1** (blue graph) confirming the coordination of pyridine rings to Co(II) ions, while the peak at 1673  $\text{cm}^{-1}$  corresponds to C=O stretching of **L1** (amide group, red graph) is slightly shifted in **1** (1652  $\text{cm}^{-1}$ ) which might be due to the hydrogen bonding with solvent molecules (DMF) (Fig. S7). Similarly, the peak at 1631  $\text{cm}^{-1}$  (C=O stretching, carboxylic group) in **H2BDC** (black graph) is shifted and flattened at 1616  $\text{cm}^{-1}$  in the spectra of **1** (blue graph) which confirms the coordination of carboxylic groups to Co(II) ions (Fig. S7). In the case of **3**, respective spectral peaks confirm the coordination of ligands with Ni(II). In addition, a sharp band at 1523  $\text{cm}^{-1}$  and a weak band at 1593  $\text{cm}^{-1}$ , respectively, confirms the presence both free and coordinated carbonyl groups (carboxylic) (Fig. S7). A shift of 16  $\text{cm}^{-1}$  (from 1676  $\text{cm}^{-1}$  (**L1**) to 1660  $\text{cm}^{-1}$ ) in **2** (Fig. S8) was observed for C=O (amide) stretching, which might be due the hydrogen bonding between amide group and lattice DMF molecules. Similarly, an observed shift in N-H (amide group) stretching frequency from 3104  $\text{cm}^{-1}$  (**L1**) to 3061  $\text{cm}^{-1}$  (**2**) is due to hydrogen bonding with DMF molecules.

Table S1- IR table

Complex	Group	Functionality	Wavenumber (cm <sup>-1</sup> )
<b>L1</b>	$\nu$ (N-H)	Amide	3105 (m, s)
	$\nu$ (C=O)	Amide	1667(s)
	$\nu$ (C=N)	Pyridine	1510 (m,s)
	$\nu$ (C-H) <sub>bending</sub>	Naphthalene	1417 (m, s)
<b>1</b>	$\nu$ (N-H)	Amide	3286 (b)
	$\nu$ (C=O)	Amide	1652 (s)
	$\nu$ (C=N)	Pyridine	1491 (w)
	$\nu$ (C-H) <sub>bending</sub>	Naphthalene	1378 (m, s)
	$\nu$ (C-H) Overtone	Naphthalene	2870 (w)
	$\nu$ (C-H)	Methyl group (DMF)	2929 (w)
<b>2</b>	$\nu$ (N-H)	Amide	3095 (w, b)
	$\nu$ (C=O)	Amide	1662 (m)
	$\nu$ (C=O)	Carboxylic	1590 (m, s)
<b>3</b>	$\nu$ (N-H)	Amide	3335 (b)
	$\nu$ (C=O)	Amide	1641 (m, s)
	$\nu$ (C=O) <sub>free</sub>	Carboxylic	1523 (s)
	$\nu$ (C=O) <sub>Coordinated</sub>	Carboxylic	1593 (m, w)



**Fig. S9** a) ORTEP diagram of **L1** at 30% probability, b) showing dihedral angle between naphthalene and amide plane.



**Fig. S10** ORTEP diagram of **1** at 30% probability.

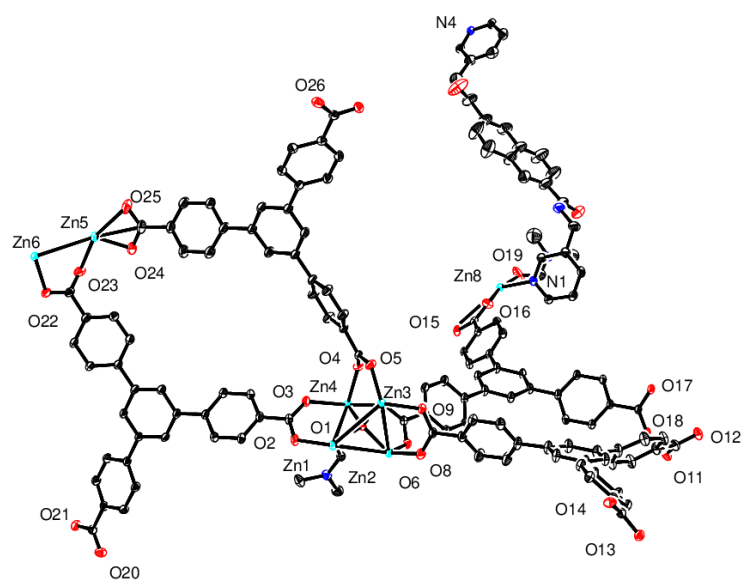


**Fig. S11** ORTEP diagram of **2** at 30% probability.



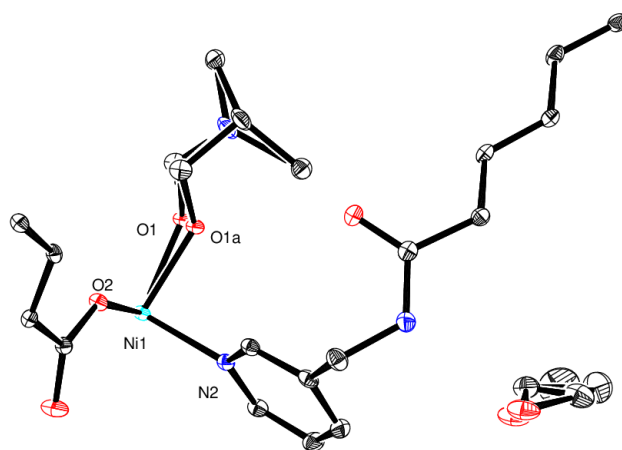


**Fig. S12** ORTEP diagram of **3** at 30% probability.

#### Thermal stability-

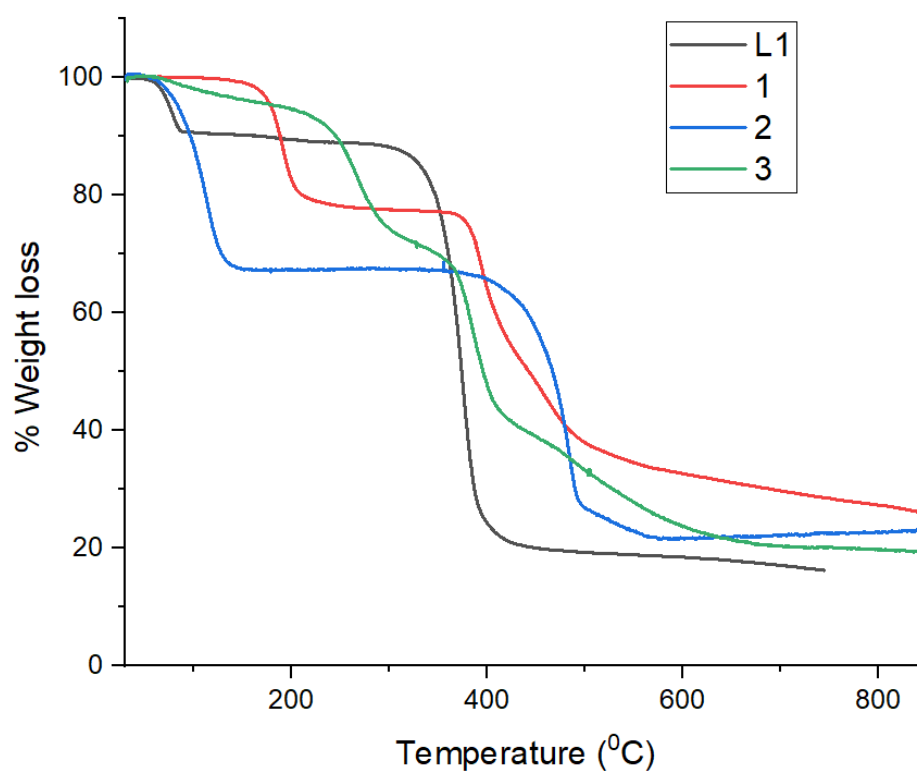


**Fig. S13** Thermal stability curves of **L1**, compound **1**, **2**, and **3**.

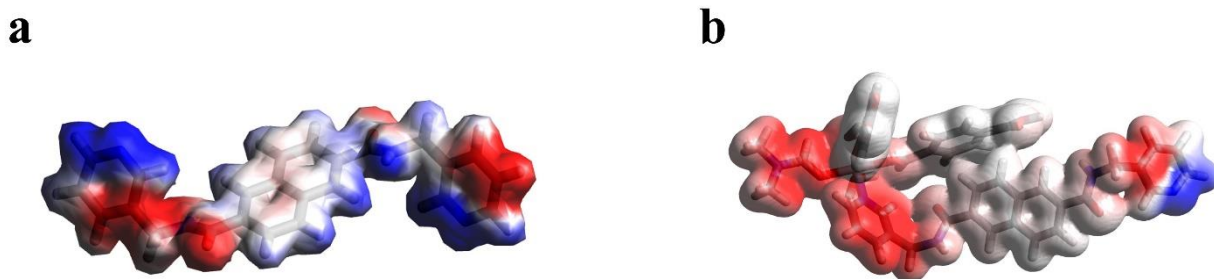


**Fig. S14** - Electrostatic potentials mapped on electron isodensity surface at 0.01 au. MEP plot a) for **L1**, and b) Co(II) complex using Avogadro software<sup>1</sup>. (RWB scheme was used, where red colour corresponds to high electron density regions and blue colour corresponds to least electron density regions)

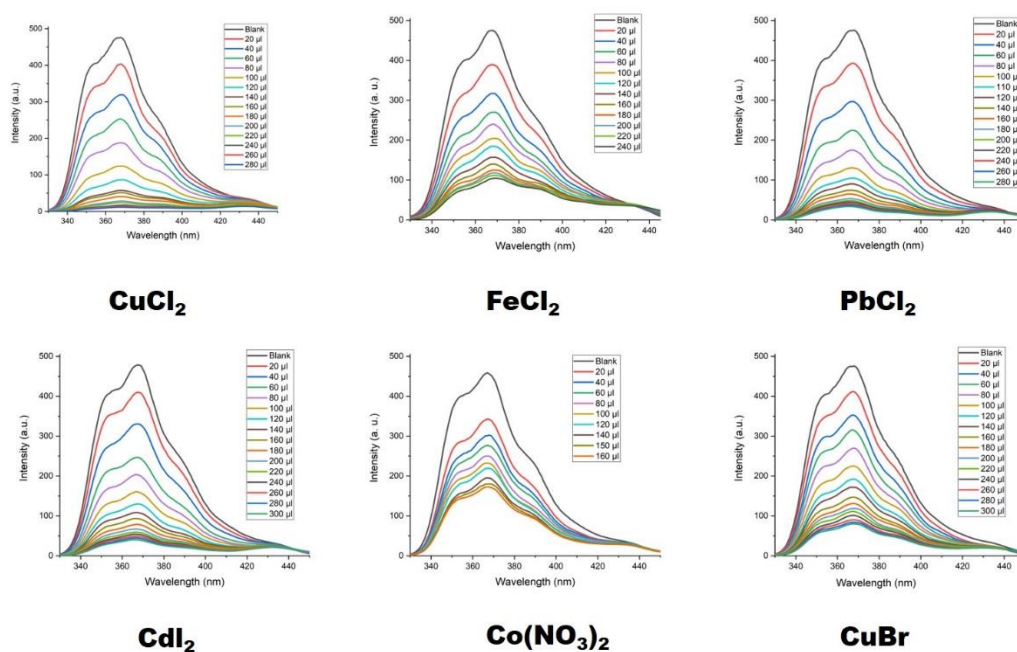


**Fig. S15** Quenching of fluorescence intensity of **1** by Cu<sup>2+</sup>, Fe<sup>2+</sup>, Pb<sup>2+</sup>, Cd<sup>2+</sup>, Co<sup>2+</sup>, and Cu<sup>+</sup> ions. (Note- Blank corresponds to the emission from **1** before the addition of analytes)

### Stern-Volmer plots

Stern-Volmer equation is used to find out the catalytic efficiency of analytes in a photophysical intermolecular deactivation process. The equation is  $(I_0/I) = K_{SV} [A] + 1$ , where in our case,  $I_0$  is the initial fluorescence intensity of **1** soaked in DMF,  $I$  is the fluorescence intensity in the presence of analyte,  $[A]$  is the molar concentration of analyte, and  $K_{SV}$  is the Stern-Volmer constant ( $M^{-1}$ ) or quenching constant.

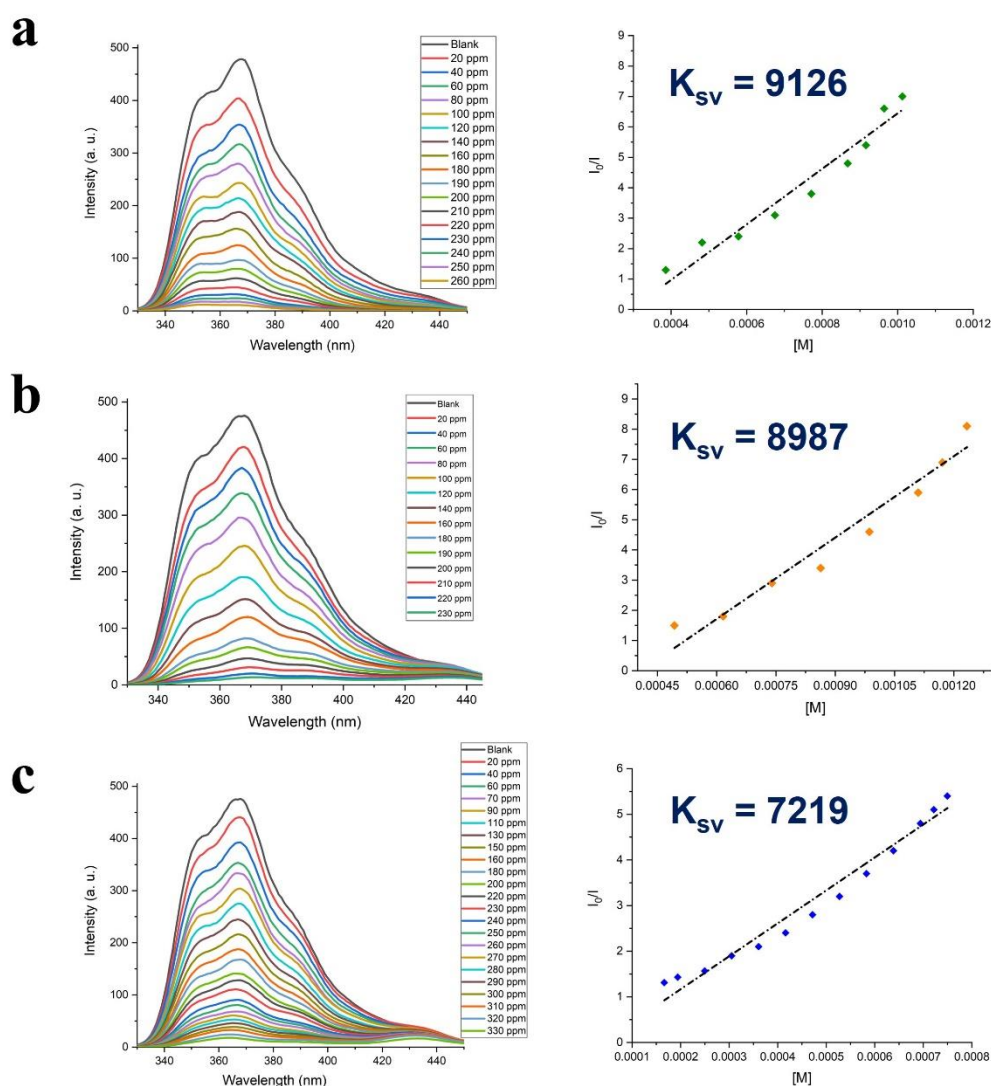


**Fig. S16-** Emission spectra and the corresponding Stern-Volmer plots of **1** in different **a)**  $Ru^{+3}$ , **b)**  $Fe^{+3}$  and **c)**  $Hg^{+2}$  concentrations in DMF.

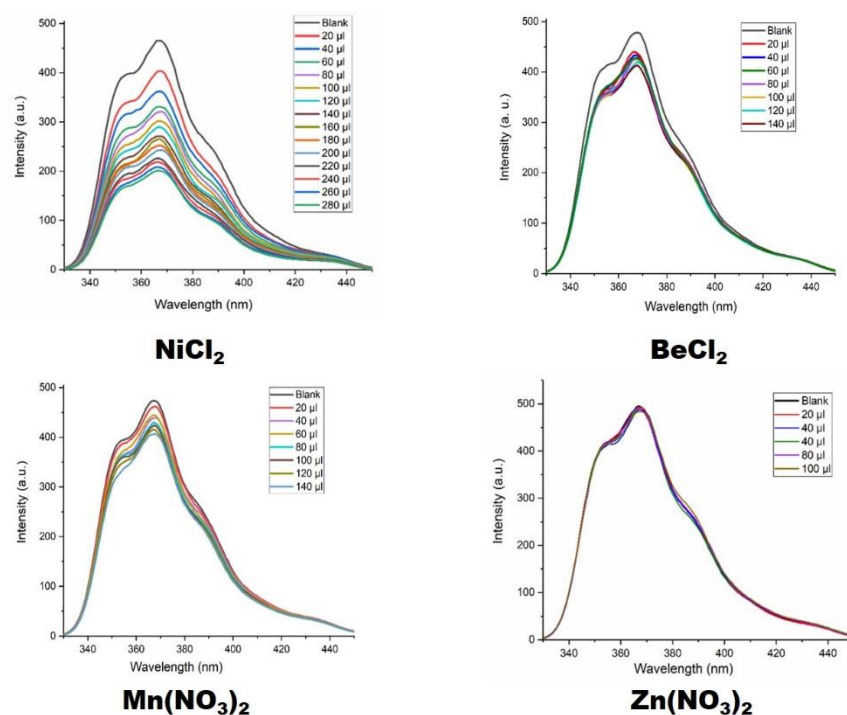


**Fig. S17** Quenching of fluorescence of **1** by  $\text{Ni}^{+2}$ ,  $\text{Be}^{+2}$ ,  $\text{Mn}^{+2}$ , and  $\text{Zn}^{+2}$  ions. (Note- Blank corresponds to the emission from **1** before the addition of analytes)

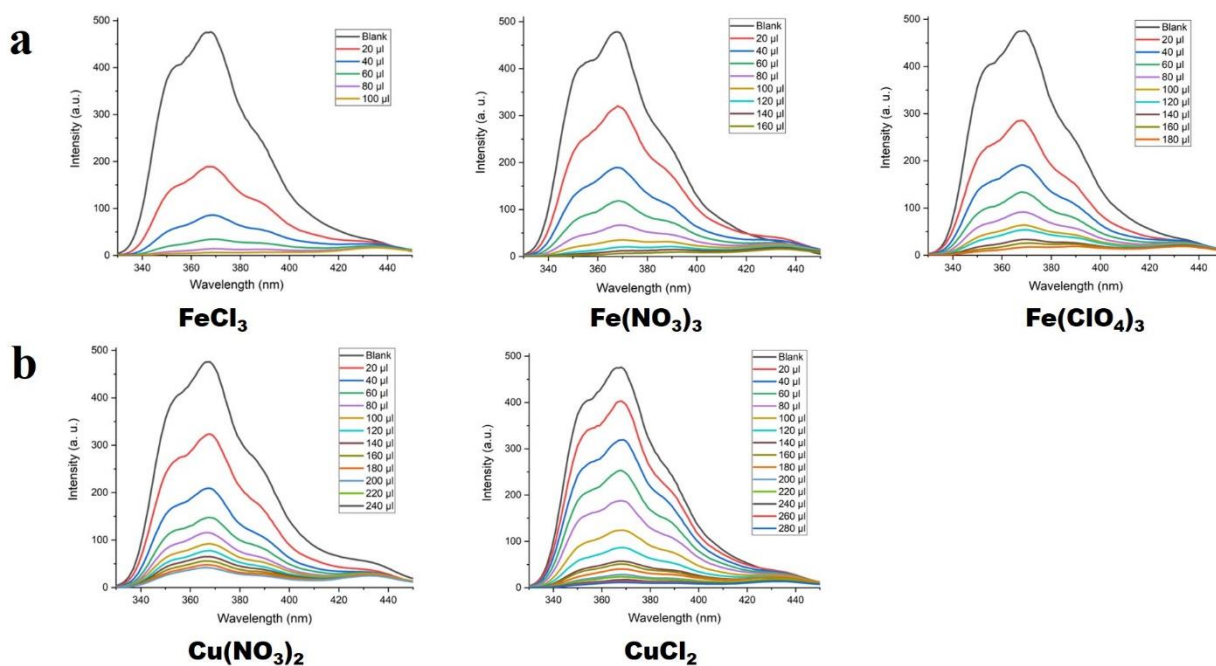


**Fig. S18** Comparison of fluorescence quenching of **1** with **a)** different Fe(III) and **b)** Cu(II) salts. (Note- Blank corresponds to the emission from Co-MOF before the addition of analytes)

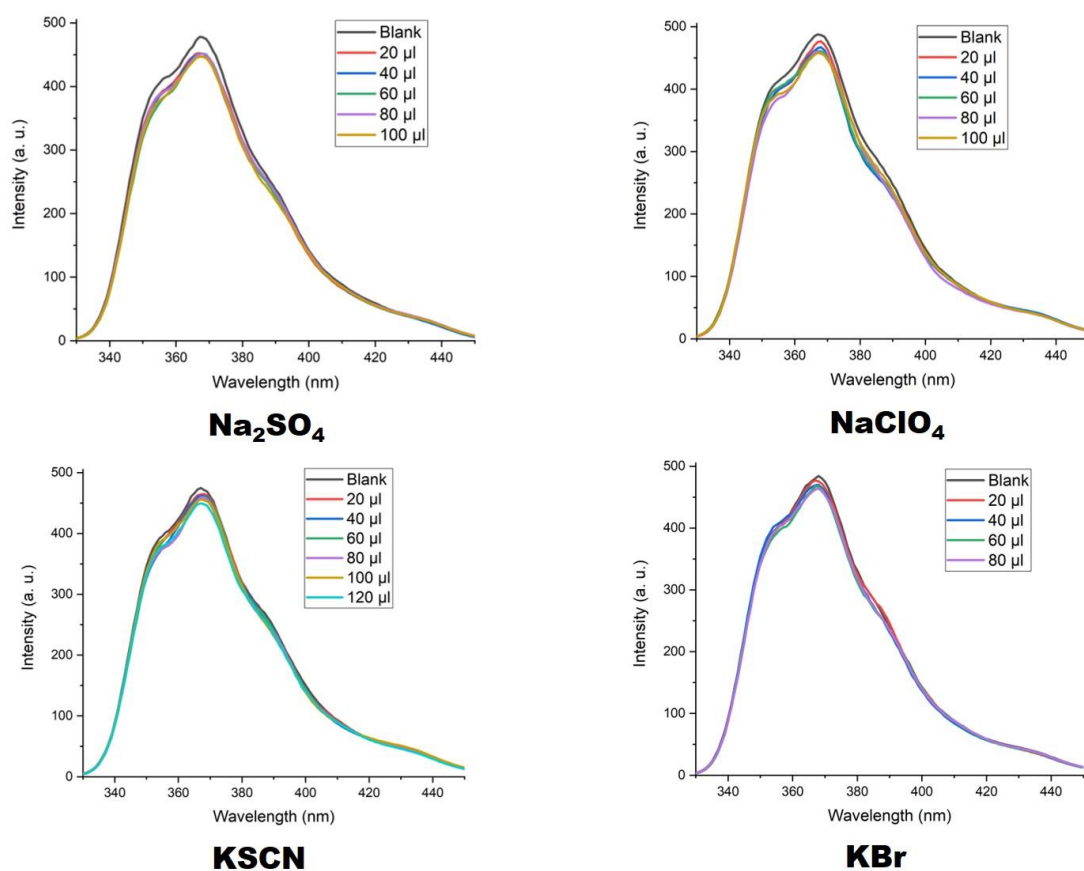


**Fig. S19** Illustrates negligible change in fluorescence intensity upon the addition of  $\text{ClO}_4^-$ ,  $\text{SCN}^-$ , and  $\text{Br}^-$  ions. (Note- Blank corresponds to the emission from **1** before the addition of analytes)

**Table S2-** Pertinent atomic parameters for compound **1**, **2**, and **3**.

<b>Bond lengths</b>		
<b>1</b>	<b>2</b>	<b>3</b>
Co4-N3 2.150(10)	Zn1-O1 1.919(2)	Ni1-N2 2.118(2)
Co2-N6 <sup>4</sup> 2.141(10)	Zn1-O2 1.908(2)	Ni1-O1 2.072(15)
Co1-O3 <sup>1</sup> 2.127(7)	Zn1-O14 <sup>1</sup> 1.983(2)	Ni1-O2 <sup>3</sup> 2.0420(18)
Co1-O4 2.048(7)	Zn1-O21 <sup>2</sup> 1.960(2)	
Co1-O13 <sup>2</sup> 2.066(6)	Zn2-O1 1.927(2)	
Co1-O13 <sup>3</sup> 2.066(6)	Zn2-O6 1.935(2)	
Co2-O1 2.154(7)	Zn2-O8 1.980(2)	
Co2-O2 2.237(7)	Zn2-O13 <sup>1</sup> 1.960(2)	
Co2-O3 2.140(7)	Zn3-O1 1.929(2)	
Co2-O5 2.021(7)	Zn3-O5 1.927(2)	
Co2-O14 <sup>3</sup> 2.034(6)	Zn3-O9 1.959(2)	
Co3-O6 2.069(7)	Zn3-O20 <sup>2</sup> 1.977(2)	
Co3-O8 <sup>5</sup> 2.054(6)	Zn4-O1 2.030(2)	
Co3-O10 <sup>5</sup> 2.116(7)	Zn4-O3 2.198(2)	
Co4-O7 2.047(7)	Zn4-O4 2.122(2)	
Co4-O9 2.021(6)	Zn4-O7 2.112(2)	
Co4-O10 2.140(8)	Zn4-O10 2.135(2)	
Co4-O11 2.261(7)	Zn4-N4 <sup>3</sup> 2.102(3)	
Co4-O12 2.135(6)	Zn5-O9 <sup>4</sup> 1.951(2)	
	Zn5-O23 2.020(3)	
	Zn5-O24 1.952(3)	
	Zn5-O25 2.384(3)	
	Zn5-O27 <sup>5</sup> 1.965(3)	
	Zn6-O9 <sup>4</sup> 1.952(2)	
	Zn6-O11 <sup>6</sup> 1.959(3)	
	Zn6-O18 <sup>6</sup> 1.974(2)	
	Zn6-O22 1.951(2)	
	Zn7-O9 1.925(2)	
	Zn7-O15 1.924(2)	
	Zn7-O17 <sup>5</sup> 1.961(2)	
	Zn7-O26 <sup>7</sup> 1.954(3)	
	Zn8-O9 1.953(2)	
	Zn8-O12 <sup>5</sup> 1.977(2)	
	Zn8-O16 2.043(3)	
	Zn8-O19 2.272(4)	
	Zn8-N1 2.031(3)	
<b>Bond angles</b>		
O3-Co1-O3 <sup>1</sup> 180	O1-Zn1-O14 <sup>1</sup> 108.56(9)	O1 <sup>3</sup> -Ni1-N2 85.3(6)
O4-Co1-O3 92.2(3)	O1-Zn1-O21 <sup>2</sup> 111.96(10)	O1-Ni1-N2 94.7(6)
O4-Co1-O3 <sup>1</sup> 92.2(3)	O2-Zn1-O1 122.81(9)	O1A <sup>3</sup> -Ni1-O1A 180.00(17)
O4-Co1-O3 <sup>1</sup> 87.8(3)	O2-Zn1-O14 <sup>1</sup> 102.98(11)	O1A <sup>3</sup> -Ni1-N2 <sup>3</sup> 85.32(14)
O4-Co1-O4 180.0(4)	O2-Zn1-O21 <sup>2</sup> 106.50(11)	O1A <sup>3</sup> -Ni1-N2 94.68(14)
O4-Co1-O13 <sup>2</sup> 85.8(3)	O21 <sup>2</sup> -Zn1-O14 <sup>1</sup> 101.72(11)	N2-Ni1-N2 <sup>3</sup> 180.0
O4-Co1-O13 <sup>3</sup> 94.2(3)	O1-Zn2-O6 115.29(9)	O2-Ni1-O1 <sup>3</sup> 90.5(7)

O13 <sup>2</sup> -Co1-O3 <sup>1</sup> 87.9(3) O13 <sup>3</sup> -Co1-O3 <sup>1</sup> 92.1(3) O13 <sup>2</sup> -Co1-O13 <sup>3</sup> 180.0 O1-Co2-O2 82.9(3) O3-Co2-O1 84.0(3) O3-Co2-O2 59.6(3) O3-Co2-N6 <sup>4</sup> 162.5(3) O5-Co2-O1 173.3(3) O5-Co2-O2 95.1(3) O5-Co2-O3 100.5(3) O5-Co2-O14 <sup>3</sup> 98.8(3) O5-Co2-N6 <sup>4</sup> 88.3(3) O14 <sup>3</sup> -Co2-O1 85.5(3) O1-Co2-O2 153.9(3) O14 <sup>3</sup> -Co2-O3 96.1(3) O14 <sup>3</sup> -Co2-N6 <sup>4</sup> 97.5(3) N6 <sup>4</sup> -Co2-O1 86.1(3) N6 <sup>4</sup> -Co2-O2 104.9(3) O6-Co3-O6 180.0(3) O6-Co3-O10 <sup>5</sup> 91.4(3) O6 <sup>5</sup> -Co3-O10 <sup>5</sup> 88.6(3) O6-Co3-O10 88.6(3) O6-Co3-O10 91.4(3) O8 <sup>5</sup> -Co3-O6 85.5(3) O8 <sup>5</sup> -Co3-O6 <sup>5</sup> 94.5(3) O8-Co3-O6 94.5(3) O8-Co3-O6 <sup>5</sup> 85.5(3) O8-Co3-O8 <sup>5</sup> 180.0(4) O8-Co3-O10 <sup>5</sup> 91.8(3) O8-Co3-O10 <sup>5</sup> 88.2(3) O8 <sup>5</sup> -Co3-O10 <sup>5</sup> 91.8(3) O8-Co3-O10 <sup>5</sup> 88.2(3) O10-Co3-O10 <sup>5</sup> 180 O7-Co4-O10 97.0(3) O7-Co4-O11 154.8(3) O7-Co4-O12 85.8(3) O7-Co4-N3 94.4(3) O9-Co4-O7 99.1(3) O9-Co4-O10 98.8(3) O9-Co4-O11 93.6(3) O9-Co4-O12 174.3(3) O9-Co4-N3 89.1(3) O10-Co4-O11 59.4(3) O10-Co4-N3 164.9(3) O12-Co4-O10 83.5(3) O12-Co4-O11 83.1(3) O12-Co4-N3 87.5(3) N3-Co4-O11 107.5(3)	O1-Zn2-O8 109.39(10) O1-Zn2-O13 <sup>1</sup> 113.61(9) O6-Zn2-O8 101.04(11) O6-Zn2-O13 <sup>1</sup> 105.44(11) O13-Zn2-O8 111.37(10) O1-Zn3-O9 112.64(11) O1-Zn3-O20 <sup>2</sup> 108.15(10) O5-Zn3-O1 116.65(9) O5-Zn3-O9 113.75(11) O5-Zn3-O20 <sup>2</sup> 108.01(12) O9-Zn3-O20 95.17(12) O1-Zn4-O3 93.19(8) O1-Zn4-O4 92.69(9) O1-Zn4-O7 94.01(9) O1-Zn4-O10 88.67(9) O1-Zn4-N4 178.66(10) O4-Zn4-O3 90.32(9) O4-Zn4-O10 174.61(9) O7-Zn4-O3 172.79(9) O7-Zn4-O4 89.08(10) O7-Zn4-O10 96.03(10) O10-Zn4-O3 84.39(9) N4-Zn4-O3 85.48(10) N4 <sup>3</sup> -Zn4-O4 87.09(10) N4 <sup>3</sup> -Zn4-O7 87.31(10) N4 <sup>3</sup> -Zn4-O10 91.43(10) O9-Zn5-O23 98.71(10) O9 <sup>4</sup> -Zn5-O25 97.20(10) O9 <sup>4</sup> -Zn5-O27 <sup>5</sup> 111.46(10) O23-Zn5-O25 157.89(11) O24-Zn5-O9 132.22(14) O24--Zn5-O23 99.73(13) O24-Zn5-O25 58.16(13) O24-Zn5-O27 110.25(15) O27 <sup>5</sup> -Zn5-O23 95.16(12) O27 <sup>5</sup> -Zn5-O25 93.19(13) O9 <sup>4</sup> -Zn6-O11 <sup>6</sup> 110.98(10) O9 <sup>4</sup> -Zn6-O18 <sup>6</sup> 109.33(9) O11 <sup>6</sup> -Zn6-O18 <sup>6</sup> 101.09(12) O22-Zn6-O9 <sup>4</sup> 119.46(10) O22-Zn6-O11 <sup>6</sup> 107.53(13) O22-Zn6-O18 <sup>6</sup> 106.83(11) O9-Zn7-O17 <sup>5</sup> 110.83(9) O9-Zn7-O26 <sup>8</sup> 114.32(10) O15-Zn7-O9 115.54(9) O15-Zn7-O17 <sup>5</sup> 110.81(10) O15-Zn7-O26 <sup>8</sup> 107.27(12) O26 <sup>8</sup> -Zn7-O17 <sup>5</sup> 96.44(13) O9-Zn8-O12 <sup>5</sup> 109.75(10) O9-Zn8-O16 98.05(10) O9-Zn8-O19 81.25(12) O9-Zn8-N1 144.95(10)	O2-Ni1-O1 <sup>3</sup> 89.5(7) O2 <sup>3</sup> -Ni1-O1A 91.05(18) O2 <sup>3</sup> -Ni1-O1A <sup>3</sup> 88.95(18) O2-Ni1-N2 90.61(8) O2-Ni1-N2 <sup>3</sup> 89.39(8) O2-Ni1-O2 <sup>3</sup> 180
---	---	--

	O12-Zn8-O16 97.44(12) O12 <sup>5</sup> -Zn8-O19 93.31(19) O12 <sup>5</sup> -Zn8-N1 102.41(11) O16-Zn8-O19 168.77(18) N1-Zn8-O16 91.10(11) N1-Zn8-O19 83.40(12) Zn1-O1-Zn2 107.90(10) Zn1-O1-Zn3 108.64(10) Zn1-O1-Zn4 109.39(9) Zn2-O1-Zn3 105.78(9) Zn2-O1-Zn4 110.45(10) Zn3 O1 Zn4 114.44(10) Zn5 <sup>7</sup> -O9-Zn6 <sup>7</sup> 108.31(10) Zn5 <sup>7</sup> -O9-Zn8 114.37(10) Zn6 <sup>7</sup> -O9-Zn8 105.06(10) Zn7-O9-Zn5 <sup>7</sup> 106.15(10) Zn7-O9-Zn6 <sup>7</sup> 108.29(9) Zn7-O9-Zn8 114.41(10)	
--	---	--

**Symmetry elements 1:** <sup>1</sup>1-X,2-Y,-Z; <sup>2</sup>1-X,2-Y,1-Z; <sup>3</sup>+X,+Y,-1+Z; <sup>4</sup>-X,1-Y,1-Z; <sup>5</sup>2-X,2-Y,1-Z; <sup>6</sup>+X,+Y,1+Z; <sup>7</sup>-X,2-Y,-Z; <sup>8</sup>3-X,2-Y,1-Z. **2:** <sup>1</sup>+X,-1/2-Y,1/2+Z; <sup>2</sup>+X,-1/2-Y,-1/2+Z; <sup>3</sup>1-X,1-Y,1-Z; <sup>4</sup>1+X,1/2-Y,1/2+Z; <sup>5</sup>+X,1/2-Y,1/2+Z; <sup>6</sup>1+X,+Y,1+Z; <sup>7</sup>-1+X,+Y,+Z. **3:** <sup>1</sup>2-X,1-Y,2-Z; <sup>2</sup>2-X,-Y,-Z; <sup>3</sup>1-X,1-Y,1-Z.

## References

1. M. D. Hanwell, D. E. Curtis, D. C. Lonie, T. Vandermeersch, E. Zurek and G. R. Hutchison, *Journal of Cheminformatics*, 2012, DOI:10.1186/1758-2946-4-17.



## Annex 2: Supplementary Information of Article 2

### Isostructural Coordination Polymers of Tethering Naphthalene Anchored Bis(2-methylpyridinecarboxamide) Ligand: Single Crystal, XPS, EDS and Theoretical studies

Love Karan Rana<sup>1</sup>, Prabhjyot Kaur<sup>1</sup>, Alborz Bavandsavadkouhi<sup>1</sup>, Gurpreet Singh Selopal<sup>2</sup>,  
and Adam Duong<sup>1\*</sup>

<sup>1</sup>*Département de Chimie, Biochimie et physique, Institut de Recherche sur l'Hydrogène and Laboratory of Functional Materials for Energy and Nanotechnology (DuongLab), Université du Québec à Trois-Rivières, Trois-Rivières, Québec, G9A 5H7, Canada*

<sup>2</sup>*Institut national de la recherche scientifique, Montréal, Québec, H2X 1E3, Canada*

\*To whom correspondence should be addressed. E-mail: [love.karan@uqtr.ca](mailto:love.karan@uqtr.ca)

#### Table of contents

Figure	Caption	Page No.
1	Comparison of PXRD pattern compound <b>1</b> with the simulated pattern.	223
2	Comparison of PXRD pattern of asynthesized compound <b>2</b> with the simulated pattern.	224
3	Comparison of PXRD pattern of asynthesized compound <b>3</b> with the simulated pattern.	225
4	BFDH morphologies of <b>L1</b> , compound <b>1</b> .	225
5	Diffraction data plots showing weak diffraction from the crystal at higher angles.	226

<b>6</b>	<sup>1</sup> H-NMR of <b>L1</b> .	226
<b>7</b>	<sup>13</sup> C-NMR of <b>L1</b> .	227
<b>8</b>	IR spectra comparison involving <b>L1</b> and compounds <b>1</b> , <b>2</b> , and <b>3</b> .	227
<b>9</b>	ORTEP diagram of <b>L1</b> at 40% probability.	229
<b>10</b>	Showing the dihedral angle between pyridine and naphthalene ring planes of <b>L1</b> .	229
<b>11</b>	ORTEP diagram of compound <b>1</b> at 40% ellipsoidal probability.	230
<b>12</b>	ORTEP diagram of compound <b>2</b> at 40% ellipsoidal probability.	230
<b>13</b>	ORTEP diagram of compound <b>3</b> at 40% ellipsoidal probability.	231
<b>14</b>	Supramolecular synthons generated in a 2D sheet and 3D hydrogen bonded framework of compound <b>1</b> .	231
<b>15</b>	XPS spectral peaks for compound <b>2</b> .	232
<b>16</b>	XPS spectral peaks for compound <b>3</b> .	232
<b>17</b>	EDS spectra of compound <b>2</b> .	233
<b>18</b>	EDS spectra of compound <b>3</b> .	233
<b>19</b>	Thermogravimetry curves for <b>L1</b> and <b>1-3</b> .	234
<b>20</b>	Energy gap between excited and ground states of compounds <b>1</b> and <b>3</b> .	234
<b>Table</b>	<b>Caption</b>	
<b>1</b>	Characteristic IR peaks for <b>L1</b> and compounds <b>1</b> , <b>2</b> , and <b>3</b> .	228
<b>2</b>	Hydrogen bonds for <b>L1</b> [Å and deg.].	235
<b>3</b>	Hydrogen bonds for <b>1</b> [Å and deg.].	236

4	Hydrogen bonds for <b>2</b> [Å and deg.].	237
5	Hydrogen bonds for <b>3</b> [Å and deg.].	238

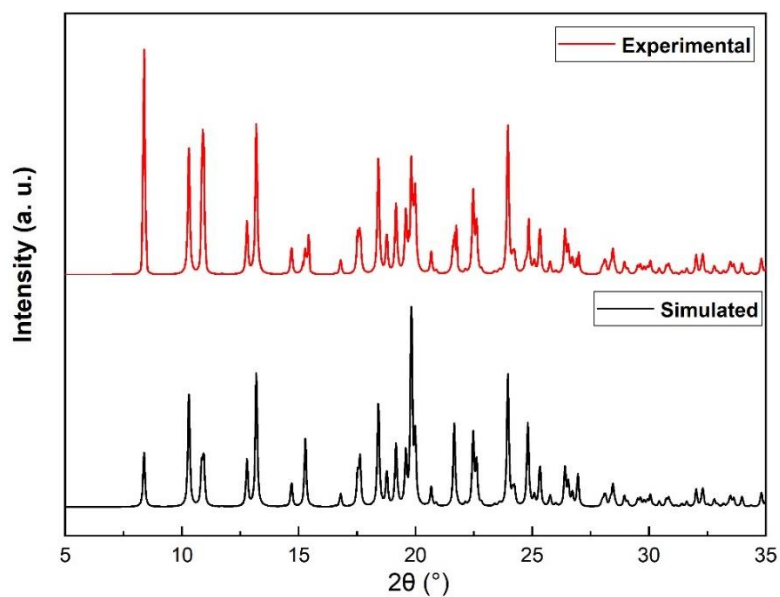


**Figure S1** Comparison of PXRD pattern compound **1** with the simulated pattern.

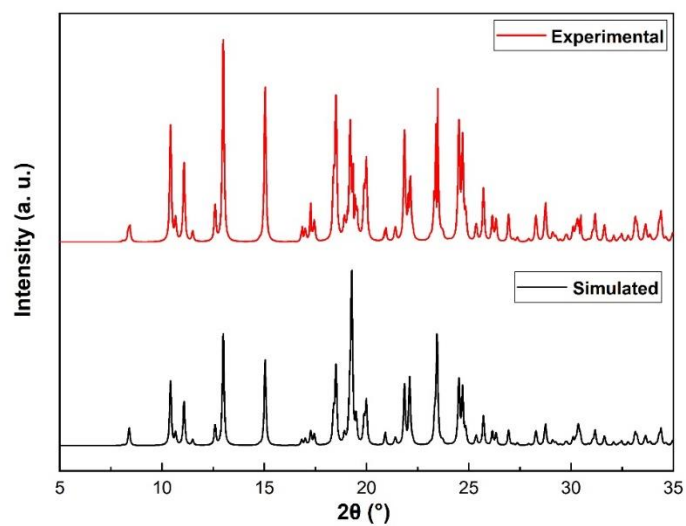


**Figure S2** Comparison of PXRD pattern compound **2** with the simulated pattern.

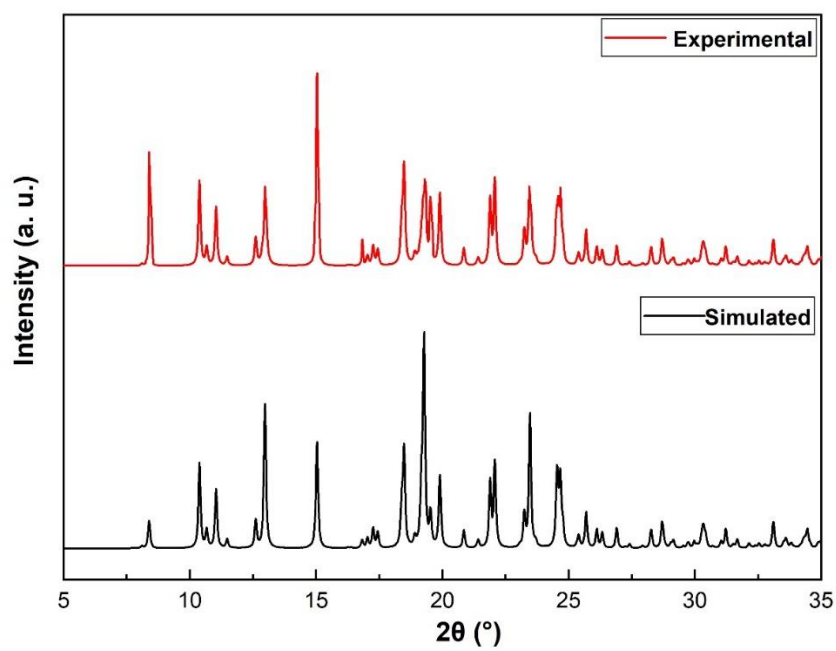


**Figure S3** Comparison of PXRD pattern compound **3** with the simulated pattern.

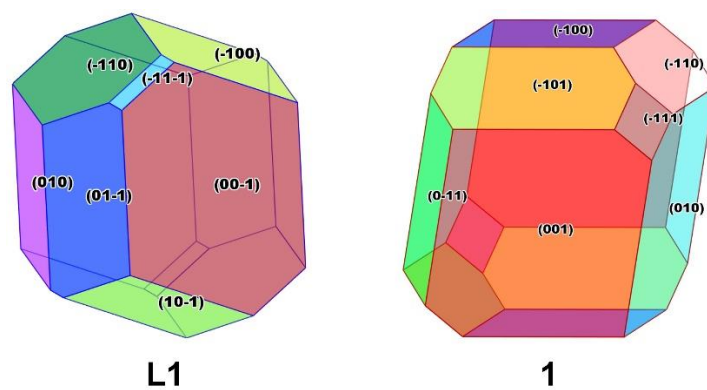


**Figure S4** BFDH morphologies of **L1** and compound **1**.

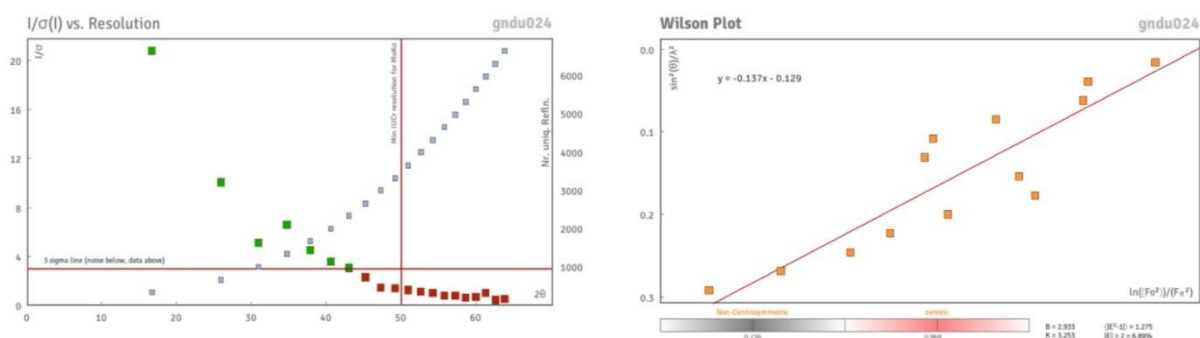


**Figure S5** Diffraction data plots showing noise at higher angles ( $I/\sigma(I)$  vs resolution plot) and poor quality of data (large deviation from straight line in Wilson plot).

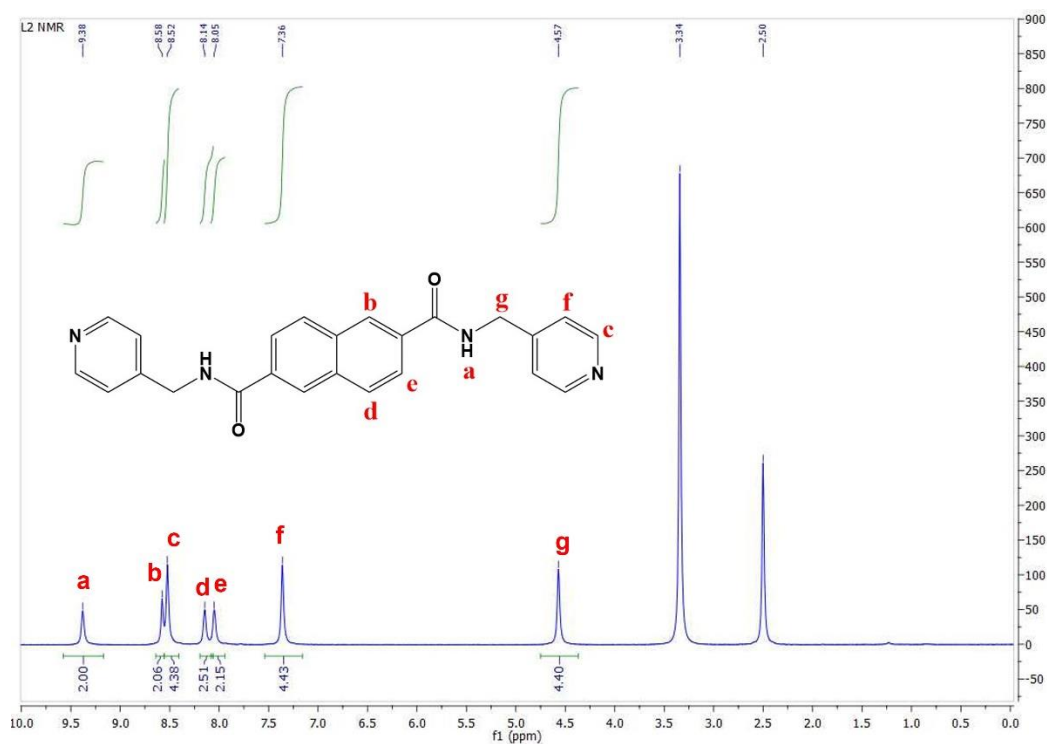


**Figure S6**  $^1\text{H}$ -NMR of L1.

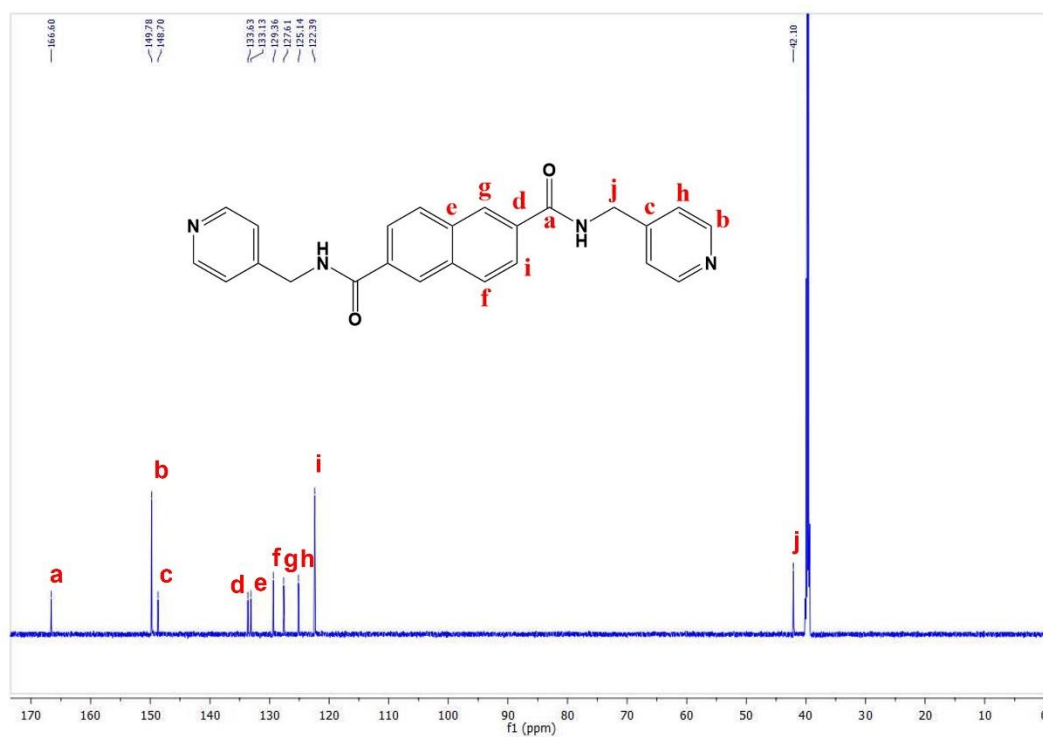


Figure S7  $^{13}\text{C}$ -NMR of L1.

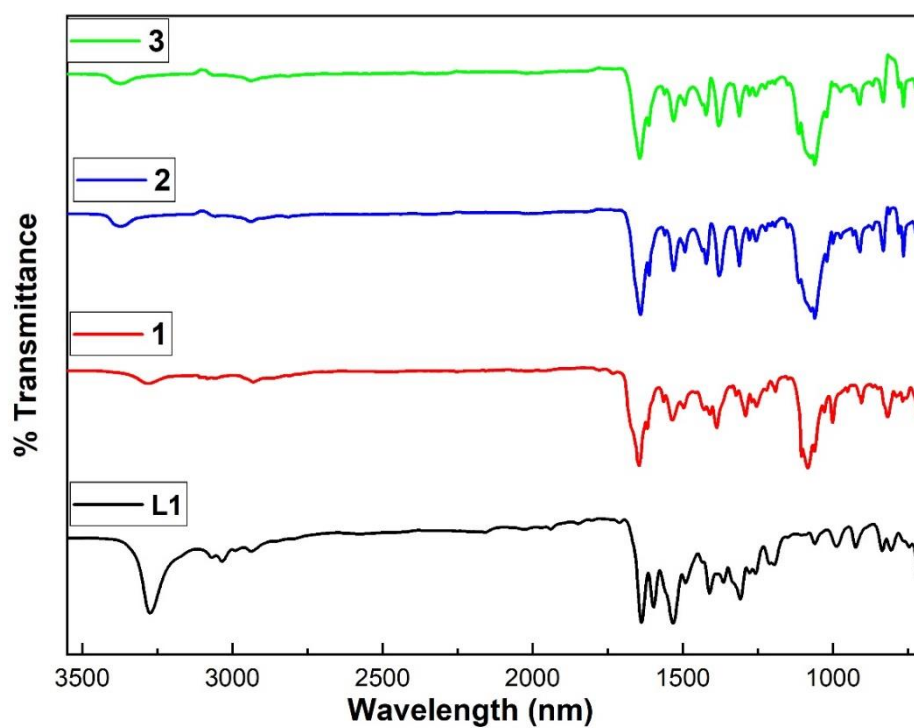
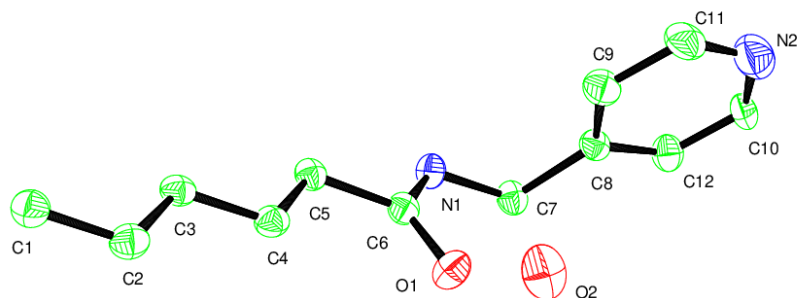


Figure S8 IR spectra comparison involving L1 and compounds 1, 2, and 3.

**Table S1** – Characteristic IR peaks for **L1** and compounds **1**, **2**, and **3**.

Complex	Group	Functionality	Wavenumber (cm <sup>-1</sup> )
<b>L1</b>	$\nu$ (O-H)Stretching	Water	3272 (s)
	$\nu$ (N-H)Stretching	Amide	3068 (w,b)
	$\nu$ (C=O)	Amide	1639 (s)
	$\nu$ (C=N)	Pyridine	1597 (s)
	$\nu$ (C=C)	Pyridine	1533 (b)
	$\nu$ (C-H)Stretching	Methylene	2937(m)
	$\nu$ (C=C)	Naphthalene	1487 (w)
<b>1</b>	$\nu$ (N-H)	Amide	3076 (w)
	$\nu$ (C=O)	Amide	1645 (s)
	$\nu$ (C=N)	Pyridine	1615 (w)
	$\nu$ (C=C)	Pyridine	1532 (m, b)
	$\nu$ (C-H)Stretching	Methylene	2932 (vw)
	$\nu$ (C=C)	Naphthalene	1494 (w)
	$\nu$ (Cl-O)	Perchlorate	1060 (w) 1081 (m) 1105 (w)
<b>2</b>	$\nu$ (N-H)	Amide	3069 (w)
	$\nu$ (C=O)	Amide	1640 (s)
	$\nu$ (C=N)	Pyridine	1611 (w)
	$\nu$ (C=C)	Pyridine	1533 (s)
	$\nu$ (C-H)Stretching	Methylene	2940 (vw)
	$\nu$ (C=C)	Naphthalene	1493 (w)
	$\nu$ (Cl-O)	Perchlorate	1019 (w) 1058 (w) 1112 (w)
<b>3</b>	$\nu$ (N-H)	Amide	3071 (w)
	$\nu$ (C=O)	Amide	1643 (s)
	$\nu$ (C=N)	Pyridine	1612 (w)
	$\nu$ (C=C)	Pyridine	1529 (s)
	$\nu$ (C-H)Stretching	Methylene	2935 (vw)
	$\nu$ (C=C)	Naphthalene	1492 (w)
	$\nu$ (Cl-O)	Perchlorate	1021 (w) 1061 (w) 1114 (w)



**Figure S9** ORTEP diagram of **L1** drawn at 40% ellipsoidal probability (Hydrogen atoms have not been shown for clarity).

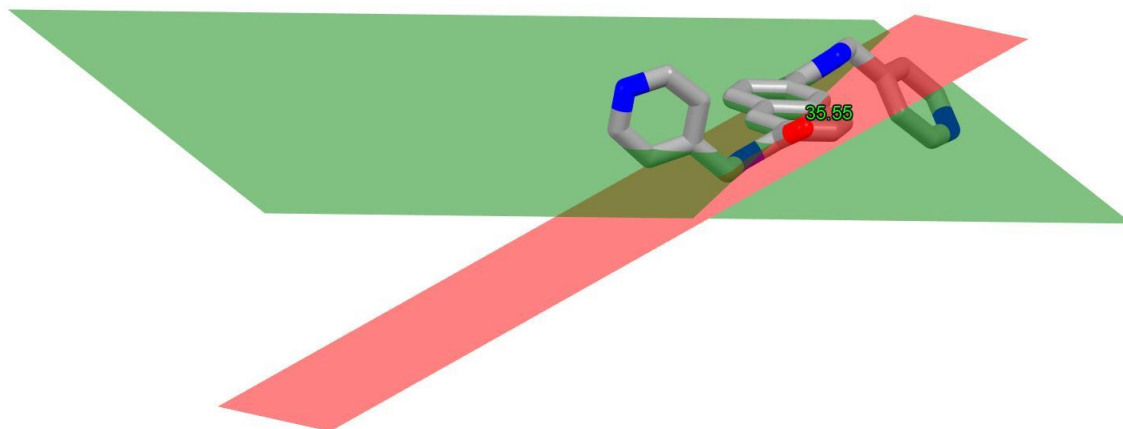


**Figure S10** Showing the dihedral angle between pyridine and naphthalene ring planes of **L1**.



[illegible]

229

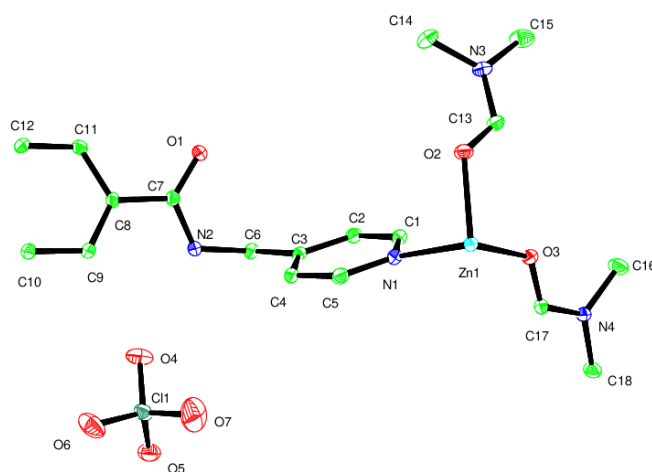


**Figure S13** ORTEP diagram of compound **3** at 40% ellipsoidal probability.

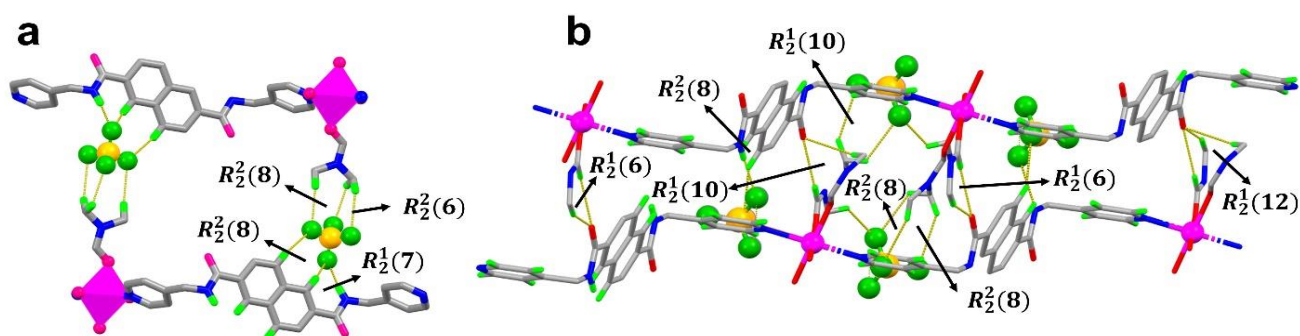


**Figure S14** Supramolecular synthons generated in a 2D sheet and 3D hydrogen bonded framework of compound **1**.

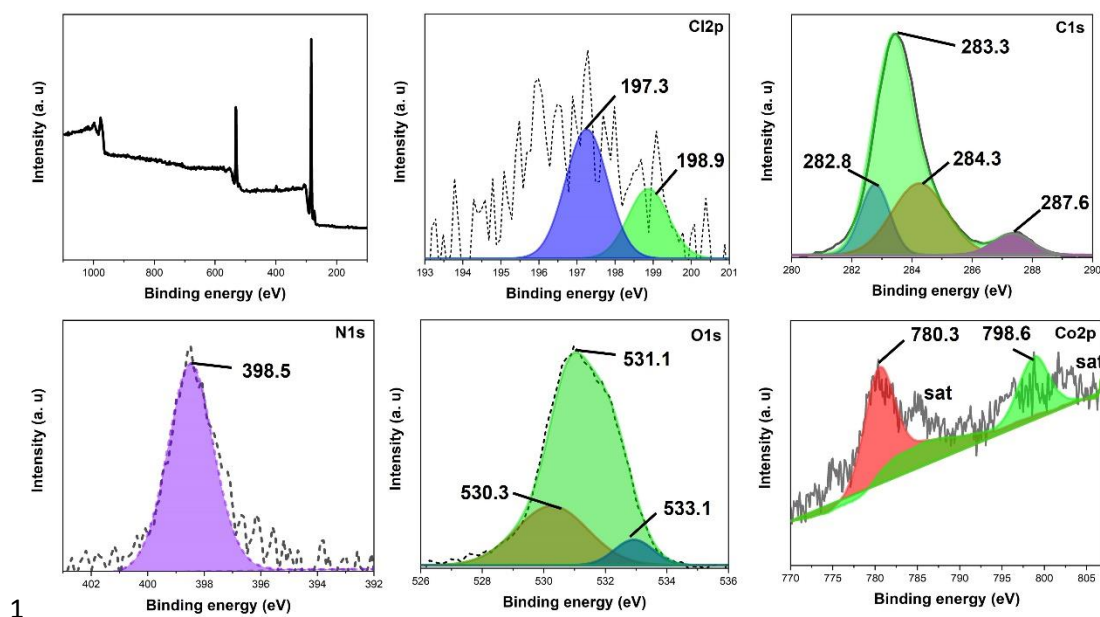


Figure S15 XPS spectral peaks for compound 2.

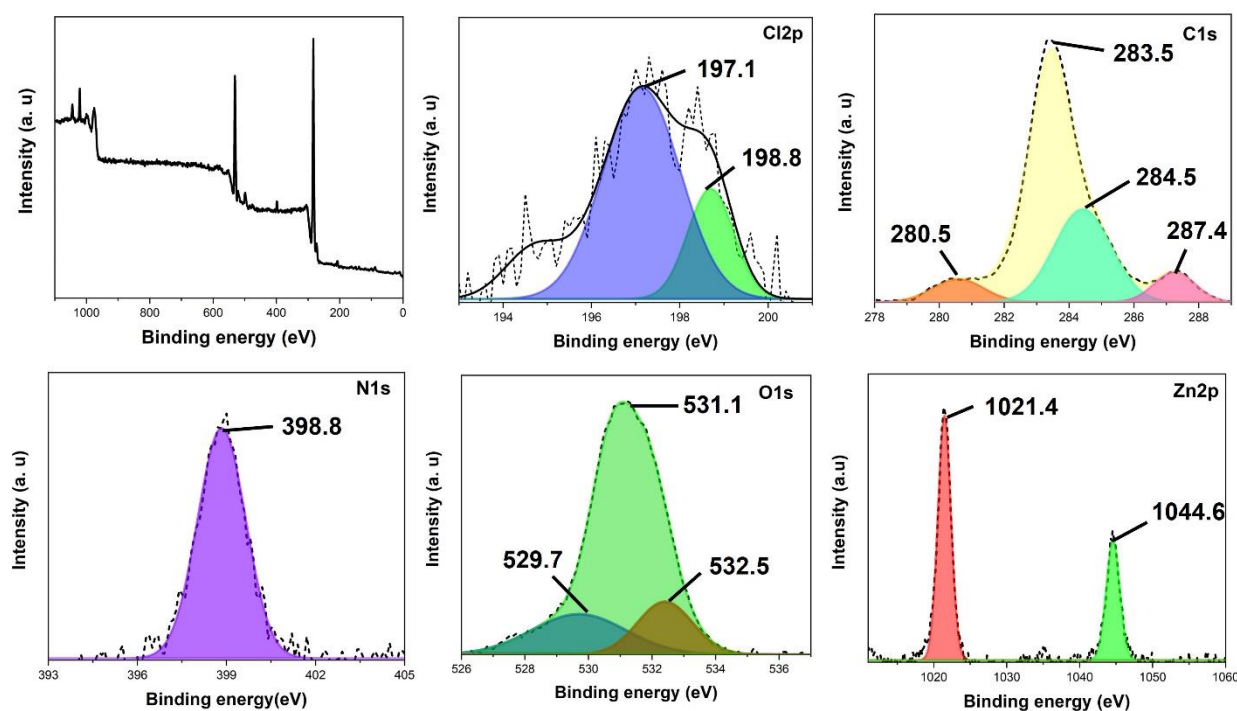


Figure S16 XPS spectral peaks for compound 3.

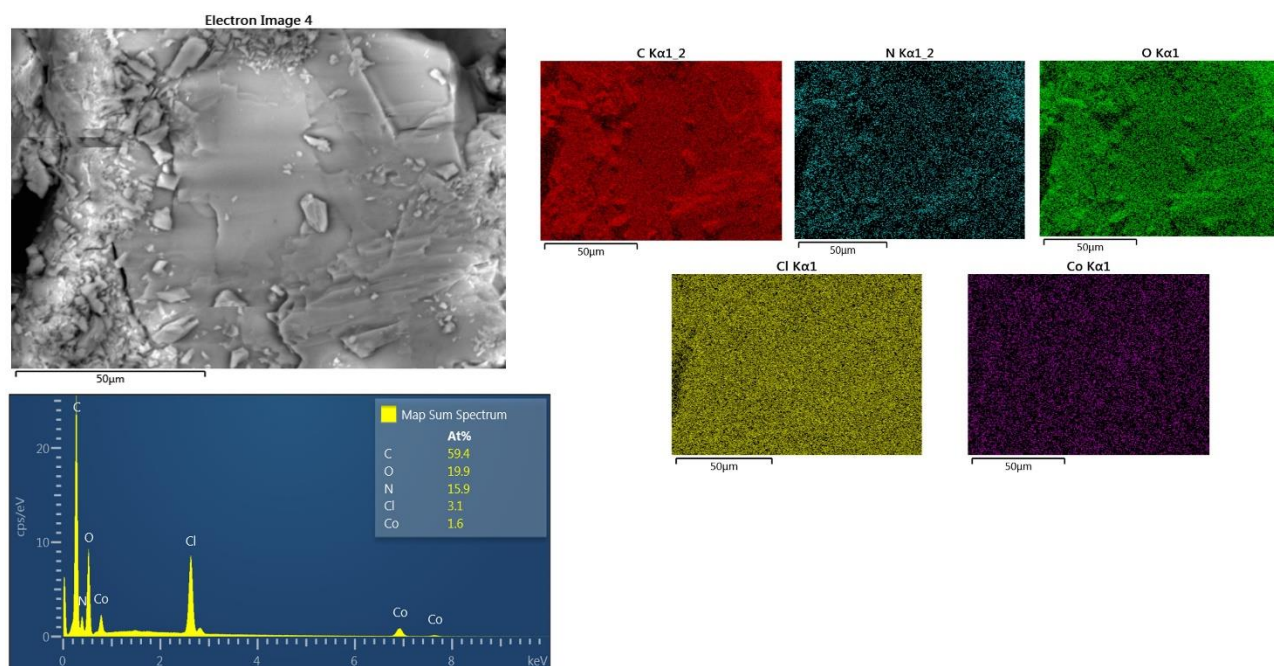


Figure S17 EDS spectra of compound 2

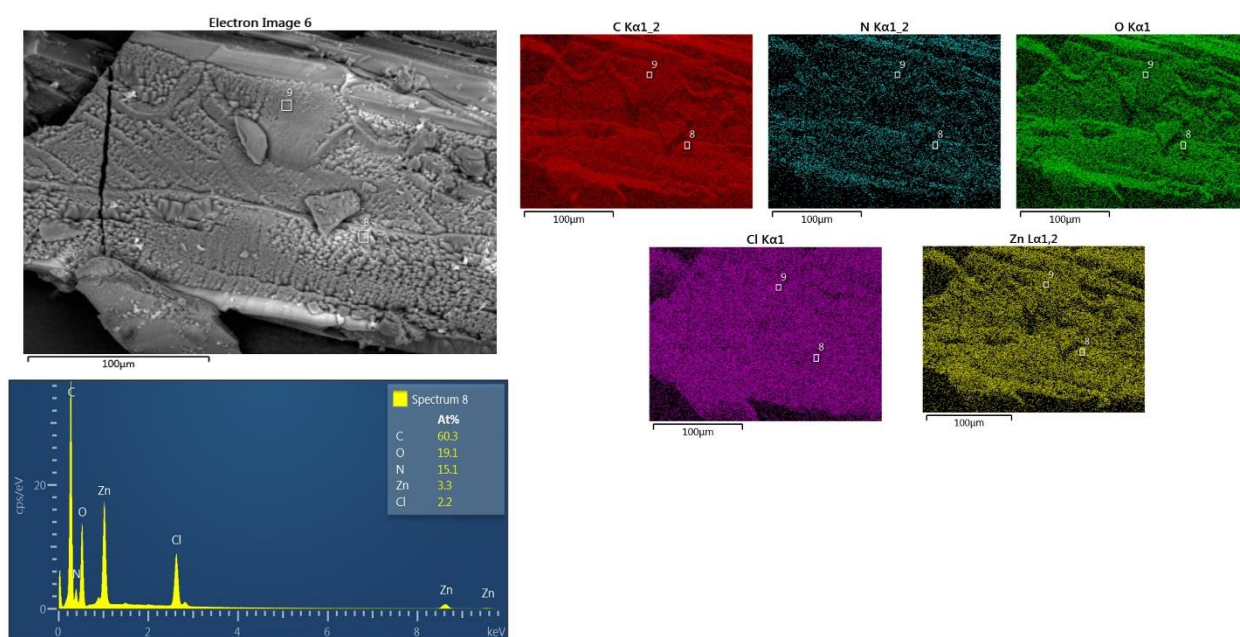
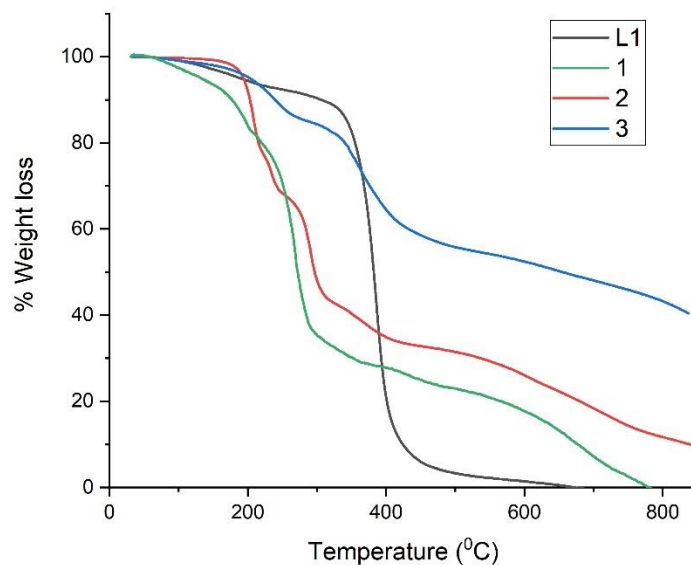
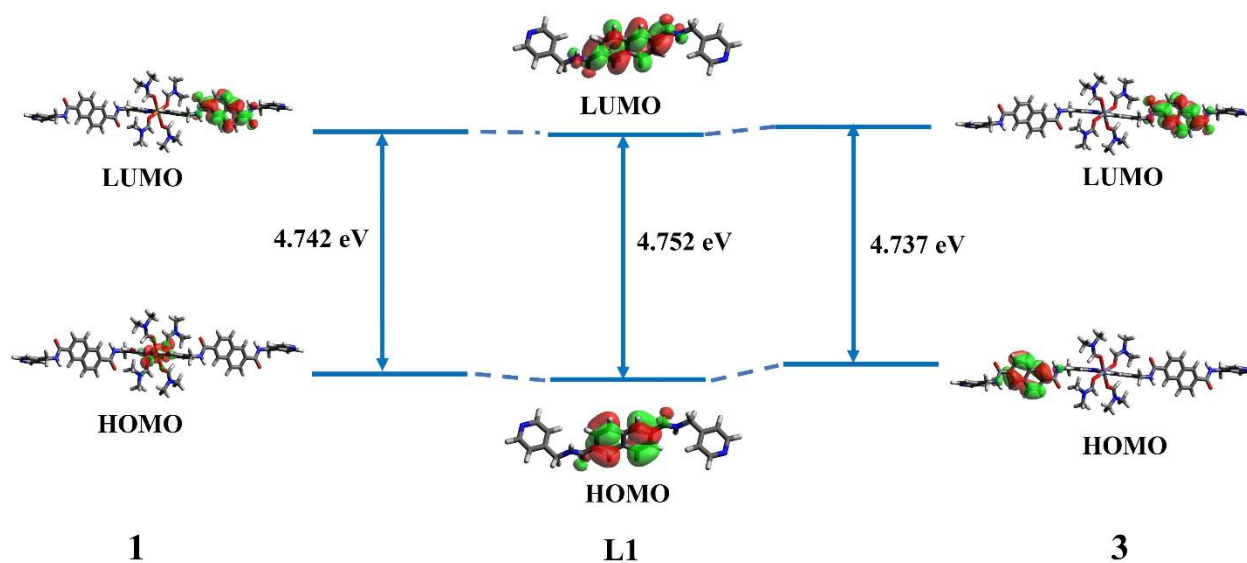


Figure S18 EDS spectra of compound 3



**Figure S19** Thermogravimetry curves for **L1** and **1-3**.



**Figure S20** Variation of HOMO-LUMO energy gap in compounds **1** and **3** relative to **L1**.

(Note- This figure is showing speculative anomaly in HOMO-LUMO energies of compounds **1** and **3** due to solvent effect of DMF. In both cases, HOMO orbitals are more affected by solvent interactions than LUMO orbitals.)

**Table S2-** Hydrogen bonds for **L1** [Å and deg.].

D-H...A	d(D-H)	d(H...A)	d(D...A)	<(DHA)
N(1)-H(1)...O(2)#1	0.88	2.02	2.801(4)	147.1
N(3)-H(3)...O(1)#2	0.88	2.05	2.821(4)	146.5
C(3)-H(3A)...O(2)#3	0.95	2.73	3.382(5)	126.6
C(6)-H(6)...N(2)#4	0.95	2.71	3.556(5)	149.3
C(4)-H(4)...N(2)#4	0.95	2.83	3.657(6)	145.8
C(1)-H(1A)...N(4)#5	0.95	2.68	3.538(5)	150.7
C(9)-H(9)...N(4)#5	0.95	2.86	3.681(6)	145.4
C(16)-H(16)...O(1)#6	0.95	2.84	3.640(6)	142.0

Symmetry transformations used to generate equivalent atoms:

#1 -x+1,-y+2,-z+1   #2 -x+1,-y+1,-z+1   #3 x+1,y,z,   #4 x-1,y-1,z-1   #5 x+1,y+1,z+1   #6 -x+2,-y+2,-z+2

**Table S3-** Hydrogen bonds for **1** [Å and deg.].

D-H...A	d(D-H)	d(H...A)	d(D...A)	<(DHA)
C(3)-H(3)...O(4 <sup>a</sup> )#1	0.950	2.574	3.197	123.3
C(3)-H(3)...O(2 <sup>a</sup> )#2	0.950	2.879	3.649	137.16
C(7)-H(7b)...O(5)#3	0.990	2.989	3.590	120.21
C(9)-H(9)...O(4 <sup>a</sup> )#4	0.950	2.862	3.687	145.88
N(2)-H(2)...O(1 <sup>a</sup> )#4	0.880	2.081	2.930	160.64
C(16 <sup>b</sup> )-H(17 <sup>a</sup> )...O(2 <sup>a</sup> )#5	0.880	2.177	2.904	139.64
C(17 <sup>b</sup> )-H(17e <sup>a</sup> )...O(3a <sup>b</sup> )#6	0.879	2.675	3.510	159.21
C(17a <sup>a</sup> )-H(17e <sup>a</sup> )...O(1 <sup>a</sup> )#6	0.980	2.977	3.899	156.4
C(11)...O(11)#6	0.950	2.439	3.292	149.34
C(18b <sup>b</sup> )-H(18a <sup>b</sup> )...O5 #7	0.980	2.418	3.314	151.68
C(18a <sup>b</sup> )-H(18e <sup>a</sup> )...O5 #7	0.882	2.519	3.314	150.25
C(14a <sup>a</sup> )-H(14c <sup>b</sup> )...O4a <sup>b</sup> #7	1.080	2.589	3.686	140
C(18a <sup>a</sup> )-H(18e)...O#7	0.980	2.519	3.182	160.5
C(15a <sup>a</sup> )-H(14b <sup>b</sup> )...N3 <sup>b</sup> #8	1.416	2.660	3.753	131.59
C(15a <sup>a</sup> )-H(15f <sup>a</sup> )...N3a <sup>a</sup> #8	0.980	2.770	3.744	172.91
C(14 <sup>b</sup> )-H(14b <sup>b</sup> )...N3 <sup>b</sup> #8	0.980	2.660	3.631	170.66
C(15 <sup>b</sup> )-H(15c <sup>b</sup> )...N(3a <sup>a</sup> )#9	0.980	2.874	3.795	156.84
C(14a <sup>a</sup> )-H(14e <sup>b</sup> )...O(3 <sup>b</sup> )#9	0.98	2.597	3.537	160.9

Symmetry transformations used to generate equivalent atoms: #1 -x+2,-y,-z #2 -x+1,+y,+z  
 #3 -x+2,-y+1,-z #4 -x+1,-y,-z #5 -x+1,-y+1,-z+1 #6 x,y+1,z #7 x-1,+y,+z #8 -x,y+1,-z+1 #9 -x+1,-y,-z+1

**Table S4-** Hydrogen bonds for **2** [Å and deg.].

D-H...A	d(D-H)	d(H...A)	d(D...A)	<(DHA)
C(17)-H(17C)...O(1)#3	0.96	2.49	3.412(3)	160.0
C(16)-H(16)...O(1)#3	0.93	2.52	3.383(3)	154.6
C(4)-H(4)...O(6)#4	0.93	2.88	3.508(3)	126.2
C(5)-H(5)...O(6)#4	0.93	2.90	3.536(3)	126.4
C(1)-H(1)...O(5)#5	0.93	2.88	3.527(3)	127.5
C(1)-H(1)...O(7)#5	0.93	2.56	3.401(3)	149.9
C(2)-H(2A)...O(4)#5	0.93	2.83	3.601(4)	141.2
C(12)-H(12)...O(6)#2	0.93	2.93	3.740(4)	147.1
C(14)-H(14C)...N(4)#6	0.96	2.91	3.767(3)	149.3
C(18)-H(18B)...O(7)#7	0.96	2.58	3.283(3)	130.0
C(14)-H(14A)...O(1)#8	0.96	2.57	3.383(3)	142.4
C(14)-H(14B)...O(6)#9	0.96	2.75	3.677(4)	162.4
C(15)-H(15A)...O(7)#9	0.96	2.64	3.290(4)	125.7
C(15)-H(15B)...O(4)#9	0.96	2.84	3.628(5)	139.6

Symmetry transformations used to generate equivalent atoms: #1 -x+1,-y+1,-z+2 #2 -x+2,-y,-z+1 #3 x-1,y,z #4 -x+1,-y,-z+1 #5 -x+1,-y+1,-z+1 #6 x+1,y,z #7 x,y+1,z+1 #8 -x+2,-y+1,-z+2 #9 x+1,y+1,z+1



**Table S5-** Hydrogen bonds for **3** [Å and deg.].

D-H...A	d(D-H)	d(H...A)	d(D...A)	<(DHA)
C(17)-H(17)...O(1)#3	0.93	2.53	3.391(3)	154.4
C(18)-H(18A)...O(1)#3	0.96	2.50	3.411(3)	158.8
C(4)-H(4)...O(6)#4	0.93	2.88	3.505(3)	125.9
C(5)-H(5)...O(6)#4	0.93	2.91	3.535(3)	126.2
C(1)-H(1)...O(4)#5	0.93	2.90	3.538(3)	127.0
C(1)-H(1)...O(5)#5	0.93	2.56	3.390(3)	149.1
C(2)-H(2A)...O(7)#5	0.93	2.83	3.600(4)	140.8
C(12)-H(12)...O(6)#2	0.93	2.94	3.755(3)	147.3
C(14)-H(14A)...N(4)#6	0.96	2.89	3.769(3)	151.9
C(16)-H(16B)...O(5)#7	0.96	2.58	3.297(3)	131.1
C(14)-H(14B)...O(6)#8	0.96	2.77	3.677(4)	158.8
C(15)-H(15B)...O(7)#8	0.96	2.87	3.662(4)	140.1
C(15)-H(15C)...O(5)#8	0.96	2.64	3.283(3)	125.0
C(14)-H(14C)...O(1)#9	0.96	2.59	3.382(3)	139.6

Symmetry transformations used to generate equivalent atoms:

#1 -x+1,-y+1,-z #2 -x,-y+2,-z+1 #3 x+1,y,z #4 -x+1,-y+2,-z+1 #5 -x+1,-y+1,-z+1 #6  
x-1,y,z #7 x,y-1,z-1 #8 x-1,y-1,z-1 #9 -x,-y+1,-z

## Annex 3: Supplementary Information of Article 4

### Isomorphous Ln-MOFs with Terphenyl Tetracarboxylate Struts: Single Crystal, Photophysical and Theoretical Studies

Love Karan Rana<sup>1\*</sup>, Prabhjyot Kaur<sup>1</sup>, Alborz Bavandsavadkouhi<sup>1</sup>, and Thierry Maris<sup>2</sup>

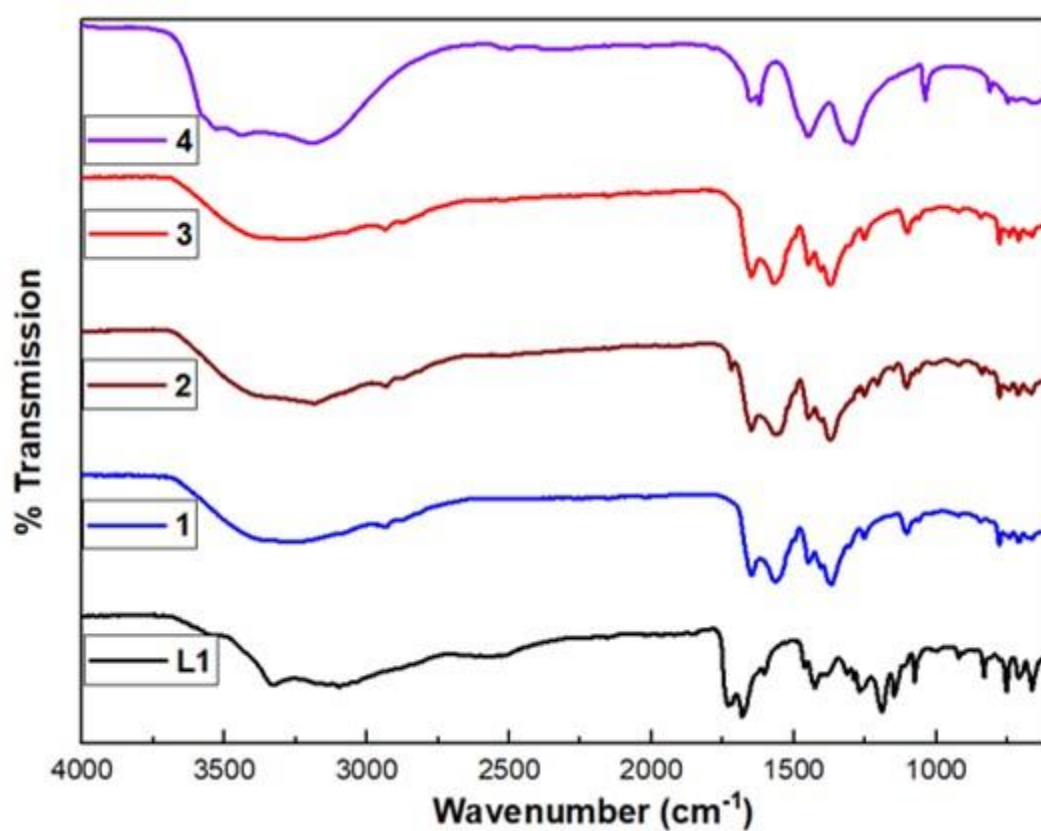
<sup>1</sup>*Département de Chimie, Biochimie et physique and Institut de Recherche sur l'Hydrogène (DuongLab), Université du Québec à Trois-Rivières, Trois-Rivières, Québec, G9A 5H7, Canada*

<sup>2</sup>*Département de Chimie, Université de Montréal, Montréal, Québec, H3C 3J7, Canada*

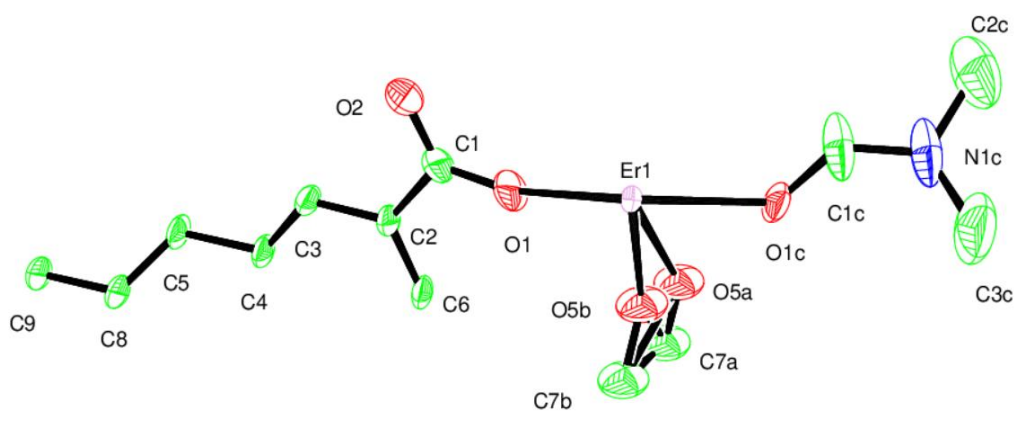
#### Table of contents

Figure	Caption	Page No.
<b>1</b>	IR spectra of <b>L</b> and compounds.	240
<b>2</b>	ORTEP representation of compound <b>2</b> at 30% ellipsoidal probability.	241
<b>3</b>	ORTEP representation of compound <b>3</b> at 30% ellipsoidal probability.	241
<b>4</b>	ORTEP representation of compound <b>4</b> at 30% ellipsoidal probability.	241
<b>5</b>	Absorption spectra of <b>L1</b> and compounds <b>1-4</b> .	242
<b>6</b>	Simplified scheme showing the photosensitization of Ln(III) ions in the compounds <b>2</b> and <b>3</b> by <b>L1</b> molecule, with associated photophysical phenomenon.	243
Table	Caption	
<b>1</b>	Crystal data and structure refinement for compound <b>1</b> .	244
<b>2</b>	Crystal data and structure refinement for compound <b>2</b> .	245

3	Crystal data and structure refinement for compound <b>3</b> .	246
4	Crystal data and structure refinement for compound <b>4</b> .	247
5	Characteristic IR frequencies for different functional groups in the compounds <b>1-4</b> .	248
6	Sub-states of Singlets.	249
7	Sub-states of Triplets.	250
8	Energy gap between excited states.	251



**Figure S1**– IR spectra of **L1** and compounds **1-4**.



**Figure S2** - ORTEP representation of compound **2** at 30% ellipsoidal probability.

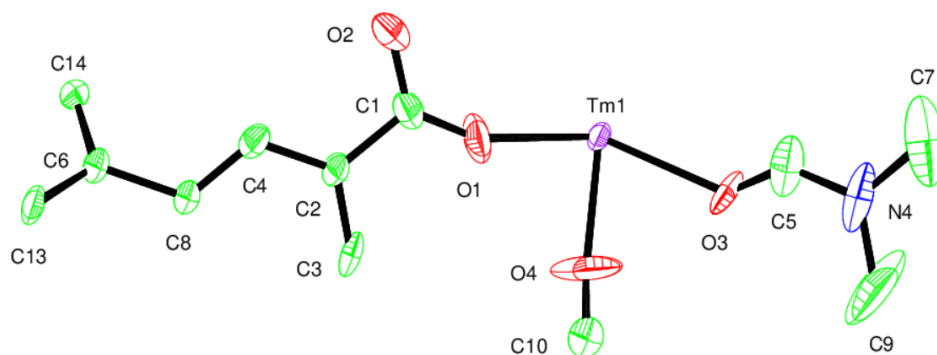


**Figure S3** - ORTEP representation of compound **3** at 30% ellipsoidal probability.

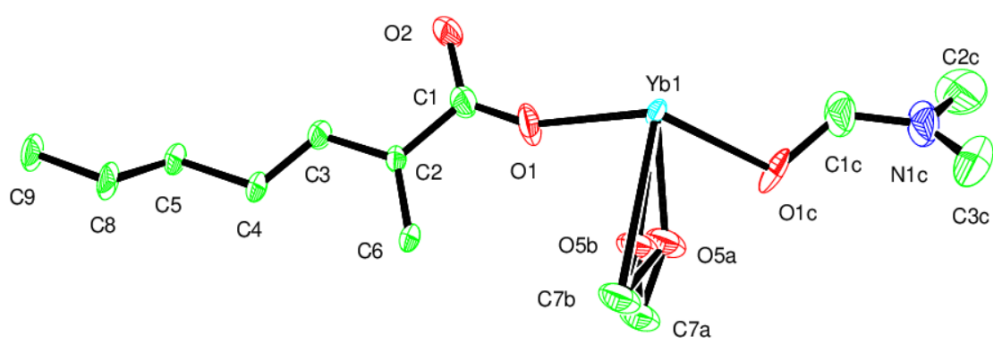


**Figure S4** - ORTEP representation of compound **4** at 30% ellipsoidal probability.

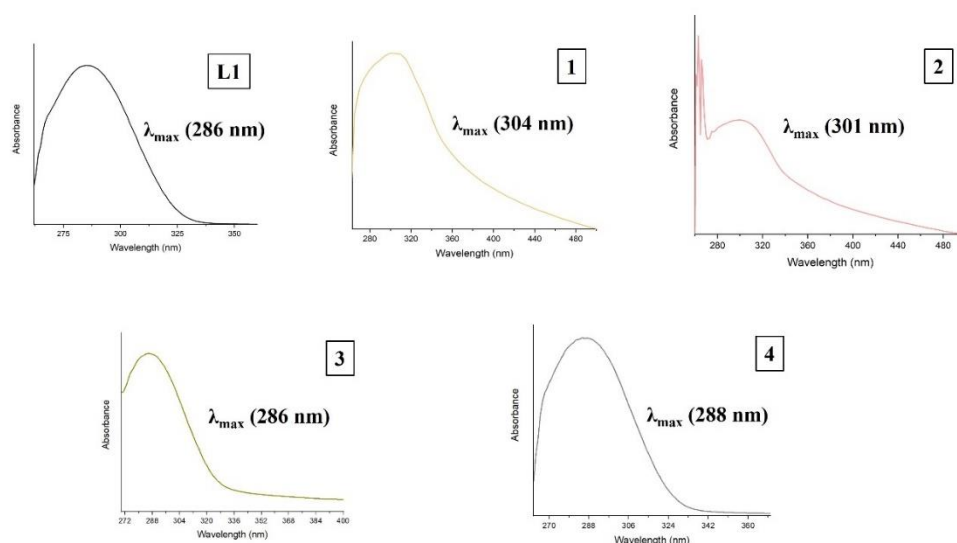


**Figure S5** – Absorption spectra of **L1** and compounds **1-4**. (Note: The absorption spectrum of the ligand is taken in DMF solution and the spectra of the compounds **1-4** are taken using solid-state suspension in DMF)

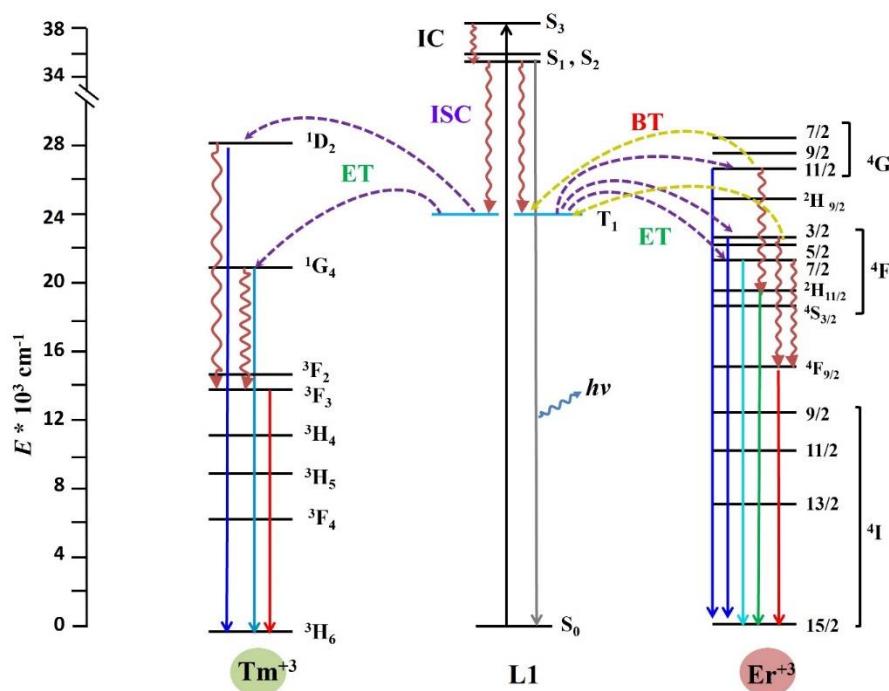


**Figure S6** – Simplified scheme showing the photosensitization of Ln(III) ions in the compounds **2** and **3** by **L1** molecule, with associated photophysical phenomenon. (IC – Internal

conversion, ISC – Intersystem crossing, ET – Energy-transfer/Photosensitization, BT- Back-transfer of energy)

**Table S1-** Crystal data and structure refinement for compound **1**.

Identification code	<b>1</b>
Empirical formula	C <sub>60</sub> H <sub>80.01</sub> Ho <sub>3</sub> N <sub>8.01</sub> O <sub>29.01</sub>
Formula weight	624.14
Temperature	150(2) K
Wavelength	1.34139 Å
Crystal system	Trigonal
Space group	R -3 m
Unit cell dimensions	a = 17.7613(3) Å      a = 90°. b = 17.7613(3) Å      b = 90°. c = 41.2244(10) Å      g = 120°.
Volume	11262.5(5) Å <sup>3</sup>
Z	6
Density (calculated)	1.656 Mg/m <sup>3</sup>
Absorption coefficient	14.478 mm <sup>-1</sup>
F(000)	5575
Crystal size	0.210 x 0.160 x 0.120 mm <sup>3</sup>
Theta range for data collection	3.119 to 60.654°.
Index ranges	-19 ≤ h ≤ 23, -23 ≤ k ≤ 22, -53 ≤ l ≤ 53
Reflections collected	61720
Independent reflections	3153 [R(int) = 0.0505]
Completeness to theta = 53.594°	99.5 %
Refinement method	Full-matrix least-squares on F <sup>2</sup>
Data / restraints / parameters	3153 / 42 / 163
Goodness-of-fit on F <sup>2</sup>	1.143
Final R indices [I > 2σ(I)]	R1 = 0.0440, wR2 = 0.1273
R indices (all data)	R1 = 0.0453, wR2 = 0.1286
Extinction coefficient	n/a

Largest diff. peak and hole	1.465 and -0.907 e.Å <sup>-3</sup>
CCDC No.	2033632

**Table S2-** Crystal data and structure refinement for compound **2**.

Identification code	<b>2</b>
Empirical formula	C61.50 H81.17 Er3 N8.50 O28.33
Formula weight	1894.57
Temperature	150(2) K
Wavelength	1.34139 Å
Crystal system	Trigonal
Space group	R -3 m
Unit cell dimensions	a = 17.7410(3) Å      a = 90°. b = 17.7410(3) Å      b = 90°. c = 41.1955(12) Å      g = 120°.
Volume	11228.9(5) Å <sup>3</sup>
Z	6
Density (calculated)	1.681 Mg/m <sup>3</sup>
Absorption coefficient	11.334 mm <sup>-1</sup>
F(000)	5642
Crystal size	0.200 x 0.140 x 0.120 mm <sup>3</sup>
Theta range for data collection	4.336 to 60.689°.
Index ranges	-20 ≤ h ≤ 21, -19 ≤ k ≤ 23, -53 ≤ l ≤ 52
Reflections collected	54404
Independent reflections	3141 [R(int) = 0.0396]
Completeness to theta = 53.594°	99.3 %
Refinement method	Full-matrix least-squares on F <sup>2</sup>
Data / restraints / parameters	3141 / 48 / 163
Goodness-of-fit on F <sup>2</sup>	1.142
Final R indices [I > 2σ(I)]	R1 = 0.0394, wR2 = 0.1124
R indices (all data)	R1 = 0.0400, wR2 = 0.1132
Extinction coefficient	n/a
Largest diff. peak and hole	1.061 and -0.951 e.Å <sup>-3</sup>
CCDC No.	2033624

**Table S3-** Crystal data and structure refinement for compound **3**.

Identification code	<b>3</b>
Empirical formula	C <sub>61</sub> H <sub>74</sub> N <sub>8.33</sub> O <sub>26.66</sub> Tm <sub>3</sub>
Formula weight	1857.25
Temperature	293(2) K
Wavelength	1.54184 Å
Crystal system	Trigonal
Space group	R -3 m
Unit cell dimensions	a = 17.6690(16) Å      a = 90°. b = 17.6690(16) Å      b = 90°. c = 41.147(2) Å      g = 120°.
Volume	11125(2) Å <sup>3</sup>
Z	6
Density (calculated)	1.663 Mg/m <sup>3</sup>
Absorption coefficient	7.172 mm <sup>-1</sup>
F(000)	5512
Crystal size	0.190 x 0.160 x 0.130 mm <sup>3</sup>
Theta range for data collection	3.081 to 71.772°.
Index ranges	-21 ≤ h ≤ 19, -21 ≤ k ≤ 19, -50 ≤ l ≤ 43
Reflections collected	8103
Independent reflections	2634 [R(int) = 0.0868]
Completeness to theta = 67.684°	99.8 %
Refinement method	Full-matrix least-squares on F <sup>2</sup>
Data / restraints / parameters	2634 / 57 / 148
Goodness-of-fit on F <sup>2</sup>	0.984
Final R indices [I > 2σ(I)]	R1 = 0.0533, wR2 = 0.1305
R indices (all data)	R1 = 0.0710, wR2 = 0.1419
Extinction coefficient	n/a
Largest diff. peak and hole	0.974 and -0.809 e.Å <sup>-3</sup>
CCDC No.	2049424



**Table S4-** Crystal data and structure refinement for compound **4**.

Identification code	<b>4</b>	
Empirical formula	C <sub>50</sub> H <sub>50.67</sub> N <sub>4.67</sub> O <sub>22.67</sub> Yb <sub>3</sub>	
Formula weight	1598.84	
Temperature	150(2) K	
Wavelength	1.34139 Å	
Crystal system	Trigonal	
Space group	R -3 m	
Unit cell dimensions	a = 17.7342(8) Å	a = 90°.
	b = 17.7342(8) Å	b = 90°.
	c = 41.081(3) Å	g = 120°.
Volume	11189.1(12) Å <sup>3</sup>	
Z	6	
Density (calculated)	1.424 Mg/m <sup>3</sup>	
Absorption coefficient	12.560 mm <sup>-1</sup>	
F(000)	4648	
Crystal size	0.210 x 0.160 x 0.120 mm <sup>3</sup>	
Theta range for data collection	4.338 to 60.889°.	
Index ranges	-23 ≤ h ≤ 22, -22 ≤ k ≤ 23, -52 ≤ l ≤ 53	
Reflections collected	49427	
Independent reflections	3132 [R(int) = 0.0640]	
Completeness to theta = 53.594°	98.9 %	
Refinement method	Full-matrix least-squares on F <sup>2</sup>	
Data / restraints / parameters	3132 / 54 / 163	
Goodness-of-fit on F <sup>2</sup>	1.099	
Final R indices [I > 2σ(I)]	R1 = 0.0479, wR2 = 0.1385	
R indices (all data)	R1 = 0.0483, wR2 = 0.1390	
Extinction coefficient	n/a	
Largest diff. peak and hole	1.528 and -1.531 e.Å <sup>-3</sup>	
CCDC No.	2033633	

**Table S5-** Characteristic IR frequencies for different functional groups in the compounds **1-4**.

Compound	Vibration	Group	Wavenumber (cm <sup>-1</sup> )
<b>L1</b>	$\nu$ (O-H)Stretching	Carboxylic	3330 (m, b)
	$\nu$ (C=O)Stretching	Carboxylic	1726 (m)
	$\nu$ (O-H)Stretching	Carboxylic	3096 (w)
	$\nu$ (O-H)bending	Carboxylic	1430 (w)
	$\nu$ (C=C)Stretching	Phenyl ring	1461 (w)
<b>1</b>	$\nu$ (C=O)Stretching	Carboxylate	1650 (s)
	$\nu$ (C=O)Stretching	DMF	1556 (m)
	$\nu$ (C=C)Stretching	Phenyl ring	1450 (w)
<b>2</b>	$\nu$ (C=O)Stretching	Formate	1726 (w)
	$\nu$ (C=O)Stretching	Carboxylate	1652 (s)
	$\nu$ (C=O)Stretching	DMF	1545 (m)
	$\nu$ (C=C)Stretching	Phenyl ring	1445 (w)
<b>3</b>	$\nu$ (C=O)Stretching	Carboxylate	1651 (s)
	$\nu$ (C=O)Stretching	DMF	1550 (m)
	$\nu$ (C=C)Stretching	Phenyl ring	1449 (w)
<b>4</b>	$\nu$ (C=O)Stretching	Carboxylate	1654 (s)
	$\nu$ (C=O)Stretching	DMF	1555 (m)
	$\nu$ (C=C)Stretching	Phenyl ring	1450 (b)

**Table S6** – Sub-states of Singlets of **L1**

Singlet state	Energy in eV	Energy in cm <sup>-1</sup>
Singlet 1	4.651	37511.7
95a -> 107a : 0.010841		
100a -> 105a : 0.032116		
100a -> 108a : 0.030513		
101a -> 105a : 0.062358		
101a -> 108a : 0.040334		
102a -> 106a : 0.205617		
102a -> 107a : 0.021027		
104a -> 106a : 0.132824		
104a -> 107a : 0.390313		
Singlet 2	4.655	37547.0
95a -> 106a : 0.012031		
100a -> 105a : 0.063473		
100a -> 108a : 0.041664		
101a -> 105a : 0.032984		
101a -> 108a : 0.030956		

102a -> 106a : 0.019277 102a -> 107a : 0.210909 104a -> 106a : 0.389841 104a -> 107a : 0.139839		
Singlet 3  102a -> 108a : 0.054768 103a -> 109a : 0.010386 104a -> 105a : 0.834927 104a -> 106a : 0.011350 104a -> 110a : 0.048959	4.797	38692.8
Singlet 4 95a -> 109a : 0.025134 103a -> 105a : 0.365528 103a -> 110a : 0.122646 103a -> 112a : 0.016314 104a -> 109a : 0.422208	5.082	40990.4

**Table S7** – Sub-states of Triplets

Triplet State	Energy in eV	Energy in cm <sup>-1</sup>
Triplet 1 95a -> 110a : 0.017607 100a -> 106a : 0.014331 100a -> 107a : 0.073993 101a -> 106a : 0.074411 101a -> 107a : 0.014027 102a -> 108a : 0.107445 102a -> 111a : 0.015498 103a -> 109a : 0.053715 104a -> 105a : 0.503956 104a -> 110a : 0.042890	3.020	24361.6
Triplet 2 95a -> 108a : 0.029832 96a -> 108a : 0.010738 99a -> 108a : 0.016314 100a -> 106a : 0.023377 100a -> 107a : 0.206356 101a -> 106a : 0.206833 101a -> 107a : 0.022934 102a -> 105a : 0.199241 102a -> 112a : 0.011708 104a -> 108a : 0.156216 104a -> 111a : 0.021544	3.321	26789.7
Triplet 3 95a -> 105a : 0.047542 96a -> 105a : 0.016935	3.706	29889.5

99a -> 105a : 0.022285		
100a -> 106a : 0.033485		
100a -> 107a : 0.173586		
101a -> 106a : 0.178048		
101a -> 107a : 0.033864		
102a -> 108a : 0.033338		
103a -> 109a : 0.158482		
104a -> 105a : 0.062745		
104a -> 110a : 0.118057		
104a -> 112a : 0.032047		
Triplet 4	3.881	31299.8
95a -> 107a : 0.029010		
96a -> 107a : 0.011664		
99a -> 107a : 0.016761		
100a -> 105a : 0.010796		
102a -> 106a : 0.045296		
102a -> 107a : 0.303229		
104a -> 106a : 0.068248		
104a -> 107a : 0.456099		

**Table S8**– Energy gap between excited states of **L1**.

Singlets cm <sup>-1</sup>	Triplets cm <sup>-1</sup>	Energy gap (Singlets) cm <sup>-1</sup>	Energy gap (Triplets) cm <sup>-1</sup>	Energy gap (Singlet-Triplet) cm <sup>-1</sup>
S <sub>1</sub> - 37511.7	T <sub>1</sub> - 24361.6	1181.1 (S <sub>3</sub> – S <sub>1</sub> )	5527.9 (T <sub>3</sub> – T <sub>1</sub> )	13150 (S <sub>1</sub> – T <sub>1</sub> )
S <sub>2</sub> - 37547.0	T <sub>2</sub> - 26789.7	1145.8 (S <sub>3</sub> – S <sub>2</sub> )	3099 (T <sub>3</sub> – T <sub>2</sub> )	
S <sub>3</sub> - 38692.8	T <sub>3</sub> -29889.5	35.3 (S <sub>2</sub> – S <sub>1</sub> )	2428.1 (T <sub>2</sub> – T <sub>1</sub> )	